



ÉCOLE  
POLYTECHNIQUE  
DE BRUXELLES



UNIVERSITÉ LIBRE DE BRUXELLES

# Photovoltaic system optimization through distributed maximum power point tracking techniques and power delivery strategies in distribution networks

**Thesis presented by Ramón LÓPEZ ERAUSKIN**

A thesis submitted in fulfilment of the requirements for the degree of  
Doctor of Philosophy in Engineering Science and Technology  
“Docteur en Sciences de l’Ingénieur et Technologie”

Academic year 2019-2020

Supervisor: Professor Johan GYSELINCK

Electrical energy group  
Bio, Electro And Mechanical Systems Department



## Thesis jury:

Prof. Dr. Ir. Patrick HENDRICK (Université libre de Bruxelles, Chair)  
Prof. Dr. Ir. Pierre HENNEAUX (Université libre de Bruxelles, Secretary)  
Prof. Dr. Ir. Philippe LATAIRE (Vrije Universiteit Brussel)  
Prof. Dr. Ir. Giovanni SPAGNUOLO (Università Degli Studi di Salerno)



UNIVERSITÉ LIBRE DE BRUXELLES

*Abstract*

École polytechnique de Bruxelles  
Bio, Electro and Mechanical Systems department

Doctor of Philosophy

**Photovoltaic system optimization through distributed maximum power point tracking techniques and power delivery strategies in distribution networks**

by Ramón LÓPEZ ERAUSKIN

In this thesis, different strategies that improve the integration of photovoltaic (PV) systems into the grid are discussed. First, the interaction of PV installations and the distribution network is addressed. A management system in charge of controlling the different PV units is implemented in real hardware. The management system deals with the grid-voltage issues caused by the distributed PV generation thanks to the contribution of all the inverters connected to the same network.

In the second part, the strategy is focused on the DC side of the PV system. Distributed maximum power point (DMPPT) architectures are adopted as an alternative to the classical PV systems, that show improved performance in mismatch conditions when compared to the classical approach. The coordination of the DMPPT functions with a central MPPT function in charge of tracking the DC-bus voltage  $V_{DC}$  is proposed and safe  $V_{DC}$  operating areas are identified. The advantages of having an adaptive  $V_{DC}$  control in partially shaded conditions is studied and demonstrated. Besides, the dynamic performance in DMPPT systems is improved, enhancing system stability.

Alternative control strategies consider the integration of batteries at module level. The batteries provide support to the PV generation and act as a backup system to compensate large mismatch conditions in systems adopting a constant  $V_{DC}$  or if the joint operation of DMPPT and CMPPT functions is not effective.

Overall, the proposed control strategies enhance the integration of PV systems, increase the PV generation and improve system stability, compared to other control strategies for PV DMPPT systems.





# *Acknowledgements*

First, I would like to express my gratitude towards my family and friends for the encouragement which helped me in completion of this manuscript. My very special thanks are for my life partner, Irene, who has always believed in me, has been supportive from the very beginning and has had tons of patience with me.

I would like to thank my supervisor Prof. Johan Gyselinck for giving me the opportunity to make the PhD in the BEAMS department and for supervising my work. I would also like to thank the other members of my PhD committee, Prof. Patrick Hendrick, Prof. Pierre Henneaux and Prof. Philippe Lataire for their encouragement and insightful comments.

My sincere thanks also goes to Prof. Giovanni Spagnuolo and Prof. Giovanni Petrone, who hosted me during my stay in the *Dipartimento di Ingegneria dell'Informazione ed Elettrica e Matematica Applicata* (DIEM), University of Salerno (UNISA), and who taught me a lot thanks to their passion for photovoltaics.

I would also like to thank my colleagues at BEAMS department for their help during my research work. Special thanks goes to Ander, with whom I have shared this journey.

Finally, I would like to thank Ariane for all the help and very nice chats we have shared. Many thanks to Pascal as well, always ready to help with the technical aspects in the laboratory.



# Contents

<b>Abstract</b>	<b>iii</b>
<b>Acknowledgements</b>	<b>v</b>
<b>List of Figures</b>	<b>xi</b>
<b>List of Tables</b>	<b>xvii</b>
<b>Abbreviations</b>	<b>xix</b>
<b>1 Introduction</b>	<b>1</b>
<b>I Integration of photovoltaic systems in the low voltage network</b>	<b>3</b>
<b>2 Introduction</b>	<b>5</b>
<b>3 Grid-voltage compensation functionalities of commercial PV inverters</b>	<b>7</b>
3.1 Voltage compensation . . . . .	7
3.1.1 Characteristics of overhead lines and underground cables in distribution systems . . . . .	9
3.2 Grid codes . . . . .	9
3.3 Photovoltaic Inverters . . . . .	10
3.3.1 General characteristics of the inverters . . . . .	10
3.3.1.1 Power factor sign convention . . . . .	11
3.3.2 Features of the inverters . . . . .	12
3.4 Test platform . . . . .	14
3.4.1 PV array emulator . . . . .	14
3.4.2 LV network impedance . . . . .	15
3.4.3 Graphical User Interface . . . . .	15
3.4.4 External control . . . . .	16
3.5 Test protocol . . . . .	16
3.6 Test results of PV inverters capabilities . . . . .	19
3.6.1 Variation of $\cos \varphi$ . . . . .	19
3.6.2 Variation of $P$ . . . . .	22
3.6.3 Voltage compensating actions . . . . .	22

3.6.4	Discussion of results . . . . .	22
<b>4</b>	<b>Photovoltaic inverters in unbalanced LV networks</b>	<b>27</b>
4.1	Test platform . . . . .	27
4.1.1	External grid . . . . .	28
4.1.2	Distribution transformer . . . . .	28
4.1.3	LV network impedance . . . . .	29
4.1.4	PV system . . . . .	29
4.2	Voltage fluctuation in the LV network . . . . .	30
4.3	Results and comparison . . . . .	33
4.3.1	Static production values . . . . .	33
4.3.2	Dynamic production values . . . . .	35
4.3.2.1	Sunny day . . . . .	35
4.3.2.2	Day with scattered clouds . . . . .	36
4.3.3	Alternatives to the voltage support by reactive power . . . . .	36
4.3.4	Discussion of results . . . . .	39
<b>5</b>	<b>Operation of photovoltaic inverters in a distributed scheme</b>	<b>41</b>
5.1	Distributed control of photovoltaic inverters in Distributed Networks . . . . .	41
5.1.1	Communication network architecture . . . . .	42
5.1.1.1	Communication protocol . . . . .	43
5.1.1.2	Control algorithm for the active management . . . . .	43
5.1.1.3	Corrective actions in the control algorithm . . . . .	44
5.2	Experimental results . . . . .	45
5.2.1	Test platform . . . . .	45
5.2.2	Local operation . . . . .	45
5.2.3	Active and reactive power support at partial load . . . . .	46
5.2.4	Active and reactive power support at full load . . . . .	47
5.2.5	Discussion of results . . . . .	49
<b>6</b>	<b>Discussion of Part I</b>	<b>51</b>
<b>II Control strategies for distributed maximum power point tracking architectures in photovoltaic applications</b>		<b>53</b>
<b>7</b>	<b>Introduction</b>	<b>55</b>
<b>8</b>	<b>Preliminary study on the viability of distributed MPPT systems</b>	<b>59</b>
8.1	Converter topologies for DMPPT architectures . . . . .	59
8.2	MPPT control algorithms in PV systems . . . . .	60
8.3	System description and basic operation . . . . .	63
8.3.1	DC/DC boost converter . . . . .	63
8.3.2	Basic operation . . . . .	64
8.3.3	Efficiencies in photovoltaic systems . . . . .	66
8.3.3.1	Maximum Power Point Tracking efficiency . . . . .	66
8.3.3.2	Converter efficiency . . . . .	67
8.3.3.3	CMPPT and DMPPT efficiency . . . . .	67

8.3.3.4	Inverter efficiency . . . . .	67
8.3.3.5	Total efficiency . . . . .	67
8.4	Averaged models . . . . .	68
8.5	CMPPT and DMPPT power vs. voltage curves . . . . .	70
8.5.1	DMPPT $V_{DC}$ operating range . . . . .	71
8.5.1.1	$V_{DC}$ in case of unavoidable mismatch . . . . .	72
8.5.2	Maximum performance: GMPP and GMPPR . . . . .	72
8.6	CMPPT and DMPPT systems full-day performance . . . . .	76
8.6.1	Irradiance profiles . . . . .	76
8.6.2	Simulation results . . . . .	76
8.7	Discussion of results . . . . .	80
<b>9</b>	<b>Centralized control strategy in DMPPT systems</b>	<b>81</b>
9.1	System description . . . . .	82
9.1.1	Non-isolated interleaved boost-3PC . . . . .	83
9.1.1.1	Averaged model . . . . .	84
9.2	Comparison of DMPPT and CMPPT systems . . . . .	85
9.2.1	Simulation results . . . . .	85
9.2.2	Experimental results . . . . .	87
9.2.2.1	Discussion of results . . . . .	89
9.3	Coordination of Distributed and Central MPPT . . . . .	90
9.3.1	Hybrid Multi-Variable P&O control . . . . .	92
9.3.1.1	Initial conditions . . . . .	94
9.3.2	Dynamic response in MV-P&O control algorithms . . . . .	95
9.3.2.1	MVPOC dynamic response . . . . .	96
9.3.2.2	MVPOV dynamic response . . . . .	97
9.3.2.3	H-MV dynamic response . . . . .	97
9.3.3	Simulation results . . . . .	98
9.3.3.1	$V_{DC}$ control . . . . .	100
	Unavoidable suboptimal operating conditions: . . . . .	101
9.3.3.2	H-MV Dynamic performance . . . . .	101
9.3.4	Experimental results . . . . .	104
9.3.4.1	H-MV MPPT performance . . . . .	104
9.3.4.2	$V_{DC}$ control . . . . .	105
9.3.4.3	H-MV Dynamic performance . . . . .	105
9.4	Discussion of results . . . . .	107
<b>10</b>	<b>Improvements in the Multi-Variable P&amp;O control</b>	<b>109</b>
10.1	Proposed centralized multi-variable control . . . . .	109
10.1.1	Time interval between two consecutive perturbations . . . . .	110
10.1.2	Design of the voltage step amplitude . . . . .	111
10.1.3	Proposed adaptive control . . . . .	112
10.2	Simulation results . . . . .	114
10.2.1	$V_{DC}$ control . . . . .	115
10.2.2	Dynamic performance of the proposed control algorithm . . . . .	116
10.3	Discussion of results . . . . .	118

---

<b>11 Control strategies for DMPPT systems including batteries</b>	<b>121</b>
11.1 MPPT operating range extension . . . . .	121
11.1.1 Proposed control algorithm . . . . .	123
11.1.1.1 $V_{DC}$ control . . . . .	123
11.1.1.2 Batteries as support to PV generation . . . . .	124
11.1.2 Simulation results . . . . .	124
11.1.3 Experimental results . . . . .	127
11.2 $V_o$ equalization . . . . .	128
11.2.1 Simulation results . . . . .	129
11.3 Discussion of results . . . . .	132
<b>12 Conclusions</b>	<b>133</b>
<b>A Universal communication protocol and specific protocols of main PV inverter brands</b>	<b>137</b>
A.1 Structure of the communication platform . . . . .	137
A.2 Universal communication protocol . . . . .	138
<b>B Simulation models and results</b>	<b>141</b>
B.1 Distributed and central MPPT functions . . . . .	141
B.1.1 Switching model of the boost DC/DC converter . . . . .	141
B.1.2 Averaged model of the central MPPT . . . . .	142
B.1.3 Averaged model of the distributed MPPT . . . . .	143
B.1.4 Additional results . . . . .	143
<b>Bibliography</b>	<b>147</b>

# List of Figures

3.1	Simplified LV network diagram representing the reverse current flow due to the injection of inverter power ( $P_{inv}$ , $Q_{inv}$ ) into the grid. . . . .	8
3.2	IEEE standard Power Factor sign convention. Own illustration based on IEEE standard. . . . .	12
3.3	PQ curves and admissible operating areas for each power control mode. Own illustration based on the European norm EN 50549-1 and the VDE-AR-N 4105 German directive. . . . .	13
3.4	Representation of the test platform . . . . .	14
3.5	Part of the available PV emulator Graphical User Interface. . . . .	16
3.6	GWio management and communication gateway used to control the inverters. . . . .	17
3.7	Response time ( $T_{response}$ ) after setting a Q reference (black dashed line and the steady state error tolerance band with solid lines), serial communication signal (blue line), and measured Q (red line). . . . .	18
3.8	Timeout after lack of response from the inverter. . . . .	18
3.9	3-phase Inv-1 $\cos \varphi$ test. At each $P_{inv}$ level (in steps of $\Delta P=25\%$ ), $\cos \varphi$ set in steps of $\Delta \cos \varphi=0.01$ . . . . .	20
3.10	3-phase Inv-2 $\cos \varphi$ test. At each $P_{inv}$ level (in steps of $\Delta P=25\%$ ), $\cos \varphi$ set in steps of $\Delta \cos \varphi=0.01$ . . . . .	21
3.11	3-phase Inv-1 test. At each $Q_{inv}$ level (in steps of $\Delta \cos \varphi= 0.25$ ), $P$ set in steps of $\Delta P=10\%P_N$ . . . . .	23
3.12	Inv-2 <i>stepwise</i> and <i>jumping from unity</i> $P$ test . . . . .	24
3.13	Inv-1 PQ compensating features. . . . .	25
3.14	Inv-2 PQ compensating features. . . . .	26
4.1	Laboratory test bench for the study of voltage fluctuations and unbalanced conditions. . . . .	28
4.2	Part of the laboratory test platform and the neutral current flow direction. . . . .	31
4.3	Voltage phasors of the LV feeder at PCC1. . . . .	32
4.4	Voltage profiles of the LV network. "L" corresponds to "Laboratory" (solid lines) and "S" to "Simulation" (dashed-dotted lines) results. . . . .	34
4.5	Simulation and experimental results of the three-phase inverter connected at PCC2 on a sunny day. . . . .	37
4.6	Results of the three-phase inverter connected at PCC2 on a day with scattered clouds. . . . .	38
5.1	Structure of the distributed communication scheme. . . . .	42

5.2	State transition diagram of the distributed control scheme. The red dotted lines are the emergency control transitions while blue dashed lines are the restoring ones. . . . .	44
5.3	Local operation mode (mode A). $Q_f(V_{tm}, P_{set})$ function. . . . .	45
5.4	Local operation mode (mode A). Voltage compensation action of Inv-1. . . . .	46
5.5	State transition diagram of testing scenario 1. Own illustration based on Fig. 5.2. . . . .	46
5.6	Measured A-B-C-D-E modes operating sequence. Voltage compensation action of Inv-1. . . . .	48
5.7	State transition diagram of testing scenario 2. Own illustration based on Fig. 5.2. . . . .	49
5.8	Measured A-B-C-D-C-D-E modes operating sequence. Voltage compensation action of Inv-1. . . . .	50
7.1	Different types of power electronics solutions for PV systems. . . . .	57
8.1	Conventional P&O control algorithm principle. . . . .	61
8.2	Flowchart of the INC control algorithm. . . . .	62
8.3	PV module subsystem formed by a PV source and a DC/DC boost converter. . . . .	63
8.4	DC/DC boost converter considered in the switching model. . . . .	69
8.5	Simulation results of the input and output voltage and powers used for characterizing the efficiency curve of the converter. . . . .	69
8.6	Efficiency (%) vs. normalized input power (p.u.) curve of the DC/DC converter adopted in the model. . . . .	70
8.7	Matching DMPPT and CMPPT P-V curves with $V_{DC,min-2}=160V$ of Inv-2 for the different PV panel mismatch configurations: $N_H=0$ and $N_L=6$ (deep-red), $N_H=1$ and $N_L=5$ (light-blue), $N_H=2$ and $N_L=4$ (green), $N_H=N_L=3$ (purple), $N_H=4$ and $N_L=2$ (yellow), $N_H=5$ and $N_L=1$ (orange), $N_H=6$ and $N_L=0$ (dark-blue). . . . .	75
8.8	Matching of the inverter input voltage with DMPPT and CMPPT P-V curves. . . . .	77
8.9	Irradiation profiles considered: sunny, scattered clouds, cloudy. . . . .	78
8.10	PV array output powers for DMPPT and CMPPT systems corresponding to each irradiance profile. . . . .	79
9.1	Central and distributed MPPT approaches for PV systems. . . . .	82
9.2	Interleaved boost-3PC topology. The branches in red are the interleaving power transfer path. . . . .	83
9.3	Performance of the CMPPT approach under homogeneous and non-homogeneous irradiance conditions. . . . .	86
9.4	Performance of the DMPPT approach under homogeneous irradiance conditions at $V_{DC1}=120V$ and non-homogeneous irradiance conditions at 4 different $V_{DCs}$ . At $t=16$ s $G_1$ changes from $600$ $W/m^2$ to $300$ $W/m^2$ , $G_2=G_3=600$ $W/m^2$ . . . . .	87
9.5	Experimental setup including a PC for supervisory control (1), 6 DC/DC converters (2), rooftop PV installation (3), 2Q power supply (4), current and voltage sensors for the data acquisition system (5), the data acquisition system (6) and a PC for data-acquisition (7). . . . .	88



9.6	PV1 to PV6 from left to right - $Sh \simeq 50\%$ static shade on PV1 and PV4. .	89
9.7	Experimental results of the DMPPT and CMPPT systems under mismatch conditions. The CMPPT system operates at LMPP before, and at GMPP after, $t=500$ s ( $P_{PV1-3}$ ). The DMPPT system operates at LMPP for $V_{DC4-6} < 140$ V, at GMPP for $V_{DC4-6} > 140$ V. . . . .	90
9.8	DMPPT architecture of the grid-connected PV system. . . . .	92
9.9	Operating point description in spherical coordinates of the vectorial approach for a system with $N = 3$ PV modules. . . . .	93
9.10	Steady state operation of DMPPT and CMPPT techniques in a centralized control. MVPOC technique in top plot shows the sequential perturbation of the PV voltages. MVPOV technique PV voltages illustrated in Fig. 9.9 are shown in bottom plot. Middle plot shows the tracking of $V_{DC}$ included in each multi-variable P&O sequence. . . . .	95
9.11	Performance of conventional SV P&O MPPT algorithms with the characteristic three-point behaviour (A-B-C) in steady state (solid lines) and voltage deviation (A-B-C'-D-E-D-F-G-H) in presence of increasing irradiance (dashed lines). . . . .	96
9.12	MVPOC dynamic response. Top to bottom: Irradiance profile, PV voltages. . . . .	96
9.13	MVPOV dynamic response. Top to bottom: Irradiance profile, vectorial variables, PV voltages. . . . .	97
9.14	Flowchart of the proposed H-MV control algorithm. . . . .	99
9.15	Measurement of the power between MPPT sampling instances . . . . .	100
9.16	HMV dynamic response. Top to bottom: Irradiance profile, vectorial variables, PV voltages. . . . .	100
9.17	H-MV performing $V_{DC}$ control. The tracking of $V_{DC}$ increases system efficiency. . . . .	102
9.18	PV voltage deviation due to an irradiance change for different control algorithms. Top to bottom: irradiance profile for the dynamic test, SV, MVPOC, MVPOV, H-MV, H-MV $V_{DC}$ control, and PV powers of the different techniques. . . . .	103
9.19	Experimental results of H-MV: start-up and steady state. Top to bottom: vectorial variables, PV voltage references and measurements, $V_{DC}$ reference and measurement. . . . .	105
9.20	H-MV experimental results at $G \simeq 400$ W/m <sup>2</sup> and PV1 covered with a static shade of $Sh=50\%$ with fixed $V_{DC}$ before, and $V_{DC}$ control after, $t_1$ . Top to bottom: PV and output voltages, sum of PV and output powers, $V_{DC}$ . . . . .	106
9.21	H-MV dynamic performance: experimental results in a day with scattered clouds. Top to bottom: vectorial variables, H-MV PV voltage references, H-MV PV and output voltages, SV PV voltage references, SV PV and output voltages, H-MV and SV PV powers. . . . .	107
10.1	Small-signal equivalent circuit. . . . .	110
10.2	Zoomed view of the PV panel operating point in presence of an irradiance variation at two different irradiance levels: $G_{low}$ and $G_{high}$ , solid lines. Increasing variation of the irradiance, dashed lines. . . . .	113
10.3	Simulation results of the steady state operation of the CMV control technique. Top plot: variables in spherical coordinates. Middle plot: PV voltages. Bottom plot: $V_{DC}$ measurement and reference. . . . .	115

10.4	Simulation results of the system adopting the MVPOV (red line) and the CMV algorithm that includes the $V_{DC}$ control (blue line). Top to bottom: PV power, AC power and CMV $V_{DC}$ .	116
10.5	EN 50530 dynamic performance test adopting either SV (top plot) and H-MV (bottom plot) control algorithms.	117
10.6	Details of the CMV control performance. Static and dynamic behaviour of the PV voltages under rising irradiance variation.	118
10.7	Details of static and dynamic behaviour of the PV voltages under lowering irradiance variation.	119
11.1	(a) Battery-integrated DMPPT system consisting of $N$ DC/DC converters for each PV panel. (b) Control algorithm managing $V_{DC}$ and output voltages of the converters.	122
11.2	Coordination of $V_{DC}$ and PV voltages to prevent an incorrect $P_{DC}$ evaluation.	125
11.3	Comparison of the system performance with (a) fixed and (b) adaptive $V_{DC}$ .	126
11.4	Performance of the system under mismatch conditions with battery compensating actions at different $SoC$ . From left to right, top to bottom: irradiance profiles, PV currents, output voltages, battery currents.	127
11.5	$V_{DC}$ control and battery compensation. Top to bottom: PV and output voltages, limits of the $V_{DC}$ range and $V_{DC}$ operating point, battery 3 current charging, total PV and DC powers.	128
11.6	$SoC_1 < SoC_{max}$ . Top to bottom: first plot: PV1 follows a varying $G_1$ with a trapezoidal profile, $G_2=G_3=300$ W/m <sup>2</sup> for PV2 and PV3. Second plot: output voltages. Third plot: BAT1 charges after $\Delta P_{o12} \leq -20$ W and $\Delta P_{o31} \geq +20$ W. Fourth plot: output powers.	130
11.7	$SoC_1 > SoC_{max}$ (BAT1 charge disabled) and $SoC_2 = SoC_3 > SoC_{min}$ . Top to bottom: first plot: PV1 follows a varying $G_1$ with a trapezoidal profile, $G_2=G_3=300$ W/m <sup>2</sup> for PV2 and PV3. Second plot: output voltages. Third plot: BAT2 and BAT3 discharge after $\Delta P_{o12} \leq -20$ W and $\Delta P_{o31} \geq +20$ W. Fourth plot: output powers.	131
11.8	$SoC_1 = SoC_2 < SoC_{max}$ . Top to bottom: first plot: PV1 and PV2 follow varying $G_1$ and $G_2$ with a trapezoidal profile, $G_3=300$ W/m <sup>2</sup> for PV3. Second plot: output voltages. Third plot: BAT1 and BAT2 charge after $\Delta P_{o31} \geq +20$ W and $\Delta P_{o23} \leq -20$ W. Fourth plot: output powers.	131
11.9	$SoC_1 = SoC_2 > SoC_{max}$ (BAT1 and BAT2 charge disabled) and $SoC_3 > SoC_{min}$ . Top to bottom: first plot: PV1 and PV2 follow varying $G_1$ and $G_2$ with a trapezoidal profile, $G_3=300$ W/m <sup>2</sup> for PV3. Second plot: output voltages. Third plot: BAT3 discharge after $\Delta P_{o31} \geq +20$ W and $\Delta P_{o23} \leq -20$ W. Fourth plot: output powers.	132
A.1	Structure of the communication platform	137
A.2	Features of the inverters	140
B.1	Nonisolated boost converter switching model and its MPPT P&O control	141
B.2	Averaged model of the CMPPT approach	142
B.3	Averaged model of the DMPPT approach	143
B.4	Model of the DC bus for the DMPPT approach	143

---

B.5 P-V curves of DMPPT and CMPPT systems for an increasing number of shaded PV panels . . . . .	144
B.6 P-V curves of DMPPT and CMPPT systems for an increasing number of shaded PV panels . . . . .	145



# List of Tables

3.1	Parameters of the commercial PV inverters considered in this work. . . .	11
3.2	Features of the PV inverters . . . . .	14
3.3	Parameters of the PV panel . . . . .	15
3.4	Test network data . . . . .	15
3.5	$\cos \varphi$ variation test conditions . . . . .	19
3.6	$\cos \varphi$ variation test response times . . . . .	22
4.1	Cable parameters. . . . .	30
4.2	Configuration of the PV arrays. . . . .	30
4.3	Active and reactive power produced by the inverters in each scenario . . .	33
4.4	Measured and calculated rms voltages at each PCC for the different operating scenarios. "L" corresponds to "Laboratory" and "S" to "Simulation" . . .	35
8.1	Characteristic parameters of the BenQ GreenTriplex PM245P00 260Wp. . .	63
8.2	Simulation parameters for the switching model . . . . .	68
8.3	DMPPT DC voltage ranges (in V) for different mismatch conditions ensuring the MPP operation of all the PV panels in the string. $G_H=1000W/m^2$ . . . . .	73
8.4	DMPPT DC voltage ranges (in V) at $G_H=1000W/m^2$ , $G_L=200W/m^2$ for different power levels. . . . .	73
8.5	Maximum performance (in W) of CMPPT and DMPPT systems at different mismatch conditions. $G_H=1000W/m^2$ . . . . .	74
8.6	CMPPT and DMPPT efficiencies (in %) corresponding to the maximum performance. . . . .	76
8.7	DMPPT and CMPPT systems output energy (in kWh) under the proposed 1 day irradiance profiles and shading conditions. . . . .	78
8.8	Overall efficiencies of DMPPT and CMPPT systems (in %) under the proposed irradiance profiles and shading conditions . . . . .	78
9.1	Characteristic parameters at STC of the BenQ GreenTriplex PM245P00 260Wp. . . . .	82
9.2	General parameters of the interleaved boost-3PC. . . . .	83
10.1	Characteristic parameters of the BenQ GreenTriplex PM245P00 260Wp. . .	111
10.2	Main parameters of the boost DC/DC converter . . . . .	111
10.3	Photovoltaic parameters for the design of $\Delta V_{PV}$ . . . . .	112
10.4	Perturbation amplitudes of the variables. . . . .	114
10.5	MPPT and conversion efficiencies (in %) for the 5 subintervals of the simulations in Fig. 10.5 with either constant irradiance ( $W/m^2$ ) or varying irradiance ( $W/m^2/s$ ). . . . .	117

---

11.1 Characteristic parameters at STC of the BenQ GreenTriplex PM245P00 260Wp. . . . .	125
11.2 Battery parameters . . . . .	127
11.3 Simulation parameters . . . . .	129

# Abbreviations

<b>3PC</b>	<b>Three Port Converter</b>
<b>AC</b>	<b>Alternating Current</b>
<b>BIPV</b>	<b>Building Integrated Photovoltaic</b>
<b>CCM</b>	<b>Continuous Conduction Mode</b>
<b>CMPPT</b>	<b>Central Maximum Power Point Tracking</b>
<b>CMV</b>	<b>Central Multi- Variable</b>
<b>DC</b>	<b>Direct Current</b>
<b>DER</b>	<b>Distributed Energy Resources</b>
<b>DMPPT</b>	<b>Distributed Maximum Power Point Tracking</b>
<b>DN</b>	<b>Distributed Network</b>
<b>EV</b>	<b>Electric Vehicle</b>
<b>EMS</b>	<b>Energy Management System</b>
<b>GMPP</b>	<b>Global Maximum Power Point</b>
<b>GMPPT</b>	<b>Global Maximum Power Point Tracking</b>
<b>GMPR</b>	<b>Global Maximum Power Regions</b>
<b>GUI</b>	<b>Graphical User Interface</b>
<b>HV</b>	<b>High Voltage</b>
<b>H-MV</b>	<b>Hybrid Multi- Variable</b>
<b>INC</b>	<b>INCremental conductance</b>
<b>LMPP</b>	<b>Local Maximum Power Point</b>
<b>LMPR</b>	<b>Local Maximum Power Regions</b>
<b>LUT</b>	<b>Look-up Table</b>
<b>LV</b>	<b>Low Voltage</b>
<b>MPP</b>	<b>Maximum Power Point</b>
<b>MPPT</b>	<b>Maximum Power Point Tracking</b>

---

<b>MPR</b>	<b>Maximum Power Regions</b>
<b>MV</b>	<b>Medium Voltage</b>
<b>MVPOC</b>	<b>Multi- Variable Perturb and Observe Cartesian</b>
<b>MVPOV</b>	<b>Multi- Variable Perturb and Observe Vectorial</b>
<b>OLTC</b>	<b>On-Load Tap Changer</b>
<b>P-V</b>	<b>Power vs. Voltage</b>
<b>P&amp;O</b>	<b>Perturb and Observe</b>
<b>PCC</b>	<b>Point of Common Coupling</b>
<b>PQ</b>	<b>Power Quality</b>
<b>PV</b>	<b>Photovoltaic</b>
<b>PWM</b>	<b>Pulse-Width Modulation</b>
<b>SoC</b>	<b>State of Charge</b>
<b>STC</b>	<b>Standard Test Conditions</b>
<b>SV</b>	<b>Single Variable</b>
<b>TFM</b>	<b>Transformer</b>
<b>UCP</b>	<b>Universal Communication Protocol</b>



*Aita eta Amari,  
Jone, Germán eta Quetzali  
eta bereziki, Ireneri.*



# Chapter 1

## Introduction

Reliable integration of distributed energy resources (DER) into the electrical grid presents unique challenges arising from their widespread growth. Photovoltaic (PV) generation is particularly challenging as it is extensively distributed throughout the grid. Thanks to its modularity, PV is the most popular DER among small-scale producers. These producers are popularly known as *prosumers*, generally household owners who in addition to consume electrical energy from the utility grid, produce and export back electricity from their own PV installation.

In this context, governments in different countries implement several regulatory frameworks and support schemes that influence residential PV installations growth [1]. Different strategies include the obligation of grid operators to accept and feed renewable energy from prosumers into the electricity grid at a fixed price (Norway [1], Germany [2, 3], Spain [4]). Feed-in-tariff schemes intend to stimulate the diffusion of small-scale renewables, targeting PV installations (Germany [2], U.K. [5], Australia [6, 7]).

Thanks to government policies, economies of scale, public and private R&D and technological maturity, the cost of PV technology has fall down dramatically over the last four decades [8], making it competitive when comparing the generation costs of PV to a standard generation technology [9]. In terms of PV system cost benchmarking, installed costs of PV systems fell over the past several years [10]. Higher-voltage inverter designs, lower inverter prices, and higher module efficiencies contribute to cost reductions which makes installed PV capacity grow across residential, commercial, and utility-scale sectors [10, 11].

The increasing penetration of PV installations and electric vehicle (EV), other local storage options and end-user flexibility may contribute to the complexity in the active

management of distribution networks (DN). Many DN experience different kind of stability issues, such as frequency and voltage oscillations arising from the interaction of DERs and loads with the electrical grid. Indeed, the PV generation is inherent to atmospheric conditions and unpredictable irradiance variations may cause a sudden voltage rise or large imbalance in the grid. National and international grid standards establish network codes on requirements for grid connection of decentralised generation units [12, 13]. However, due to the expansion of DERs in DNs, corrective actions of individual units are often not enough to avoid grid instabilities. Proper load and generation profile management that helps maintaining the flow limits and voltage constraints in DNs can be achieved through centralized supervisory control systems.

Small-scale building-integrated PV (BIPV) is often subjected not only to the intermittent irradiation arising from changing meteorological conditions, but also to mismatched generation due to static shading caused by obstacles in the surroundings of the installation area. In most of the PV applications only part of the available power is processed because of the adopted PV architecture and the lack of active management by a centralized control system.

In this thesis, some strategies are proposed that improve the integration of PV systems into the grid. The thesis is divided in two parts. The first part implements in real hardware a management system that controls the interaction of PV installations with the DN. The management system deals with the grid-voltage issues caused by the distributed PV generation thanks to the contribution of all the inverters connected to the same DN. For this purpose, a Universal communication protocol is developed that is valid for commercial PV inverters of different brand, because it homogenises the variety of specific communication protocols that are in the market.

In the second part the PV generation mismatch is addressed. The PV system adopts a distributed maximum power point tracking (DMPPPT) architecture that includes module-level batteries, in which different strategies are proposed to increase PV generation, acting on the central MPPT (CMPPT) and DMPPPT functions of the system.

## Part I

# Integration of photovoltaic systems in the low voltage network



## Chapter 2

# Introduction

The increasing connection of PV systems to low-voltage (LV) networks causes voltage variations and leads to power quality (PQ) issues that should be avoided for a proper integration of PV arrays into the grid. These PQ issues are, up to a certain point, due to nonlinear loads and PV systems without any active and reactive modulation capability.

The operation of grid-connected PV systems is characterized by several uncertainties depending on the number of currently operating units, their location along the electrical grid, and the delivered power. At present, LV networks transport energy not only for household consumption. Indeed, residential PV generation is commonly injected into the grid. The balance between generation and consumption defines thus the direction of the power flow in the LV network. Due to the historical design of LV networks, grid-connected PV generation units can have adverse effects and cause voltage deviations as a results of reversed power flow [14].

In this context, several standards regulate the connection of PV systems to the LV network and its voltage quality [15]. However, PV systems are commonly disconnected from the grid during voltage sags or swells and/or overvoltage and undervoltage, due to the lack of compensating action, which leads to large power imbalance and grid instability. Regarding the PV generation itself, cloud transients can lead to voltage fluctuation and flicker in these LV networks [16]. Also, overvoltage may be caused in LV networks with high penetration of PV systems caused by generation peaks [17]. However, inverters with the abovementioned capability can help support the grid in case of abnormal working conditions, such as undervoltage and overvoltage.

In order to comply with these standards and work towards a better integration of PV systems, several solutions have been proposed in literature. The most common one entails the use of the PV Inverter itself for compensating voltage sags and swells with

reactive power regulation [18], [19] and adjustment of the active power production [20]. A scheme that controls the active and reactive power of inverters [21] may serve this purpose: with the necessary information about the state of the grid, corrective actions can be taken to prevent unwanted situations. The first step toward the validation of the control scheme is to reproduce in a laboratory the behaviour of a LV network under different voltage and unbalance conditions.

The first part of the work covers the following aspects: Chapter 3 focuses on testing the capabilities and limits of commercial inverters regarding the above-mentioned PQ issues and associated compensation features, in a reliable and flexible manner. Indeed, the potential of these commercial inverters to modulate reactive power and adjust their active power production is used to help support the grid and avoid disconnection. PV and grid emulators reproduce a realistic environment, under normal and unbalanced grid conditions. Moreover, automatic test protocols are developed in order to perform the tests. Chapter 4 studies the effect of active and reactive power variations on the voltage profile of the LV network. The lab network is numerically modelled and simulations are performed for each operating scenario. The results from both, real measurements and simulations are then compared. Chapter 5 analyses the implementation of a collaborative control scheme [21] in DN with PV generation and Chapter 6 shed some conclusions and future lines on the LV network voltage issue.



## Chapter 3

# Grid-voltage compensation functionalities of commercial PV inverters

This chapter discusses the ability of commercial inverters to locally compensate voltage differences in three-phase LV networks. Section 3.1 discusses the relation between power regulation and voltage compensation, Section 3.3 introduces technical characteristics and main features of the selected inverters, Section 3.4 describes the test platform and Section 3.5 presents the automatic test protocol developed in order to carry out the experimental results shown in Section 3.6.

Part of this work has been presented at the Solar Integration Workshop 2015 Brussels (Belgium) [22].

### 3.1 Voltage compensation

Fig. 3.1 depicts a voltage drop and a phase shift between two arbitrary points of the grid, caused by a current flow. Distributed generation units commonly connect to the LV networks which include inductive and resistive components [23].

This study considers an operating scenario without loads. The apparent power flowing through the point of common coupling (PCC) results in:

$$\underline{S}_{\text{inv}} = P_{\text{inv}} + jQ_{\text{inv}} \quad (3.1)$$

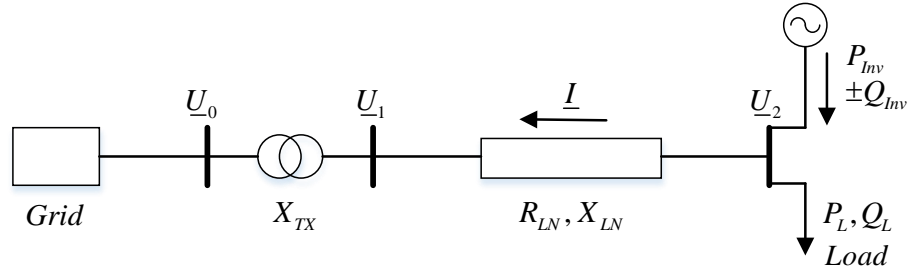


FIGURE 3.1: Simplified LV network diagram representing the reverse current flow due to the injection of inverter power ( $P_{inv}$ ,  $Q_{inv}$ ) into the grid.

The voltage at the PCC is considered as reference with  $\underline{U}_2 = U_2 \angle 0^\circ$  while the grid voltage  $\underline{U}_1 = U_1 \angle \delta$  and the grid current  $\underline{I} = I \angle \varphi$  are phase-shifted by angles  $\delta$  and  $\varphi$ , respectively. The grid current yields:

$$I^* = \frac{S_{inv}}{U_2} \quad (3.2)$$

where  $I^*$  is the complex conjugate of the current phasor. This results in the following expression for the voltage drop  $\underline{\Delta U}$  in the grid [24]:

$$\begin{aligned} \underline{\Delta U} &= (R_{LN} + jX_{LN})\underline{I} \\ &= \frac{(P_{inv}R_{LN} + Q_{inv}X_{LN}) + j(P_{inv}X_{LN} - Q_{inv}R_{LN})}{U_2} \end{aligned} \quad (3.3)$$

considering that the impedance is  $R + jX$ , where  $R$  the resistance and  $X$  is the reactance of the cable. Since the LV network impedance is essentially resistive [25, 26], the amplitude of the voltage drop in phase with the voltage at the PCC is approximately equal to the real part of (3.3):

$$\Delta U_d = \frac{(P_{inv}R_{LN} + Q_{inv}X_{LN})}{U_2} \quad (3.4)$$

The voltage compensation introduced in the grid can thus be directly obtained in function of the active and reactive power coming from the inverter. In particular, (3.4) suggests that if the inverter absorbs reactive power the voltage drop at the grid also reduces.

We can also express the power regulation and voltage compensation in terms of phase shift between the grid current and the voltage at the PCC with the displacement power factor:

$$\cos \varphi = \frac{P_{\text{inv}}}{\sqrt{P_{\text{inv}}^2 + Q_{\text{inv}}^2}} \quad (3.5)$$

In case a load is connected at the PCC, the active and reactive powers in the LV network are expressed by:

$$P_{\text{PCC}} = P_{\text{inv}} - P_{\text{L}} \quad (3.6)$$

$$Q_{\text{PCC}} = Q_{\text{inv}} - Q_{\text{L}} \quad (3.7)$$

where  $P_{\text{L}}$  and  $Q_{\text{L}}$  are the active and reactive power consumed by the load, respectively. Then the expression in (3.4) becomes:

$$\Delta U_d = \frac{(P_{\text{PCC}} R_{\text{LN}} + Q_{\text{PCC}} X_{\text{LN}})}{U_2} \quad (3.8)$$

### 3.1.1 Characteristics of overhead lines and underground cables in distribution systems

Transmission and three-phase distribution lines are mainly inductive lines [23]. LV distribution networks are characterised by having a more resistive behaviour [25, 26] and this behaviour is usually defined using the  $X/R$  ratio. In Europe, the lower the voltage level, the higher the share of underground lines. Electrical energy distribution in DNs is almost evenly shared between overhead power lines and underground cables [27]. Overhead lines and underground cables have different electrical characteristics. Underground cables have less resistance and inductance compared to overhead lines [28]. In this work, priority is given to the LV network resistive behaviour, selecting cable impedances with  $X/R < 1$ . Some parts of this work consider a higher reactance value to study the effect of the reactive power in the grid voltage compensation.

## 3.2 Grid codes

National and international grid standards establish the requirements for grid connection of DERs. In Belgium, the network code is regulated by Synergrid, the association of

electricity and gas network operators. The C10/11 standard establishes the technical requirements for integrating distributed generation units into the grid. It is based on the European commission regulation (EU) 2016/631 of 14 April 2016 [12]. The references throughout the manuscript to the C10/11 standard are made considering both the 2012 version [13] and the ongoing<sup>1</sup>2019 draft version [29].

### 3.3 Photovoltaic Inverters

This first part of the manuscript studies single- and three-phase commercial inverters, with special attention given to their power regulation functionalities and the resulting voltage compensation capability. The selection of the inverters is done concerning the most spread PV inverters in the Belgian market (2013-2017), the availability to externally control the inverter through a communication port (e.g. RS485 communication protocol) and especially their compensation capabilities. For commercial inverters, power regulation implies active power reduction (w.r.t. the default maximum power production) and reactive power compensation.

#### 3.3.1 General characteristics of the inverters

Table 3.1 gathers the main characteristics of the PV inverters used in this study. For a nominal power larger than  $P_N=5\text{kW}$ , three-phase inverters are commonly used (Inv-1). Three-phase inverters do both power injection and compensation evenly. Inv-2 is a single-phase inverter with a rated power below 5kW. Single-phase inverters may contribute more to possible voltage imbalances when injecting power into the grid but also to compensate voltages differences between phases. Each inverter is equipped with two MPP trackers that allow the input of independent PV strings. The outputs of the MPP trackers are connected in parallel to the DC-link of the inverter.

According to C10/11 standard [29], the PV systems used in this work must follow the criteria for small power systems connected to the LV DN, named *petite installation de production*. A small power system must fulfil one of the following requirements: if single-phase connected, the apparent power  $S_{AC}\leq 5\text{kVA}$ ; if three-phase connected, the apparent power  $S_{AC}\leq 10\text{kVA}$ . According to the European commission regulation (EU) 2016/631 [12], the PV systems considered must follow the EN 50549-1 norm that details the requirements for generating plants of type A from 0.8kW to up to 1MW connected to a LV DN.

---

<sup>1</sup>Accessed on 2019/02/11.

TABLE 3.1: Parameters of the commercial PV inverters considered in this work.

Symbol	Description	Inv-1	Inv-2	Units
$V_{DC-OP}$	Admissible DC-voltage range	150 - 1000	160 - 600	[V]
$V_{DC-init}$	Initial DC-voltage	188	160	[V]
$V_{DC-MPP}$	DC-voltage MPPT range	245 - 800	160 - 530	[V]
$P_{DC-Max}$	Max. DC input power	5.15	3.5	[kW]
$S_{AC}$	Rated apparent power	5.0	3.3	[kVA]
$P_{AC}$	Rated active power	5.0	3.0	[kW]
$V_{AC}$	Nominal AC voltage	400	230	[V]
$\cos \varphi$	Power Factor	-0.8..1..+0.8	-0.9..1..+0.9	-

### 3.3.1.1 Power factor sign convention

The Power Factor (PF) is the ratio of the active power to the apparent power and is mathematically equal to:

$$\cos \varphi = \frac{P_{AC}}{S_{AC}} \quad (3.9)$$

The PF can be either lagging or leading and depends on the nature of the load. A lagging PF indicates that, representing the current and the voltage on the phasor diagram, the current is delayed with respect to the voltage. The current lags behind the voltage for an inductive load. Thus, lagging corresponds to an inductive load. A leading PF indicates that the current leads the voltage and this occurs for capacitive loads. Thus, leading corresponds to a capacitive load.

The meaning of the sign that precedes the PF value is determined by the standard adopted. IEEE standard defines the PF sign as dependent on the load and not on the direction of active power flow [30]. In Fig. 3.2, the diagram shows the correlation between P, Q and PF as well as the type of load for the IEEE standard. According to the IEEE sign convention, a positive active power flows into a load (energy consumed by the load) and a negative active power flows out of the load (energy generation).

The Belgian C10/11 standard and the European norm EN 50549-1 follow the IEEE sign convention determining it from the generation point of view [29]. The sign is reversed, making the active power flow positive when it flows out of the load. Therefore, a positive sign for both PF and reactive power (provision of reactive energy) corresponds to an inductive load. On the contrary, a negative sign for both PF and reactive power

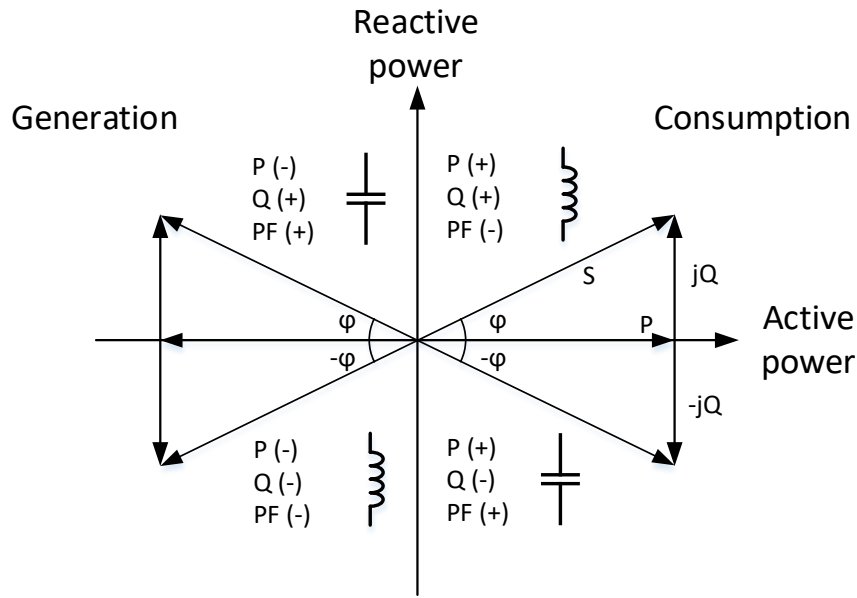


FIGURE 3.2: IEEE standard Power Factor sign convention. Own illustration based on IEEE standard.

(absorption of reactive energy) corresponds to a capacitive load. In Table 3.1 a negative sign indicates a leading PF while a positive sign indicates a lagging PF.

### 3.3.2 Features of the inverters

Depending on the inverter, the reactive power compensation can be set in different ways; it can be adapted to the needs of the system (static or dynamic  $\cos\varphi$  setpoint) or to the country grid standards. Most of the country grid standards require the reactive power setpoint to be either fixed or adjustable by a signal from the network operator. The setpoint value is either a fixed displacement factor (static  $\cos\varphi$ ), a variable displacement factor depending on the active power ( $\cos\varphi(P)$ ), a fixed reactive power value in VAr (dynamic  $\cos\varphi$ ) or a variable reactive power depending on the voltage  $Q(U)$  [31]. The user (e.g. network operator) controls the different operating points of the inverter through the communication port of the inverter. This work focuses on the following features:

- *Active power setpoint*: A reference with the absolute value or a percentage of the nominal value modifies the actual active power operating point. This feature works in fixed active power mode.

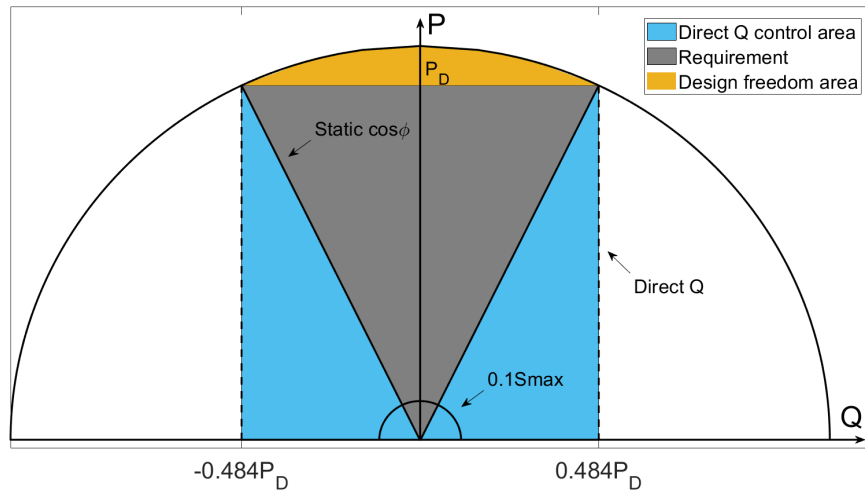


FIGURE 3.3: PQ curves and admissible operating areas for each power control mode. Own illustration based on the European norm EN 50549-1 and the VDE-AR-N 4105 German directive.

- *Direct reactive power control* (dynamic  $\cos \varphi$ ): This mode allows setting the reactive power value independently of the active power delivered by the inverter. Within the operating area delimited by the maximum allowed reactive power, the active power can change due to a change in the setpoint reference or a power variation at the input of the inverter, without affecting the reactive power operating point.
- *Static  $\cos \varphi$*  (dynamic reactive power control): As opposed to the dynamic  $\cos \varphi$  operating mode,  $\cos \varphi$  is fixed. The variation of active power results in the variation of reactive power.

Fig 3.3 represents the PQ curves for *Direct reactive power control* and *Static  $\cos \varphi$*  operating modes according to the VDE-AR-N 4105 German directive for connecting generating plants to the low-voltage power grid [32]. The grey area represents the PF constraint for the inverters connected to the distribution system and it is not desirable to operate at PFs below a certain limit. It is directly linked to the *Static  $\cos \varphi$*  operating mode. This limit varies with each country's grid code [33]. The blue area is the *Direct reactive power control* mode area, an additional performance based on manufacturer's decision to cover different grid codes and provide flexibility to the user. If the inverter is well designed and the input power is sufficient, the operation in the design freedom (yellow) area allows full active power delivery and reactive power support. The sign convention follows the EN 50549-1 norm as stated in 3.3.1.1. Table 3.2 gathers the features relevant for this study, as well as their availability per inverter.

TABLE 3.2: Features of the PV inverters

	READ				WRITE		
	$V_{OUT}$	$P_{OUT}$	$Q_{OUT}$	$\cos \varphi$	$P_{OUT}^*$	$Q_{OUT}^*$	$\cos^* \varphi$
Inv-1	✓	✓	✓	✗	✓	✓	✓
Inv-2	✓	✓	✗	✓	✓	✗	✓

### 3.4 Test platform

The platform consists first of a PV array emulator connected to the DC input of the inverter under test. The AC output terminals of the inverter are connected to the grid emulator through a LV network (Fig. 3.4). The emulators and possibly also the inverter are controlled via a Graphical User Interface (GUI), through the dSPACE platform.

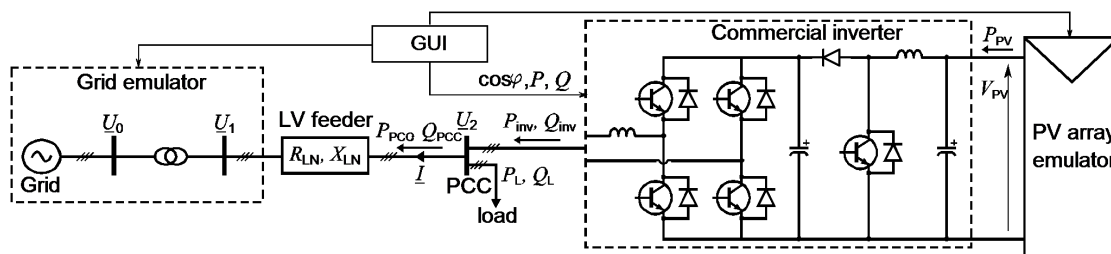


FIGURE 3.4: Representation of the test platform

#### 3.4.1 PV array emulator

The PV array emulator allows the reproduction of the characteristics of a standard PV installation in a reliable and flexible manner [34]. This PV emulator is model-based and developed in Matlab-Simulink environment. It uses the single-exponential model of the solar cells [35] with an adjustable number of panels in parallel and series in function of the output characteristics required and takes into account the influence of the in-plane irradiance and the PV cell temperature. The characteristic parameters of the PV panels used for the PV array emulation are grouped in Table 3.3. The emulator is able to reproduce realistic atmospheric conditions either with the clear-sky model or actual recorded data. In addition, shading can be easily set in the GUI of the emulator in order to test the Maximum Power Point Tracking (MPPT) capabilities of the PV inverters under these conditions [34], [36]. In particular, shading results in several local maxima on the instantaneous power versus voltage (P-V) curve of the PV array, which requires an appropriate algorithm for proper MPPT.



TABLE 3.3: Parameters of the PV panel

Symbol	Description	Value	Units
$V_{OC}$	Open-circuit voltage	37.3	[V]
$I_{SC}$	Short-circuit current	8.52	[A]
$V_{MPP}$	MPP voltage	30.5	[V]
$I_{MPP}$	MPP current	8.04	[A]
$P_{MPP}$	MPP power	245	[W]

### 3.4.2 LV network impedance

The laboratory LV network emulates a typical residential power line characterised by having a resistive behaviour [37, 38]. The impedance values of the laboratory network are gathered in Table 3.4, with an impedance ratio  $X/R=1/4$ . This ratio has been selected with the available laboratory material. The purpose of the test platform is to serve as a tool to validate the developed external control of the inverters and observe the voltage compensating actions thanks to the active and reactive control features. Therefore, the values of the emulated grid impedance are not critical.

TABLE 3.4: Test network data

Symbol	Description	Value	Units
$V$	Grid line-to-line rms voltage	400	V
$R_{LN}$	LV network resistance	0.26	$\Omega$
$X_{LN}$	LV network reactance	65.97	m $\Omega$

### 3.4.3 Graphical User Interface

ControlDesk software is used together with the dSPACE ds1104 platform for the GUI (Fig. 3.5). The user can observe the relevant system variables, such as the grid voltages and currents, and the DC-side voltage and current. Also, the instantaneous characteristic curves of the PV array for the adjustable meteorological conditions set are displayed, so that the evolution of the working point can be observed.

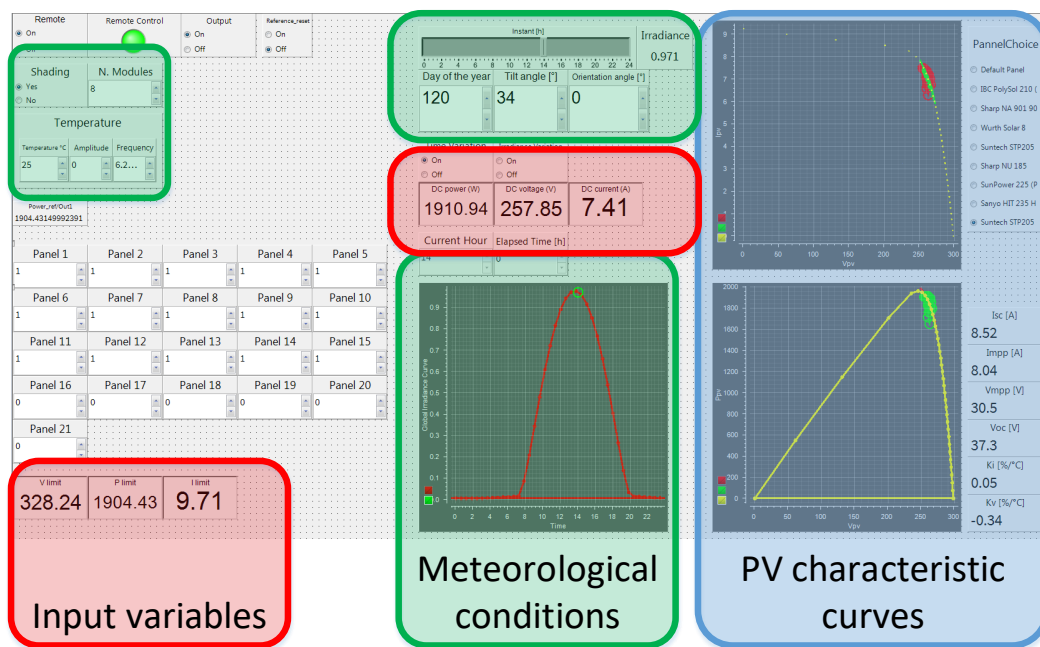


FIGURE 3.5: Part of the available PV emulator Graphical User Interface.

### 3.4.4 External control

The external control of the inverters is made using a computer or a *management and communication gateway*<sup>2</sup>. The former uses a USB-RS485 converter to communicate with the inverters. The latter is a small control device (Fig. 3.6) conceived to be located in each inverter. It consists of communication ports (e.g. RS485) to interact with the inverter,  $\mu$ controllers enabling local control and information storage and allows remote GPRS<sup>3</sup> and 3G/4G communication. Local information can be used to facilitate the status of individual devices to a server and provide remote monitoring and control.

## 3.5 Test protocol

Testing PV inverters is of relevant importance for validating their capabilities. For economical, flexible and reproducible reasons, a variety of test platforms for PV inverters are used in laboratories: an automatized PV inverter interconnection test system based on IEEE 1547 standard is developed by Taiwan Electric Research and Testing center [39]; in [40] a PV inverter test layout is presented to investigate the dynamic performance of three-phase PV inverters during voltage and frequency fluctuations and oscillations

<sup>2</sup><https://www.greenwatch.be/en/energy-management/> (Accessed on 2019/02/11).

<sup>3</sup>GPRS: General Packet Radio Services, packet-based wireless communication service that promises data rates from 56 up to 114 Kbps and continuous connection to the Internet.

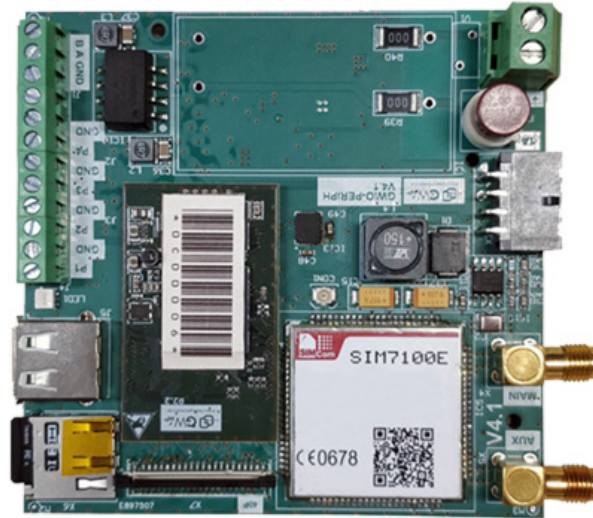


FIGURE 3.6: GWio management and communication gateway used to control the inverters.

typically found on the grid; authors in [41] evaluate the power control performance of a 3 kW solar inverter. Other laboratories set up a test bed for European efficiency, as well as for static and dynamic MPPT efficiency evaluation [42].

The development of automatic test protocols pursue various objectives, specially the reproducibility of the tests for a reliable comparison between devices under test and the reduction of time in the testing procedure. The most interesting feature to be tested is the ability of inverters to provide support to some grid instabilities, specially overvoltage and voltage imbalances. This is typically done by controlling both the active and reactive power setpoints. Tests post-processing evaluates the following features:

- Response time: Time required to reach the steady state operating condition after setting a reference change.
- Accuracy: The precision between the reference and the measured value.

Fig. 3.7 shows the communication signal and the reactive power ( $Q$ ). The new  $Q$  reference value is represented with dashed line and the steady state is considered within a certain tolerance that is the steady state error. The response time of the system is the settling time between a new reference is sent via communication port and the measured variable enters the steady state.

Each spike in the communication signal means that a telegram has been sent to the inverter under test. This telegram can be a request of information (read mode), the setting of a new reference (write mode), or both at the same time. A delay of  $t_d=2s$  is

set to give the system enough time to reach the steady-state and avoid collisions in the communication bus. This is a generic time delay for any kind of communication speed and it should completely avoid communication collisions. However, communication errors may arise and lead to a problem in setting a new reference. If there is no response from the inverter or the response is not correct or incomplete, the telegram is sent again after a timeout of  $t_{\text{timeout}}=3\text{s}$  for a total of three times (Fig. 3.8). If the communication is not successful, the input and the output of the channel is flushed. After a waiting time of  $t=t_{\text{timeout}}+5\text{s}$ , the next reference is set.

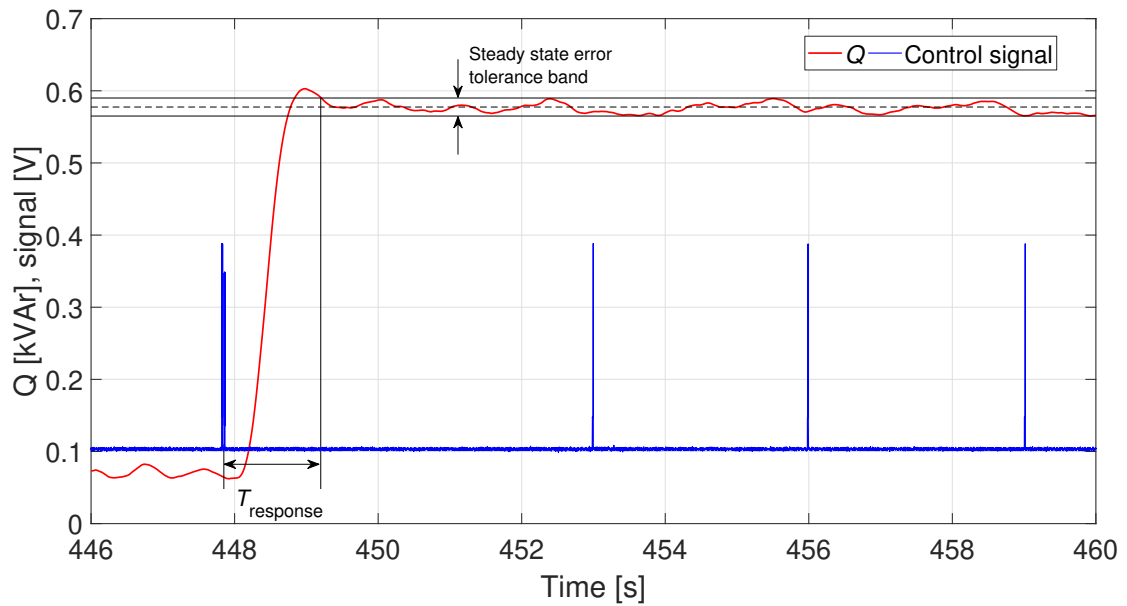


FIGURE 3.7: Response time ( $T_{\text{response}}$ ) after setting a Q reference (black dashed line and the steady state error tolerance band with solid lines), serial communication signal (blue line), and measured Q (red line).

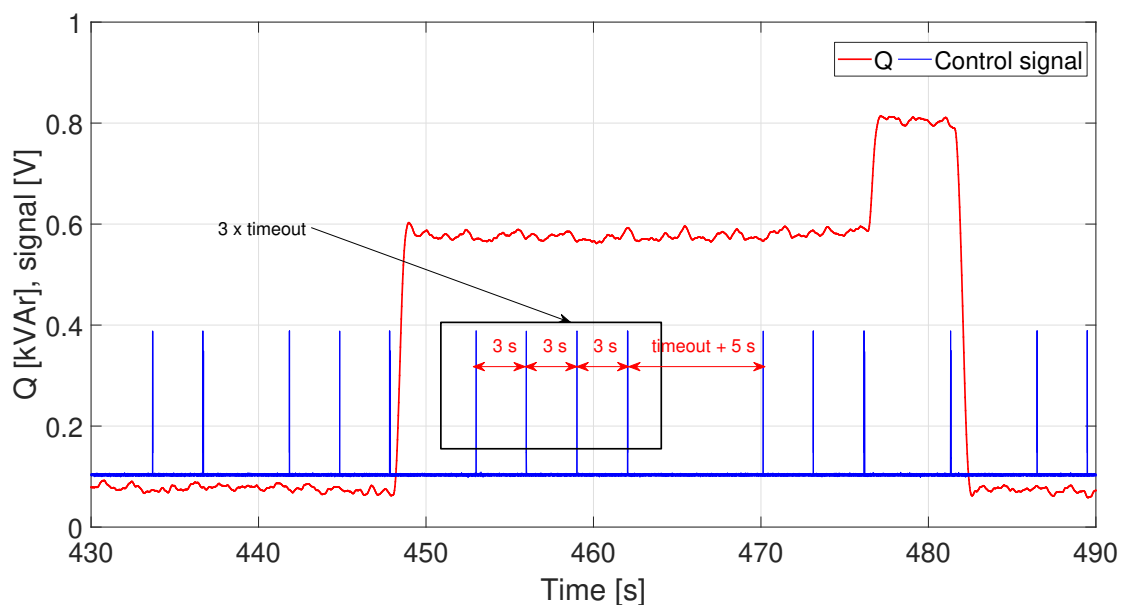


FIGURE 3.8: Timeout after lack of response from the inverter.

### 3.6 Test results of PV inverters capabilities

This section discusses the experimental results of inverters' voltage compensation features. The focus is on  $\cos \varphi$  setpoint variation and  $P$  reduction capabilities. In terms of reactive compensation capabilities, direct  $\cos \varphi$  setpoint control has been chosen, that can be adapted to the needs of the system. The tests are performed as follows:

- Programmable power sources emulating PV arrays supply the inverters. Emulated PV arrays reproduce real PV panels behaviour using the parameters in Table 3.3.
- An acquisition board collects measured data from the output of the inverter. Data are post-processed for further analysis.
- A Gateway or a general purpose computer (controller) controls externally the operation of the inverter. In addition, the controller manages the logging in the communication interaction with the inverter.

The algorithms in these test protocols are designed to sweep the whole perimeter of the operating area allowed by the inverter under test, delimited by the maximum apparent power, the minimum active power output and the minimum  $\cos \varphi$ .

TABLE 3.5:  $\cos \varphi$  variation test conditions

	$P_N$ [kW]	$\Delta P$	$\cos \varphi$ range	$\Delta \cos \varphi$
Inv-1	5.0	25% $P_N$	-0.8..1..0.8	0.01
Inv-2	3.0	25% $P_N$	-0.9..1..0.9	0.01

#### 3.6.1 Variation of $\cos \varphi$

First disabling the MPPT function of the inverter, a number of fixed  $P$  levels are set in steps defined by  $\Delta P$ , e.g. Inv-1  $P$  is reduced in steps equivalent to 25% of its nominal AC power ( $P_N=5.0\text{kW}$ ):  $P_1=1 \times P_N$ ,  $P_2=\frac{3}{4} \times P_N$ ,  $P_3=\frac{1}{2} \times P_N$ ,  $P_4=\frac{1}{4} \times P_N$ . For each level,  $\cos \varphi$  reference is set *stepwise* and *jumping from unity to the reference value* in  $\cos \varphi$  steps defined by  $\Delta \cos \varphi$ , e.g. Inv-1  $\Delta \cos \varphi=0.01$ . Table 3.5 summarizes the different testing conditions adopted for each inverter. At each power level the tests sweep the  $\cos \varphi$  range.

Figs. 3.9(a) and 3.9(b) show the results of the *stepwise* and *jumping from unity*  $\cos \varphi$  test of Inv-1, respectively. Figs. 3.10(a) and 3.10(b) show the equivalent results of  $\cos \varphi$  variation for Inv-2. Lagging (injecting Q, positive Q) and leading (absorbing Q, negative

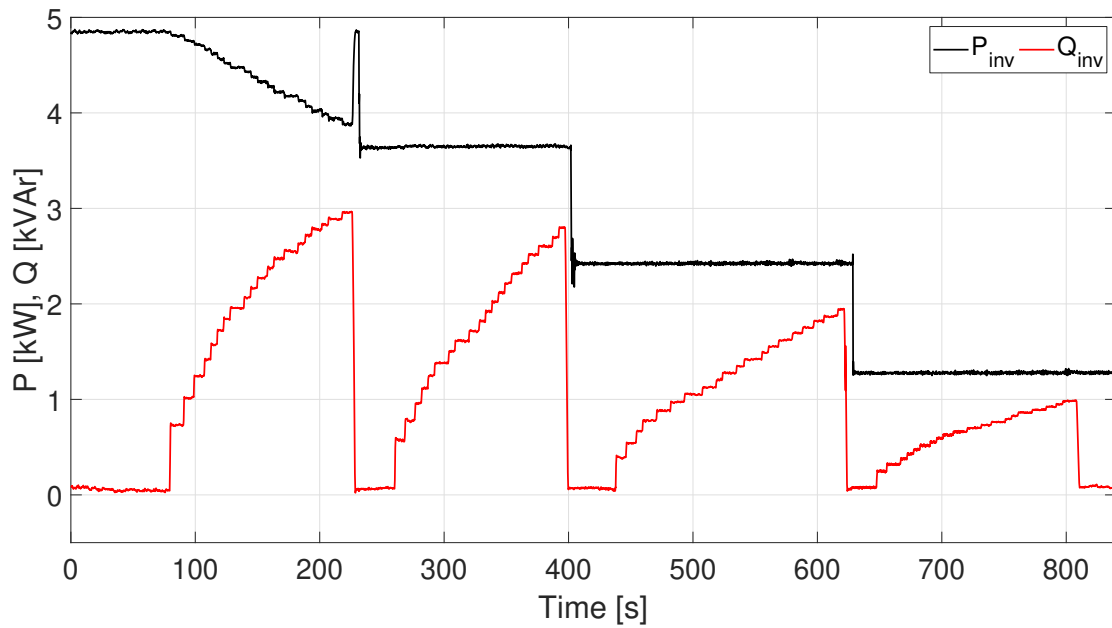
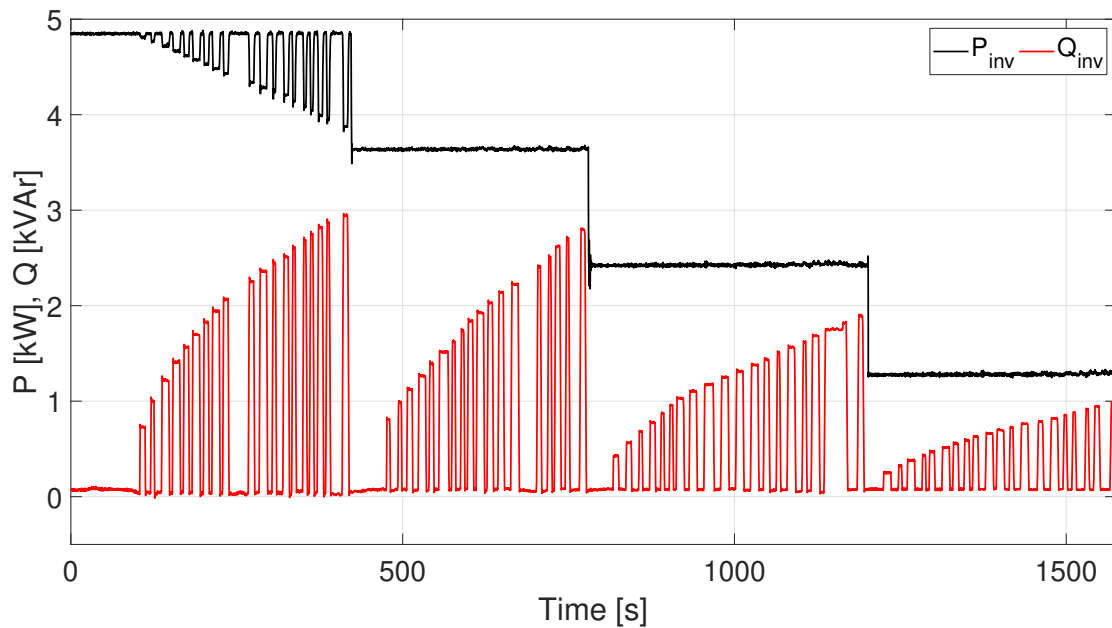
(a) Inv-1 *stepwise*  $\cos \varphi$  test.(b) Inv-1 *jumping from unity*  $\cos \varphi$  test.

FIGURE 3.9: 3-phase Inv-1  $\cos \varphi$  test. At each  $P_{inv}$  level (in steps of  $\Delta P=25\%$ ),  $\cos \varphi$  set in steps of  $\Delta \cos \varphi=0.01$ .

Q)  $\cos \varphi$  tests have been implemented to obtain the total P-Q curves of the inverters. In Figs. 3.13(a) and 3.13(b) the P-Q curves of Inv-1 and Inv-2 can be seen.

Table 3.6 gathers the maximum and minimum response times for each inverter. The maximum response time ( $t_{r,max}$ ) corresponds to the time in which the minimum  $\cos \varphi$  reference is set,  $\cos \varphi$  starting from unity. For Inv-1,  $t_{r,max}=3.02s$ .

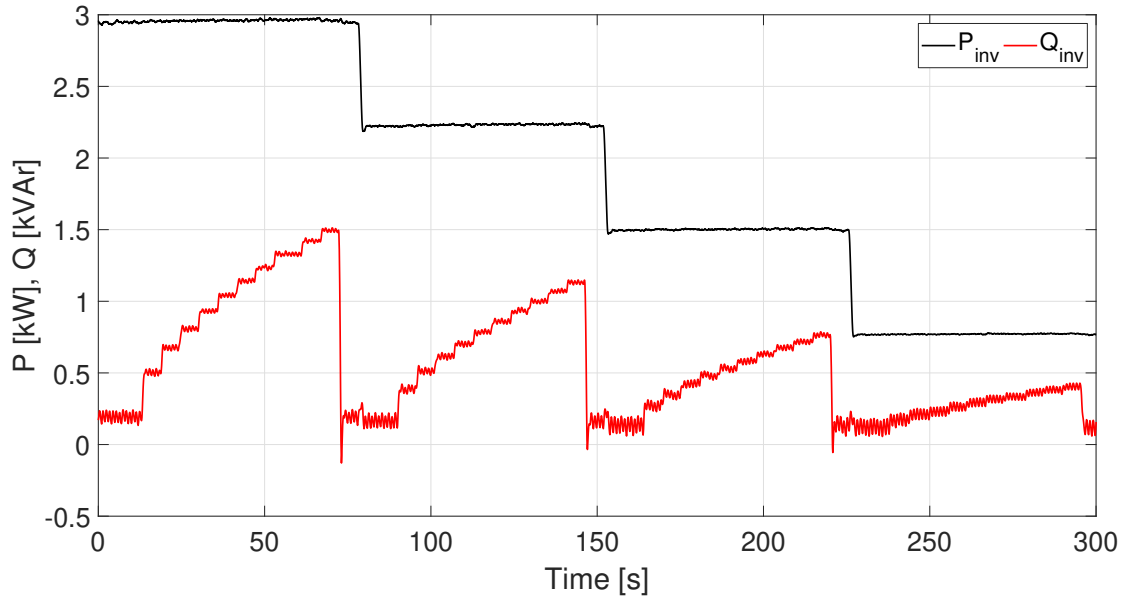
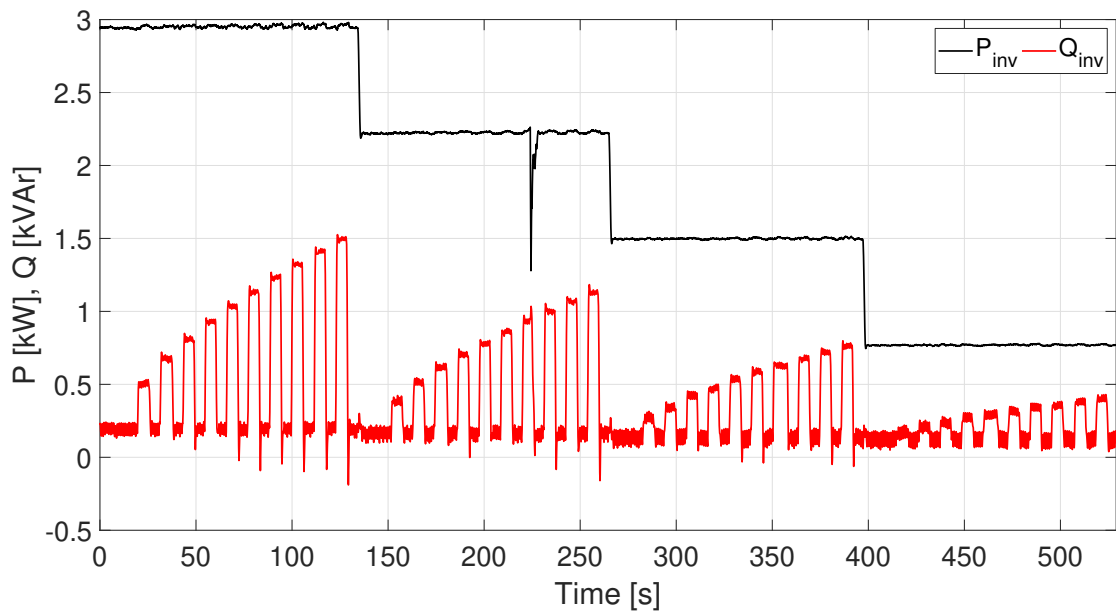
(a) Inv-2 stepwise  $\cos \varphi$  test.(b) Inv-2 jumping from unity  $\cos \varphi$  test.

FIGURE 3.10: 3-phase Inv-2  $\cos \varphi$  test. At each  $P_{inv}$  level (in steps of  $\Delta P=25\%$ ),  $\cos \varphi$  set in steps of  $\Delta \cos \varphi=0.01$ .

TABLE 3.6:  $\cos \varphi$  variation test response times

	Inv-1		Inv-2	
	Stepwise	Jump	Stepwise	Jump
Min. $t_r$ [s.]	0.5	0.92	0.5	0.7
Max. $t_r$ [s.]	1.3	3.02	1.09	1.3

### 3.6.2 Variation of $P$

First disabling the MPPT function of the inverter, a number of fixed  $\cos \varphi$  levels in steps of  $\Delta \cos \varphi = 0.25$  are set. For each level,  $P$  reference is set *stepwise* and *jumping from  $P_N$*  in steps of  $\Delta P = 10\% P_N$ . Figs. 3.11(a) and 3.11(b) show the results of the *stepwise* and *jumping from  $P_N$*   $P$  test of Inv-1, respectively. Fig. 3.12 shows the equivalent results of  $P$  variation for Inv-2.

### 3.6.3 Voltage compensating actions

In Fig. 3.13 the reduction of the voltage can be seen, thanks to the Q compensating action (Fig. 3.13(b)) and P reduction (Fig. 3.13(c)). Fig. 3.14 also shows the reduction of the voltage thanks to the Q compensating action (Fig. 3.14(b)) and P reduction (Fig. 3.14(c)).

### 3.6.4 Discussion of results

Voltage compensation effectiveness is directly linked with the impedance behaviour of the grid. LV networks commonly present resistive behaviour, hence grid voltage compensation responds better to active power reduction in residential applications.

In terms of reactive compensation capabilities, static  $\cos \varphi$  control seems to be the most convenient control feature. Some of the inverters provide larger  $\cos \varphi$  range (see Table 3.1) compared to that allowed by some country grid standards [13]. This involves the implementation of additional limitations in the control of the inverters. Some inverters only provide the dynamic functionality by setting the reactive power reference. This implies additional mathematical operations in the conversion of the desired  $\cos \varphi$  to the new reactive power reference to be set. Therefore, a control variable allowing for a direct control of  $\cos \varphi$  seems a better option.

The nominal power ratio of the PV system affects the reactive compensation actions of the inverter at full load operation. Reducing this ratio (i.e. adding more panels to



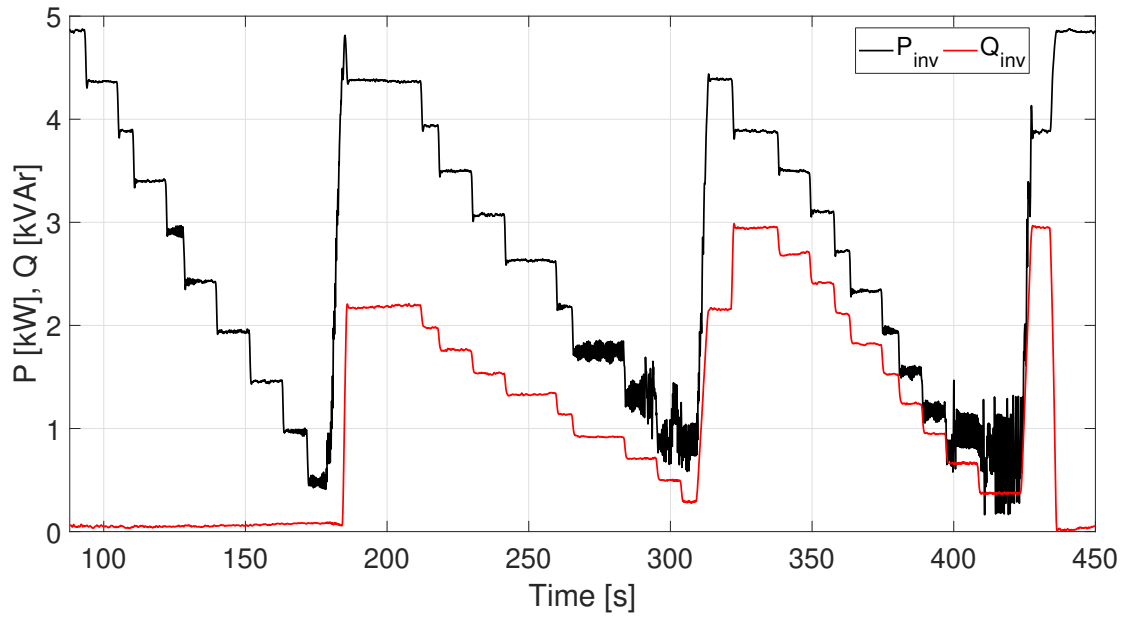
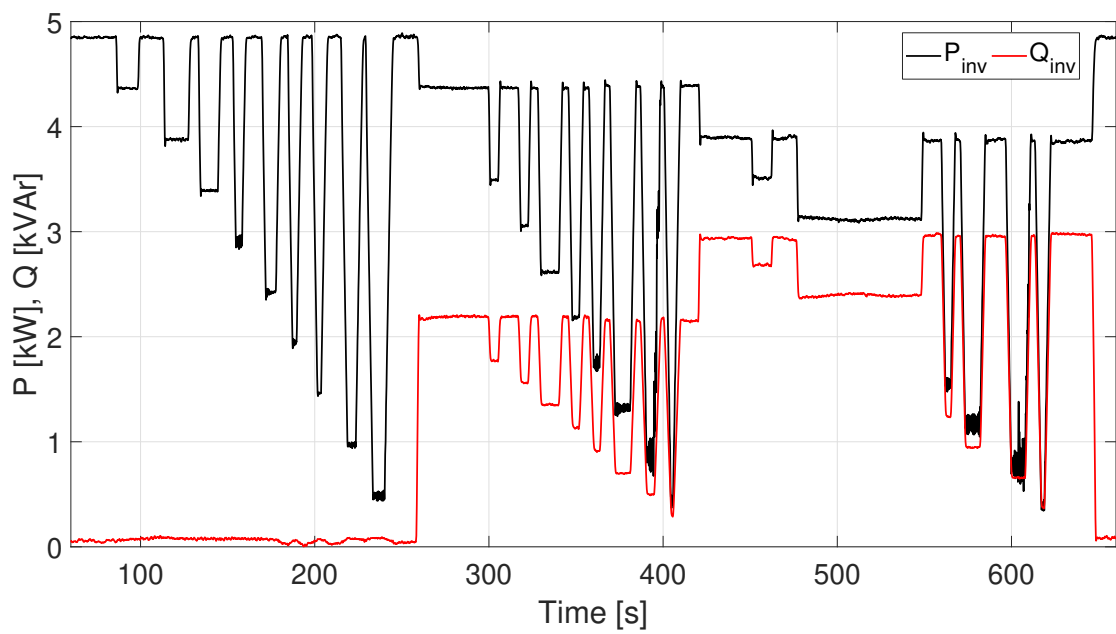
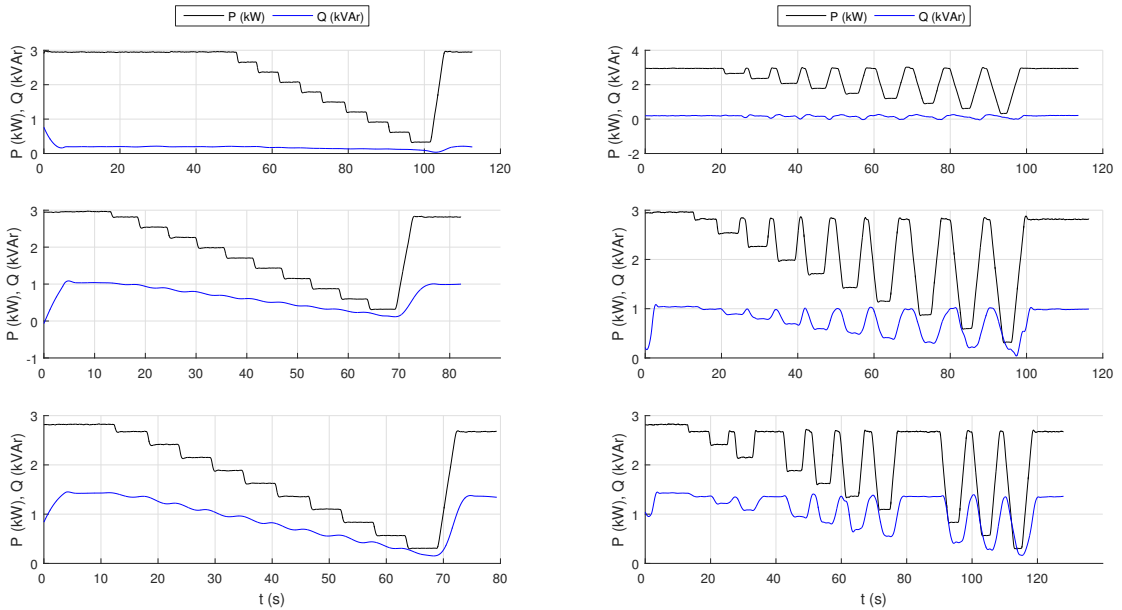
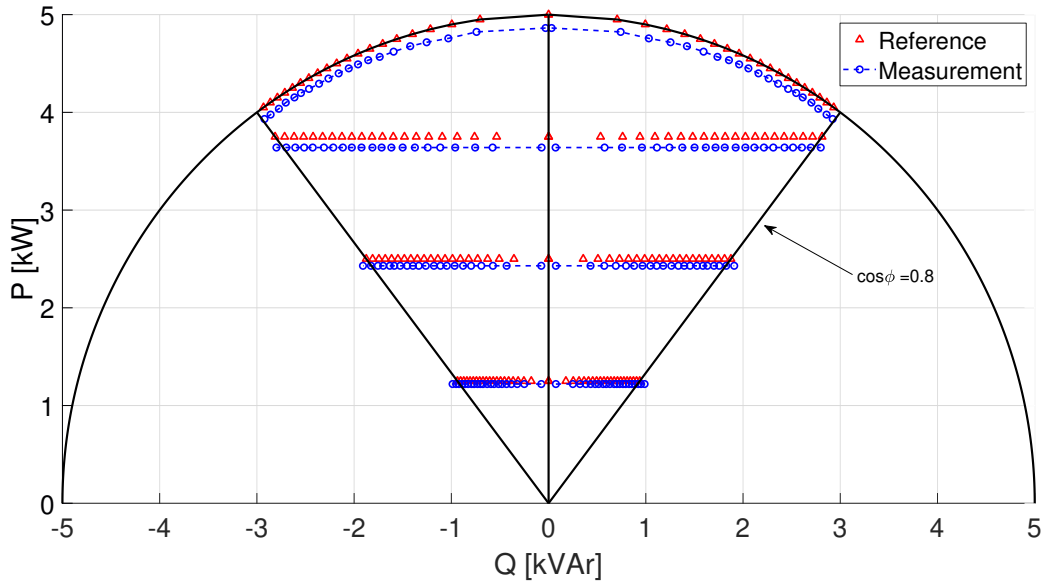
(a) Inv-1 stepwise  $P$  test.(b) Inv-1 jumping from unity  $P$  test.

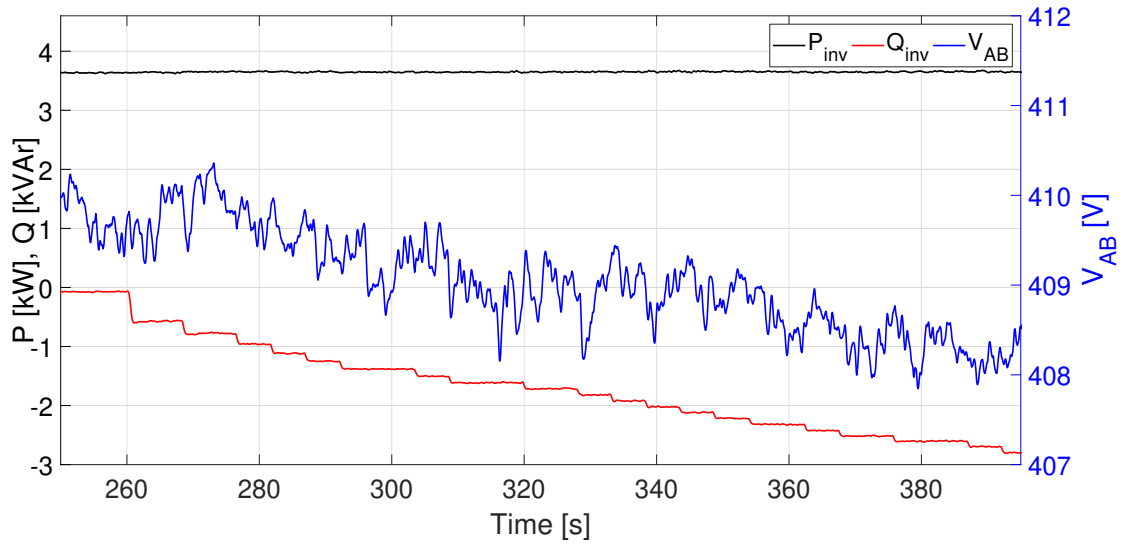
FIGURE 3.11: 3-phase Inv-1 test. At each  $Q_{\text{inv}}$  level (in steps of  $\Delta \cos \varphi = 0.25$ ),  $P$  set in steps of  $\Delta P = 10\% P_N$ .

FIGURE 3.12: Inv-2 stepwise and jumping from unity  $P$  test

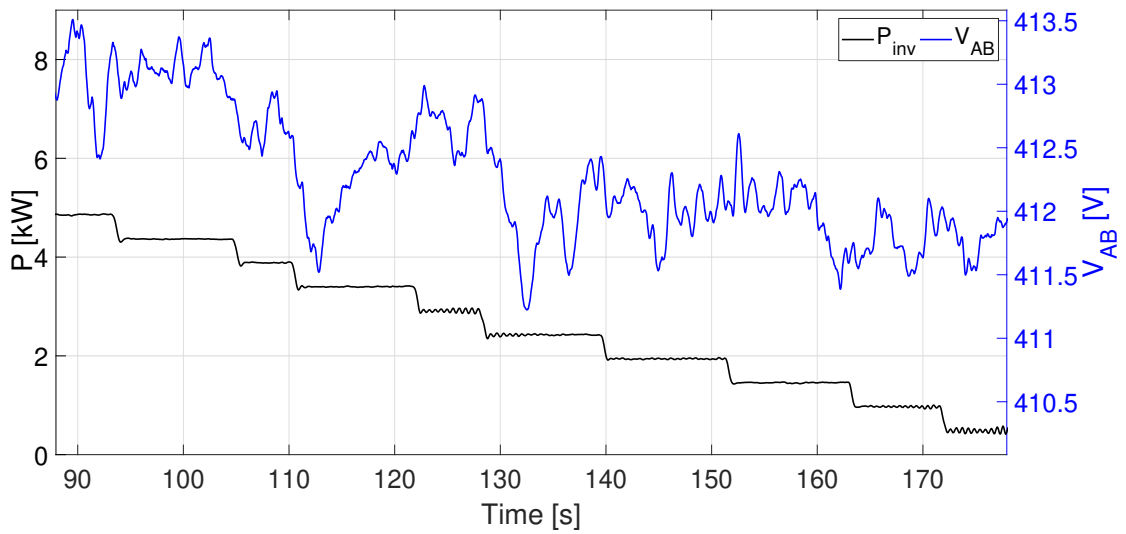
the PV array) would be a tentative solution. Amongst the devices tested in this work, Inv-2 is able to provide reactive compensation at full load without compromising the active power injection into the grid. Even then, the question lies on the effective use of the peak PV power. A second solution, better suited for Inv-1, suggests otherwise: increasing the nominal power of the inverter. This ensures the full active power delivery for any reactive power operating point. The drawback in this case is the under-utilization of the power conversion capability of the inverter. Although out of scope of this work, optimal dimensioning of the PV installation becomes challenging here.



(a) Inv-1 P-Q curve characterised at 4 P levels implementing lagging and leading  $\cos\phi$  sweep.

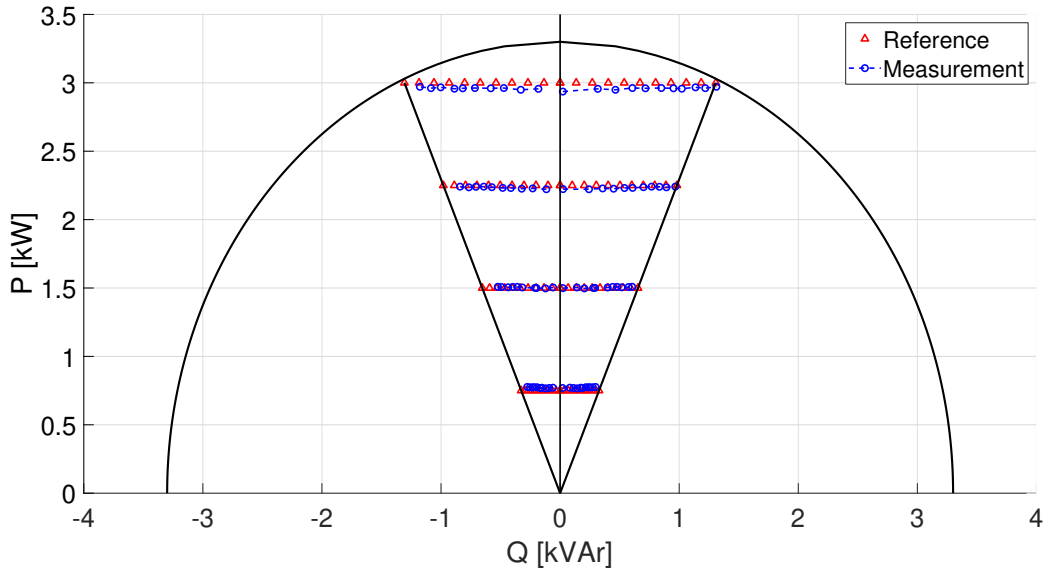


(b) Voltage compensation thanks to absorbing Q (leading) by Inv-1.

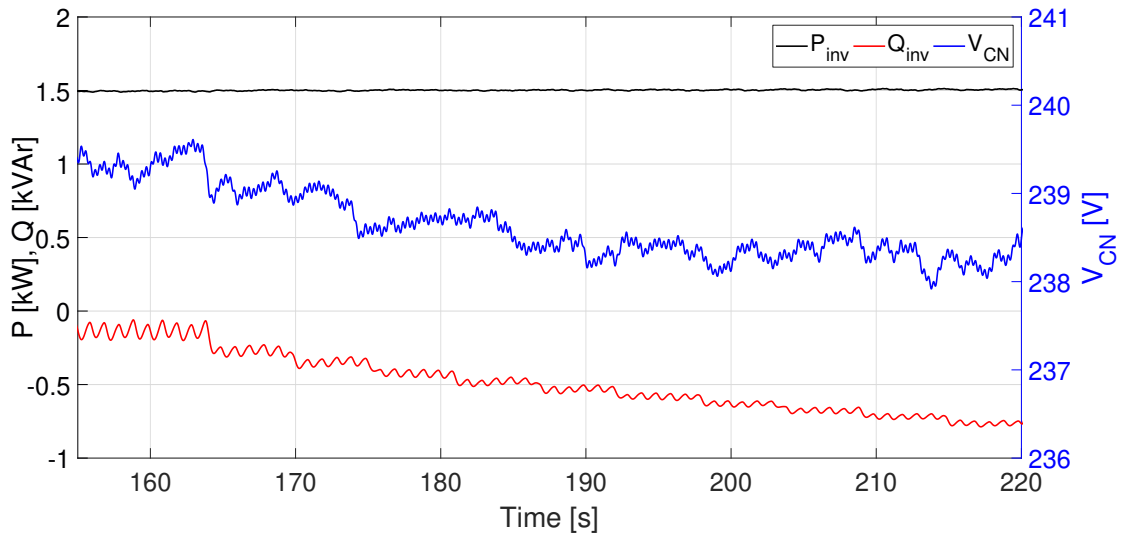


(c) Voltage compensation thanks to P reduction by Inv-1.

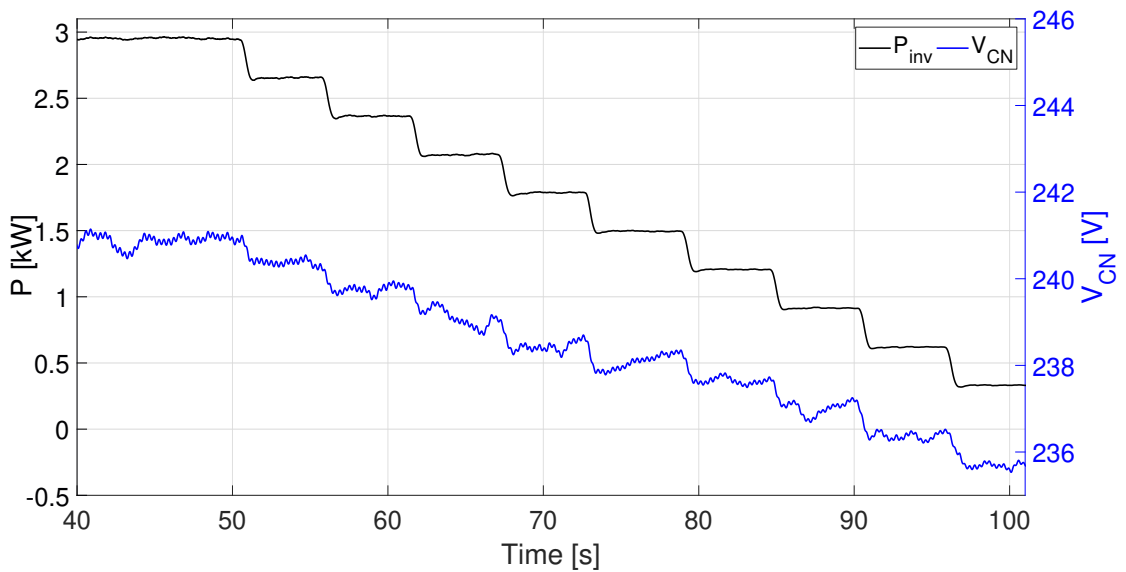
FIGURE 3.13: Inv-1 PQ compensating features.



(a) Inv-2 P-Q curve characterised at 4P levels implementing lagging and leading  $\cos \varphi$  sweep.



(b) Voltage compensation thanks to absorbing  $Q$  (leading) by Inv-2.



(c) Voltage compensation thanks to  $P$  reduction by Inv-2.

FIGURE 3.14: Inv-2 PQ compensating features.

## Chapter 4

# Photovoltaic inverters in unbalanced LV networks

This chapter studies the penetration of grid-connected photovoltaic systems. Particular attention is paid to how the inverse current flow and unbalance situations affect the voltage in the LV network. Photovoltaic arrays are emulated and subjected to different irradiance profiles and the inverters are controlled to produce at different irradiance conditions. A model developed in PowerFactory, a power system analysis software, reproduces some of the operating conditions in a similar working environment. Both simulation and experimental results are compared.

Part of this work has been presented at Young Researchers Symposium 2016 Eindhoven (The Netherlands) [43].

### 4.1 Test platform

The main elements in the LV network are the external grid, the distribution transformer, the cables and the domestic PV systems. In this study loads representing households are not considered. Loads reduce the PV power injected into the LV network and thus decrease voltage variations, a behaviour that we specifically want to exhibit in the results. The test platform in Fig. 4.1 is an updated version of the platform in Fig. 3.4. This section describes every part of the test platform that was not previously included and its laboratory implementation is explained.

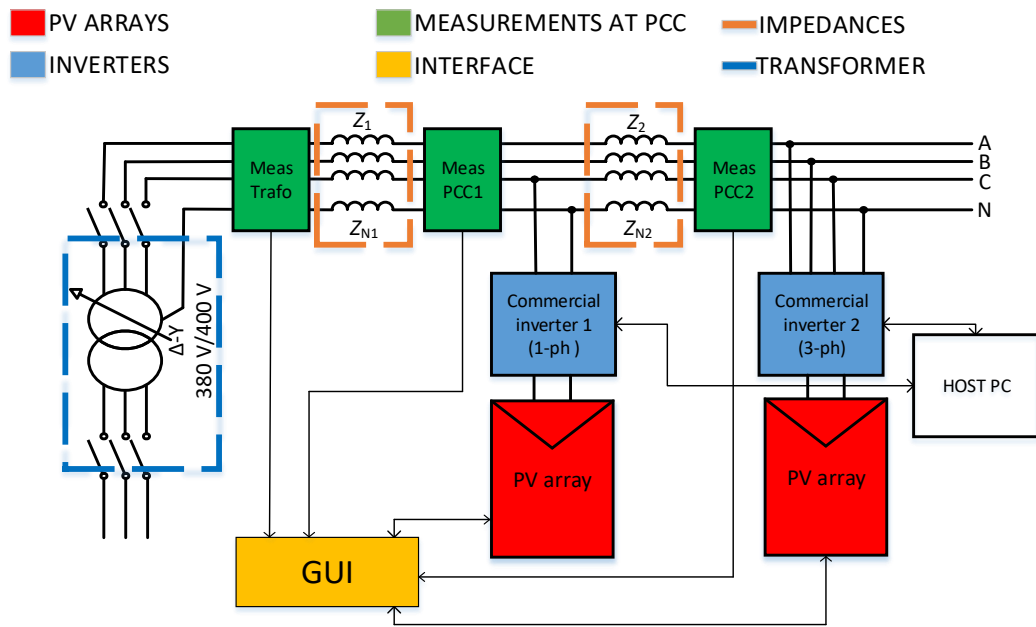


FIGURE 4.1: Laboratory test bench for the study of voltage fluctuations and unbalanced conditions.

#### 4.1.1 External grid

Voltage levels according to European standardisation bodies CEN/CENELEC are LV (<1kV), medium-voltage (MV) (1-36kV) and HV (>36kV) [27]. In Belgium, the voltage levels used in MV level distribution networks are 6kV, 11kV, 15kV and 36kV according to federal legislation<sup>1</sup>, but regional legislations<sup>2</sup> regulating electricity distribution below 70kV specify that 30-70kV lines are operated by the Transmission System Operator (TSO). Distribution System Operators (DSOs) operate grids usually below 15kV [44].

In a typical setting, the external grid is the MV network at a voltage between 6kV and 36kV [45]. The distribution transformer steps down the high voltage to a low voltage of 400V. For the simulation in PowerFactory environment, a constant-voltage slack bus of 15kV models the external grid.

#### 4.1.2 Distribution transformer

The transformer that feeds the LV network reproduced in the laboratory has the following characteristics: Dyn11 transformer of kVA rating  $S_n=100\text{kVA}$ , the Primary (380V,

<sup>1</sup>Legislated by the Belgian Federal Commission for Electricity and Gas Regulation (CREG) <https://www.creg.be/en>.

<sup>2</sup>Flemish Regulation Entity for Electricity and Gas (VREG) <https://www.vreg.be/en>, Walloon Commission for Energy (CWaPE) <https://www.cwape.be/> and Commission for the Energy Regulation in the Brussels-Capital Region (Brugel) <https://www.brugel.brussels/>

50Hz, three-phase, delta) and the Secondary (400V, 50Hz, three-phase, four-wire). The emulation of abnormal grid conditions, e.g. overvoltage, allows testing the behaviour and the compensation features of the inverters. The impedance in the transformer is estimated considering the standardized short-circuit voltage for distribution transformers. For ratings  $S_{\text{trafo}} \leq 630$  kVA,  $V_{\text{SC}} = 4\%$  of the phase-to-neutral voltage ( $V_{\text{ph-n}}$ ) [37]:

$$V_{\text{SC}} = 4\% V_{\text{ph-n}} = 0.04 \cdot 230\text{V} = 9.2\text{V} \quad (4.1)$$

where the short-circuit current is

$$I_{\text{SC}} = \frac{S_{\text{n}}}{\sqrt{3} \cdot 4\% V_{\text{Nom}}} = \frac{100\text{kVA}}{\sqrt{3} \cdot 4\% \cdot 400\text{V}} = 3600\text{A} \quad (4.2)$$

and the reactance and inductance values yield:

$$X_{\text{L, trafo}} = \frac{V_{\text{SC}}}{I_{\text{SC}}} = 2.55\text{m}\Omega \quad (4.3)$$

$$L_{\text{trafo}} = \frac{X_{\text{L, trafo}}}{\omega} = 8.15\mu\text{H} \quad (4.4)$$

where  $\omega = 2\pi f$  is the angular frequency and  $f = 50$  Hz.

### 4.1.3 LV network impedance

The cables are emulated with a set of impedances available in the laboratory. These impedances are placed between the transformer and the PCC (Fig. 4.1). Indeed, the impedance characteristics will determine the actual voltage variations in the network (section 4.2), as well as the effect of the active and reactive power compensating capabilities in the LV network voltage. Table 4.1 gathers the values of the impedances, with an impedance ratio  $X/R = 2/3$  with reduced resistance compared to the impedance values in Table 3.4 (section 3.4.2) but it is reasonable for the objective of this part of the work, that is to observe the voltage compensating actions in a LV network thanks to both the active and reactive control features and compare them with numerical simulation results.

### 4.1.4 PV system

Two PV array emulators feed the single- and three-phase inverters under test. The single-phase inverter connects Array 1 to the grid, while the three-phase inverter does

TABLE 4.1: Cable parameters.

Symbol	Description	Value	Units
$R$	Phase line resistance	100	m $\Omega$
$X$	Phase line reactance	65.97	m $\Omega$
$R_N$	Neutral line resistance	165	m $\Omega$
$X_N$	Neutral line reactance	108.9	m $\Omega$

likewise with Array 2 (Table 4.2). The PV panel characteristics can be found in Table 3.3, Section 3.4. Two independent controllers implement external control to the inverters.

TABLE 4.2: Configuration of the PV arrays.

Array	N. of panels	$V_{\max}$ [V]	Peak power [kWp]
1	11	410.3	2.7
2	20	746	4.9

## 4.2 Voltage fluctuation in the LV network

$\underline{V}_1 = V_1 \angle 0^\circ$  is the voltage reference at PCC1 in Fig. 4.2. The one at the transformer (TFM)  $\underline{V}_{\text{TFM}} = V_{\text{TFM}} \angle \delta$  and the grid current  $\underline{I} = I \angle \varphi$  are phase-shifted by angles  $\delta$  and  $\varphi$ , respectively. The complex power at the PCC1 is expressed as  $\underline{S}_{\text{PCC1}} = P_{\text{PCC1}} + jQ_{\text{PCC1}}$ , as a result of the sum of the powers the inverters inject into the grid.

Under unbalanced operating conditions the existing neutral impedance displaces the neutral voltage  $V_{N1}$  from the one at the transformer ( $V_N$ ). This is a characteristic of the available LV network setup (Fig. 4.2). The single-phase inverter is connected between phase C and the neutral, where the inverter voltage is in phase with  $V_C$ . Represented in Fig. 4.3,  $V_A$ ,  $V_B$  and  $V_C$  (in dark blue) are the line voltages at PCC1.

The voltage drop at the impedance between TFM and PCC1 is:

$$\underline{\Delta V}_x = \underline{Z}_1 \cdot \underline{I}_x \quad (4.5)$$

where x stands for each phase A, B and C and the feeder impedance is considered the same for all phases  $\underline{Z}_1 = R_1 + jX_1$ . The phase x voltage at TFM is therefore:

$$\underline{V}_{xN} = \underline{V}_x - \underline{\Delta V}_x \quad (4.6)$$



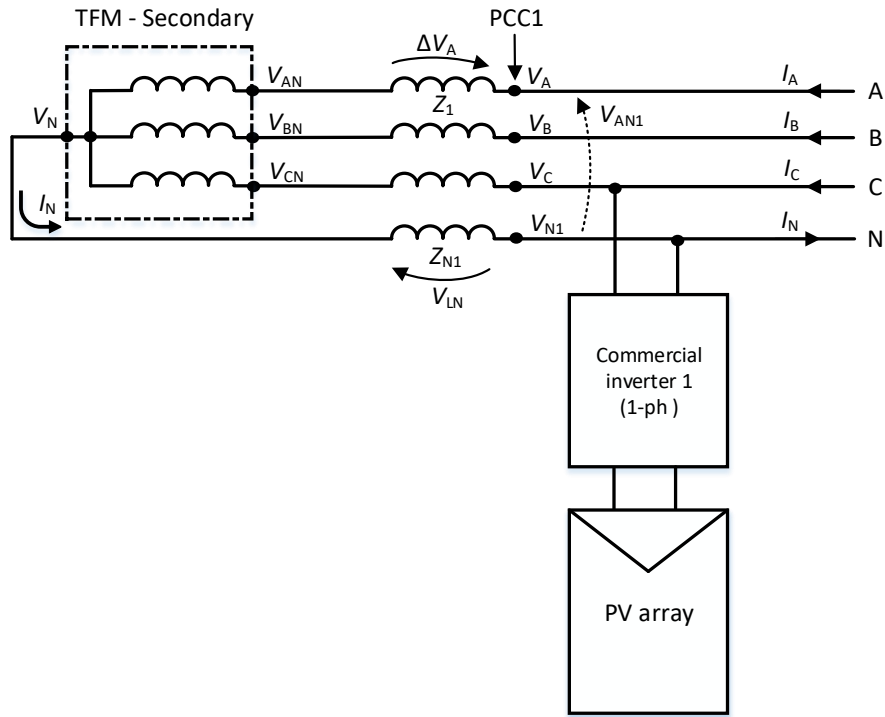


FIGURE 4.2: Part of the laboratory test platform and the neutral current flow direction.

and its neutral voltage:

$$\underline{V}_N = \underline{V}_{N1} + \underline{V}_{LN} \quad (4.7)$$

where  $\underline{V}_{N1}$  is the neutral voltage at PCC1 and  $\underline{V}_{LN}$  is the voltage drop at the neutral impedance  $Z_{N1}$ , caused by the current  $\underline{I}_N$  flowing through the neutral line:

$$\underline{V}_{LN} = \underline{I}_N \cdot \underline{Z}_{N1} \quad (4.8)$$

considering the neutral impedance  $\underline{Z}_{N1} = R_{N1} + jX_{N1}$ . The neutral voltage at PCC1 satisfies the following expression:

$$\underline{V}_{N1} = \underline{V}_N - \underline{V}_{LN} \quad (4.9)$$

and the phase x to neutral voltage at PCC1 is:

$$\underline{V}_{xN1} = \underline{V}_x - \underline{V}_{N1} \quad (4.10)$$

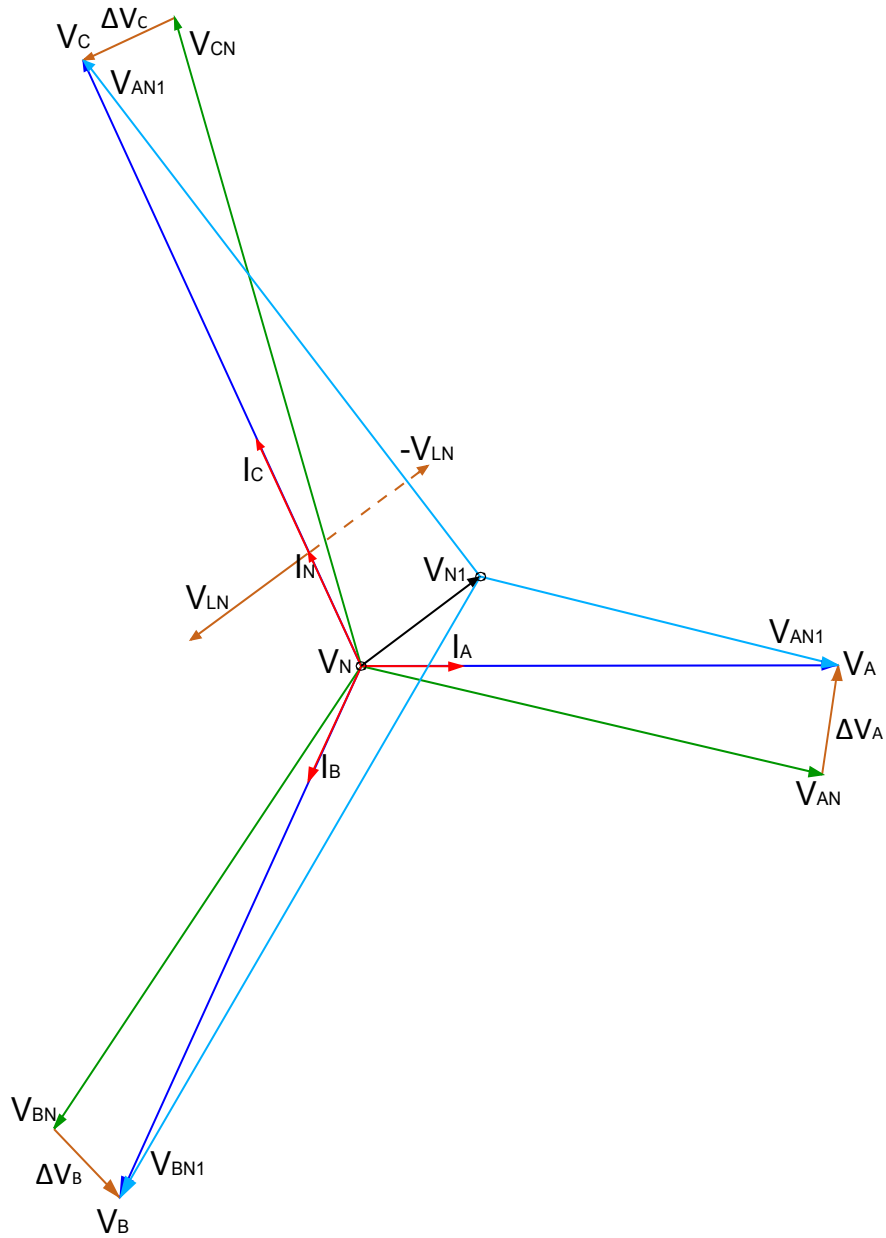


FIGURE 4.3: Voltage phasors of the LV feeder at PCC1.

The displacement of  $\underline{V}_{N1}$  from the neutral point of the transformer  $\underline{V}_N$  changes the magnitude of the vector in each phase. This situation is depicted in Fig. 4.3 and the resulting effect on the voltages (in light blue) is observed at PCC1 and by extension affects the voltages at PCC2. In the representation of Fig. 4.3, phase A to neutral voltage at PCC1 ( $\underline{V}_{AN1}$ ) is lower than phase B and C voltages,  $\underline{V}_{BN1}$  and  $\underline{V}_{CN1}$ , respectively.

## 4.3 Results and comparison

The tests for the single- and three-phase inverters focus on their power regulation functionality and the resulting voltage compensation capability. Table 4.1 summarizes the general parameters of the platform. The system is analysed operating at different static and dynamic production values.

### 4.3.1 Static production values

Three different operating scenarios are considered (see Table 4.4).

Operating scenario 1 (OP1): all the inverters are producing at their maximum power, without reactive power compensation (Fig. 4.4(a)). The figure shows the influence of the injected power on the grid voltage for each PCC. The furthest the PV inverter is from the TFM, the highest is the voltage level at the PCC for  $V_{BN}$  and  $V_{CN}$ . In this situation, the inverters linked to it are the first to disconnect from the grid if an overvoltage occurs. However, the same does not apply to  $V_{an}$ , affected by the displacement of the neutral voltage  $V_{N1}$  from the TFM neutral point  $V_N$ , as explained in Section 4.2.

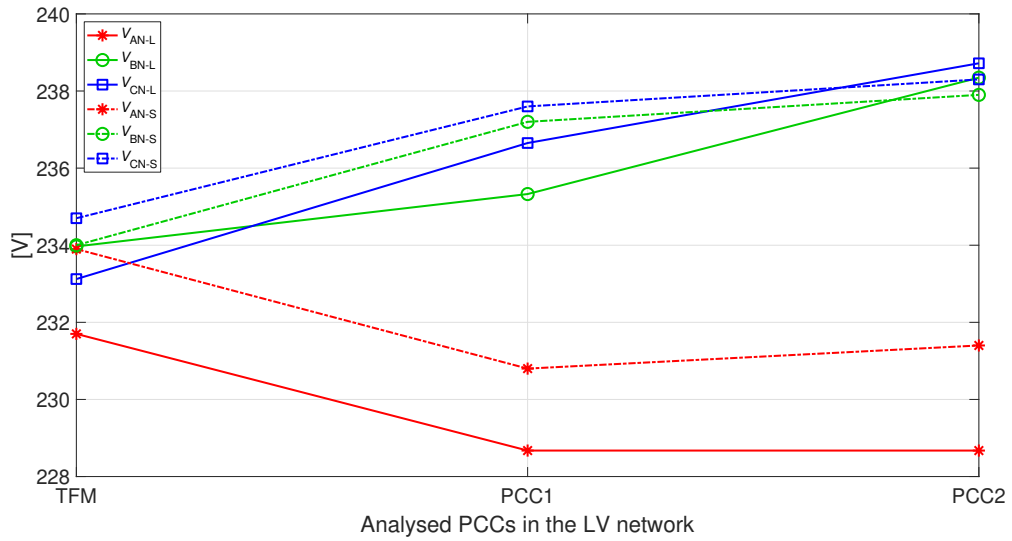
Operating scenario 2 (OP2): all PV inverters in Fig. 4.4(b) generate at half their maximum active power with a lower influence in the voltage.

Operating scenario 3 (OP3): all PV inverters generate at half their maximum active power and absorb the maximum reactive power. This last operating scenario allows us to observe the influence of reactive power on the voltages at the LV level. The voltage at phase C decreases more notably than at the others due to the two inverters' reactive power consumption.

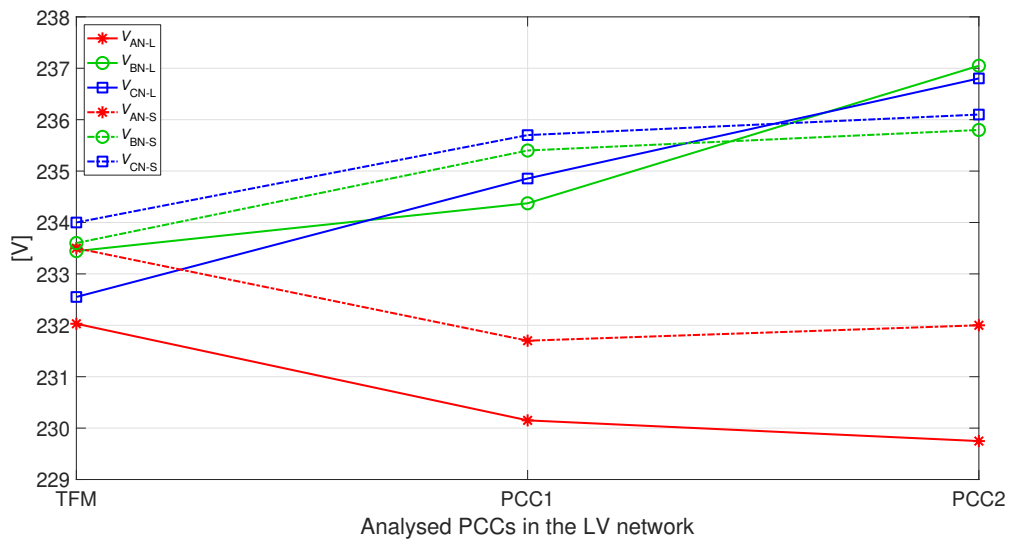
TABLE 4.3: Active and reactive power produced by the inverters in each scenario

	Single-phase inverter		Three-phase inverter	
	P [W]	Q [VAr]	P [W]	Q [VAr]
OP1	2317	0	4810	0
OP2	1200	0	2460	0
OP3	1200	-1700	2460	-2500

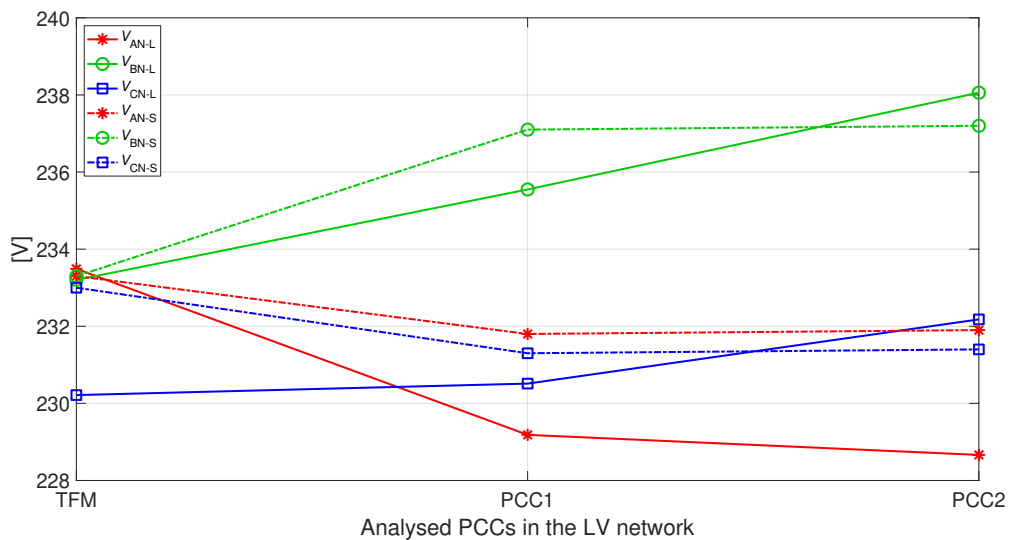
According to (4.5)-(4.10), the voltage drop ( $\Delta V_x$ ) due to the line impedance depends on the feeder characteristics, and the direction and quantity of the flowing current. Simulation and experimental results show similar behaviour of the voltage profile along the different points of the feeder. Table 4.4 gathers the resulting voltage values in



(a) Operating scenario 1.



(b) Operating scenario 2.



(c) Operating scenario 3.

FIGURE 4.4: Voltage profiles of the LV network. "L" corresponds to "Laboratory" (solid lines) and "S" to "Simulation" (dashed-dotted lines) results.

Figs. 4.4(a)-4.4(c) for the three operation scenarios. A voltage shift between experimental and simulation results can be noticed (e.g. measured  $V_{AN}=231.7V$  and simulated  $V_{AN}=233.9V$  in Fig. 4.4(a)). This can be explained by the non-ideality in the real application, with e.g. different impedance values between TFM phases. In simulation, the software considers that all the TFM phase impedances are of the same value.

TABLE 4.4: Measured and calculated rms voltages at each PCC for the different operating scenarios. "L" corresponds to "Laboratory" and "S" to "Simulation"

	OP1L	OP1S	OP2L	OP2S	OP3L	OP3S
$V_{AN,Tr}$ [V]	231.7	233.9	232	233.5	233.5	233.3
$V_{BN,Tr}$ [V]	233.9	234	233.4	233.6	233.2	233.3
$V_{CN,Tr}$ [V]	233.1	234.7	232.5	234	230.2	233
$V_{AN,PCC1}$ [V]	228.7	230.8	230	231.7	229	231.8
$V_{BN,PCC1}$ [V]	235.3	237.2	234.4	235.4	235.5	237.1
$V_{CN,PCC1}$ [V]	236.7	237.6	234.9	235.7	230.5	231.3
$V_{AN,PCC2}$ [V]	228.7	231	229.8	232	228.7	231.8
$V_{BN,PCC2}$ [V]	238.4	237.9	237	235.8	238.1	237.2
$V_{CN,PCC2}$ [V]	238.7	238.3	236.8	236.1	232.2	231.4

### 4.3.2 Dynamic production values

The PV emulator described in section 3.4.1 allows reproducing the irradiance profiles adopted for the experiments. The model uses real data extracted from a Belgian meteorological station<sup>3</sup>. The data has been sampled every minute. The irradiance variation is executed in the PV emulator every 2s, thus accelerating the execution time by a factor of 30. This way, experimental results can be obtained faster than with field measurements

Two different irradiance profiles are proposed, a sunny day (Fig. 4.5(a)) and a day with scattered clouds (Fig. 4.6(a)). This subsection analyses the results at PCC2 and its dynamic behaviour during a day, exposed to different irradiance conditions.

#### 4.3.2.1 Sunny day

Fig. 4.5(b) shows the evolution of the active power flows and 4.5(c) of the output voltages of the inverters, that corresponds to the irradiance profile  $G$  for a sunny day (Fig. 4.5(a)). The spikes in Fig. 4.5(b) are caused by the power source used for

<sup>3</sup>Irradiance data provided by GreenWatch SA, taken in Aubange, Belgium on the 03/07/2014 (sunny) and 04/09/2015 (day with scattered clouds).

emulating the PV array for certain variations of the irradiance profile and should be ignored. Similarly to the case for the static production values (section 4.3.1), the output behaviour of the inverters is analysed in the PowerFactory model. The model adopts the parameters predefined in the real test platform (section 3.4). Both simulation and experimental results present similar evolutions, although the offset in the measured voltages is meaningful. PowerFactory cannot reproduce the voltage differences related to the unbalance in the real TFM.

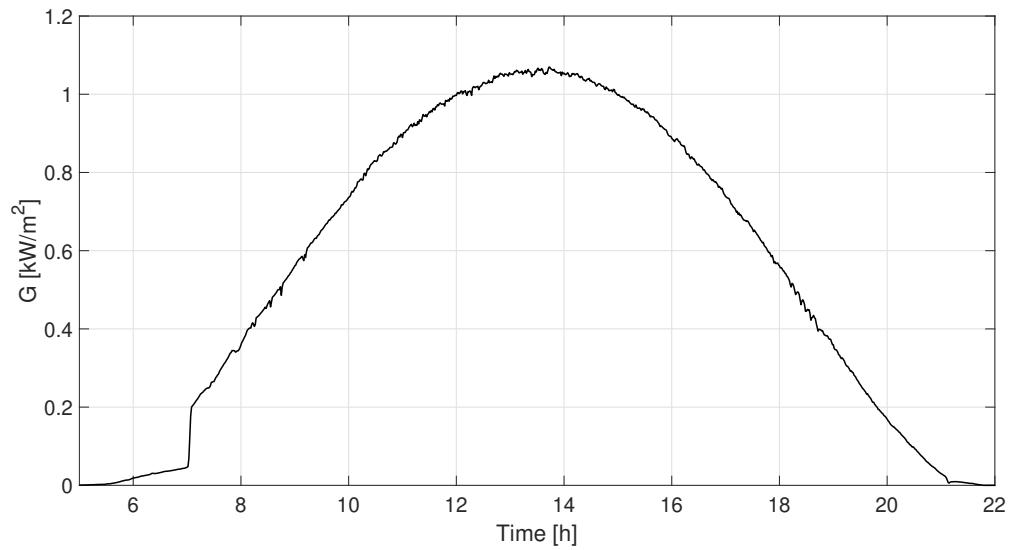
#### 4.3.2.2 Day with scattered clouds

For this experiment, a cloudy day with relatively fast changing irradiance conditions is chosen. This test intends to analyse the dynamic response of the PV inverters and the LV network under this generating condition.

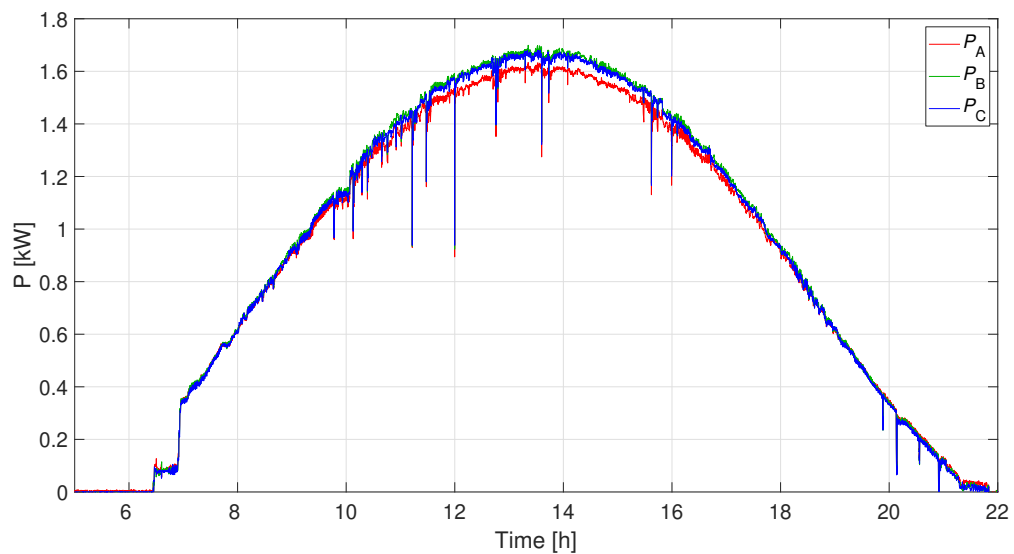
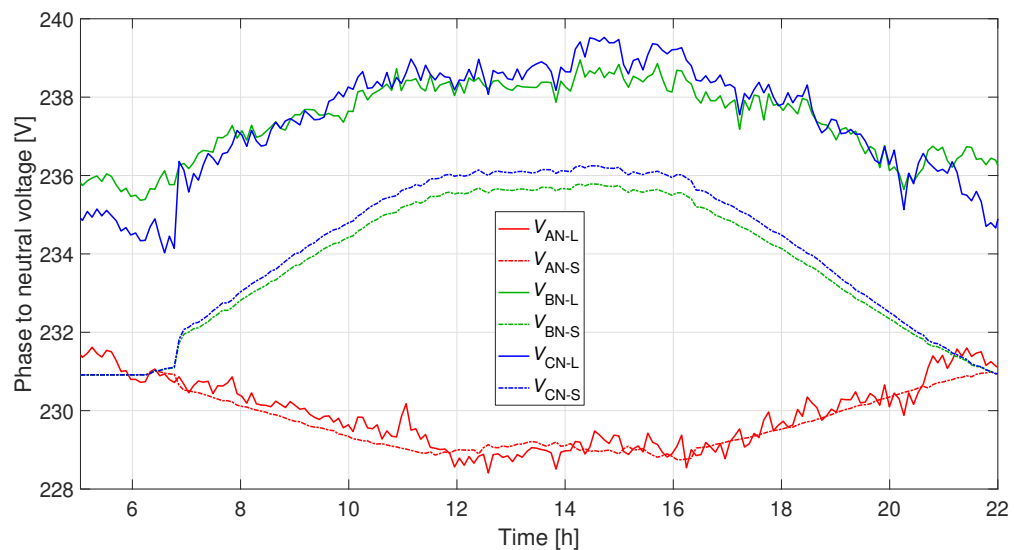
#### 4.3.3 Alternatives to the voltage support by reactive power

The transformer considered in this work allows to manually change the voltage level in the secondary side, which provides some flexibility for laboratory purposes. Intensive use transformers are normally equipped with tap-changers in the high voltage side allowing for a minimum of three different voltage levels (-5%, 0%, 5% of nominal voltage). Distribution transformers are provided with de-energised tap-changers, thus the voltage adjustment in distribution networks is realised under off load conditions. Something impractical that is not carried out on a regular basis. In fact, the transformer level voltage is regulated in the commissioning and normally is not adjusted again.

Transformers in high-voltage (HV) grids are provided with on-load tap changers (OLTCs) [46]. OLTCs change the voltage transformation ratio by altering the turns of the transformer winding under load conditions. Due to the increasing presence of small PV generation in the grid, transformers with OLTCs are an attractive solution for DNs voltage stabilisation [47]. Three type of tap-changers can be found: electromechanical, hybrid and full-electronic [48]. The operation of the electromechanical switches makes the tap-changing process slow. Each mechanical tap-change operation needs a minimum of 3s. Considering a transformer with the minimum configuration of three taps, the tap-changing operation takes 9s. The electronic OLTC transformers, on the other hand, use solid-state switches, reducing the tap changing process time to less than 20ms [49]. An interesting alternative that could facilitate, in addition, low voltage ride-through capabilities at transformer level, thanks to the fast response of these full-electronic OLTCs.

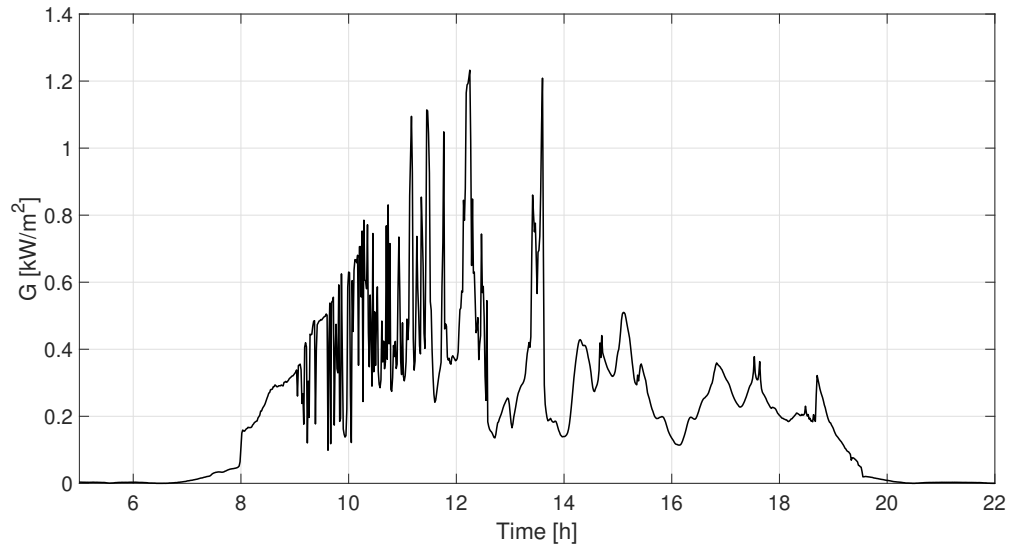


(a) Irradiance profile on a sunny day.

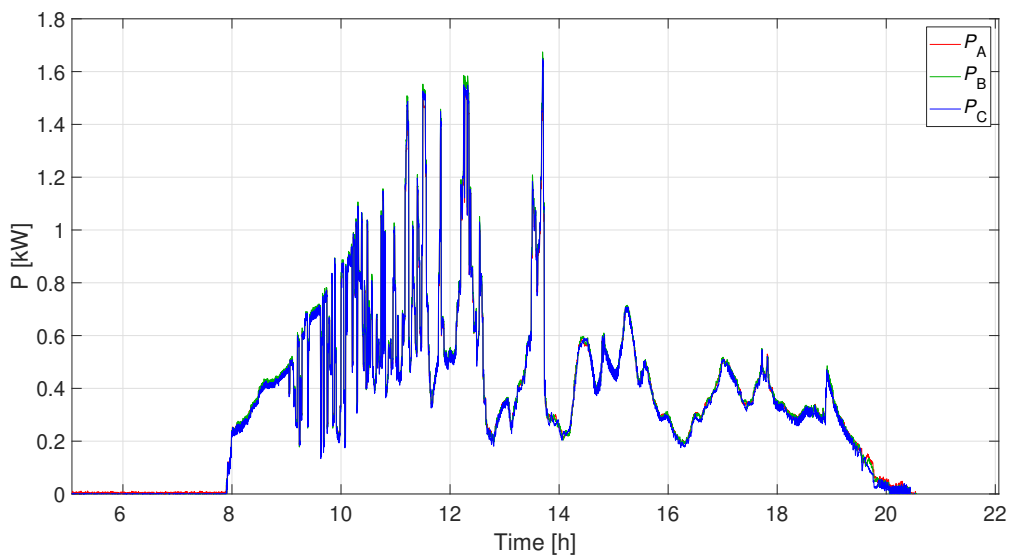
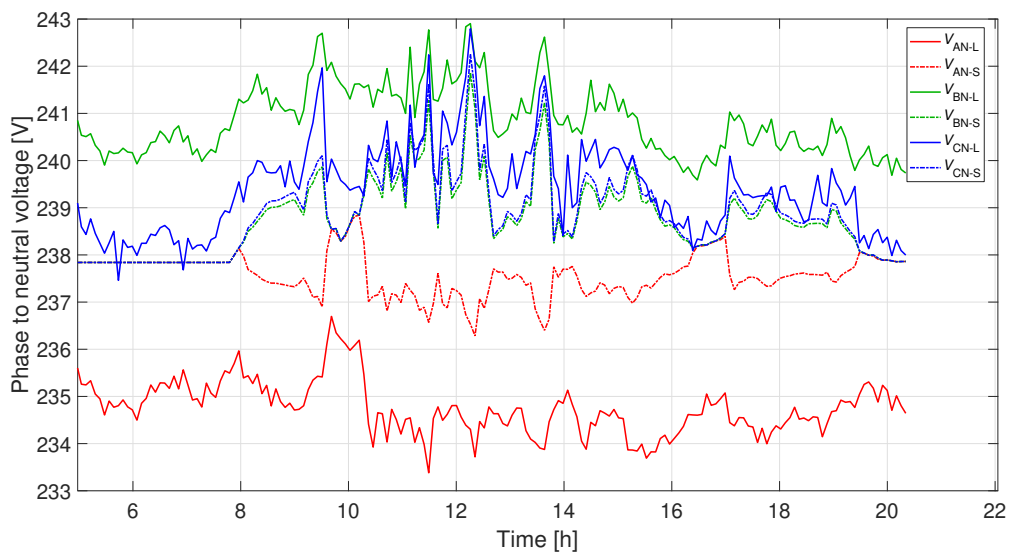
(b) Active power variation over time at PCC2 on a sunny day.  $P_A$ ,  $P_B$  and  $P_C$  are phase A, B and C powers, respectively.

(c) Phase-to-neutral rms voltages evolution over time at PCC2 on a sunny day. "L" corresponds to "Laboratory" (solid lines) and "S" to "Simulation" (dashed-dotted lines) results.

FIGURE 4.5: Simulation and experimental results of the three-phase inverter connected at PCC2 on a sunny day.



(a) Irradiance profile on a day with scattered clouds.

(b) Active power variation over time at PCC2 on a day with scattered clouds.  $P_A$ ,  $P_B$  and  $P_C$  are phase A, B and C powers, respectively.

(c) Phase-to-neutral rms voltages evolution over time at PCC2 on a day with scattered clouds. "L" corresponds to "Laboratory" (solid lines) and "S" to "Simulation" (dashed-dotted lines) results.

FIGURE 4.6: Results of the three-phase inverter connected at PCC2 on a day with scattered clouds.



#### 4.3.4 Discussion of results

In this chapter, the penetration of grid-tied inverters in LV networks has been analysed. The design and reproduction of a complete test platform comprising the electrical grid, PV emulators and the grid-connected power devices under test allowed the study of unbalanced operation in LV networks with PV generation presence. Experiments carried out with the real hardware validate the numerical results though the non-idealities in the real environment should be taken into consideration.

In addition, the effect of local neutral point displacement has been exhibited and explained. Such effect changes the phase-to-neutral voltages in magnitude and phase and can aggravate the unbalance situation.

According to [15], the european grid standard EN 50160 (voltage characteristics of electricity supplied by public distribution networks) allows a maximum voltage unbalance between phases of 3%. The EN 50160 determines that the distribution systems have to maintain the distribution voltage level within the  $\pm 10\%$  of the nominal voltage in all operating points of the grid. With the recent growth of distributed PV generation, the maximum voltage rise is defined as 3% in LV networks [47]

German grid standard VDE-0126-1-1 (2006) states that the impedance monitoring can be replaced by line-to-line voltage monitoring if the control of each phase current is done independently. In this context, some manufacturers promote power balancing by means of three-phase systems that basically include three single-phase inverters, considered small-scale central inverters (e.g. Sunny minicentral) [50]. Another interesting solution to the unbalance situation are the single-phase inverters with three-phase grid-connection that bring the possibility to reconfigure the connection to the grid and feed a different phase of lower voltage (e.g. KACO powador solar inverters) [51].



## Chapter 5

# Operation of photovoltaic inverters in a distributed scheme

This chapter discusses the active management of grid-connected PV systems. The focus is on PV units sharing the same LV network. A distributed control scheme [21] that manages the interaction between PV inverters and the grid is implemented. The control scheme modifies the active and reactive power of PV units to mitigate overvoltage issues.

In practice, a wide variety of inverters of different brand, power rating and connection type is found in the same LV network. Even the controllable features offered by each manufacturer are usually different. The external control provides certain interaction between the inverter and the end-user and power-related functionalities are accessible by the user. Manufacturers implement standard communication protocols allowing for this remote control. Nevertheless, the transmission format of the messages is developed and decided by each manufacturer and is generally not compatible with other manufacturers' messages. Homogeneity in the communication eases the implementation of an active management for PV generation units in DN. This chapter validates the distributed control algorithm proposed in [21] with a universal communication scheme that facilitates its implementation.

### 5.1 Distributed control of photovoltaic inverters in Distributed Networks

The distributed control scheme proposed in [21] can be divided in two main parts: first, the normal operation entails a local control for each device, without any interaction with the surrounding network and devices. Second, a collaborative control assumes the

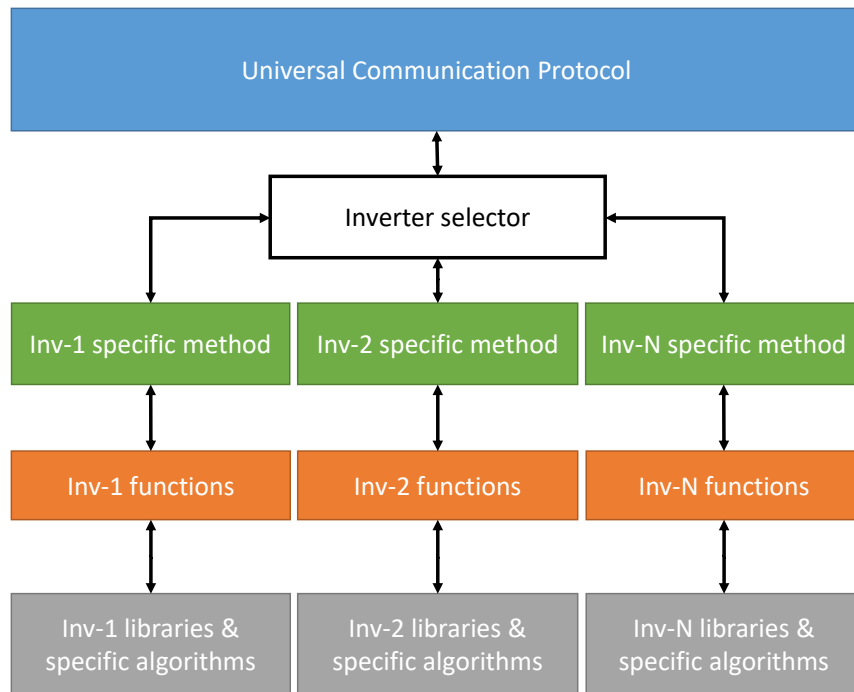


FIGURE 5.1: Structure of the distributed communication scheme.

cooperation of all the inverters. The controllers in charge of inverters' operation make use of limited communication. Only when it is necessary, an emergency signal alerts the PV units to begin the collaboration process and activate compensation actions. In terms of control actions, the control algorithm prioritizes first the active power delivery, second the reactive power compensation and third the active power curtailment.

### 5.1.1 Communication network architecture

The purpose of the universal communication protocol UCP (Fig. 5.1) is to serve as an *interpreter* between the external controller (e.g. a gateway or a computer) and the inverters to ease the implementation of the remote control and monitoring. It has a vertical structure: the UCP selects the control module of an inverter that contains the specific method of this particular inverter. Each specific method addresses to the functions that build the communication telegrams. Finally, the functions make use of libraries or specific algorithms if necessary. Details on the UCP can be found in Appendix A. The specific communication scheme as well as transmission message formats are protected by license rights and cannot be published in this manuscript.

### 5.1.1.1 Communication protocol

Here, the external control is done via the RS485 serial communication method. This communication interface allows to connect several units to a network structure or communication bus. A host computer assumes the Master function, whereas the inverters act as slaves. The Master sends queries over the RS485 communication bus. The devices connected to the bus receive these data and respond to the Master. In serial communication there is a risk of data collision, thus the implementation of error detection in a higher level control is necessary to detect incomplete data transmission and repeat it at a later time.

### 5.1.1.2 Control algorithm for the active management

The control algorithm is composed of five modes of operation (Fig. 5.2):

- Mode A: Local operation. If there is no overvoltage, the controllers adjust the reactive power setpoint of the inverters individually. The inverters perform the MPPT for the active power setpoint. There is no communication with other controllers and only local measurements are used for the reactive power compensation.
- Mode B: If the controller detects overvoltage, an emergency signal alerts other units for coordinated reactive power consumption.
- Mode C: If the overvoltage situation persists even after all PV units have used the maximum reactive power capability, each controller performs active power curtailment.
- Mode D: If the overvoltage condition disappears, the emergency signal stops and each controller restores the active power MPPT.
- Mode E: If the voltage level is within an acceptable range, each controller restores the reactive power operation to normal conditions.

If the overvoltage situation reoccurs or the controller receives a new emergency signal, the control algorithm steps back to one of the voltage compensation modes (B or C).

Modes B-C-D-E define an operating time to accomplish the tasks in each mode. The selection of these operating times is based on the ongoing Belgian standard C10/11 [29] that determines a maximum operating time of 10 minutes if the inverter detects overvoltage in its output terminals (230V+10%), as well as on the empirical experience during the implementation of the control algorithm.  $t_{DQ}=2\text{min}$  is the reactive power

( $Q$ ) depleting time,  $t_{DP}=2\text{min}$  the active power ( $P$ ) depleting time,  $t_{RP}=4\text{min}$  the  $P$  restoring time and finally,  $t_{RQ}=4\text{min}$   $Q$  restoring time. Restoring times were chosen to be larger than depleting times because of the following reason: in an overvoltage situation it is preferred to reduce the voltage level in a relatively short time and avoid disconnection or device damage. On the other hand, larger restoring times ensure a smooth rise of the grid voltage.

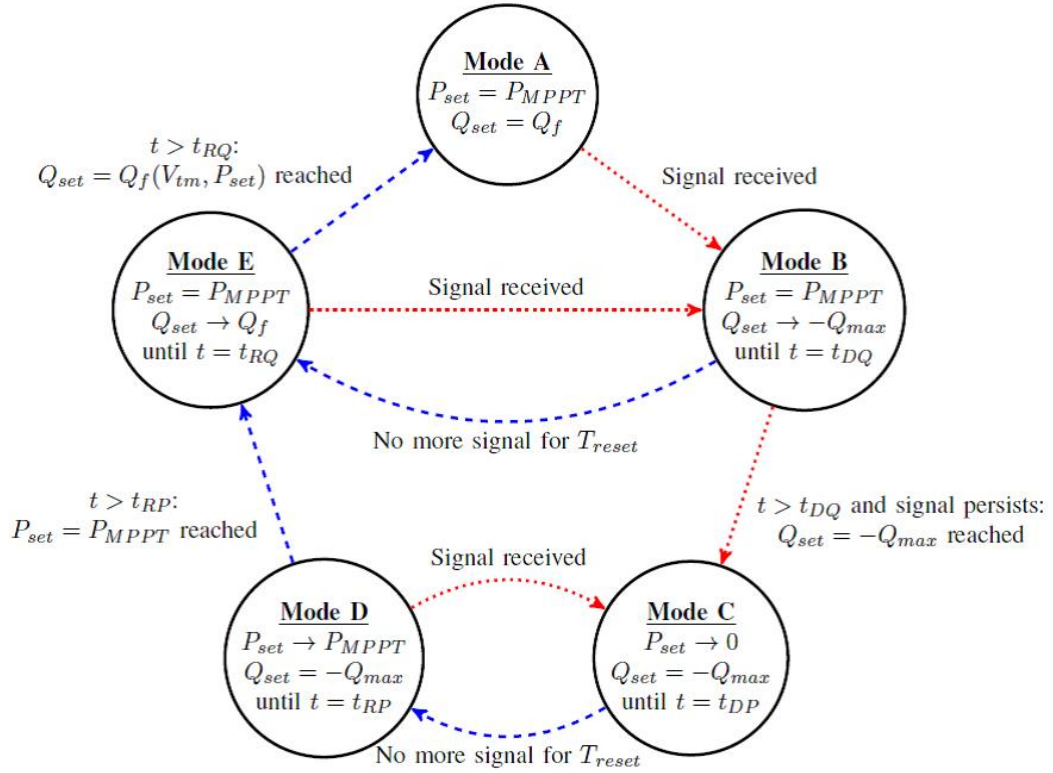


FIGURE 5.2: State transition diagram of the distributed control scheme. The red dotted lines are the emergency control transitions while blue dashed lines are the restoring ones [21].

### 5.1.1.3 Corrective actions in the control algorithm

As opposed to the control algorithm, the power hierarchy of the inverters studied prioritizes the reactive power compensation that leads to the depletion of the active power (e.g. working at full load). Accordingly, the control algorithm implements additional calculations: first, instantaneous active power is measured. Second, considering the maximum apparent power of the inverter, a new maximum reactive power is set.

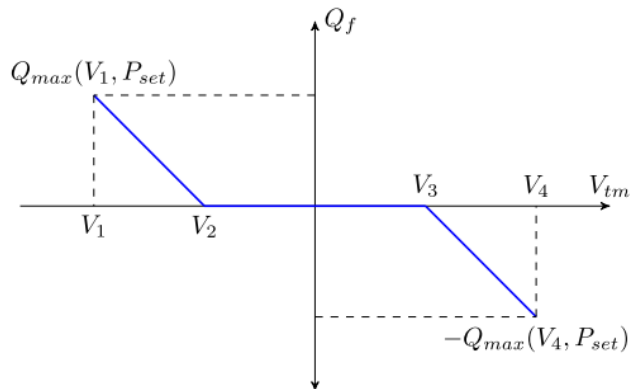


FIGURE 5.3: Local operation mode (mode A).  $Q_f(V_{tm}, P_{set})$  function [21].

## 5.2 Experimental results

### 5.2.1 Test platform

The test platform in section 3.4 is used. The PV emulator emulates a PV array of 21 series-connected PV panels with the characteristics in Table 3.3 and results in a peak power of  $P_{PV} = 5.15\text{kWp}$ . The three-phase Inv-1 (see section 3.3) with a rated apparent power of  $S_{AC} = 5.0\text{kVA}$  is tested.

### 5.2.2 Local operation

If the voltage at the PCC of the inverter is inside a predefined range  $[V_1, V_2]$  or  $[V_3, V_4]$ , the inverter modulates its reactive power as a function of its output voltage ( $V_{tm}$  and delivered active power ( $P_{set}$ ) (Fig. 5.3).  $V_1$  and  $V_4$  are the limits for a normal operation, corresponding to the maximum voltage amplitude variation allowed for distribution systems that, according to the norm EN 50160 is  $\pm 10\%$  of the nominal grid voltage [15].

Based on local measurements, the voltage compensation action rests with the inverter that detects the voltage rise (Fig. 5.4). The test implements a ramp to the PV array emulator (see section 3.4.1), starting from an input power equivalent to  $P_{PV} = 1.5\text{ kW}$  to  $P_{PV} = 5.0\text{ kW}$ . The reactive power varies according to Fig. 5.3 as far as the apparent power does not exceed its maximum. The hierarchy in the control algorithm (i.e. priority to the active power delivery) affects the reactive compensation capability above  $P_{PV} = 4.0\text{ kW}$ , coincident with its minimum  $\cos \varphi$  at full power (see Table 3.1).

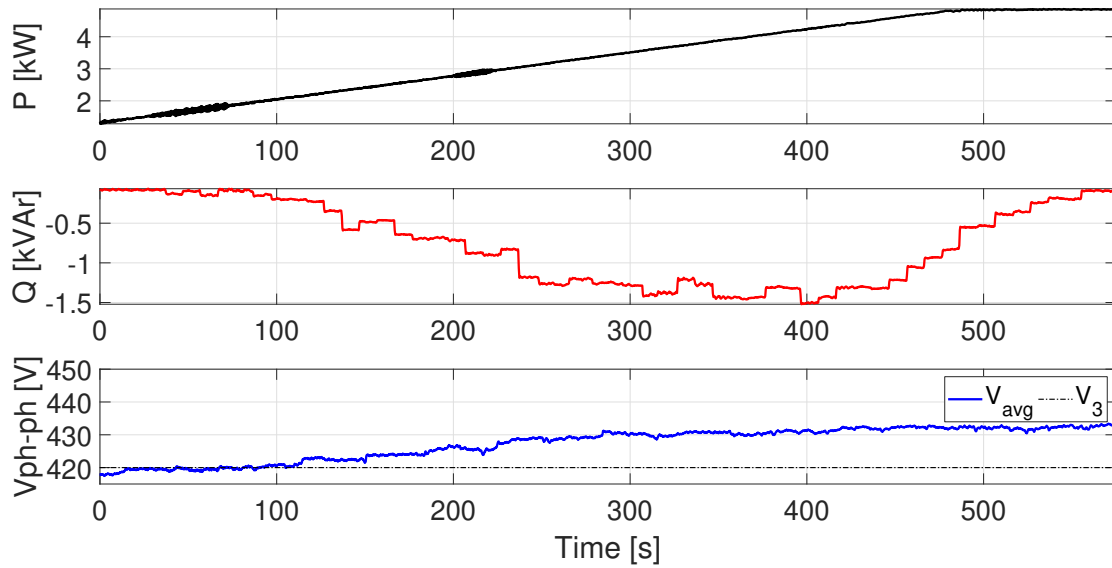


FIGURE 5.4: Local operation mode (mode A). Voltage compensation action of Inv-1.

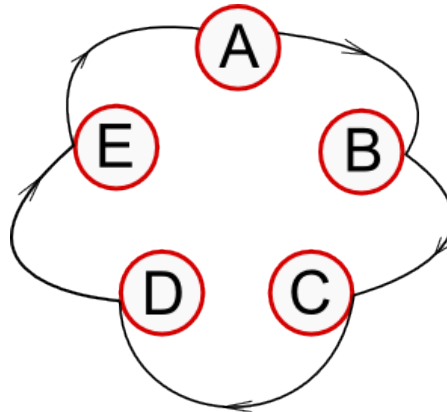


FIGURE 5.5: State transition diagram of testing scenario 1. Own illustration based on Fig. 5.2 [21].

### 5.2.3 Active and reactive power support at partial load

This test considers the state transition diagram in Fig. 5.5 at partial load operation under the following test conditions:

- Delivered active power: 80% of the nominal power ( $G = 800 \text{ W/m}^2$ )
- Initial operating mode: mode A
- Voltage level within the acceptable range ( $V_N \pm 10\%$ )

The partial load operation in Fig. 5.6 considers a realistic operating scenario under an irradiance level of  $G=800\text{W/m}^2$ . The equivalent PV power for this irradiance is  $P_{\text{PV}} = 4.12\text{kW}$ . This enables the utilization of the reactive power compensation when



a voltage level issue emerges, without affecting the active power generation. Local measurements show a normal operation (operating mode A in Fig. 5.6(a)) within a safe voltage range (Fig. 5.6(b)). At  $t_s = 40$  s, the inverter receives an emergency signal (another PV unit sharing the same LV network has detected an overvoltage) and the control algorithm changes to the operating mode B. As long as the controller receives the repeating emergency signal, it adjusts increasingly the reactive power of the inverter. The target is to reach its maximum reactive power at  $t=t_{DQ}+t_s=160$ s.

In mode C, the controller reduces the active power delivered by the inverter until the distress signal disappears or in a time period of  $t_{DP}=120$ s at  $t=t_{DP}+t_{DQ}+t_s=280$ s. The active power reduction is limited to a minimum security level of 10%  $P_N$  to avoid damaging the devices, as recommended by the manufacturers.

Once the overvoltage situation disappears, the control algorithm changes to operating mode D, after a period without receiving an emergency signal ( $t_{reset} = 40$  s). In this mode, the active power is restored stepwise in  $t_{RP}=240$ s at  $t=t_{RP}+t_{reset}+t_{DP}+t_{DQ}+t_s=560$ s.

As there is no overvoltage in the output of the inverter and the controller does not receive any emergency signal, the control algorithm changes to mode E to smoothly adjust the reactive power setpoint in a time period equal to  $t_{RQ}=240$ s at  $t=t_{RQ}+t_{RP}+t_{reset}+t_{DP}+t_{DQ}+t_s=800$ s.

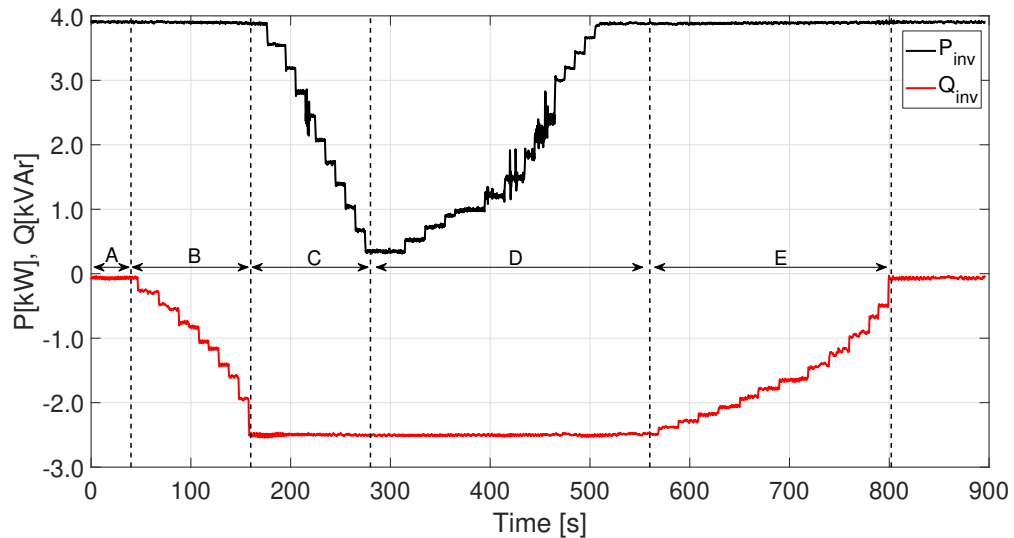
Grid voltages are considerably reduced thanks to the active power reduction rather than to the reactive power compensation capability. This result is highly influenced by the resistive behaviour of the LV networks. The voltage level also changes independently from the operation of the PV inverter, influenced by a neighbouring device interacting with the same DN. In this case, the connection of a three-phase load or the disconnection of a three-phase inverter creates a sudden change around  $t = 750$  s in Fig 5.6(b).

#### 5.2.4 Active and reactive power support at full load

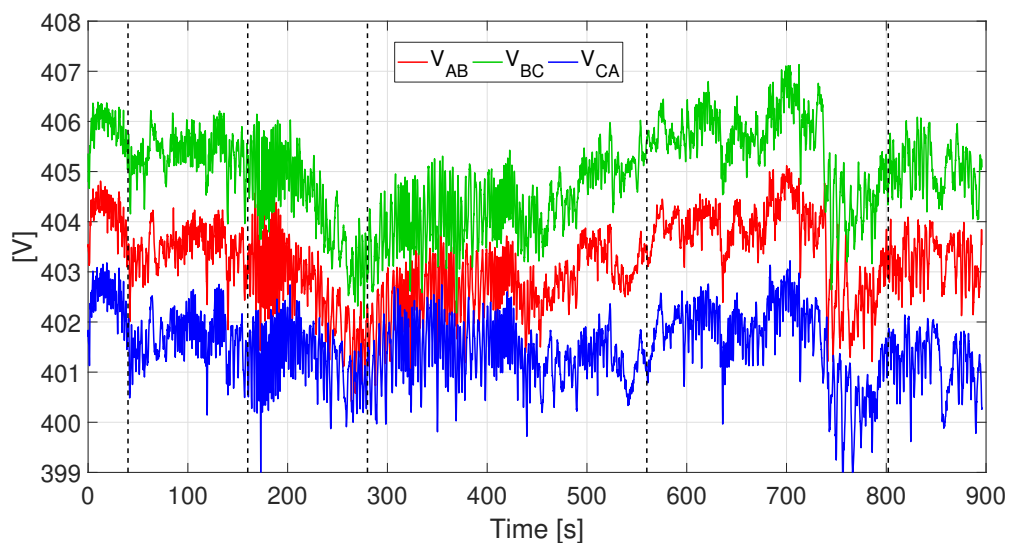
This test considers the state transition diagram in Fig. 5.7 at full load operation under the following test conditions:

- Delivered active power: 100% of the nominal power ( $G=1000\text{W}/\text{m}^2$ )
- Initial operating mode: mode A
- Voltage level within the acceptable range ( $V_N \pm 10\%$ )

The operating conditions are similar to the previous case at partial load. The power hierarchy of the control algorithm prevents the modulation of the reactive power in



(a) Active and reactive power evolution over time.



(b) Phase to phase grid voltages evolution over time.

FIGURE 5.6: Measured A-B-C-D-E modes operating sequence. Voltage compensation action of Inv-1.

mode B (in  $t_{DQ}=120s$ ), avoiding the active power reduction. In mode C ( $t_{DP}=120s$ ), thanks to the active power curtailment, the voltage reduces and the emergency signal disappears. The control algorithm changes to mode D, restoring active power stepwise. In this case, the controller receives a new emergency signal, changing back to depletion mode (mode C) and repeating the process. The sequence in this case study is, therefore, A-B-C-D-C-D-E.

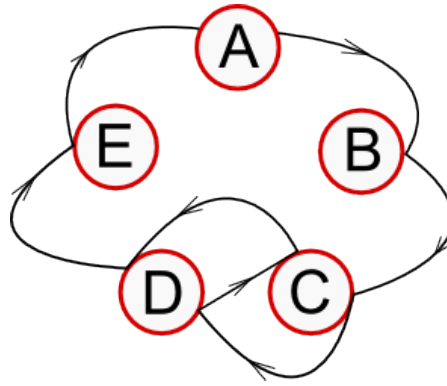
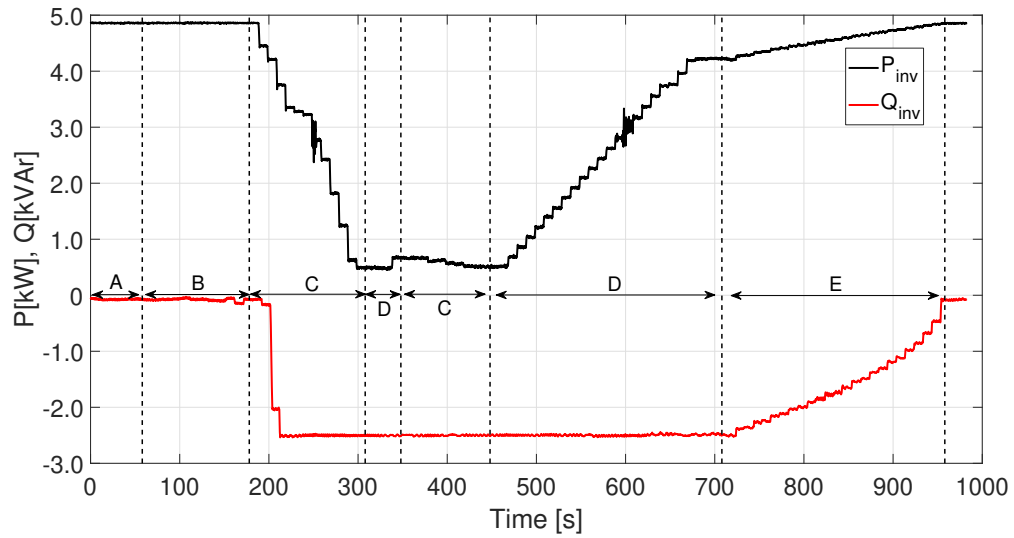


FIGURE 5.7: State transition diagram of testing scenario 2. Own illustration based on Fig. 5.2 [21].

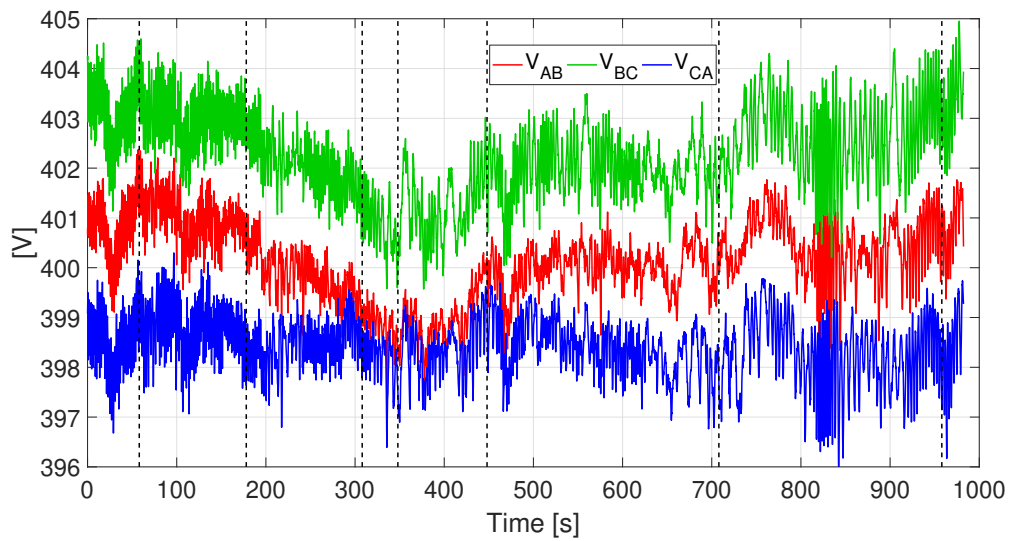
### 5.2.5 Discussion of results

The development of a universal communication protocol facilitates the implementation of active management control schemes in DN. Especially for LV networks with PV systems of different brands, a tool which serves as a *bridge* or an *interpreter* turns out to be necessary. The active management in DN provides information about the status of the different PCCs along the grid. Moreover, the collaborative operation of the PV units in the distributed control scheme contributes to improving the safe operation of the LV network. Overall, it constitutes a feasible solution to the overvoltage and grid unbalance issues from the grid voltage instability point of view.

Nevertheless, the results show that the grid voltage is not affected only by the inverter's operating point. The local information is not enough to overcome grid voltage issues arising from the operation of other loads and generation units. Energy management systems (EMSs) have to be more and more complete and handle increasing numbers of devices of different requirements. The information about the status of the devices that interact with the grid must be included in these EMSs.



(a) Active and reactive power evolution over time.



(b) Phase to phase grid voltages evolution over time.

FIGURE 5.8: Measured A-B-C-D-C-D-E modes operating sequence. Voltage compensation action of Inv-1.

## Chapter 6

# Discussion of Part I

Voltage compensation capabilities of PV inverters, i.e. active and reactive power control, help to the stability of LV networks. The possibilities that individual PV generation units provide have been analysed in this first part of the manuscript. However, the compensation actions of individual inverters that effectively influence in the stability of the grid are limited, due to design constraints and limitations certain country grid standards impose [13]. For that reason, the advantages of having a collaborative network of several units has been discussed and demonstrated in this work. An active management control scheme for distributed PV generation units has been implemented in order to control commercial inverters. The UCP proposed in this work provides a way to control inverters of different brand connected to the same LV-network.

As the LV networks are characterised by having a more resistive behaviour, they experience larger voltage oscillations with the exchange of the active power rather than the reactive power. In general, inverters' reactive power compensation capability is less effective than reducing the active power delivered to the grid. Besides, voltage compensation via reactive power provision can increase power losses in the PV inverters and operational costs of the PV installation [52]. Hence, active power control capabilities must take priority for inverters connected to LV networks. Some country grid standards oblige grid-connected PV systems to integrate the active power curtailment feature in the hardware of the DC/AC conversion device. The grid voltage instability is ensured, but at the cost of having less profitable PV installations.

A possible alternative to the power curtailment could be the storage of the PV energy in batteries before the DC/AC conversion. Thus, the energy supplying the grid is reduced for a certain period but not curtailed. The adoption of batteries in PV systems offers various advantages, including the rescheduling of the energy injected into the grid or the compensation of the energy generation mismatch between PV panels.



## Part II

# Control strategies for distributed maximum power point tracking architectures in photovoltaic applications





## Chapter 7

# Introduction

Classical grid-tied PV systems (Fig. 7.1(a)) consist of a number of series-connected PV panels, i.e. strings. Depending on the PV plant's nominal power, each string can be connected to an input of a string inverter or some strings can be connected in parallel and the resulting field is plugged to the input of an inverter. In case of irradiance mismatching phenomena affecting the PV strings, e.g. due to shading or uneven ageing, the presence of bypass diodes allows to reduce the consequent power drop. Unfortunately, bypass diodes lead to a multi-modal P-V curve of the string and of the whole field showing several maximum power points (MPPs). Among them, only one is the global MPP that provides the highest power [53]. The multi-modality of the P-V curve makes the MPP Tracking (MPPT) operation unreliable and the system process only part of the available power in the string. Indeed, in commercial string and central inverters, the latter is performed using on-line local optimization algorithms, which are based on the hill-climbing principle known as Perturb and Observe (P&O) method. Global MPPT algorithms (GMPPT) perform periodical voltage sweeps in the string using different techniques, in order to detect the operating point providing the highest maximum power [54, 55]. This is a great advantage over the algorithms performing less advanced MPPT control that can be trapped in a suboptimal operating point, known as local MPP (LMPP). Nevertheless, GMPPT techniques do not guarantee the extraction of all the power available in the PV string under mismatch conditions.

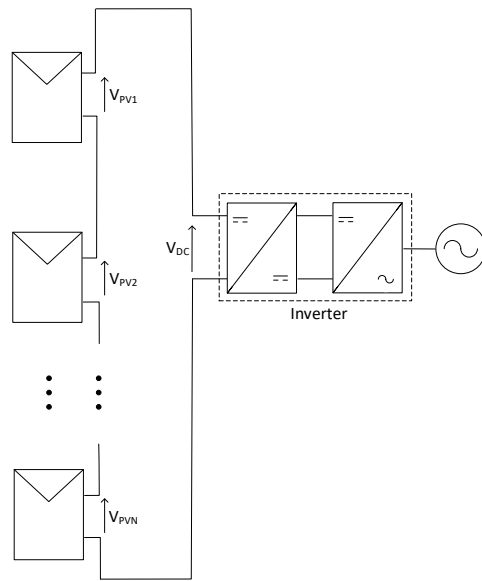
DMPPT systems have emerged as an alternative to the traditional CMPPT approach. The DMPPT system is based on the use of distributed power electronics equipped with their own MPPT control thus maximizing the power produced by a small number of series-connected panels, ideally one. The power electronics are divided in two main families, micro-inverters [56, 57] and DC power optimizers [58–60]. Micro-inverters (Fig. 7.1(b)) interface directly with single PV panels, performing individual MPPT. This offers

a great advantage in terms of loss minimization due to power mismatch and system scalability. Nonetheless, the micro-inverters show a low conversion efficiency (typically 93%-95%) compared to conventional high-voltage string and central inverters (above 98%). Indeed, it is quite difficult to reach the grid voltage from the output of a single PV panel in an efficient and reliable way. In addition, the cost is significantly higher than for a system that uses a central inverter, as the amount of power electronic components considerably increases [61].

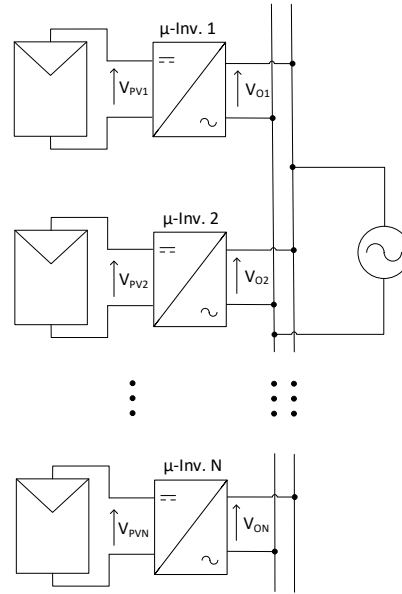
DC power optimizers are more suitable than micro-inverters for commercial and utility-scale systems. A DC power optimizer is basically a low-voltage DC/DC converter. The output terminals of the converters can be connected in series (Fig. 7.1(c)) or in parallel (Fig. 7.1(d)). The parallel connection requires high-boosting converters or a second boosting DC/DC stage to meet the DC bus voltage level required by the grid-connected inverter [62]. The need to adapt the PV voltage to a higher level ( $\simeq 325$  Vdc for single-phase inverters,  $\simeq 565$  Vdc for three-phase inverters) implies low power conversion efficiency and high stress of components. This may lead to lower durability of the power electronics. Non-isolated converters have a limited voltage gain, because the voltage conversion ratio depends on the modulation of the duty cycle. Isolated topologies can help adapt the different voltage levels thanks to the use of a high-frequency transformer that isolates low and high voltage sides of the converter. However, the number of components in non-isolated converters is larger and normally increases the cost in hardware [10, 63].

The string of DC/DC converters substitutes the string of PV panels. The high boosting requirement per converter is not necessary and non-isolated topologies can be implemented. In the last decade, these power optimizers [64–67] have penetrated the PV market, e.g. reaching 37% of the total California residential market share in 2017 [10], demonstrating that the amount of harvested energy is increased from 20% to 45% under partially shaded conditions [60, 68–73]. Unlike CMPPT, any partial shading that occurs in a single PV panel of a DMPPT system will only affect the power output of the corresponding module [74].

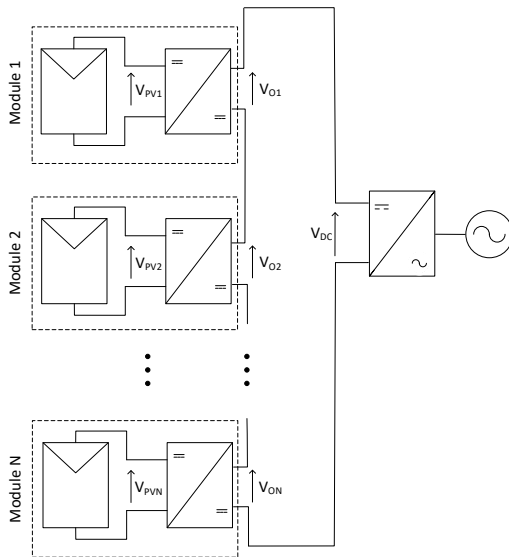
A preliminary study in chapter 8 analyses the characteristic P-V curves of CMPPT and boost-based DMPPT systems under different operating conditions and the results are compared in terms of system efficiency and voltage operation. Specific characteristics of the DMPPT system used for the study of the proposed control strategies are provided in chapter 9, such as the adopted DC/DC converter topology and PV panels, the number of elements that compose the system, and the electrical parameters. A detailed analysis of the operation of DMPPT and CMPPT systems is carried out with both simulation and experimental results. Moreover, it analyses the influence of the DC-bus



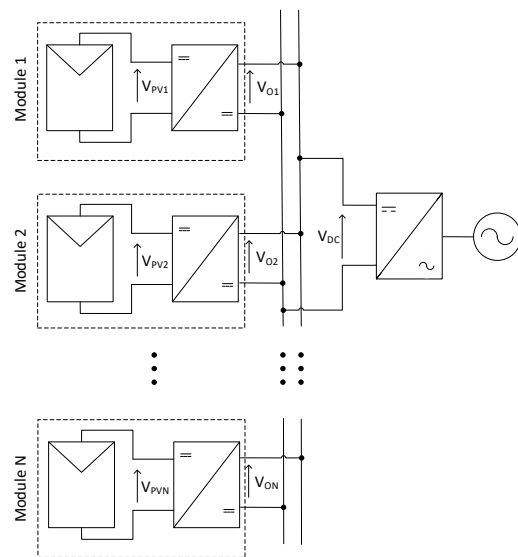
(a) Central MPPT architecture.



(b) Micro-inverters.



(c) DC power optimizer system. Series connection.



(d) DC power optimizer system. Parallel connection.

FIGURE 7.1: Different types of power electronics solutions for PV systems.

voltage on the performance of the distributed converters under homogeneous and non-homogeneous generating conditions. In particular, a control strategy that coordinates both central and distributed MPPT functions is proposed that enhances the overall system efficiency. Chapter 10 is devoted to improving the dynamics of the multi-variable control in DMPPT systems. Chapter 11 introduces the alternative DMPPT system including batteries at module level and proposes some strategies for extending the MPP operating range of the converters. Finally, chapter 12 draws some conclusions and future research lines.

## Chapter 8

# Preliminary study on the viability of distributed MPPT systems

This chapter introduces the DMPPT system. Characteristics of the system are provided, such as the architecture, the adopted DC/DC converter topology and PV panels, together with the electrical parameters. Basic operating principles of the DMPPT system are presented, as well. Averaged models of both DMPPT and CMPPT systems have been developed allowing for fast simulations and the P-V curves are analysed under different atmospheric conditions. Full-day performance of both approaches is analysed using different irradiance profiles under different shading and non-shading conditions. The results are compared in terms of energy exploitation, system efficiency and operating voltage. The matching of the DMPPT approach with the DC-bus voltage is also addressed.

### 8.1 Converter topologies for DMPPT architectures

Authors in [58] analyse four different non-isolated DC/DC converters as possible candidates for DMPPT applications: the buck, the boost, the Cúk and the buck-boost converter. After a thorough comparison, it concluded that although the buck-boost and Cúk converters are more flexible in voltage ranges, they are always at an efficiency and/or cost disadvantage. The most efficient topologies are found to be the buck and the boost. The boost converter is best if a significant voltage step up is required, such as with a low number of panels, while the buck is best suited for long strings.

Under certain mismatch conditions between PV panels, a boost converter string cannot always deliver all the power. If the DC-bus current ( $I_{DC}$ ) is higher than the maximum

PV current of a certain panel, the converter is not able to perform the boosting operation. A buck converter string is able to deliver all the power under any generation condition, but a larger number of panels is required to reach the same DC-bus voltage ( $V_{DC}$ ). This increments costs and complexity to the system. Buck converters optimally work in systems with a few PV panels experiencing shade. By installing the buck converters only in those panels affected by a lower irradiance, they can process the generated power that otherwise would not be recovered [69].

In [59] buck-boost and boost converters operation is analysed under different irradiance and temperature conditions, adopting devices with the same voltage and current ratings. Authors identify feasible MPP operating regions of the whole PV system, showing that boost converters are characterized by having larger MPP operating regions, thus the MPP operation of the boost converters occurs more frequently compared to the buck-boost case. Besides, buck-boost converters normally involve additional components and higher voltage stress [75].

The aforementioned considerations suggest that the boost converter is best suited in DMPPT systems equipped with one DC/DC converter per PV panel, taking into account the efficiency in the power stage, voltage and current stress of components and cost [62].

## 8.2 MPPT control algorithms in PV systems

Amongst several MPPT techniques the following stand out: perturb & observe (P&O) and incremental conductance (INC), both considered part of the hill-climbing control family. In fact, INC is a method derived from the P&O technique in which the type of perturbation differs from the P&O approach. Authors in [76] discuss the implementation of four different algorithms, indicating that P&O and INC are the best algorithms for DC/DC converters in DMPPT systems, considering that the control is individually implemented in each converter.

Fig. 8.1 shows the principle of the P&O control algorithm. It perturbs the PV voltage and compares the resulting PV power with the one prior to the perturbation. If the PV power increases, the perturbation direction is the right one and the operating point moves towards the MPP. If the PV power decreases, the perturbation direction is wrong and the next perturbation will have an opposite sign.

The INC method (Fig. 8.2) searches the MPP in a similar way to the P&O method. As explained in [77], this method is based on the fact that at MPP the PV power slope is equal to zero ( $dP/dV = 0$ ). At this operating point, the conductance is equal to the incremental conductance, represented by  $\frac{\Delta i}{\Delta v} = -\frac{i}{v}$  and the system stops perturbing the

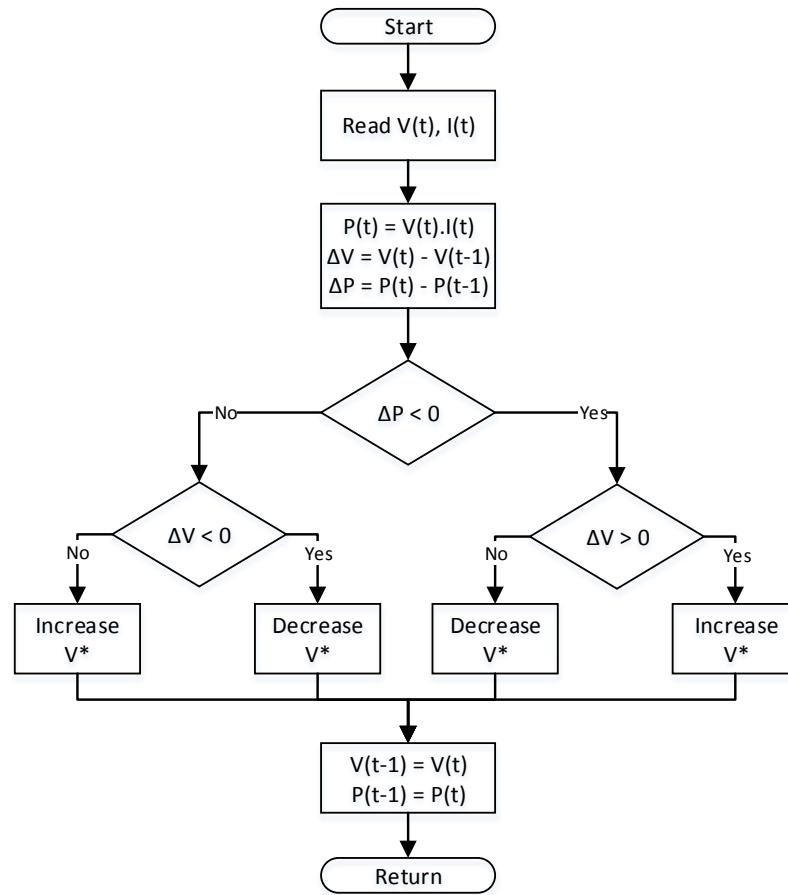


FIGURE 8.1: Conventional P&amp;O control algorithm principle.

operating point. The power slope is positive in the left and negative in the right of the MPP of the characteristic P-V curve represented by  $\frac{\Delta i}{\Delta v} > \frac{i}{v}$  and  $\frac{\Delta i}{\Delta v} < \frac{i}{v}$  respectively.

The main advantage of the P&O technique is its ease of implementation. Previous knowledge of the PV panel characteristics is not required and it generally exhibits good performance if the irradiation does not vary too quickly [78]. The major drawback of this continuous MPP tracking is that in steady-state conditions the operating point oscillates around its maximum and it causes power losses. In addition, the P&O method shows poor efficiency at low irradiation conditions and erratic behaviour under fast changing atmospheric conditions. This may result in incorrect MPPT performed in opposite direction to the MPP [78]. Moreover, the latter circumstance can deceive the P&O algorithm and implement the tracking in the wrong direction [79–81].

INC method is capable of tracking the MPP more precisely in highly variable weather conditions [82], and the operating point moves less around the MPP, even for optimized P&O methods [83]. It presents very good transient performances when subjected to

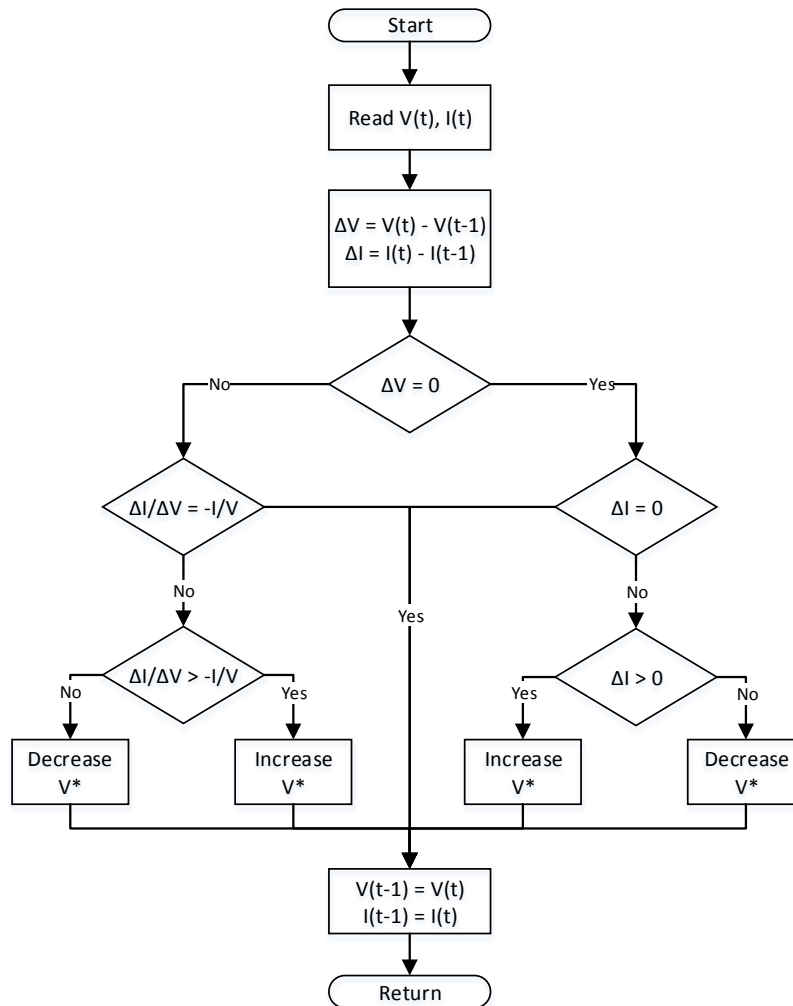


FIGURE 8.2: Flowchart of the INC control algorithm.

rapidly changing atmospheric conditions. However, possible output instabilities may appear due to the use of a derivative algorithm. Another disadvantage is that under low irradiance levels it is hard to carry out the differentiation process and the results are unsatisfactory [82]. Although INC is often claimed as a more accurate MPPT method, it causes more severe thermal stresses compared to P&O [84]. For a sharp irradiance change, the turn-on switching losses showed to be higher when INC method is selected rather than P&O. According to the authors in [84], duty cycle changes during INC operation are more drastic and the current shows a more oscillatory behaviour during each cycle compared to P&O algorithm. In addition, the adoption of INC compared to P&O shows higher power loss profile at high irradiance levels.



TABLE 8.1: Characteristic parameters of the BenQ GreenTriplex PM245P00 260Wp.

Electrical characteristics	Value @ STC <sup>1</sup>
Short-circuit current $I_{SC}$	8.83 [A]
Open-circuit voltage $V_{OC}$	37.7 [V]
MPP current $I_{MPP}$	8.34 [A]
MPP voltage $V_{MPP}$	31.2 [V]
Temperature coefficient of $I_{SC}$ ( $\alpha_I$ )	0.065 [%/°C]
Temperature coefficient of $V_{OC}$ ( $\alpha_V$ )	-80 [mV/°C]

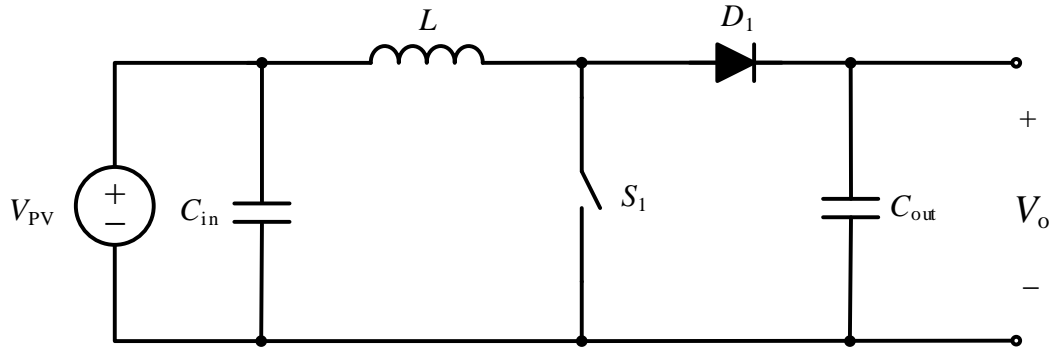


FIGURE 8.3: PV module subsystem formed by a PV source and a DC/DC boost converter.

### 8.3 System description and basic operation

The PV system adopts the DMPPT architecture in Chapter 7 Fig. 7.1(c). Each DC/DC converter undertakes the MPPT of a single PV panel. The subsystem formed by a PV panel and its DC/DC converter will hereinafter be referred to as *module*. BenQ Green-Triplex PM245P00 260Wp poly-crystalline PV panels are considered in the different stages of this study, in simulations and experimental analysis. The characteristics of the PV panel at standard test conditions (STC) are gathered in Table 8.1.

#### 8.3.1 DC/DC boost converter

The non-isolated DC/DC boost converter topology (Fig. 8.3) is used in this study. The converter is analysed in continuous conduction mode (CCM). Considering ideal components, the output voltage ( $V_o$ ) of the boost converter is defined by:

$$V_o = \frac{1}{1-D} V_{in} \quad (8.1)$$

<sup>1</sup>STC: standard test conditions,  $G=1000\text{W}/\text{m}^2$ ,  $T_{amb} = 25^\circ\text{C}$ , Air Mass 1.5 spectral distribution

where  $V_{\text{in}}$  is the input voltage and  $D$  is the duty cycle, given as a reference by the control algorithm implemented in the controller of the converter. The voltage gain of the boost converter is defined by:

$$k = \frac{V_o}{V_{\text{in}}} = \frac{1}{1 - D} \quad (8.2)$$

The converter will perform the correct tracking of the PV panel MPP as long as  $k$  is between its maximum and minimum values:

$$k_{\text{min}} < k < k_{\text{max}} \quad (8.3)$$

Ideally,  $D$  operates in the range  $[0,1]$ , so the output voltage  $V_o$  is equal to or higher than the input voltage  $V_{\text{in}}$ . In practice, the maximum duty cycle ( $D_{\text{max}}$ ) is given by the maximum voltage gain limitation  $k_{\text{max}}$ :

$$D_{\text{max}} = 1 - \frac{1}{k_{\text{max}}} = 1 - \frac{V_{\text{in}}}{V_{o,\text{max}}} \quad (8.4)$$

In boost converters, the value of  $k_{\text{max}}$  is normally influenced by the finite ratings of the switch  $S_1$  in parallel to the output terminals of the converter:

$$V_{\text{off}} < V_{\text{ds,max}} \quad (8.5)$$

$$I_{\text{on}} < I_{\text{ds,max}} \quad (8.6)$$

where  $V_{\text{ds,max}}$  is the maximum allowed source to drain voltage of the switch,  $V_{\text{off}}$  the voltage across the switch in OFF state,  $I_{\text{ds,max}}$  the maximum allowed current in the switch and  $I_{\text{on}}$  the peak current in ON state.

### 8.3.2 Basic operation

The inverter, controlling the DC bus voltage ( $V_{\text{DC}}$ ), requires a minimum voltage on its DC side to work properly. To this end, the output of the modules are connected in series, forming a string of  $N$  modules. The number of modules will depend on the input power and voltage ratings of the inverter. In a general form,  $V_{\text{DC}}$  is the addition of the output voltages:

$$V_{DC} = \sum_{i=1}^N V_{oi} \quad (8.7)$$

The output voltage of the  $i$ -th module ( $V_{oi}$ ) is proportional with the output power of that module ( $P_{oi}$ ) for a given total power generated in its string ( $P_{DC}$ ):

$$V_{oi} = \frac{P_{oi}}{P_{DC}} V_{DC} \quad (8.8)$$

The input current in boost converters needs to be greater than the output current, otherwise control over them is lost. In this case the input current is the PV current, and the output current is controlled by the inverter. The system is able to keep all the PV panels operating at their MPP, as long as the MPP current of each PV panel is high enough.

To exemplify, let's consider the system of  $N$  modules operating under mismatch conditions. The mismatch condition is represented by the shading parameter  $Sh$ . A first group of  $N_H$  PV panels is subjected to a high irradiance ( $G_H$ ). A second group of  $N_L$  PV panels operate at low irradiance level ( $G_L$ ), affected by  $Sh$ . For simplicity, a 100% efficiency is considered in the converters, and all PV panels are considered to be working at their MPP. Assuming that the shading of each PV panel only affects to its current capability and that the voltage remains unchanged,  $Sh=0$  stands for completely shaded and  $Sh=1$  for no shading. The PV current for each panel under  $G_L$  ( $I_{PV,L}$ ), is given by  $I_{PV,L}=I_{MPP}Sh_L$ , and the related PV power is:

$$P_{PV,L} = V_{MPP}I_{MPP}Sh_L = V_{o,L}I_{DC} \quad (8.9)$$

where  $V_{MPP}$  and  $I_{MPP}$  are the MPP PV voltage and current @ STC, respectively. The DC-bus current  $I_{DC}$ , controlled by the inverter, will be the total power over the DC-bus voltage:

$$I_{DC} = \frac{\sum_{i=1}^N P_i}{V_{DC}} = \frac{N_H P_{MPP} + N_L V_{MPP} I_{MPP} Sh_L}{V_{DC}} \quad (8.10)$$

Since the limit to keep control of the power conversion in the converters with lower power is  $I_{DC}=I_{MPP}Sh_L$ , substituting this value in (8.10), yields:

$$I_{DC} = I_{MPP}Sh_L = \frac{(N - N_L) P_{MPP}}{V_{DC} - N_L V_{MPP}} \quad (8.11)$$

which highly depends on  $V_{DC}$ . For a system of  $N=6$  modules with  $N_L=3$  and  $N_H=3$  configuration and two DC bus voltage values arbitrarily chosen, the maximum DC current is calculated:

- $I_{DC}=3.78$  A or  $Sh_L=0.45$  @  $V_{DC}=300$ V
- $I_{DC}=2.93$  A or  $Sh_L=0.35$  @  $V_{DC}=360$ V

meaning that, at  $I_{DC}=I_{MPP}Sh_L$  the group of  $N_L$  panels receive 45% and 35% of irradiance at 300V and 360V, respectively, when compared to  $N_H$  panels. If the irradiance level goes under  $Sh_L$  in any of the  $N_L$  panels, the corresponding converters will not perform the MPPT. In such case,  $I_{DC}$  will be equal to the  $I_{MPP}$  of the PV panel illuminated by the lowest irradiance level.

The selection of the optimal value of  $V_{DC}$  in a DMPPT system depends on several factors. Indeed, the number of series-connected modules, the generation mismatch between PV panels, as well as the physical voltage and current ratings of the DC/DC converters' components strongly influence the DC bus voltage level that allows each converter to work on its MPP. Depending on the mismatch level, the extraction of all the available power is not always achievable and bypassing the modules processing the lowest power in the string might be necessary, in order to maximize the overall PV generation.  $V_{DC}$  plays an important role in this matter and it is one of the subjects of study in this manuscript.

### 8.3.3 Efficiencies in photovoltaic systems

PV systems can be evaluated in terms of the efficiency at the different stages of the conversion process. In this section, the efficiencies taken into account for the evaluation of the system are defined.

#### 8.3.3.1 Maximum Power Point Tracking efficiency

The MPPT efficiency evaluates the power losses due to the continuous MPP tracking. It is classified in either static or dynamic MPPT efficiency [42]. The static MPPT efficiency is the ability to track the MPP at constant irradiance and ambient temperature. The dynamic MPPT efficiency takes into account the ability to track the MPP in case of variable conditions. The MPPT is calculated as follows:

$$\eta_{MPPT} = \frac{\int_0^T V_{PV}(t)I_{PV}(t)dt}{\int_0^T P_{MPP}(t)dt} \quad (8.12)$$

where  $V_{PV}(t)$  and  $I_{PV}(t)$  are the instantaneous PV voltage and current,  $P_{MPP}(t)$  is the maximum available power and  $T$  is the considered period of operation. In static conditions,  $\eta_{MPPT}$  is averaged for the steady state period  $T$  where the MPPT is continuously tracking the MPP and no other variations perturb the MPP operation.

A trapezoidal irradiance profile is normally used to evaluate the dynamic MPPT [42]. In the dynamic test,  $T$  is equivalent to the dynamic test period.

### 8.3.3.2 Converter efficiency

The converter efficiency is the ratio between the output power ( $P_O$ ) and input power ( $P_{IN}$ ) of the converter. In this case,  $P_{IN}$  corresponds to the power coming from the PV source ( $P_{PV}$ ):

$$\eta_{conv} = \frac{P_O}{P_{PV}} \quad (8.13)$$

### 8.3.3.3 CMPPT and DMPPT efficiency

These efficiencies are the ratio between the target power and the maximum available power for each approach under mismatch conditions and are given at string level.

$$\eta_{xMPPT} = \frac{P_{DC}}{P_{available}} \quad (8.14)$$

### 8.3.3.4 Inverter efficiency

The inverter efficiency is determined by comparing its output power to its input power. Thus, it considers the DC/AC conversion losses and it is given by:

$$\eta_{inv} = \frac{P_{AC}}{P_{DC}} \quad (8.15)$$

### 8.3.3.5 Total efficiency

The total efficiency of a system or the overall efficiency takes into account the conversion losses for each conversion stage:  $\eta_{xMPPT}$  (includes  $\eta_{MPPT}$  from (8.12)),  $\eta_{conv}$ ,  $\eta_{inv}$  and yields:

TABLE 8.2: Simulation parameters for the switching model

Converter parameters	Value	Simulation parameters	Value
Inductance $L$	450 [ $\mu\text{H}$ ]	Switching frequency $f_{\text{SW}}$	25 [kHz]
Input capacitance $C_{\text{in}}$	100 [ $\mu\text{F}$ ]	Input voltage range $V_{\text{in}}$	0-38 [V]
Output capacitance $C_{\text{out}}$	1 [mF]	Input current range $I_{\text{in}}$	0-9 [A]
Max. source-to-drain voltage $V_{\text{ds,max}}$	100 [V]	Output load $R_{\text{L}}$	33 [ $\Omega$ ]
Capacitor ESR <sup>2</sup>	1 [m $\Omega$ ]	PV voltage step $\Delta V_{\text{PV}}$	0.01 [V]
MOSFET resistance $R_{\text{on}}$	0.1 [ $\Omega$ ]	Diode resistance $R_{\text{on}}$	1 [m $\Omega$ ]
MOSFET int. diode resistance $R_{\text{d}}$	0.01 [ $\Omega$ ]	Diode forward voltage $V_{\text{f}}$	0.8 [V]

$$\eta_{\text{Total}} = \eta_{\text{MPPT}} \cdot \eta_{\text{conv}} \cdot \eta_{\text{inv}} \quad (8.16)$$

Depending on the application,  $P_{\text{DC}}$  is equivalent to  $P_{\text{O}}$  or the sum of several  $P_{\text{O}}$ s or  $P_{\text{PVs}}$ .

## 8.4 Averaged models

Averaged models reproducing the characteristics of DMPPT and CMPPT systems are developed in the MATLAB-Simulink environment. Each model considers ideal atmospheric conditions accounting for irradiance variations, but keeping ambient and cell temperatures constant. Each model contains  $N=6$  PV panels BenQ GreenTriplex PM245P00 260Wp (see Table 8.1). In the DMPPT model six boost DC/DC converters are dedicated to individually control each PV panel, while the CMPPT one implements a single scaled-up DC/DC converter accounting for the control of the whole PV string. The parameters of the PV panels are used as input to the PV Array block provided within the Simscape Power Systems library, consisting of a single-diode model.

The averaged models consider 1-D lookup tables (LUT) that contain the efficiency curve of the DC/DC converter as a function of the input power. This efficiency curve has been computed in a first simulation using a single-panel single-converter switching model. The switching model adopts the simplified non-isolated boost converter (Fig. 8.4). Characteristic parameters of the converter and additional simulation parameters are specified in Table 8.2.

The converter in the switching model implements a conventional P&O control algorithm in order to track the PV power, described in Fig. 8.1. The full irradiance range from  $G=0\text{W}/\text{m}^2$  to  $G=1000\text{W}/\text{m}^2$  is applied to the converter, implementing increasing steps of  $\Delta G=50\text{W}/\text{m}^2$ . Fig 8.5 shows the PV and output voltages ( $V_{\text{PV}}$  and  $V_{\text{O}}$ ) and powers

<sup>2</sup>ESR: Equivalent series resistance.

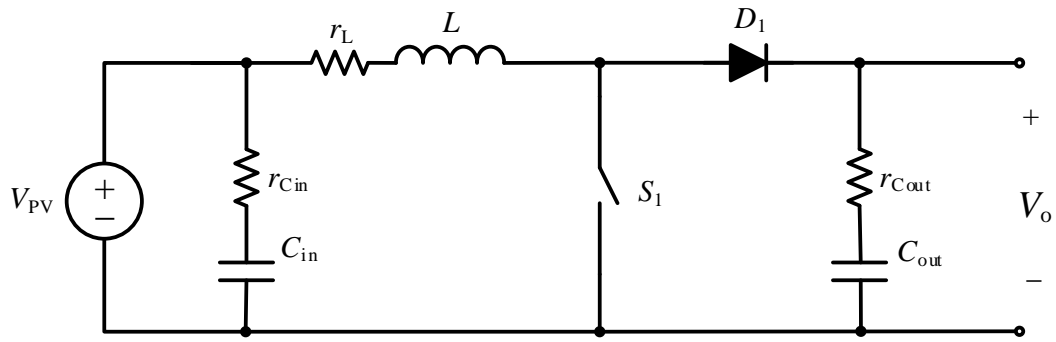


FIGURE 8.4: DC/DC boost converter considered in the switching model.

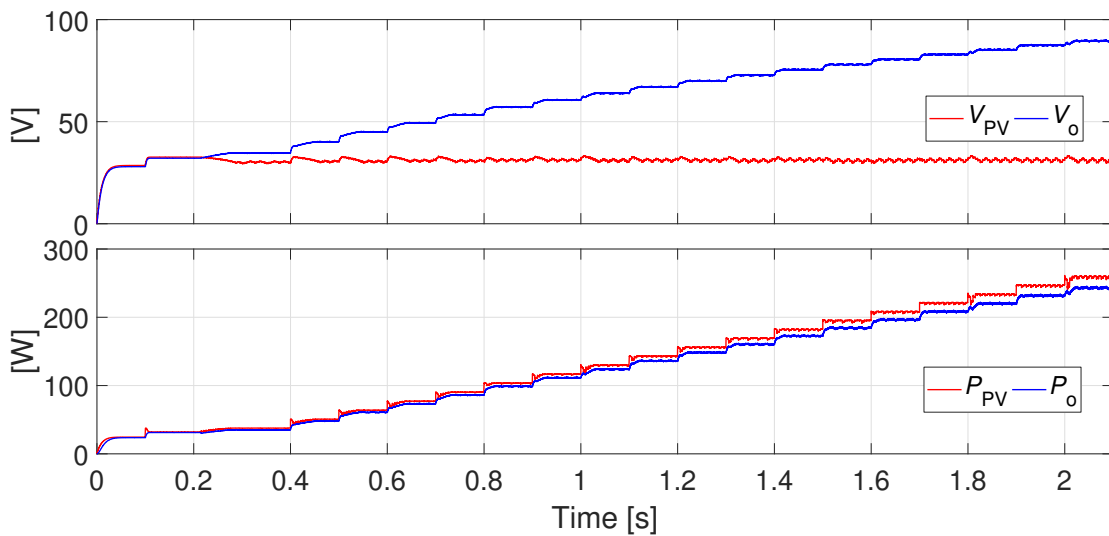


FIGURE 8.5: Simulation results of the input and output voltage and powers used for characterizing the efficiency curve of the converter.

( $P_{PV}$  and  $P_o$ ) for the efficiency test. The MPP for each irradiance level is considered to calculate the efficiency curve (Fig. 8.6). This method accurately models the characteristics necessary for calculating total energy harvest, including input and output voltage limits, current limits, and conversion efficiency. The switching model and the code developed in the Matlab-Simulink environment can be found in Appendix B.

The central MPPT system architecture is represented in chapter 7, Fig. 7.1(a). The PV panels are connected in series to the input of a grid-connected inverter. The analysis is realised at the input of this inverter that is modelled with a 2-D LUT and takes into account the efficiency and the operating voltage, with typical inverter efficiency curves above 96% [85]. The conversion efficiency and the energy delivered into the grid will depend on the selected inverter. This inverter tracks the power of the entire PV string. Output voltages and currents for each PV panel are computed and next summed, giving the total PV power of the string.

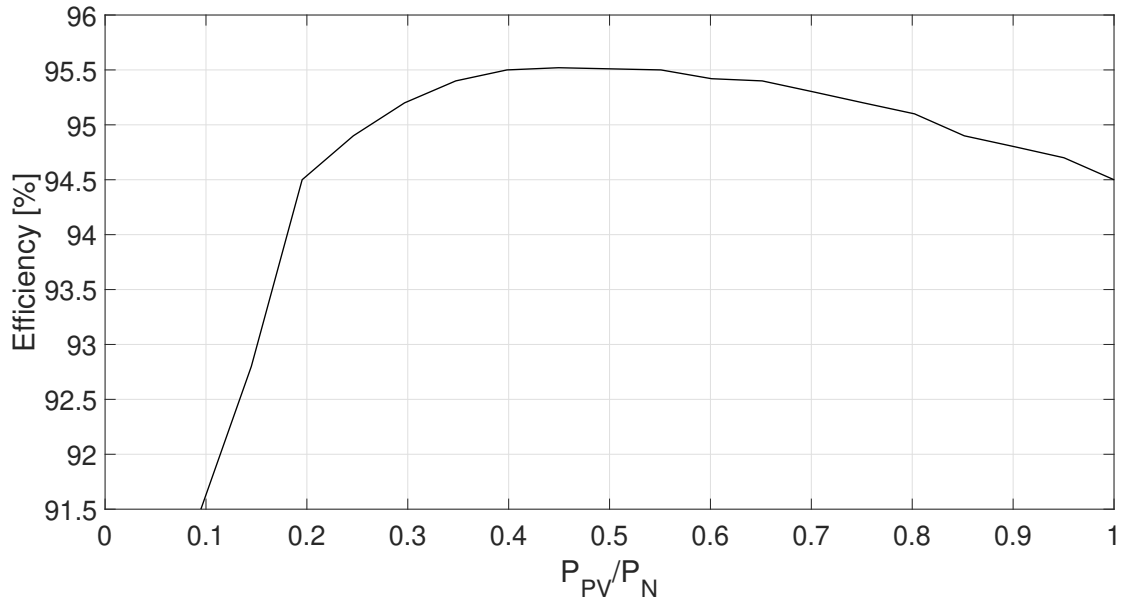


FIGURE 8.6: Efficiency (%) vs. normalized input power (p.u.) curve of the DC/DC converter adopted in the model.

The distributed MPPT system architecture is represented in chapter 7, Fig. 7.1(c). Each PV panel is controlled by a dedicated DC/DC converter performing individual P&O MPPT. Each PV power inputs one 1-D LUT that provides the output power. Each output power is divided by the DC current to get the corresponding output voltage. This voltage is fed into a controlled voltage source to simulate the behaviour of the series-connected DC/DC converters. Both, CMPPT and DMPPT models can be found in Appendix B.

## 8.5 CMPPT and DMPPT power vs. voltage curves

The characteristic CMPPT and DMPPT P-V curves under different irradiance conditions are simulated using the models described in section 8.4. The irradiance mismatch determines the  $V_{DC}$  belonging to the maximum performance of the CMPPT and DMPPT systems. The CMPPT P-V curve shows different MPPs belonging to the different irradiance levels: Global MPP (GMPP) provides the maximum performance in the system and LMPPs bring lower MPPs. The DMPPT P-V curve is characterized by maximum power regions (MPR). Similar to the MPPs in the PV string, MPRs can be classified in two types: Global MPR (GMPP) belonging to the maximum performance region in the string and local MPR (LMPP) that corresponds to lower power regions.

In this section, the combination of PV panels under different irradiance illustrates the influence of  $V_{DC}$  in the PV operation. Moreover, the matching of the  $V_{DC}$  operating point



and the input voltage range of the inverter ( $R_{\text{inv}}$ ) is studied.  $R_{\text{inv}}$  plays an important role in the performance of the system, as it establishes the  $V_{\text{DC}}$  operating range.

### 8.5.1 DMPPT $V_{\text{DC}}$ operating range

The static analysis conducted in [61] allows to define a  $V_{\text{DC}}$  range where all the converters track each PV panel's MPP. Assuming that all PV panels' MPP voltage ( $V_{\text{MPP}}$ ) is the same under any irradiance condition,  $V_{\text{DC}}$  can be expressed as:

$$V_{\text{DC}} = kV_{\text{MPP}} \sum_{i=1}^N \alpha_i. \quad (8.17)$$

where  $\alpha_i$  is the  $\alpha$  affecting the  $i$ -th PV panel.  $\alpha$  is a number ranging from 0 to 1 proportional to the irradiance level.  $k$  is the voltage conversion ratio of the converter associated to the most illuminated PV panel in the string ( $\alpha=1$ ). The amplitude and position of the optimal  $V_{\text{DC}}$  range is provided by the maximum and minimum voltage values that let all the PV panels work at their MPP [61]:

$$V_{\text{DC,max}} = k_{\text{max}}V_{\text{MPP}} \sum_{i=1}^N \alpha_i. \quad (8.18)$$

$$V_{\text{DC,min}} = \frac{k_{\text{min}}}{\alpha_{\text{low}}}V_{\text{MPP}} \sum_{i=1}^N \alpha_i. \quad (8.19)$$

where the maximum and minimum values of  $V_{\text{DC}}$  allowing for the MPP operation of all the PV panels is reached at  $k=k_{\text{max}}$  and  $k=k_{\text{min}}/\alpha_{\text{low}}$ , respectively.  $\alpha_{\text{low}}$  represents the lowest  $\alpha_i$  in the string. For boost-type converters,  $k_{\text{min}}$  is equal to 1 and  $k_{\text{max}}$  will depend on the desired maximum output voltage ( $V_{\text{o,max}}$ ). In this case, it is set to  $V_{\text{o,max}}=80\text{V}<V_{\text{ds,max}}$  (Table 8.2). This preliminary study assumes that each converter includes the necessary protections to be consistent with this limit.

According to [61], the maximum avoidable mismatch problem corresponds to:

$$\alpha_{\text{min}} = \frac{k_{\text{min}}}{k_{\text{max}}}. \quad (8.20)$$

Therefore, if  $\alpha_{\text{low}}$  in (8.19) is lower than  $\alpha_{\text{min}}$ ,  $V_{\text{DC,min}}>V_{\text{DC,max}}$ . In this work, this is considered as an unavoidable mismatch, meaning that there is no  $V_{\text{DC}}$  able to extract all the available power in the string.

The combination of PV panels under a high irradiance level ( $G_H=1000\text{W/m}^2$ ) and three different low irradiance levels ( $G_L=800\text{W/m}^2$ ,  $G_L=500\text{W/m}^2$  and  $G_L=200\text{W/m}^2$ ) is used to show the dependency of GMPR  $V_{DC}$  to the irradiance mismatch. The different  $G_L$ s are imposed from  $N_L=1$  to  $N_L=6$  PV panels. Table 8.3 gathers  $V_{DC,\max}$  and  $V_{DC,\min}$ , calculated using (8.18) and (8.19), respectively.  $V_{DC,\max}=480\text{V}$  and  $V_{DC,\min}=187.2\text{V}$  if all the PV panels are illuminated at  $G_H$ .  $V_{DC,\max}>V_{DC,\min}$  for any PV configuration under  $G_L=500\text{W/m}^2$  and  $G_L=800\text{W/m}^2$ . On the contrary, for the mismatch case  $G_H$  and  $G_L=200\text{W/m}^2$ ,  $V_{DC,\min}>V_{DC,\max}$  and the mismatch is unavoidable using  $V_{DC}$  regulation. If  $V_{DC}=V_{DC,\max}$ , the converters of the  $G_L$  PV panels stop performing the MPPT. Conversely, if  $V_{DC}=V_{DC,\min}$  the converters of the  $G_H$  PV panels will reach dangerous voltage levels above the ratings of the MOSFET and some of the components could be damaged.

### 8.5.1.1 $V_{DC}$ in case of unavoidable mismatch

The analysis about the best  $V_{DC}$  operating level in case of unavoidable mismatch requires a different approach. Both GMPR and LMPR have to be re-evaluated taking into account the different combination of  $G_H$  and  $G_L$  PV panels. Indeed, at the GMPR, the  $V_{DC}$  range is defined between  $V_{DC,\min}^{\text{GMPR}}$  and  $V_{DC,\max}^{\text{GMPR}}$ :

$$V_{DC,\max}^{\text{GMPR}} = N_H V_{o,\max} \quad (8.21)$$

$$V_{DC,\min}^{\text{GMPR}} = N_H V_{\text{MPP}} \quad (8.22)$$

where  $V_{o,\max}=k_{\max}V_{\text{MPP}}$  as in (8.18). The LMPP that can be observed at the LMPR corresponds to a  $V_{DC}$  of:

$$V_{DC}^{\text{LMPP}} = N_H V_{o,\max} + N_L V_{\text{MPP}}^{\text{LMPP}}. \quad (8.23)$$

where  $V_{\text{MPP}}^{\text{LMPP}}=V_{\text{MPP}}$  at  $G_L$ . Therefore, for any PV configuration at  $G_H$  and  $G_L=200\text{W/m}^2$ , the GMPR  $V_{DC}$  is calculated using (8.21) and (8.22) (Table 8.4). Above the maximum voltage value in GMPR and up to  $NV_{o,\max}$ ,  $V_{DC}$  corresponds to the LMPR, with the LMPP voltage  $V_{DC}^{\text{LMPP}}$  characterized by the sum of all the maximum output voltages of the operational converters and the MPP voltages of the  $G_L$  PV panels.

### 8.5.2 Maximum performance: GMPP and GMPR

Fig. 8.7 shows the P-V curves of CMPPT and DMPPT systems for  $G_H$  and  $G_L=200\text{W/m}^2$ ,  $G_H$  and  $G_L=500\text{W/m}^2$ ,  $G_H$  and  $G_L=800\text{W/m}^2$ . The results are grouped with reference

TABLE 8.3: DMPPT DC voltage ranges (in V) for different mismatch conditions ensuring the MPP operation of all the PV panels in the string.  $G_H=1000\text{W}/\text{m}^2$ .

PV config.		$G_L=800\text{W}/\text{m}^2$		$G_L=500\text{W}/\text{m}^2$		$G_L=200\text{W}/\text{m}^2$	
$N_L$	$N_H$	$V_{\text{DC,min}}$	$V_{\text{DC,max}}$	$V_{\text{DC,min}}$	$V_{\text{DC,max}}$	$V_{\text{DC,min}}$	$V_{\text{DC,max}}$
1	5	226.2	464	343.2	440	811.2	416
2	4	218.4	448	312.0	400	686.4	352
3	3	210.6	432	280.8	360	561.6	288
4	2	202.8	416	249.6	320	436.8	224
5	1	195.0	400	218.4	280	312.0	160
6	0	185.4	480	180.4	480	171.3	480

TABLE 8.4: DMPPT DC voltage ranges (in V) at  $G_H=1000\text{W}/\text{m}^2$ ,  $G_L=200\text{W}/\text{m}^2$  for different power levels.

PV config.		GMPP		LMPP
$N_L$	$N_H$	$V_{\text{DC,min}}$	$V_{\text{DC,max}}$	$V_{\text{DC}}^{\text{LMPP}}$
1	5	156	400	428.5
2	4	124.8	320	377.1
3	3	93.6	240	325.65
4	2	62.4	160	274.2
5	1	31.2	80	222.75
6	0	171.3	480	-

to the mismatch level, so the different combinations of mismatched panels are superimposed. Additional results for other combinations of  $G_H$  and  $G_L$  can be found in Appendix B. Solid lines represent the P-V curves of the string of PV panels, showing one GMPP and one LMPP. Dashed lines correspond to the P-V curves of the string of converters, characterized by one GMPP and one LMP.

Table 8.5 and Table 8.6 compare both DMPPT and CMPPT systems' maximum performance and efficiencies, respectively. At no mismatch conditions, a CMPPT efficiency of  $\eta_{\text{CMPPT}}=100\%$  is obtained. The DMPPT efficiency, affected by the power losses in the converters, is  $\eta_{\text{DMPPT}}=94.55\%$ . The maximum CMPPT and DMPPT powers for all the 6 PV panels at  $G_H$  are  $P_{\text{CMPPT}}=1561.3\text{ W}$  and  $P_{\text{DMPPT}}=1476.0\text{ W}$ , respectively.

For any PV configuration at  $G_H$ ,  $G_L=800\text{W}/\text{m}^2$  and  $G_H$ ,  $G_L=500\text{W}/\text{m}^2$ , the DMPPT approach performs better than CMPPT. In the CMPPT system, due to the series connection of the PV panels,  $G_L$  PV panels affect the operating point of the  $G_H$  PV panels and oblige them to move away from their MPP, negatively impacting on its performance.

TABLE 8.5: Maximum performance (in W) of CMPPT and DMPPT systems at different mismatch conditions.  $G_H=1000\text{W}/\text{m}^2$ .

PV config.		$G_L=800\text{W}/\text{m}^2$		$G_L=500\text{W}/\text{m}^2$		$G_L=200\text{W}/\text{m}^2$	
$N_L$	$N_H$	$P_{\text{DMPPT}}$	$P_{\text{CMPPT}}$	$P_{\text{DMPPT}}$	$P_{\text{CMPPT}}$	$P_{\text{DMPPT}}$	$P_{\text{CMPPT}}$
1	5	1433.0	1375.8	1356.0	1301.1	1231.0	1301.1
2	4	1387.0	1338.7	1234.0	1040.9	984.40	1040.9
3	3	1338.0	1307.6	1112.0	830.33	738.30	780.67
4	2	1290.0	1280.2	983.30	800.98	492.10	520.45
5	1	1241.0	1255.4	866.20	773.91	374.30	297.25
6	0	1173.0	1232.6	715.10	748.69	273.10	282.61

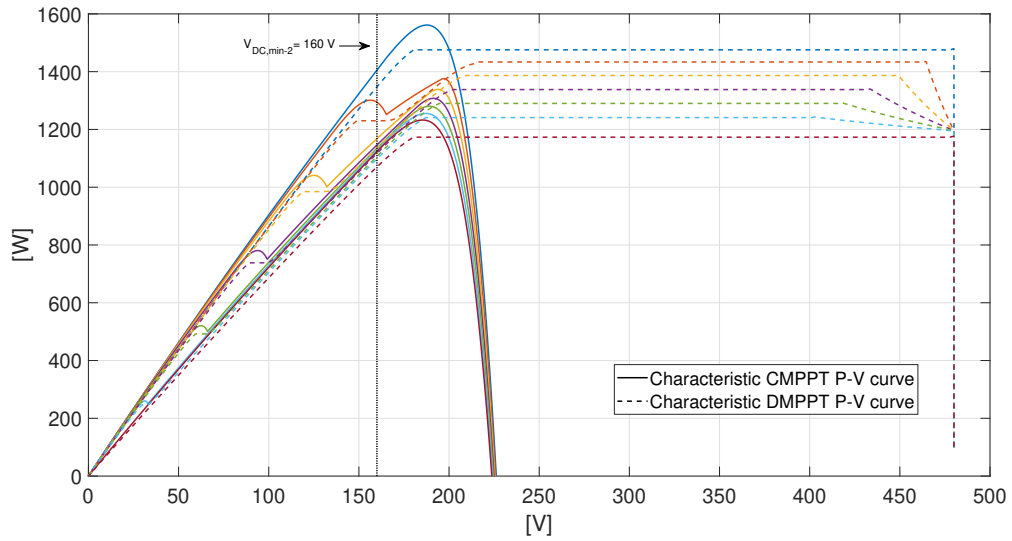
In the DMPPT system, each PV panel operates at its MPP. Note that, at strong irradiance mismatch ( $G_H, G_L=200\text{W}/\text{m}^2$ ), the central solution shows higher efficiencies for almost all the mismatch configurations between PV panels, except for  $N_L=5, N_H=1$ .

Maximum performance is not always possible. The main constraint is given by the  $V_{\text{DC}}$  range allowed by the inverter. If the range is too narrow or the boundaries are not adequate, the maximum performance may be affected. To illustrate this, the characteristics of the Inv-2 are adopted (Chapter 3.3, Table 3.1). Among the single-phase inverters available, Inv-2 has the lowest minimum input voltage requirement at  $V_{\text{DC},\text{min}}=160\text{V}$  and  $R_{\text{inv}}=[160-600]\text{V}$ .

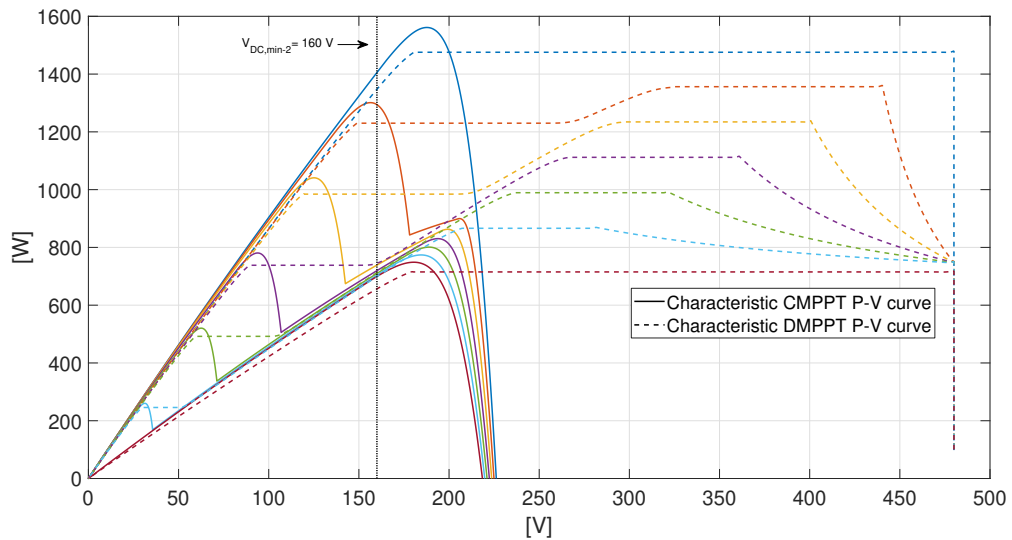
At  $G_H, G_L=800\text{W}/\text{m}^2$ ,  $R_{\text{inv}}$  is compatible with the GMPP and GMPPR for any PV configuration. For the other mismatch conditions the CMPPT system cannot operate at GMPP. For the combination of e.g.  $N_L=2$  and  $N_H=4$  at  $G_H, G_L=500\text{W}/\text{m}^2$ , the CMPPT system can extract a maximum power of  $P_{\text{CMPPT,LMPP}}=862.88\text{W}$  instead of  $P_{\text{CMPPT,GMPP}}=1040.9\text{W}$  (Table 8.5) and the efficiency drops from  $\eta_{\text{CMPPT,GMPP}}=79.99\%$  (Table 8.6) to  $\eta_{\text{CMPPT,LMPP}}=66.31\%$ . The case at  $G_L=200\text{W}/\text{m}^2$  is even more meaningful, in which for the PV configuration of  $N_L=1$  and  $N_H=5$ , the highest efficiency at GMPP is  $\eta_{\text{CMPPT,GMPP}}=96.51\%$  vs. the one at LMPP  $\eta_{\text{CMPPT,LMPP}}=27.27\%$ .

DMPPT GMPPR is within  $R_{\text{inv}}$  boundaries at  $G_H, G_L=500\text{W}/\text{m}^2$ . At  $G_H, G_L=200\text{W}/\text{m}^2$ , it can only operate at LMPPR for the PV configurations  $N_L=5, N_H=1$  and  $N_L=4, N_H=2$ . For the DMPPT system, the biggest efficiency difference operating at GMPPR and LMPPR is found at  $G_L=200\text{W}/\text{m}^2$  with the PV configuration  $N_L=4$  and  $N_H=2$  ( $\eta_{\text{DMPPT,GMPPR}}=69.42\%$  vs.  $\eta_{\text{DMPPT,LMPPR}}=64.77\%$ ). For the majority of the cases, the efficiency in DMPPT system is kept above 90%.

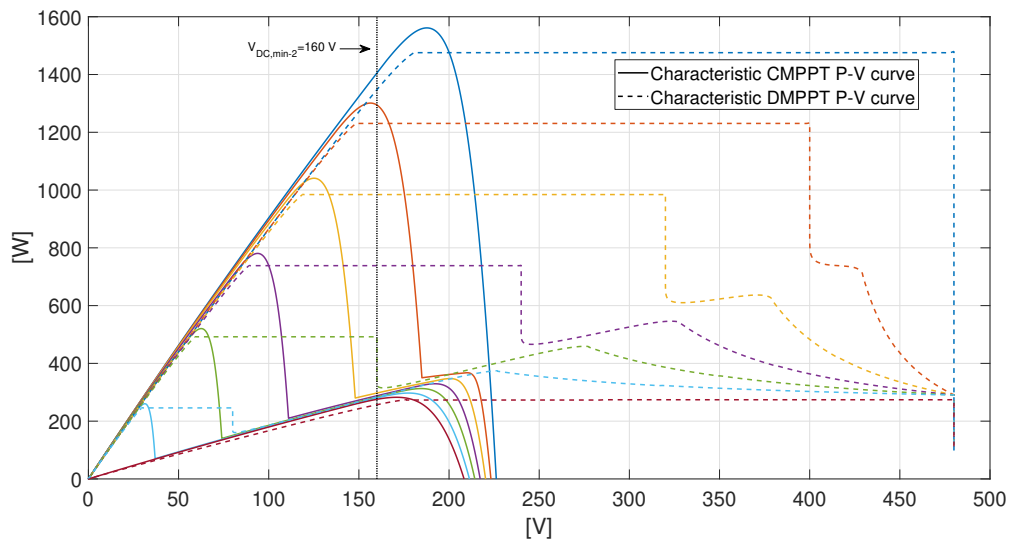
Fig. 8.8 shows two cases with randomly chosen PV mismatch configuration of three different irradiance levels. The matching with the admissible input DC voltage of Inv-2 is



(a)  $N_H$  panels at  $G_H=1000\text{W/m}^2$  and  $N_L$  panels at  $G_L=800\text{W/m}^2$ .



(b)  $N_H$  panels at  $G_H=1000\text{W/m}^2$  and  $N_L$  panels at  $G_L=500\text{W/m}^2$ .



(c)  $N_H$  panels at  $G_H=1000\text{W/m}^2$  and  $N_L$  panels at  $G_L=200\text{W/m}^2$ .

FIGURE 8.7: Matching DMPPT and CMPPT P-V curves with  $V_{DC,min-2}=160\text{V}$  of Inv-2 for the different PV panel mismatch configurations:  $N_H=0$  and  $N_L=6$  (deep-red),  $N_H=1$  and  $N_L=5$  (light-blue),  $N_H=2$  and  $N_L=4$  (green),  $N_H=N_L=3$  (purple),  $N_H=4$  and  $N_L=2$  (yellow),  $N_H=5$  and  $N_L=1$  (orange),  $N_H=6$  and  $N_L=0$  (dark-blue).

TABLE 8.6: CMPPT and DMPPT efficiencies (in %) corresponding to the maximum performance.

PV config.		$G_L=800\text{W}/\text{m}^2$		$G_L=500\text{W}/\text{m}^2$		$G_L=200\text{W}/\text{m}^2$	
$N_L$	$N_H$	$\eta_{\text{DMPPT}}$	$\eta_{\text{CMPPT}}$	$\eta_{\text{DMPPT}}$	$\eta_{\text{CMPPT}}$	$\eta_{\text{DMPPT}}$	$\eta_{\text{CMPPT}}$
0	6	94.55	100	94.55	100	94.55	100
1	5	94.95	91.16	94.75	90.92	91.31	96.51
2	4	95.18	91.86	94.84	79.99	86.72	91.7
3	3	95.22	93.05	94.96	70.91	80.08	84.67
4	2	95.34	94.62	95.05	76.96	69.42	73.42
5	1	95.39	96.5	95.11	84.98	70.26	55.8
6	0	95.13	100	95.51	100	95.56	100

also shown. For the first case in Fig. 8.8(a) the CMPPT system is able to operate only at the lowest LMPP, with an efficiency of  $\eta_{\text{CMPPT,LMPP-1}} = 51.8\%$ . In the second case in Fig. 8.8(b), the CMPPT system performs at a LMPP with an efficiency of  $\eta_{\text{CMPPT,LMPP-2}} = 44.66\%$ . The operating voltage range in the DMPPT system allows the maximum performance with an efficiency of  $\eta_{\text{DMPPT,GMPR-1}} = 84.48\%$  and  $\eta_{\text{DMPPT,GMPR-2}} = 80.81\%$ .

## 8.6 CMPPT and DMPPT systems full-day performance

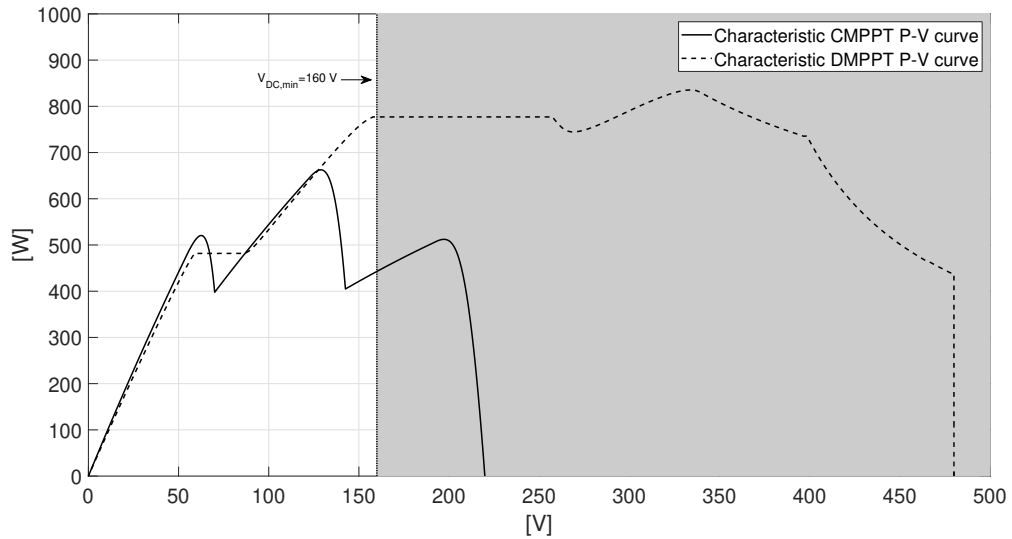
### 8.6.1 Irradiance profiles

Three different irradiance profiles<sup>3</sup> are used as input for the averaged models: a sunny day, a day with scattered clouds and a cloudy day (Fig. 8.9). In addition to the weather-dependent evolution of the irradiance profiles, static shading is applied to some of the PV panels in the simulations.

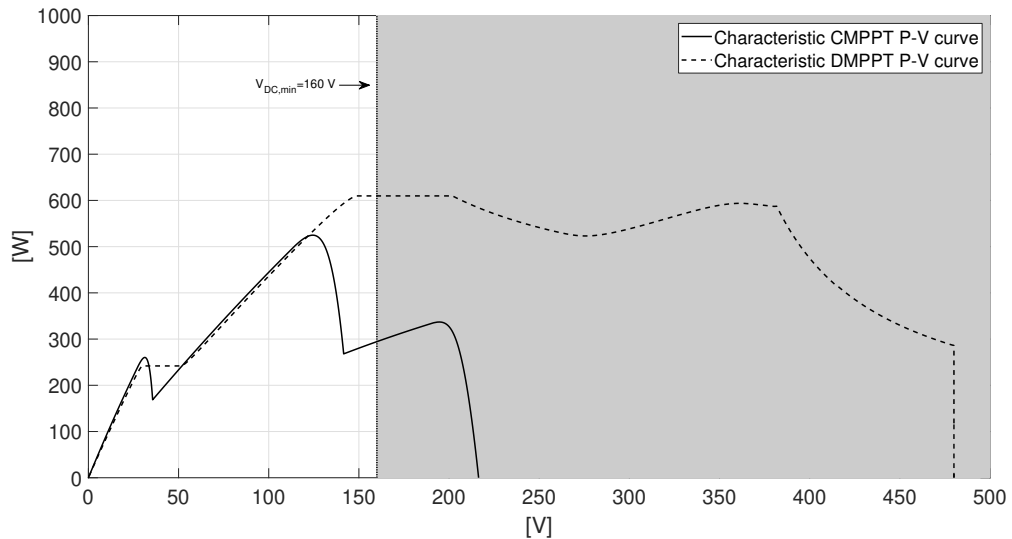
### 8.6.2 Simulation results

Two different scenarios are considered for each irradiance condition: (i) All the six panels operate under non-shaded uniform conditions and (ii) three panels out of six operate under a 50% static shading condition. For the latter scenario, the P-V curve in the CMPPT approach will show two maxima, one corresponding to the MPP voltage for the three unshaded PV panels and the other corresponding to the sum of all the PV voltages with the PV panels operating at the current imposed by the shaded panels (see

<sup>3</sup>Irradiance data provided by GreenWatch SA, taken in Aubange, Belgium on the 03/07/2014 (sunny), 04/09/2015 (mixed) and 29/10/2014 (cloudy)



(a) P-V curve for a mixed combination of mismatch conditions:  $N_H=2$  at  $G_H=1000\text{W}/\text{m}^2$ ,  $N_{L1}=2$  at  $G_L=600\text{W}/\text{m}^2$  and  $N_{L2}=2$  at  $G_L=300\text{W}/\text{m}^2$ .



(b) P-V curve for a mixed combination of mismatch conditions:  $N_H=1$  at  $G_H=1000\text{W}/\text{m}^2$ ,  $N_{L1}=4$  at  $G_L=500\text{W}/\text{m}^2$  and  $N_{L2}=2$  at  $G_L=200\text{W}/\text{m}^2$ .

FIGURE 8.8: Matching of the inverter input voltage with DMPPT and CMPPT P-V curves.

Fig. 8.7(b)). The maximum performance of the system is considered. For the DMPPT approach, a fixed DC bus voltage of  $V_{DC}=300\text{V}$  is imposed allowing all the PV panels to perform at their own MPP.

The results show the global output power during the whole day. For each irradiance profile (sunny, scattered clouds and cloudy) four cases are presented: DMPPT and CMPPT systems, each performing with and without static shading. The energy extracted for each case is computed using:

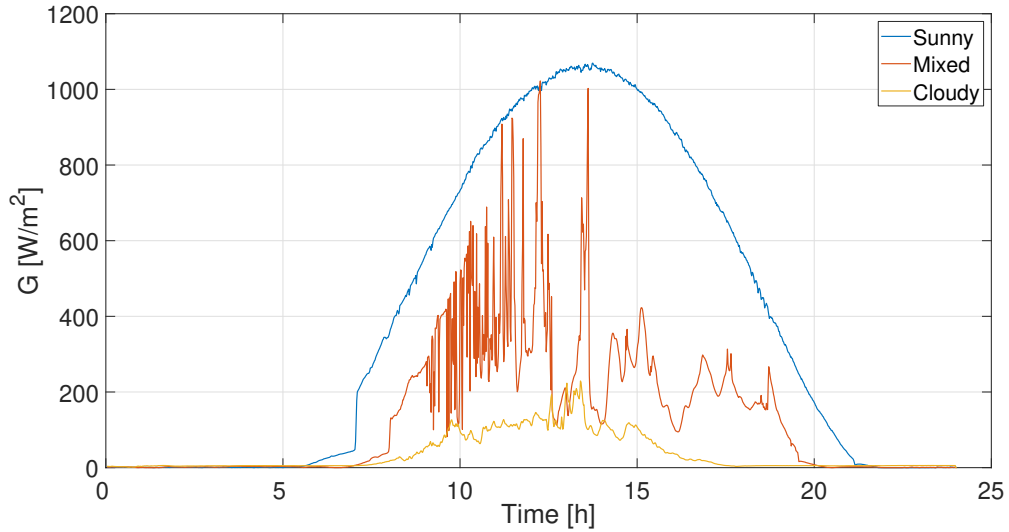


FIGURE 8.9: Irradiation profiles considered: sunny, scattered clouds, cloudy.

TABLE 8.7: DMPPT and CMPPT systems output energy (in kWh) under the proposed 1 day irradiance profiles and shading conditions.

	Sunny		Scattered		Cloudy	
	no shade	shaded	no shade	shaded	no shade	shaded
DMPPT	11.46	8.00	4.67	3.18	0.905	0.56
CMPPT	12.13	6.23	4.91	2.58	0.984	0.52

TABLE 8.8: Overall efficiencies of DMPPT and CMPPT systems (in %) under the proposed irradiance profiles and shading conditions

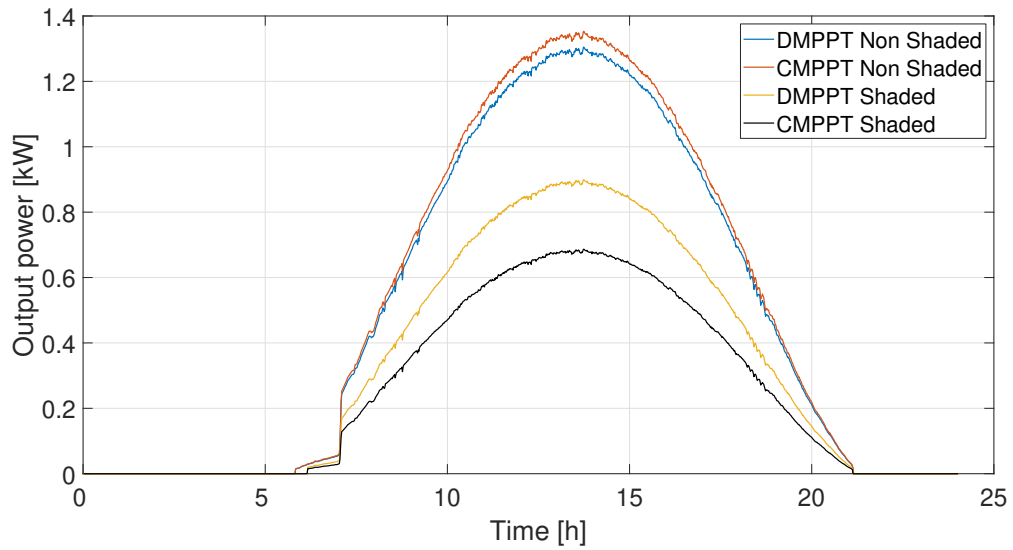
	Sunny		Scattered clouds		Cloudy	
	no shade	shaded	no shade	shaded	no shade	shaded
DMPPT	94.5	95	95.1	94.3	91.9	89.3
CMPPT	100	74.4	100	76.5	100	82.5

$$E_{DC} = \int_{t_1}^{t_2} P_{DC} dt \quad (8.24)$$

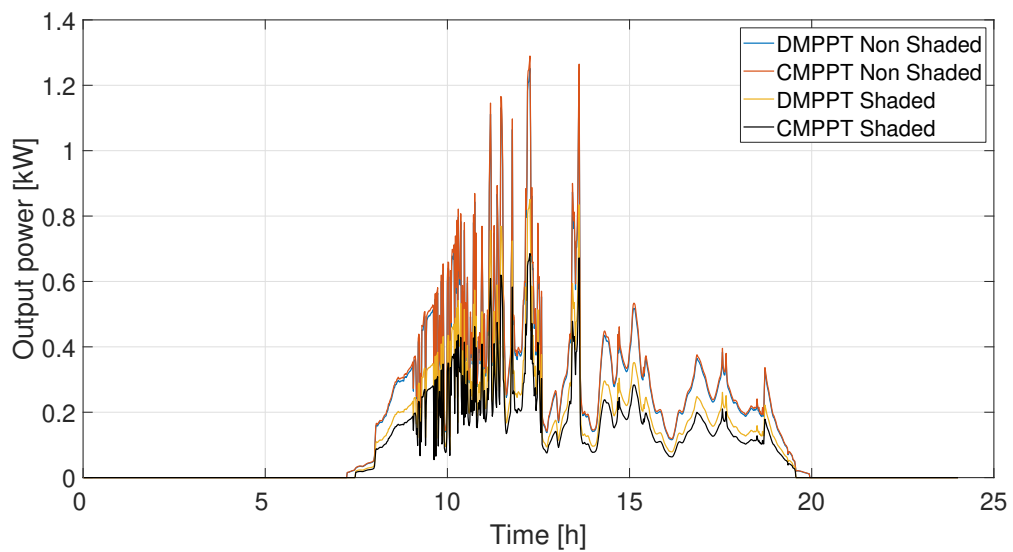
where  $E_{DC}$  is the extracted energy at each string, and  $t_1$  and  $t_2$  are the starting and end time of the considered time interval.

Fig. 8.10 shows the evolution of output powers for the different profiles considered in this study. For all three weather conditions, the efficiency gain under mismatched generating conditions is bigger if the DMPPT system is adopted, with  $\eta_{DMPPT}=95\%$  vs.  $\eta_{CMPPT}=74.4\%$  for a sunny day with static shading blocking the 50% of the irradiance in three out of six PV panels. Furthermore,  $\eta_{DMPPT}$  is always above 89%.

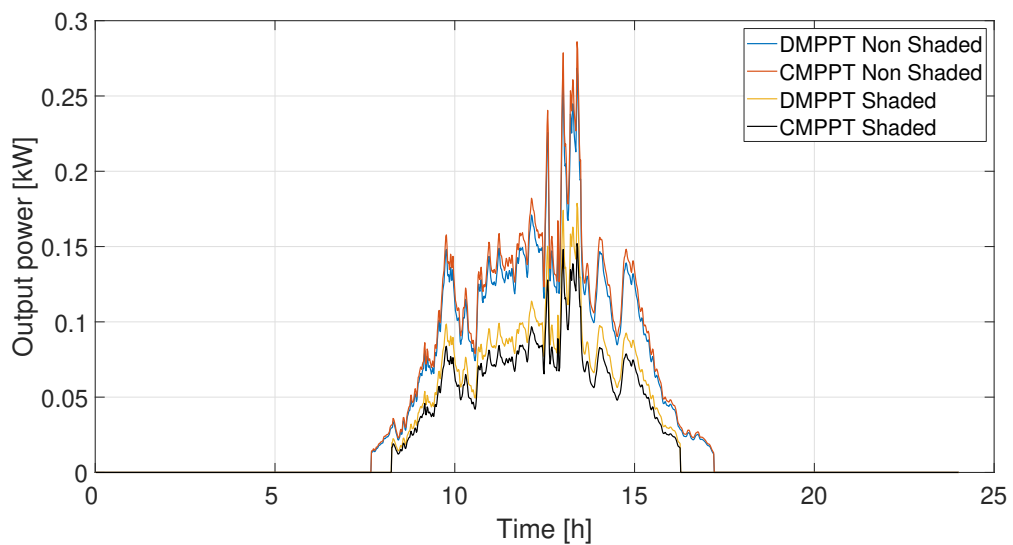




(a) Output power of the different scenarios for a sunny day.



(b) Output power of the different scenarios for a mixed day.



(c) Output power of the different scenarios for a cloudy day.

FIGURE 8.10: PV array output powers for DMPPT and CMPPT systems corresponding to each irradiance profile.

## 8.7 Discussion of results

Under strong mismatch conditions, CMPPT systems find their global MPP at a low voltage, which may not be sufficient to fulfil the operation requirements for certain PV applications. Indeed, the grid-connected systems adopting the inverters in chapter 3.3 do not operate below a certain DC voltage level, even when equipped with a boosting DC/DC stage. If a high DC-bus voltage is required, the contribution of all the PV panels in the string may be necessary and CMPPT systems may be forced to work at suboptimal operating conditions. As the PV panels of the CMPPT system share the same output current, shaded panels impose a current limit, affecting the operating point of the non-shaded ones.

In the absence of mismatch between PV panels, adopting the DMPPT system is not justified as no meaningful energy gain exists. Furthermore, the implementation of the converters at string level adds efficiency losses. In the design of a PV installation, an analysis of static shading affecting the panels may help deciding which panels are interesting to optimize through the implementation of module-level DC/DC converters.

Atmospheric conditions, number of PV panels in the string, mismatch level between PV panels, number of PV panels and their associated converters under each different irradiance level, conversion gain limitations of the DC/DC stage at the PV panel level, and the DC-bus voltage level affect the performance of DMPPT systems. In general, the adoption of a larger number of PV panels and converters will improve the performance of the system. The mismatch affecting a single PV panel will influence to a lower extent the distribution of the DC-bus voltage and, therefore the distribution of the voltage at the output terminals of the converters controlling the PV panels at higher irradiance levels. The voltage stress for the DC/DC converters components in parallel to the output will definitely be reduced.

The voltage level at which the system can get its maximum performance depends on the mismatch conditions. Adopting a constant DC-bus voltage often implies a suboptimal operation of DMPPT systems. The control over the DC-bus voltage can improve the performance of the system. The coordination of the DMPPT function together with a central function that tracks the voltage operating point of the entire string can help solving this situation, improving the overall performance of the system.

## Chapter 9

# Centralized control strategy in DMPPT systems

This chapter proposes a new control algorithm that improves the performance of DMPPT systems. The classical DMPPT approach adopts distributed DC/DC power electronics and control without any centralized action, which makes it difficult to know whether the system is working in its optimal operating point or not. Normally, the inverter keeps the  $V_{DC}$  constant. This leads to poor system performance when the PV panels operate under non-homogeneous irradiance conditions. If CMPPT at the DC-bus is performed in addition to the control of the distributed converters, the PV generation could considerably increase and achieve system performance optimization. However, the effective implementation of the DMPPT and CMPPT functions requires coordination between them.

The new control algorithm proposed in this chapter utilizes the sequential operation of the multi-variable perturb & observe logic to match DMPPT and CMPPT functions. Moreover, it also acts on the control sequence in presence of varying irradiance conditions, improving the dynamic performance of the system and reducing voltage stresses at the DC/DC converters' output terminals. The effectiveness of the proposed approach is demonstrated using a complete test-bench. The DMPPT system used for the validation of the proposed approach is described first. The output power of the DMPPT system is analysed at different  $V_{DC}$  values and compared to the performance of the classical CMPPT system. Then, the centralized control is introduced. The coordination of the DMPPT and CMPPT functions is explained and a method to avoid dangerous output voltage differences is provided. Simulation and experimental results validate the proposed approach showing improved dynamic performance and system stability.

TABLE 9.1: Characteristic parameters at STC of the BenQ GreenTriplex PM245P00 260Wp.

Electrical characteristics	Value
Short-circuit current $I_{SC}$	8.83 [A]
Open-circuit voltage $V_{OC}$	37.7 [V]
MPP current $I_{MPP}$	8.34 [A]
MPP voltage $V_{MPP}$	31.2 [V]
Temperature coefficient of $I_{SC}$ ( $\alpha_I$ )	0.065 [%/°C]
Temperature coefficient of $V_{OC}$ ( $\alpha_V$ )	-80 [mV/°C]

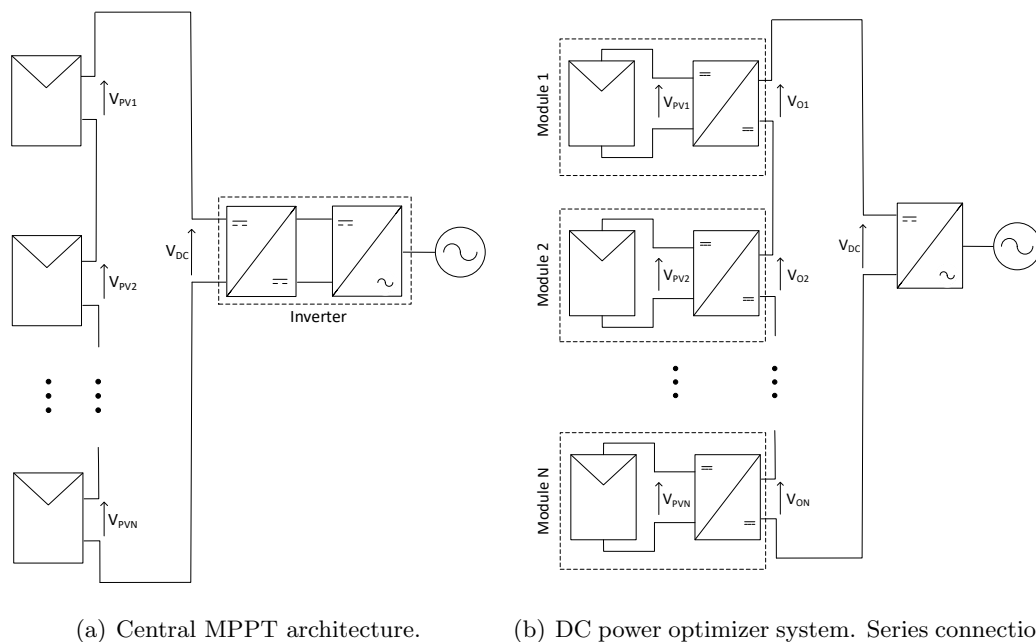


FIGURE 9.1: Central and distributed MPPT approaches for PV systems.

Part of this work is under review for future publication in *IEEE Transactions on Sustainable Energy* [86].

## 9.1 System description

The PV system adopts the DMPPT architecture in Fig. 9.1(b). The series-connected modules are each composed of a PV panel and a DC/DC converter, as in chapter 8. A small portion of the full-sized system of  $N=3$  modules is considered for both simulation and experimental analysis. Each of the three modules contains a BenQ GreenTriplex PM245P00 260Wp poly-crystalline PV panel with the characteristic parameters listed in Table 9.1. The DC/DC converter topology is described hereafter.

TABLE 9.2: General parameters of the interleaved boost-3PC.

General parameters	Value
Inductance $L_1, L_2$	450 [ $\mu\text{H}$ ]
Input capacitance $C_{\text{in}}$	100 [ $\mu\text{F}$ ]
Output capacitance $C_{\text{out}}$	1 [mF]
Max. $V_{\text{ds}}$ voltage $V_{\text{ds,max}}$	100 [V]
Switching frequency $f_{\text{sw}}$	50 [kHz]

### 9.1.1 Non-isolated interleaved boost-3PC

The DC/DC converters have the non-isolated interleaved boost three-port converter (3PC) topology [87] (Fig. 9.2). It has a reduced number of components and provides the functionality of three classical non-isolated boost converters. In addition to controlling individual PV panels, each converter includes module-level electrical storage. In this converter the power can flow from: PV to output, PV to battery, and battery to output via a single power conversion path. For the correct operation of this converter, the output voltage  $V_o$  has to be higher than the battery voltage  $V_b$  and, similarly, the battery voltage has to be higher than the PV voltage ( $V_o > V_b > V_{\text{PV}}$ ). The minimum  $V_b$  is always above  $V_{\text{PV}}$  to fulfil the aforementioned inequality and avoid problems in the converter. In any case, if the battery is at low charging level, the switch  $S_3$  will be disabled. If the battery is not considered, the output voltage is simply above the PV voltage ( $V_o > V_{\text{PV}}$ ). The PV and battery controls are implemented separately. This provides high flexibility to the system, allowing the user to decide on the available power sources. The parameters of the converter are gathered in Table 9.2.

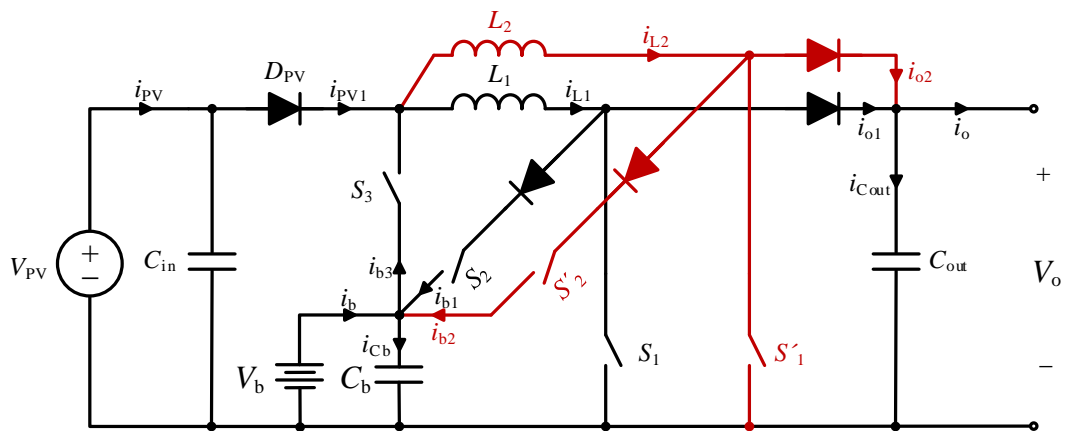


FIGURE 9.2: Interleaved boost-3PC topology. The branches in red are the interleaving power transfer path [87].

### 9.1.1.1 Averaged model

An averaging time-window width equal to the switching period of the switches is applied to the detailed model of the interleaved boost-3PC [87]. The averaged model is obtained with the following equations:

$$L_1 \frac{dI_{L1}}{dt} = -r_{L1}I_{L1} + (1 - d_3)V_{PV} + d_3V_b - (1 - d_1 - d_2)V_o - d_2V_b \quad (9.1)$$

where  $I_{L1}$  is the average value of the current through the inductor  $L_1$ , and  $d_1$  to  $d_3$  the duty cycles corresponding to switches  $S_1$  to  $S_3$ . The equation of the interleaved branch is:

$$L_2 \frac{dI_{L2}}{dt} = -r_{L2}I_{L2} + (1 - d_3)V_{PV} + d_3V_b - (1 - d'_1 - d'_2)V_o - d'_2V_b \quad (9.2)$$

where  $I_{L2}$  is the average value of the current through the inductor  $L_2$ , and  $d'_1$  and  $d'_2$  are the duty cycles corresponding to switches  $S'_1$  and  $S'_2$ . We can obtain the following average currents selecting the necessary duty cycles:

$$I_{PV1} = (1 - d_3)(I_{L1} + I_{L2}) \quad (9.3)$$

$$I_b - I_{Cb} = (d_3 - d_2)I_{L1} + (d_3 - d'_2)I_{L2} \quad (9.4)$$

$$I_{Cout} = (1 - d_1 - d_2)I_{L1} + (1 - d'_1 - d'_2)I_{L2} - I_o \quad (9.5)$$

In this chapter the batteries are not used and only the PV-to-output operation is considered. Thus, the interleaved boost-3PC operates as a conventional boost converter with two interleaved branches. Switches  $S_3$ ,  $S_2$  and  $S'_2$  are in OFF state. Switches  $S_1$  and  $S'_1$  operate at half the switching frequency ( $f_{sw}$ ), including a phase shift of  $180^\circ$  between the pulse-width modulation (PWM) carriers of each switch [87]. Compared to the preliminary study in section 8 a more detailed analysis of the PV-to-output operation can be made using this averaged model. The LUT in section 8 accounts for the efficiency curve of the converters, without any detail on the implementation of the P&O control algorithm or the dynamics of the system. The averaged model described using (9.1)-(9.5) can be used with larger time steps than the switching model, and reduce the required simulation time and it is accurate enough for controller design and system-level simulation.

## 9.2 Comparison of DMPPT and CMPPT systems

### 9.2.1 Simulation results

The simulations are carried out in the MATLAB-Simulink environment. The CMPPT system model includes a string of  $N=3$  series-connected PV panels with the characteristics of Table 9.1. In practice, each PV panel includes three bypass diodes to bypass a third part of the panel in case of uneven shading. However, the model only considers one bypass diode per panel. This approach do not affect the results of this work, as uniform shading and homogeneous irradiance variations are considered. The PV string is connected to an inverter modeled with a DC-link of  $C_{DC}=300 \mu\text{F}$  and a controlled current source block. A P&O algorithm controls the inverter. The  $V_{DC}$  step is  $\Delta V_{DC}=1$  V. The time interval between two consecutive MPPT sampling instants is set to  $\Delta t=1\text{s}$ . The averaged model described in section 9.1.1.1 is used for the DMPPT system converters. Each converter is individually controlled by independent P&O control algorithms. The control of the individual converters is performed simultaneously. The  $V_{PV}$  step is  $\Delta V_{PV}=0.4$  V. The string of modules (PV panel+DC/DC converter) is connected to an inverter providing a constant  $V_{DC}$ .

The CMPPT system comprises PV panels 1 (PV1), 2 (PV2), and 3 (PV3). Fig. 9.3 shows the performance of the CMPPT system at homogeneous and non-homogeneous irradiance conditions. The simulations follow the predetermined irradiance profile in the top plot of the figure. A constant irradiance of  $G_2=G_3=600 \text{ W/m}^2$  is imposed to PV2 and PV3 during the whole simulation. PV1 is subjected to an irradiance profile that becomes different at  $t=21$  s from  $G_1=600 \text{ W/m}^2$  and goes down to  $G_1=300 \text{ W/m}^2$ .

Starting from the top, the second plot in Fig. 9.3 shows the PV voltages ( $V_{PVs}$ ) when the system performs at local MPP (LMPP) after the irradiance change. To track the MPP and maintain the required  $V_{DC}$ , the inverter pulls DC current ( $I_{DC}$ ) from the string of series-connected PV panels. PV1 is the less illuminated panel thus PV1 current limits the maximum  $I_{DC}$ . PV1 operates around its MPP, while PV2 and PV3 operate at a higher  $V_{PV}$ , in the right side of their P-V curve. This side is characterised by a sharp slope, with a large PV power increment ( $\Delta P_{PV}$ ) with respect to the  $V_{PV}$  derivative  $\Delta V_{PV}$  ( $\Delta P_{PV}/\Delta V_{PV}$ ). To obtain the same  $\Delta P_{PV}$ , variations in  $V_{PV2}$  and  $V_{PV3}$  are small ( $V_{PV2,L}, V_{PV3,L}$ ), while  $V_{PV1}$  needs to perform large changes ( $V_{PV1,L}$ ). Middle plot shows the system performing at GMPP.  $V_{DC}$  is shifted right after the irradiance variation, bypassing PV1. Thus, PV2 and PV3 perform around their MPP. GMPP and LMPP are compared in the fourth plot starting from the top, ( $P_{PV1-3,G}=310.1$  W vs.  $P_{PV1-3,L}=260$  W) and the corresponding  $V_{DCs}$  are shown in bottom plot ( $V_{DC1-3,G}$  and  $V_{DC1-3,L}$ , respectively).

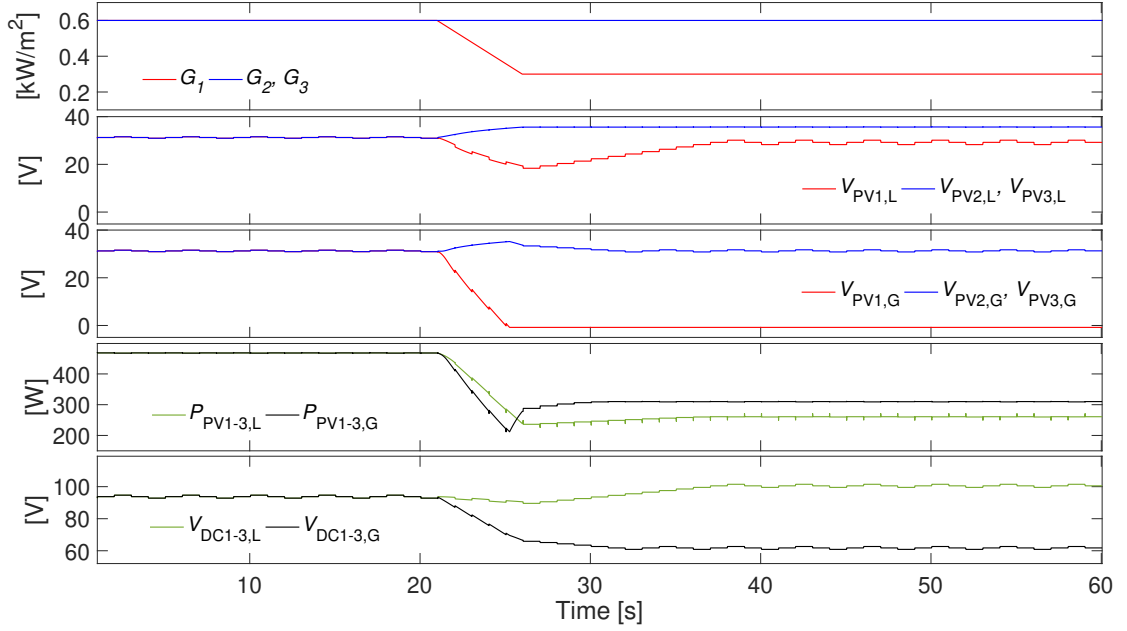


FIGURE 9.3: Performance of the CMPPT approach under homogeneous and non-homogeneous irradiance conditions.

The DMPPT system comprises PV panels 4 (PV4), 5 (PV5), and 6 (PV6). Simulation results under homogeneous and non-homogeneous irradiance conditions can be observed in Fig. 9.4. PV5 and PV6 are subjected to a constant irradiance of  $G_5=G_6=600$  W/m<sup>2</sup> and PV panel 4 (PV4) to an irradiance profile that becomes different at  $t=16$  s from  $G_4=600$  W/m<sup>2</sup> and goes down to  $G_4=300$  W/m<sup>2</sup>. The mismatch condition is extended for a longer period, to observe its performance at different  $V_{DC}$  values (bottom plot,  $V_{DC-1}=120$  V,  $V_{DC-2}=140$  V,  $V_{DC-3}=160$  V,  $V_{DC-4}=180$  V).

$V_{PV}$  and  $V_{DC}$  set-points are changed simultaneously. This test intends to show the influence of different  $V_{DC}$  values on the DMPPT performance. The coordination of the different controls is addressed later.

For  $V_{DC} < V_{DC-3}$ , converter 4 does not perform MPPT and  $I_{DC}$  passes through PV4. As a consequence of the voltage drop in the diodes of converter 4, its output voltage ( $V_{O4}$ ) is lower than PV4 voltage ( $V_{PV4}$ ) (see Fig. 9.2). On the contrary, if  $V_{DC} > V_{DC-3}$ , all the PV panels work at their MPP (Third plot starting from the top,  $P_{PV4-6}=389.9$  W).

The total output powers obtained at the different  $V_{DC}$  values are:  $P_{DC4-6}=317.3$  W at  $V_{DC}=120$  V,  $P_{DC4-6}=368.7$  W at  $V_{DC}=140$  V,  $P_{DC4-6}=371.4$  W at  $V_{DC}=160$  V,  $P_{DC4-6}=371.9$  W at  $V_{DC}=180$  V. Computing the energy for DMPPT in  $t=[70, 120]$  s time interval, the DMPPT efficiency obtained is  $\eta_{DMPPT}=95.38$  %. The maximum CMPPT efficiency is  $\eta_{CMPPT}=79.53$  % ( $t=[40, 60]$  s time interval).



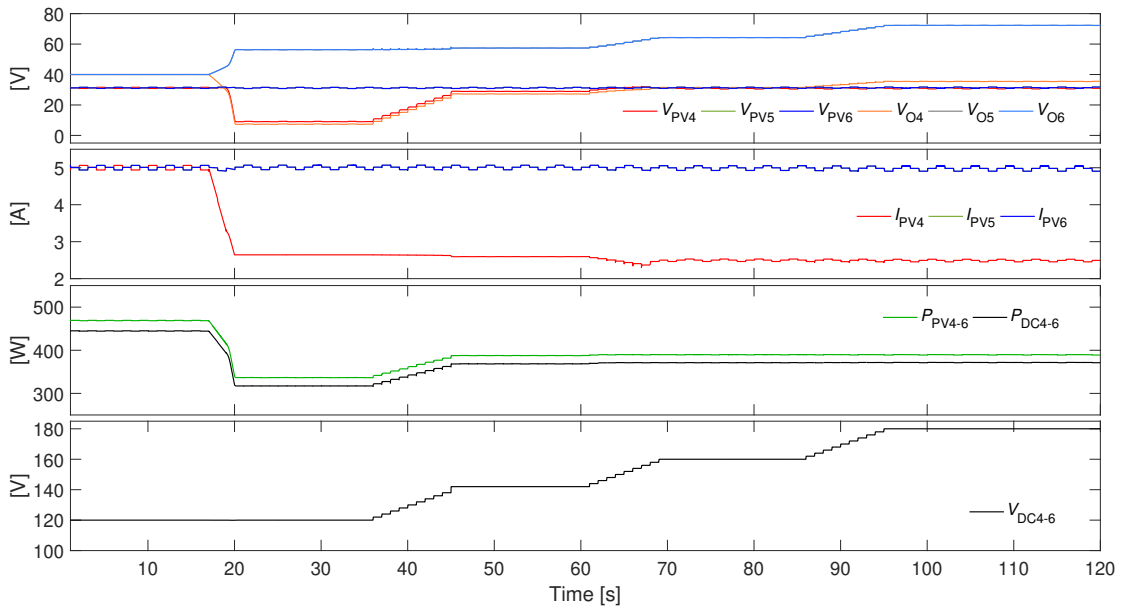


FIGURE 9.4: Performance of the DMPPT approach under homogeneous irradiance conditions at  $V_{DC1}=120V$  and non-homogeneous irradiance conditions at 4 different  $V_{DC}$ s. At  $t=16$  s  $G_1$  changes from  $600$   $W/m^2$  to  $300$   $W/m^2$ ,  $G_2=G_3=600$   $W/m^2$ .

### 9.2.2 Experimental results

The experimental results have been carried out on a laboratory test-bench, shown in Fig. 9.5. For the CMPPT system, a controllable 2-quadrant power supply serves as central inverter. The power supply is controlled by the supervisory control through serial communication. For the DMPPT system, the string of modules is connected to a 1-quadrant voltage source with a constant  $V_{DC}$  and a resistive load in parallel. Each module contains an embedded control implementing the MPPT. The selected control card contains a TMS320F28069M DSP from Texas Instruments. Each DSP is controlled by the supervisory control through CAN bus communication, and the 1-quadrant power supply voltage is set manually. The data is logged using a LabVIEW-based fully-independent data-acquisition system, that comprises the following components: a NI cDAQ-9178 base, four NI 9233 cards and a NI 9205 card. The voltage and current transducers attached to it are the CV 3-1000 and LA 55-P respectively, both from LEM. The sampling frequency is 2kHz and each recorded point is obtained from the averaging of 500 samples, giving an effective (and filtered) data logging at 4Hz frequency.

The test is carried out in a morning thus the irradiance shows a slowly increasing value of around  $G=600$   $W/m^2$ . For each system of three PV panels, 1 PV panel out of three is partly covered to obtain a mismatch situation. Note that each PV panel has three bypass diodes connected in anti-parallel to a subgroup of PV cells. Each subgroup is formed by the third part of the cells in the PV panel. When a subgroup is affected by a shade, the corresponding bypass diode conducts and causes a voltage drop. To

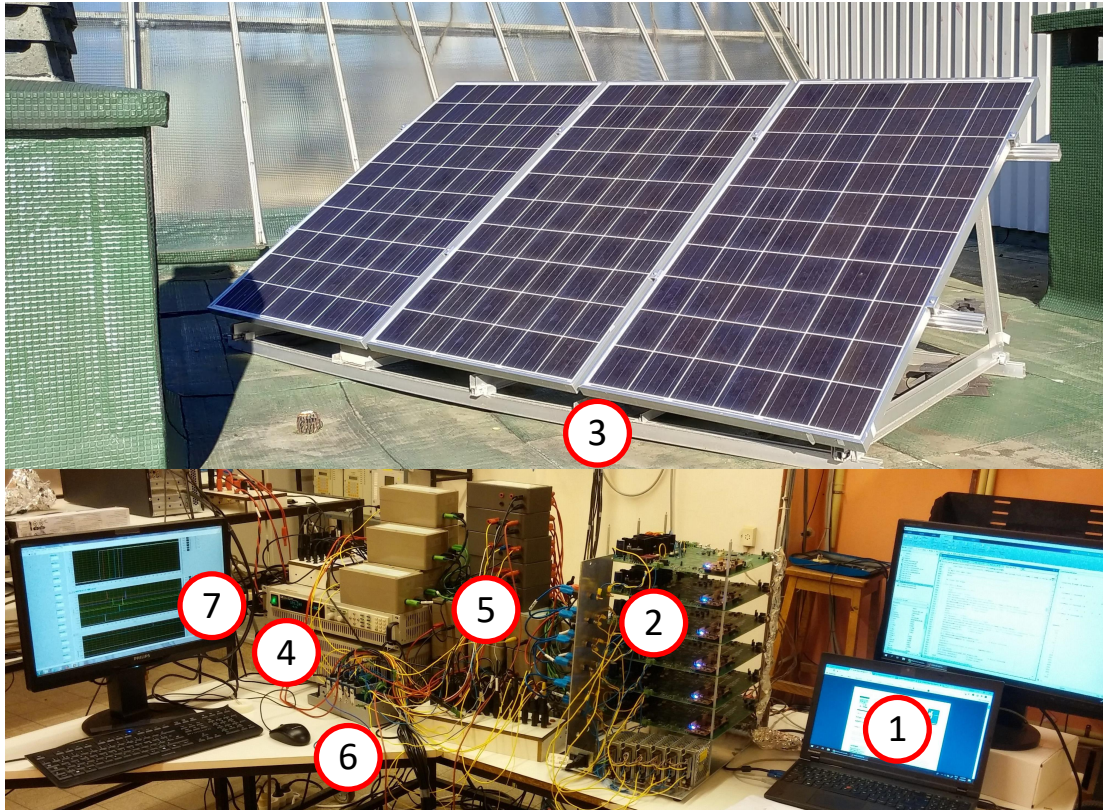


FIGURE 9.5: Experimental setup including a PC for supervisory control (1), 6 DC/DC converters (2), rooftop PV installation (3), 2Q power supply (4), current and voltage sensors for the data acquisition system (5), the data acquisition system (6) and a PC for data-acquisition (7).

avoid the voltage drop and obtain a homogeneous irradiance mismatch in the PV panel, each subgroup of PV cells is equally covered as in Fig. 9.6. This way, a static shade of  $Sh \simeq 50\%$  is imposed on PV1 and PV4, and the operating conditions considered in simulations (sec. 9.2.1) are reproduced. The CMPPT system starts from the PV string  $V_{OC}$  and tracks the LMPP until  $t \simeq 500$  s. It can be observed that  $V_{PV1}$  is subjected to larger variations than  $V_{PV2}$  and  $V_{PV3}$ , as a consequence of the mismatch between panels as previously explained in the simulations section 9.2.1. A voltage sweep tracks for a higher MPP and finds the GMPP at  $V_{DC1-3} = 49$  V. PV1 is bypassed and CMPPT performs the MPPT at this GMPP for the rest of the test.

The DMPPT system starts performing at  $V_{DC4-6} = 110$  V. The same voltages as in the simulation are manually set to the 1Q power supply (120 V, 140 V, 160 V, 180 V). For  $V_{DC4-6} \geq 160$  V, the DMPPT system is considered to be operating at its GMPR. The energy yield of both systems is computed for [1403, 1990] s time interval. The maximum available energy in the PV string is  $E_{PV4-6} = 987.84$  Wh. The power losses associated to the DC/DC conversion stage yield a DMPPT efficiency of  $\eta_{DMPPT} = 89.37\%$ . Thus, the effective energy yield of the DMPPT system is  $E_{DC4-6} = 882.81$  Wh. The



FIGURE 9.6: PV1 to PV6 from left to right -  $Sh \simeq 50\%$  static shade on PV1 and PV4.

CMPPT system obtains an energy yield of  $E_{PV1-3}=801.6$  Wh and results in a CMPPT efficiency of  $\eta_{CMPPT}=81.15$  %. Note that the  $\eta_{DMPPT}$  obtained in the experiments is lower compared to the one in the simulations. The averaged model used in simulations only considers conduction losses. In reality switching losses occur as well.

### 9.2.2.1 Discussion of results

If the mismatch between PV panels is considerable, the DMPPT approach demonstrates a superior performance compared to the traditional one. Under static mismatch conditions, the energy yield obtained in the DMPPT system is higher than the PV energy yield in the CMPPT system. This is a great advantage with regard to the classical arrangement in PV installations. The adoption of the distributed architecture in traditional PV installations may require only the inclusion of an additional DC/DC stage between the affected PV panel and the central DC/DC power electronics. Especially in BIPV applications, where static shades due to surrounding obstacles are sometimes unavoidable. The already existing inverter can be used, without the need to replace it, thus facilitating the integration of the distributed electronics. This is valid only if the voltage at the input of the inverter is properly controlled. A fixed  $V_{DC}$  implies a poor performance of the system if the generating conditions between PV-level converters are



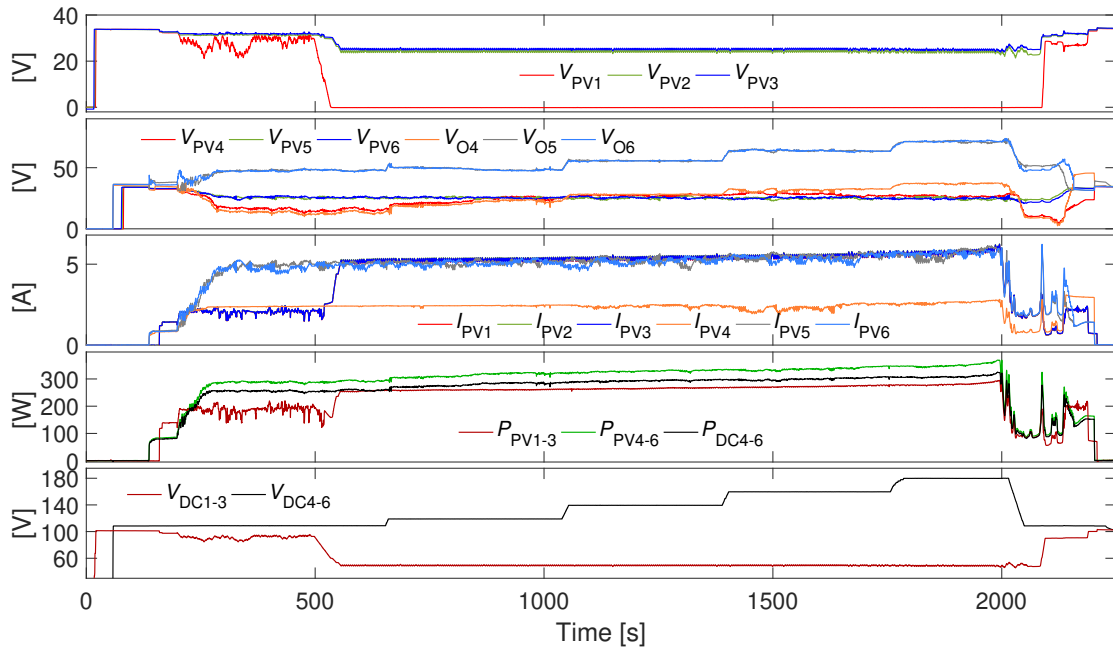


FIGURE 9.7: Experimental results of the DMPPT and CMPPT systems under mismatch conditions. The CMPPT system operates at LMPP before, and at GMPP after,  $t=500$  s ( $P_{PV1-3}$ ). The DMPPT system operates at LMPR for  $V_{DC4-6} < 140$  V, at GMPP for  $V_{DC4-6} > 140$  V.

different. This implies the use of different control functionalities in the operation of the PV system, discussed hereafter.

### 9.3 Coordination of Distributed and Central MPPT

Early research activities in DMPPT systems [60, 70–73, 88–90] were focused on independent DC/DC converters with an individual single-variable (SV) MPPT control, not interacting with each other. These approaches perform the MPPT at PV-panel level, without any view of a possible global optimal operating condition at the overall system level. A tentative approach presented in literature proposes the centralized control of distributed DC/DC power electronics using a single current sensor at the DC-bus [91, 92]. In [91] the Multi-Variable P&O Cartesian (MVPOC) algorithm is based on the sequential perturbation of the control variable of each DC/DC converter in the string, the control variable being the duty cycle or a reference voltage acting in the closed-loop control of the DC/DC converter. The aim is to maximize the overall power at the DC-bus. The authors in [92] act on the polar coordinates of these control variables, introducing the Multi-Variable P&O vectorial (MVPOV) control. Differently from MVPOC, where only one control variable is perturbed at each perturbation time step, MVPOV perturbs all the control variables at the same time, so that the MPPT promptness with respect to irradiance changes is improved.

The aforementioned approaches assume that the DC-bus voltage is kept at a constant value by the inverter. This assumption is a limitation to the global power harvested and injected into the DC-bus, as demonstrated in section 9.2.1. Actually, a fixed  $V_{DC}$  means a fixed sum of the DC/DC converters' output voltages. The output voltage of each DC/DC converter depends on the power transferred to its output, so that an irradiance mismatch affecting the PV sources turns into differences in the DC/DC converter output voltages. A large irradiance mismatch between converters may lead to dangerous overvoltage in the modules presenting greater output powers, damaging some of the DC/DC converters' components (e.g. MOSFETs and capacitors in parallel to the output). Thus, reduced tracking time improves the system reliability.

An additional MPPT control on the DC input voltage of the inverter, working independently of the DC/DC MPPT ones, might improve the power processing capabilities of the converters [75, 93]. Even then, this central MPPT control (CMPPT) may drive the DC-bus voltage far from the range wherein the inverter transfers the maximum amount of energy to the grid. This could deteriorate the overall efficiency. These issues were envisaged in [94], by evidencing the unsuccessful MPPT of some PV sources when the mismatch between them is significant. The authors in [61, 95] demonstrate that all the PV sources operate at their own MPPs if  $V_{DC}$  is operating inside a precise range. The analysis in [62] suggests the need for a strategy that couples both the DMPPT function and the control of the DC-bus voltage if the optimal operation of the whole system is pursued.

Reliable communication between controllers implementing SV control is crucial for the coordination between DMPPT and CMPPT functions, a fact that cannot always be guaranteed. In contrast, multi-variable algorithms naturally provide the advantage of a coordinated operation. In this work, the MVPOV algorithm presented in [92] has been extended, accounting for the control of the DC-bus voltage and proposing a hybrid multi-variable (H-MV) control that matches CMPPT and DMPPT functions. The proposed approach achieves a superior coordination that benefits from the sequential execution that multi-variable algorithms provide without additional control routines, reducing its complexity.

On the other hand, the dynamic performance in DMPPT systems, i.e. MVPOC and MVPOV, has not been analyzed in depth until now. For instance, under rising irradiance, multi-variable algorithms may perform an incorrect MPPT. Indeed, due to the increase of the output power due to the irradiance level rise, both the MVPOC and the MVPOV methods should continue tracking the same variable in the multi-variable sequence by keeping the others at the initial value. This leads the PV system far from the absolute MPP, leading to a poor dynamic MPPT performance. In order to solve

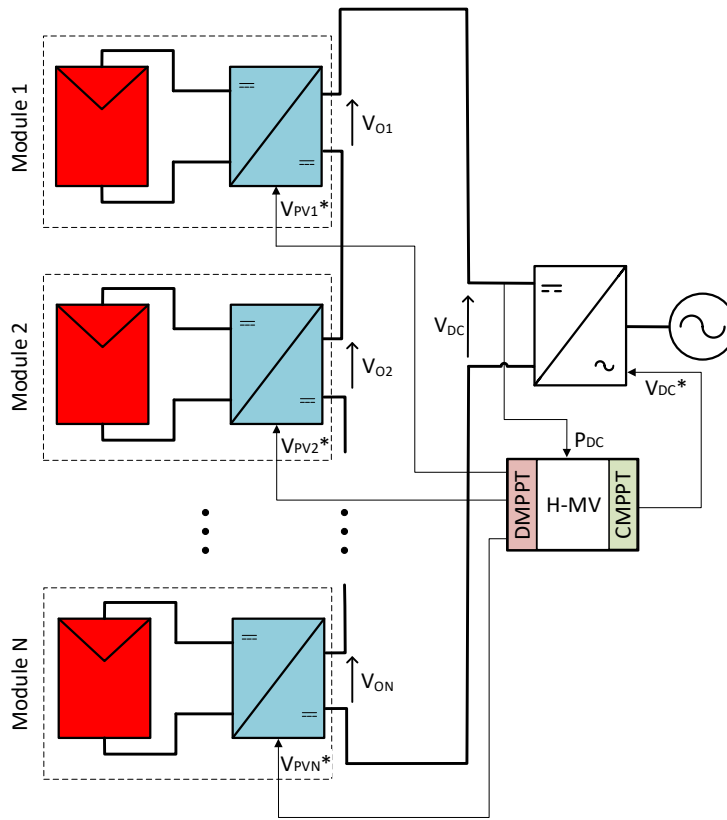


FIGURE 9.8: DMPPT architecture of the grid-connected PV system.

this issue, the proposed control modifies the multi-variable MPPT sequence according to the irradiance conditions.

### 9.3.1 Hybrid Multi-Variable P&O control

This section proposes a novel method to coordinate DMPPT and CMPPT functions. It exploits the advantage the multi-variable operation provides by including the control of  $V_{DC}$  into both Cartesian and vectorial multi-variable operating sequences.

For a system with  $N=3$  modules, MVPOC adopts the following form:  $\{V_{PV1}, V_{PV2}, V_{PV3}, V_{DC}\}$  where  $V_{PVx}$  is the PV voltage corresponding to the module  $x$ . The voltage references in this sequence are independent from each other. On the other hand, MVPOV implements the multi-variable P&O logic to the polar coordinates of the PV voltages (Fig. 9.9), expressed as:

$$V_{PV1} = |V_{ec}| \cdot \sin \theta_1 \cdot \sin \theta_2 \quad (9.6)$$

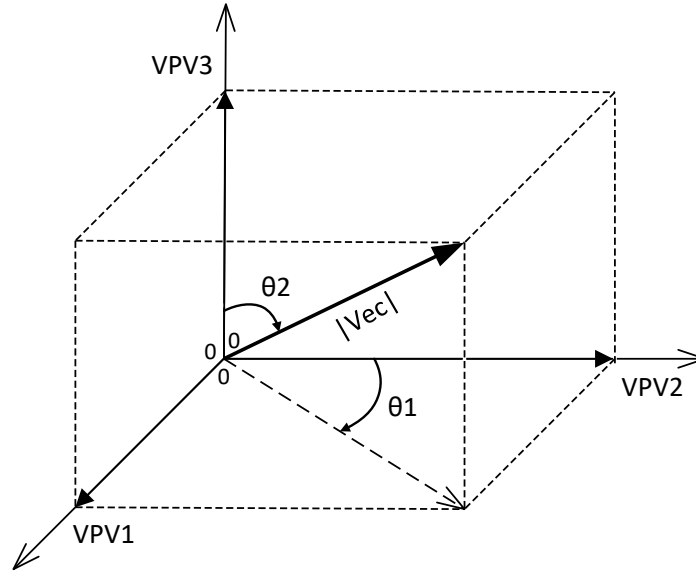


FIGURE 9.9: Operating point description in spherical coordinates of the vectorial approach for a system with  $N = 3$  PV modules.

$$V_{PV2} = |V_{ec}| \cdot \cos \theta_1 \cdot \sin \theta_2 \quad (9.7)$$

$$V_{PV3} = |V_{ec}| \cdot \cos \theta_2 \quad (9.8)$$

where the vector magnitude  $|V_{ec}|$

$$|V_{ec}| = \sqrt{V_{PV1}^2 + V_{PV2}^2 + V_{PV3}^2} \quad (9.9)$$

and the angles  $\theta_1$  and  $\theta_2$  substitute  $V_{PV1}$ ,  $V_{PV2}$  and  $V_{PV3}$  as control variables. Therefore, the control sequence becomes:  $\{|V_{ec}|, \theta_1, \theta_2, V_{DC}\}$ . Any change in the magnitude of  $|V_{ec}|$  generates a simultaneous change for each PV voltage. Any change in  $\theta_1$  or  $\theta_2$  changes the PV voltage vector. We can find the vectorial variables by recombining the equations above. Combining (9.6) and (9.7), we obtain:

$$\frac{V_{PV1}}{V_{PV2}} = \frac{|V_{ec}| \cdot \sin \theta_1 \cdot \sin \theta_2}{|V_{ec}| \cdot \cos \theta_1 \cdot \sin \theta_2} \Rightarrow \tan \theta_1 = \frac{V_{PV1}}{V_{PV2}} \quad (9.10)$$

and  $\theta_1$  results in:

$$\theta_1 = \arctan \left( \frac{V_{PV1}}{V_{PV2}} \right) \quad (9.11)$$

Combining (9.7), (9.8) and (9.11), we obtain:

$$\frac{V_{PV2}}{V_{PV3}} = \frac{|V_{ec}| \cdot \cos \theta_1 \cdot \sin \theta_2}{|V_{ec}| \cdot \cos \theta_2} \Rightarrow \tan \theta_2 = \frac{V_{PV2}}{V_{PV3} \cdot \cos \left( \arctan \left( \frac{V_{PV1}}{V_{PV2}} \right) \right)} \quad (9.12)$$

and  $\theta_2$  results in:

$$\theta_2 = \arctan \left[ \frac{V_{PV2}}{V_{PV3} \cdot \cos \left( \arctan \left( \frac{V_{PV1}}{V_{PV2}} \right) \right)} \right] \quad (9.13)$$

$|V_{ec}|$  is also obtained from (9.8):

$$|V_{ec}| = \frac{V_{PV3}}{\cos \theta_2} \quad (9.14)$$

The multi-variable approach can be extended to an  $N$ -dimensional space. In a general form, PV voltages in spherical coordinates are defined by:

$$V_{PV_i} = |V_{ec}| \cdot \cos \theta_{(i-1)} \cdot \prod_{j=i}^{N-1} \sin \theta_j \quad (9.15)$$

where  $i \in [1, N]$ , taking into account that  $\theta_0=0$  (for  $i=1$ ).

### 9.3.1.1 Initial conditions

We assume that all PV voltages have the same value ( $V_{PV1}=V_{PV2}=V_{PV3}=V_{PV}$ ). From (9.11) we obtain the value of the initial  $\theta_1$ :

$$\theta_{1,init} = 0.7854 \text{ rad} = 45^\circ \quad (9.16)$$

and from (9.13) the initial  $\theta_2$  is:

$$\theta_{2,init} = 0.9553 \text{ rad} = 54.73^\circ \quad (9.17)$$

Before any of the modules is operating, the PV panels are at their open-circuit voltage ( $V_{PV}=V_{OC}$ ). Using (9.14) or (9.9) the initial value of  $|V_{ec}|$  is:



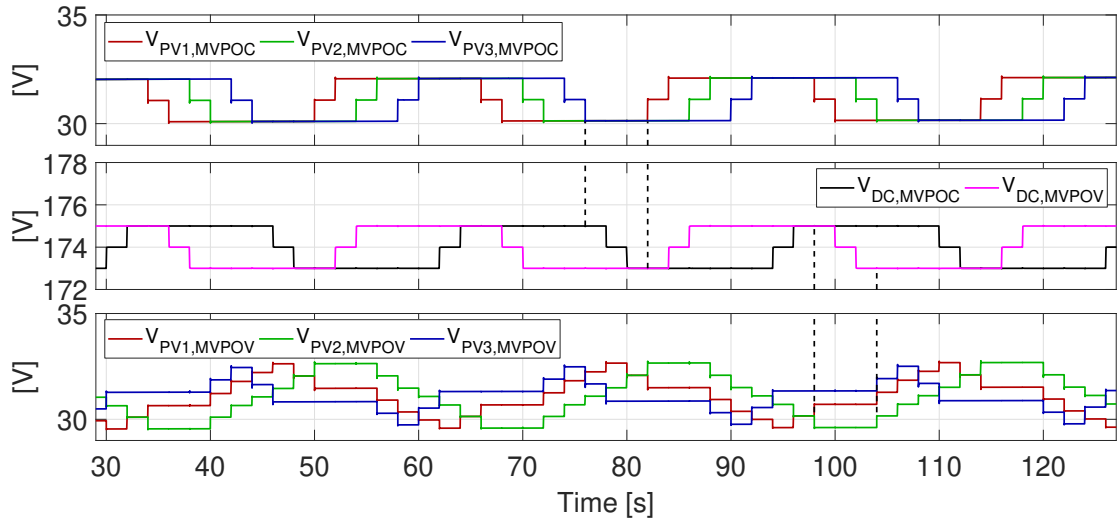


FIGURE 9.10: Steady state operation of DMPPT and CMPPT techniques in a centralized control. MVPOC technique in top plot shows the sequential perturbation of the PV voltages. MVPOV technique PV voltages illustrated in Fig. 9.9 are shown in bottom plot. Middle plot shows the tracking of  $V_{DC}$  included in each multi-variable P&O sequence.

$$|V_{ec}|_{init} = \sqrt{3}V_{OC} \quad (9.18)$$

According to Table 8.1,  $|V_{ec}|_{init}=65.298V$  and its MPP value at STC  $|V_{ec}|_{MPP,STC}=54V$ .

Simulation results in Fig. 9.10 show the steady state behavior of the system for both algorithms. For the MVPOV, the multi-variable P&O is applied to the vectorial variables  $|V_{ec}|$ ,  $\theta_1$  and  $\theta_2$ , and the PV voltages change according to (9.6), (9.7) and (9.8).

### 9.3.2 Dynamic response in MV-P&O control algorithms

The dynamic response presents additional challenges. Fig. 9.11 illustrates P&O algorithms' PV voltage deviation for a change in power due to an irradiance variation  $\dot{G}$  (in  $W/m^2/s$ ) ( $\Delta P_G$ ) higher than the change in power due to the voltage perturbation step  $\Delta V_{PV}$  ( $\Delta P_V$ ): instead of performing the classical three-point-behaviour in steady state (sequence A-B-C and backwards), the P&O algorithm continuously modifies the control variable in the same direction as long as the power increases (sequence A-B-C'-D-E) and changes the direction, climbing towards the MPP once the irradiance is constant again (sequence E-D-F-G-H). This might not be a significant issue if all the individual P&O controllers are synchronized, as all PV and output voltages will deviate similarly. In the case of multi-variable P&O algorithms, the sequential control may cause deviations between PV voltages.

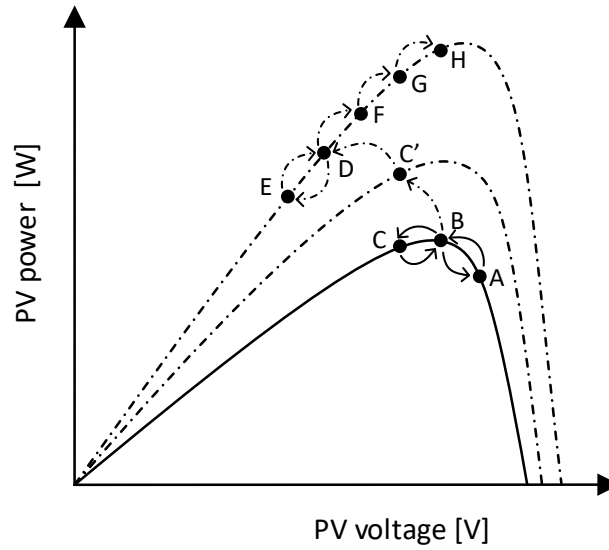


FIGURE 9.11: Performance of conventional SV P&O MPPT algorithms with the characteristic three-point behaviour (A-B-C) in steady state (solid lines) and voltage deviation (A-B-C'-D-E-D-F-G-H) in presence of increasing irradiance (dashed lines).

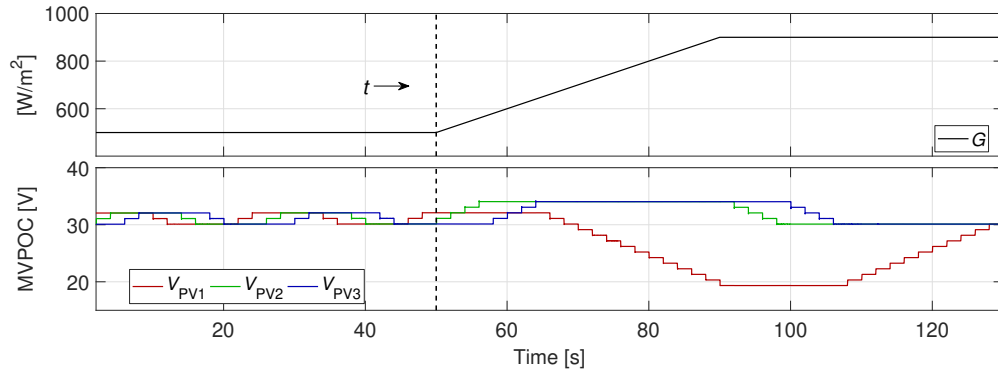


FIGURE 9.12: MVPOC dynamic response. Top to bottom: Irradiance profile, PV voltages.

### 9.3.2.1 MVPOC dynamic response

MVPOC controls the PV voltages sequentially. Under rising irradiance (top plot), if  $\Delta P_G > \Delta P_G$ , MVPOC will continuously modify the  $V_{PV}$  evaluated at the instant the irradiance rise  $\dot{G}$  occurs and as long as  $\dot{G} \neq 0 \text{ W/m}^2/\text{s}$ . Fig. 9.12 shows this effect. At time  $t$ ,  $\dot{G} = 10 \text{ W/m}^2/\text{s}$ . Initially, few additional steps of  $V_{PV2}$  and  $V_{PV3}$  that deviate from the P&O steady state three-point behaviour compensate the power rise (bottom plot). For higher irradiance levels, the implemented  $\Delta V_{PV}$  is not enough to ensure a correct MPPT. This denotes different  $\Delta P_{PV}/\Delta V_{PV}$  of the P-V curve for different irradiance levels. As a consequence, MVPOC keeps tracking  $V_{PV1}$  until  $\dot{G} = 0 \text{ W/m}^2/\text{s}$

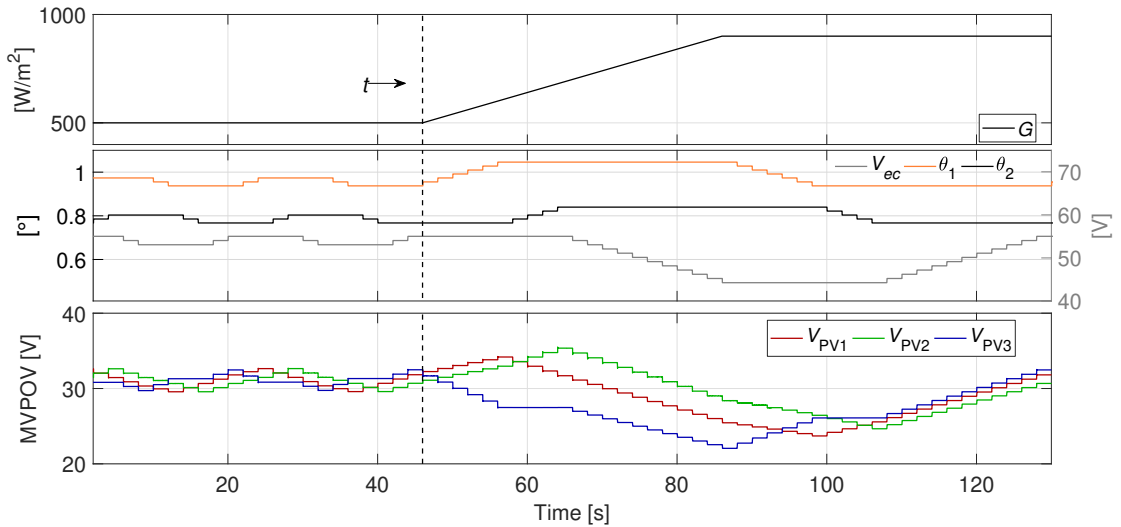


FIGURE 9.13: MVPOV dynamic response. Top to bottom: Irradiance profile, vectorial variables, PV voltages.

again. This voltage deviation strongly affects the PV generation and the output voltage in the corresponding converter.

### 9.3.2.2 MVPOV dynamic response

MVPOV controls sequentially the vector  $V_{ec}$  and the angles  $\theta_1$  and  $\theta_2$ . As stated before, these variables represent the PV voltages in the polar spherical coordinates. Fig. 9.13 shows in detail the evolution of these vectorial variables (middle plot) and the simultaneous change of the PV voltages (bottom plot) for each change. This simultaneity improves the MPPT promptness. However, MVPOV still shows some voltage variations. Similar to MVPOC, this approach continuously tracks the same variable until the output power is lower than the previously evaluated one.

### 9.3.2.3 H-MV dynamic response

To overcome this problem, the novel H-MV solution derived from the MVPOV is introduced. Apart from coordinating the distributed and centralized MPPT functions, H-MV control manages the timing of the control variables depending on the irradiance variation speed. The new approach is fully represented in the flowchart of Fig. 9.14 and explained hereafter. The initial values of the vectorial variables are set considering each PV panel's  $V_{OC}$ . The total power generated in the DC/DC converters string  $P_{DC}$  is also measured.  $V_{DC}$  is set to a value above the sum of the PV voltages. For a correct initialization, H-MV starts setting a negative step to  $|V_{ec}|$  to ensure that PV voltages move towards their MPP value. The irradiance variation derives from the power

variation between two consecutive sampling instances, with an additional power measurement at the DC-bus, as in [96]. This power variation is calculated as illustrated in Fig. 9.15, where  $\Delta P_1 = P_{k+1} - P_k$  indicating the increment or decrement of power due to the  $k$ -th PV voltage perturbation and  $\Delta P_2 = P_{k+1} - P_x$  indicating the power variation due to a possible external perturbation (e.g. irradiance variation) where no new PV voltage reference has been set by the control. Then, the difference between them is computed:  $\Delta P = \Delta P_1 - \Delta P_2$ .

- If  $\Delta P = 0$ , the system is in steady-state irradiance condition ( $\dot{G} = 0$ ) and the control operates as a vectorial MPPT including the DC-bus voltage control, (as in Fig. 9.10). If  $\Delta P_1 < 0$ , the variable index is updated to  $j = j + 1$  as long as  $j \leq N$ . If  $j > N$  the sequence restarts, setting  $j = 1$ . The sign of the tracking direction of each variable's previous operation is held ( $s_j(k) = s_j(k-1)$ ) and used in the next iteration.
- If  $\Delta P \neq 0$  the irradiance is changing ( $\dot{G} \neq 0$ ), the control sets the variable index  $j = 1$  and operates by perturbing only the variable  $|V_{ec}|$ , setting all PV voltages at a time.

At each sampling instance, the irradiance level  $G$  equivalent to the power  $P$  can be evaluated as follows:

$$G = 1\text{kW/m}^2 \cdot \frac{P}{P_{@G=1\text{kW/m}^2}} \quad (9.19)$$

and the irradiance variation  $\dot{G}$  is calculated substituting  $P$  for  $\Delta P$  in (9.19).

First, the vectorial variables are analysed and  $V_{DC}$  is not included in the control. Thus, the control sequence is as follows:  $V_{ec}, \theta_1, \theta_2$ . Once the irradiance rises after time  $t$  (top plot), HMV detects a power increase and acts on the control sequence. It blocks  $\theta_1$  and  $\theta_2$ , modifying only the reference of  $V_{ec}$ , as it can be appreciated in the second plot of Fig 9.16. The PV voltages (bottom plot) follow simultaneously the same profile as  $V_{ec}$ , as described previously in Fig. 9.9. Thanks to this low deviation between PV voltages, voltage stresses at the DC/DC converters' output terminals are reduced.

### 9.3.3 Simulation results

The simulations are carried out in the MATLAB-Simulink environment using an averaged model of the DC/DC converters [97]. The settling time of the PV voltage loop is 0.5s. In order to ensure a correct measurement after the system reaches the steady state condition, the time interval between the sampling instance  $k$  and the additional

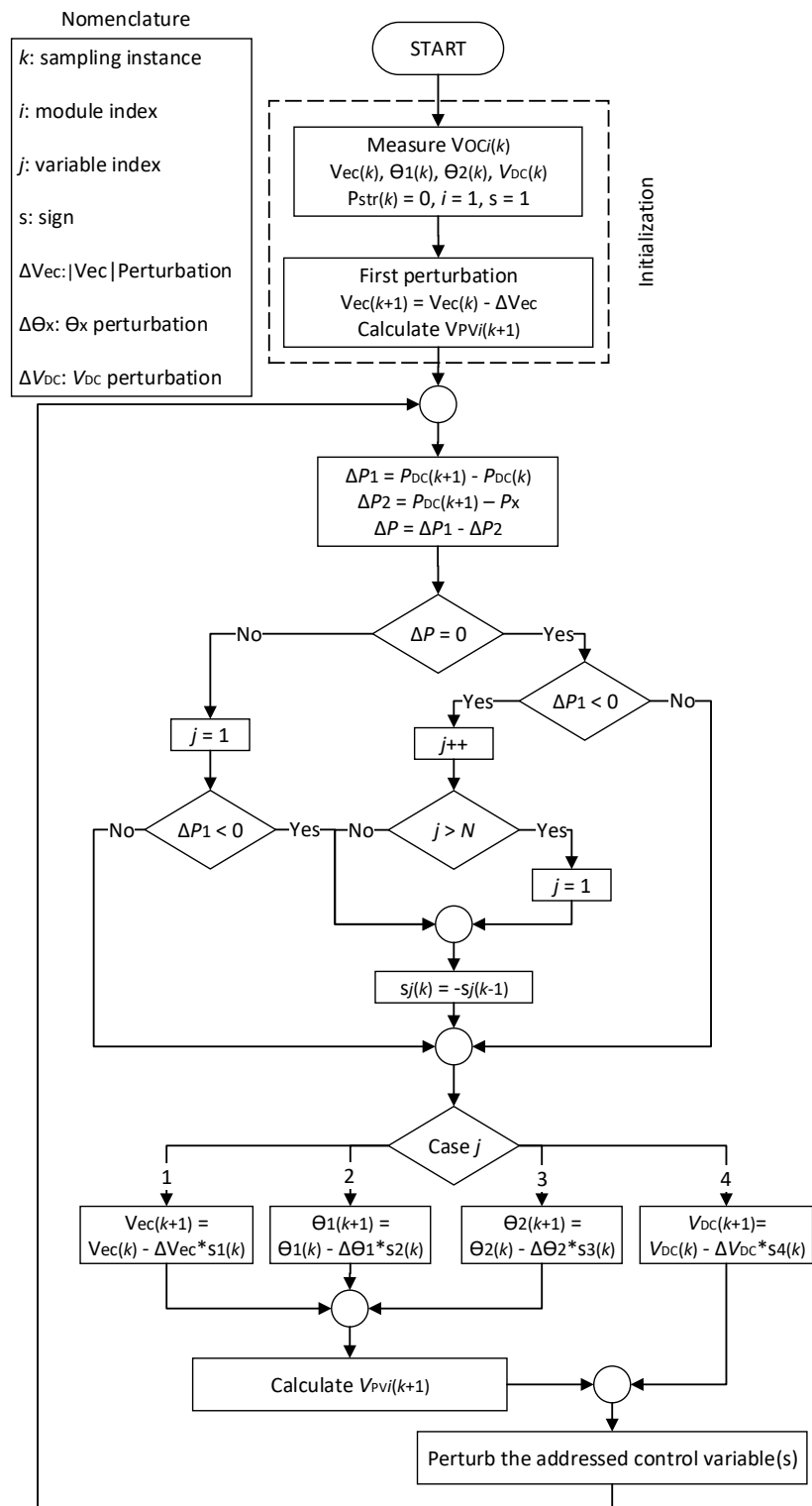


FIGURE 9.14: Flowchart of the proposed H-MV control algorithm.

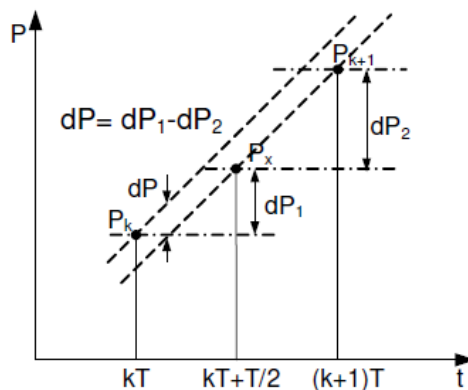


FIGURE 9.15: Measurement of the power between MPPT sampling instances [96].

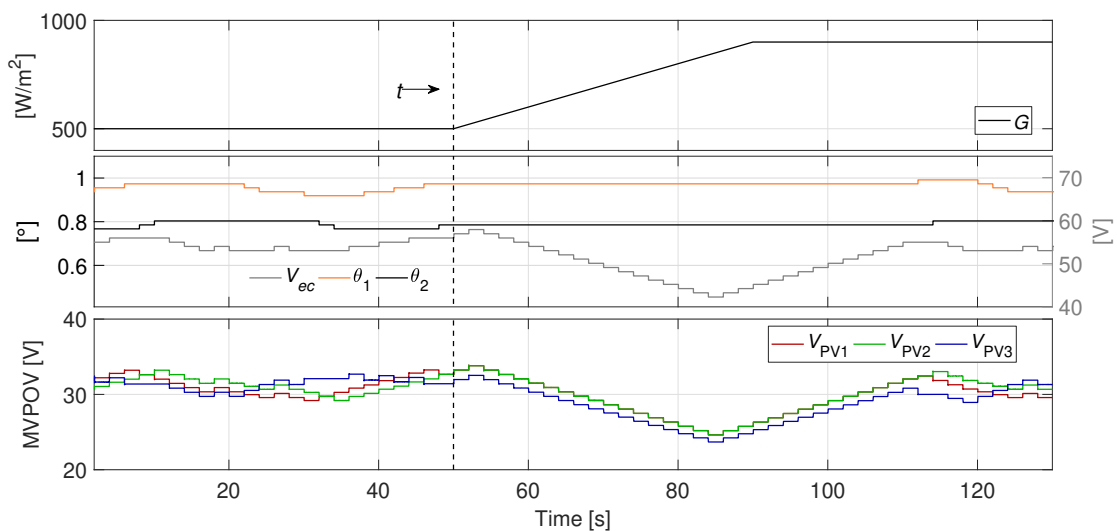


FIGURE 9.16: HMV dynamic response. Top to bottom: Irradiance profile, vectorial variables, PV voltages.

measurement  $P_x$  is set to 1s. Therefore, the total time interval between two consecutive MPPT sampling instants is equal to  $\Delta t=2s$ . The PV voltage step for each module is set to  $\Delta V_{PV}=0.4V$ , i.e. large enough to avoid measurement errors. The DC-bus voltage step is chosen to be  $\Delta V_{DC}=1V$ , and  $V_{DC}$  limited to  $[120, 180]$  V range to avoid overvoltage at the converters' output terminals.

### 9.3.3.1 $V_{DC}$ control

In order to show the effectiveness of the  $V_{DC}$  control, the following assumption is considered: initially, PV1 is in a mismatch situation in relation with PV2 and PV3. The irradiance affecting PV1 is  $G_L=200$  W/m<sup>2</sup> while PV2 and PV3 are illuminated by  $G_H=1000$  W/m<sup>2</sup>. The P-V curve is represented in solid blue in Fig. 9.17(a). First, the system is operating in its GMPT at  $V_{DC}=120$  V (point A). At a certain time, the

irradiance affecting PV1 changes to  $G_L=500 \text{ W/m}^2$  changing also the P-V curve (dashed red line). At the new operating conditions the maximum power extraction corresponds to GMPT-2, for  $V_{DC}=[148, 200] \text{ V}$ . In a DMPPT system with a constant  $V_{DC}=120 \text{ V}$  the system operates at a suboptimal level (point B). To move the working point to GMPT-2,  $V_{DC}$  has to increase, shift to the right.  $V_{DC}$  control is based on the hill-climbing P&O principle thus, it performs the MPPT and reaches GMPT-2.

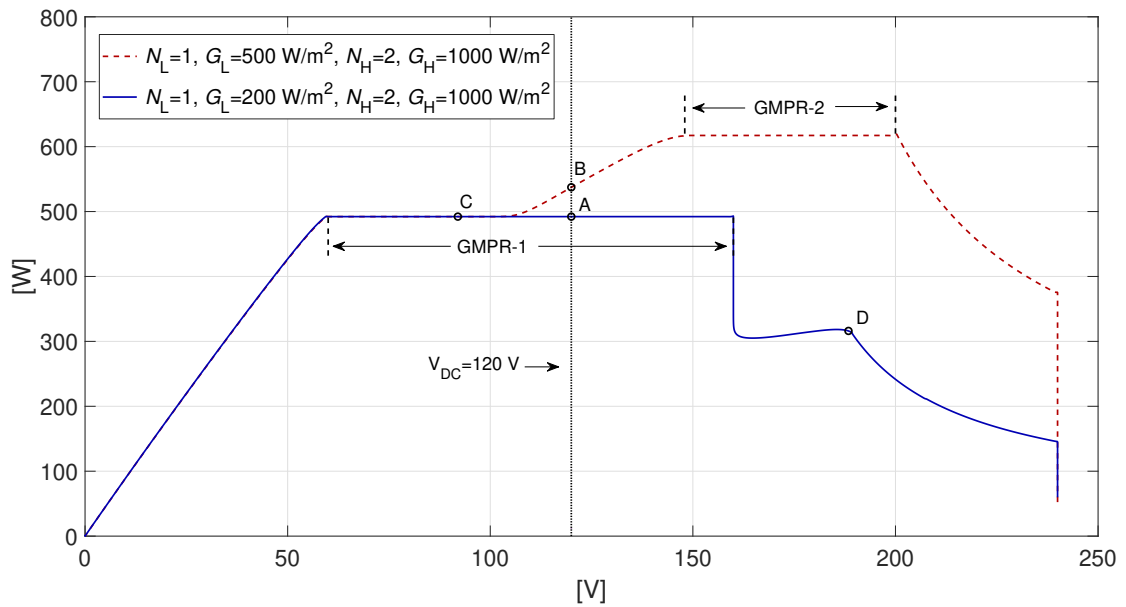
Fig. 9.17(b) shows the difference between the DMPPT system with fixed  $V_{DC}=120\text{V}$  and implementing  $V_{DC}$  control. The simulation starts at point B under these conditions:  $N_L=1$ ,  $G_L=500 \text{ W/m}^2$ ,  $N_H=2$ ,  $G_H=1000 \text{ W/m}^2$  and  $V_{DC}=120 \text{ V}$ . Initially, the DMPPT system with fixed  $V_{DC}=120\text{V}$  performs at a suboptimal level. The efficiency under these conditions is  $\eta_{\text{DMPPT}}=81.8 \%$ . At  $t=107\text{s}$ , the  $V_{DC}$  control is activated. The control tracks  $V_{DC}$  and sets it in GMPT-2, in the vicinity of  $V_{DC}=148 \text{ V}$ , obtaining an efficiency of  $\eta_{\text{DMPPT}}=94.7 \%$ .

**Unavoidable suboptimal operating conditions:** Unfortunately, optimal system operation is not always achievable. Some  $V_{DC}$  operating points can be trapped into LMPRs. For instance,  $V_{DC}$  working point can be point C in Fig. 9.17(a). Initially, the system is operating at GMPT-1 (blue line, PV1 at  $G_L=200 \text{ W/m}^2$ , PV2 and PV3 at  $G_H=1000 \text{ W/m}^2$ ). The irradiance change to  $G_L=500 \text{ W/m}^2$  in PV1 does not affect the side of the P-V curve where  $V_{DC}$  is located. As the  $V_{DC}$  is in a flat LMPR, a  $\Delta V_{DC}$  results in  $\Delta P_{DC}=0$ . The  $V_{DC}$  control will therefore track in the opposite direction and will operate in steady state at suboptimal level.

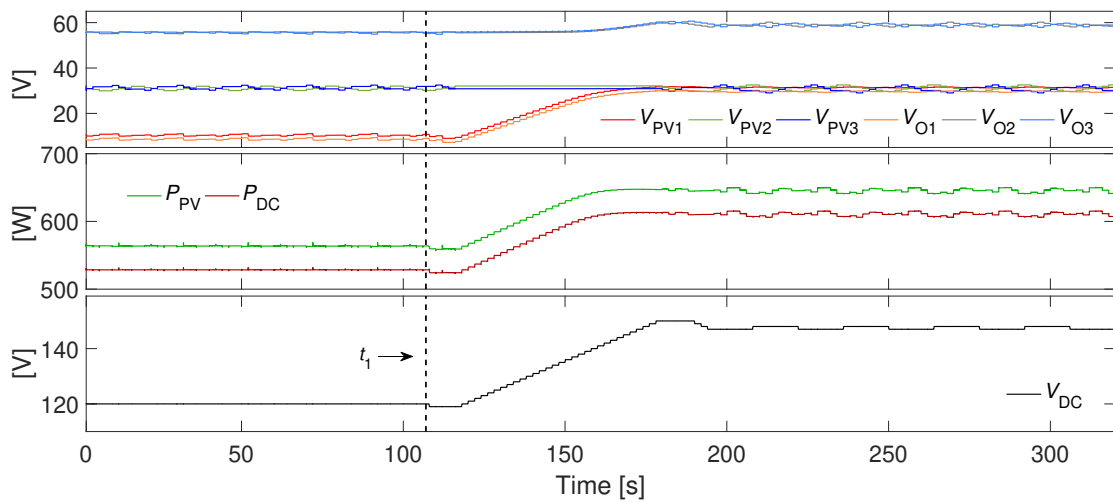
A second suboptimal scenario can be found at e.g. point D. As long as the mismatch condition is kept at the initial conditions (blue line, PV1 at  $G_L=200 \text{ W/m}^2$ , PV2 and PV3 at  $G_H=1000 \text{ W/m}^2$ ), the  $V_{DC}$  control will be continuously tracking around the point D, with no possibility to reach a higher power level.  $V_{DC}$  control might be combined with an additional technique that calculates or detects the maximum available power regions under mismatch situations to overcome these suboptimal operating conditions.

### 9.3.3.2 H-MV Dynamic performance

The dynamic response of the system for different MPPTs is shown in Fig. 9.18. A trapezoidal irradiance profile (top plot,  $G_{PV1}$ ) is used to analyse the performance of each MPPT.  $G_{PV1}$  starts at  $0.5 \text{ kW/m}^2$ , at  $t_1=50 \text{ s}$  an irradiance variation  $\dot{G}=10 \text{ W/m}^2/\text{s}$  rises up  $G_{PV1}$  until  $G_{PV1}=0.9 \text{ kW/m}^2$  at  $t_2=90 \text{ s}$ . Each PV panel is subjected to a different irradiance level ( $G_{PV2}=1.05G_{PV1}$ ,  $G_{PV3}=0.95G_{PV1}$ ). From top to bottom, for the tests performed with SV (2nd plot), MVPOC (3rd plot) and MVPOV (4th plot)



(a) P-V curve of  $N=3$  modules at two different irradiance conditions. Point A (optimal) in GMPR-1 for  $N_L=1, G_L=200 \text{ W/m}^2, N_H=2, G_H=1000 \text{ W/m}^2$ . Point B at a suboptimal level for  $N_L=1, G_L=500 \text{ W/m}^2, N_H=2, G_H=1000 \text{ W/m}^2$



(b) Increased performance of the system operating at  $N_L=1, G_L=500 \text{ W/m}^2, N_H=2, G_H=1000 \text{ W/m}^2$  after adjusting  $V_{DC}$  from point B to MPR-2 in 9.17(a).

FIGURE 9.17: H-MV performing  $V_{DC}$  control. The tracking of  $V_{DC}$  increases system efficiency.



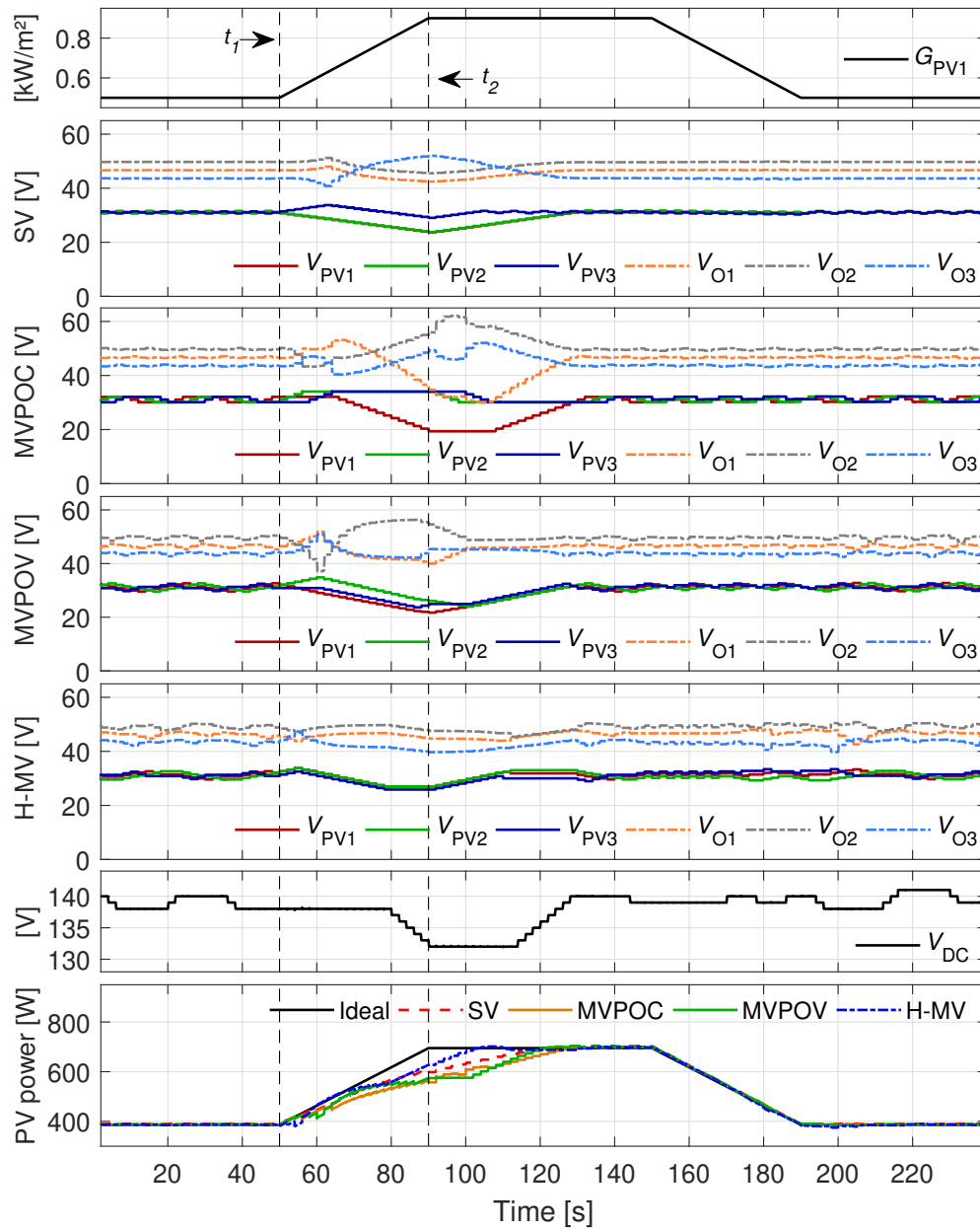


FIGURE 9.18: PV voltage deviation due to an irradiance change for different control algorithms. Top to bottom: irradiance profile for the dynamic test, SV, MVPOC, MVPOV, H-MV, H-MV  $V_{DC}$  control, and PV powers of the different techniques.

controls, the system works at a  $V_{DC}=140V$ . At constant irradiance, H-MV (5th plot) tracks  $V_{DC}$  (6th plot) in the vicinity of  $V_{DC}=140V$ .

At  $t_1$ , the PV power increases due to the increasing  $\dot{G}$ . With the conventional SV, the PV voltages deviate as a consequence of the uncoordinated operation; MVPOC tracks the same PV voltage as long as  $P_{DC}$  due to  $\dot{G}$  is higher than  $P_{DC}$  due to  $\Delta V_{PV}$ . For almost all the time the irradiance rises, it perturbs  $V_{PV1}$ ; MVPOV shows smaller PV voltage deviation than MVPOC, thanks to its MPPT promptness. All these deviations cause power differences between modules and, consequently, differences between module's output voltages. Finally, H-MV manages the control sequence, blocks  $\theta_1$ ,  $\theta_2$  and  $V_{DC}$  and performs the tracking on  $|V_{ec}|$ , avoiding PV and output voltage deviations. The maximum output voltage differences are  $\Delta V_{O,SV}=10.39V$  for SV,  $\Delta V_{O,MVPOC}=16.6V$  for MVPOC,  $\Delta V_{O,MVPOV}=14.8V$  for MVPOV and  $\Delta V_{O,H-MV}=8.16V$  for H-MV.

In addition, H-MV shows the fastest MPP recovery at  $t=100s$ , while any of the other methods reach the MPP after  $t=120s$ . The power reduction is detected faster by the MPPT techniques when the irradiance comes down than in steady state or under rising irradiance. Therefore, the perturbation direction in the SV control and the variable in the MV controls change more often, showing very small voltage deviations when the irradiance ramps-down.

The energy yield obtained with H-MV is higher than the other MPPT approaches, as can be appreciated in the bottom plot in Fig. 9.18. It shows good dynamic performance and fast MPP recovery under changing conditions. Computed global MPPT efficiencies during the overall test in Fig. 9.18 for SV, MVPOC, MVPOV and H-MV techniques result in: 97.9%, 97.2%, 97.6% and 98.7%, respectively.

### 9.3.4 Experimental results

#### 9.3.4.1 H-MV MPPT performance

Fig. 9.19 shows the start-up and steady-state of the system. The open-circuit voltage of the PV panels is  $V_{OC}\approx 33V$  and the vectorial variables are set at their corresponding values  $|V_{ec,init}|=57.32V$ ,  $\theta_{1,init}=45.16^\circ$ , and  $\theta_{2,init}=54.49^\circ$ .  $V_{DC}$  is set 20V above the sum of PV voltages ( $V_{DC}=\sum V_{PV}+20V$ ,  $V_{PV}=V_{OC}$ ) at  $V_{DC,init}=120V$ . The management in the execution of the control variables (setting only  $|V_{ec}|$ ) ensures the simultaneous rise-up of the PV voltages towards their MPP value and the system reaches faster its steady state.

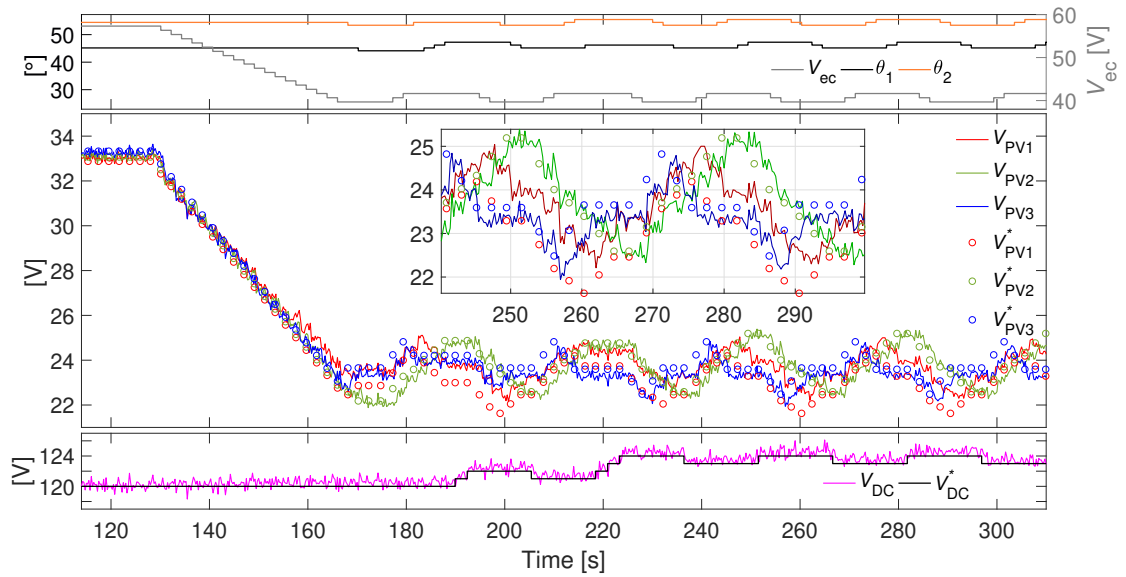


FIGURE 9.19: Experimental results of H-MV: start-up and steady state. Top to bottom: vectorial variables, PV voltage references and measurements,  $V_{DC}$  reference and measurement.

### 9.3.4.2 $V_{DC}$ control

The benefit of including the  $V_{DC}$  MPPT in the DMPPT system is highlighted in Fig. 9.20 with a test similar to the one in simulations (Fig. 9.17(b)) but with an irradiance of  $G \simeq 400 \text{ W/m}^2$ .

Half of PV1 is covered to obtain the half of the irradiance with respect to PV2 and PV3 and reproduce the mismatch conditions considered in the simulation. Initially, the performance of the system with fixed  $V_{DC}=120 \text{ V}$  is shown, with a DMPPT efficiency of  $\eta_{\text{DMPPT}}=79.2\%$ . At  $t_1=510 \text{ s}$ ,  $V_{DC}$  control is activated. H-MV tracks  $V_{DC}$  as long as  $P_{DC}$  increases to reach the GMPT. Once the system is performing at its GMPT,  $V_{DC}$  is tracked in the vicinity of  $140 \text{ V}$ . The DMPPT efficiency after the  $V_{DC}$  correction is  $\eta_{\text{DMPPT}}=92.3\%$ . Note the voltage drops in the performance of  $V_{DC}$  tracking, that are a consequence of occasional communication errors.

### 9.3.4.3 H-MV Dynamic performance

The dynamic test (Fig. 9.21) has been performed on a day with scattered clouds. Two identical DMPPT systems of  $N=3$  modules are used, with the same architecture as in Fig. 9.8. The first system performs the proposed H-MV algorithm while the second performs the conventional, distributed and uncoordinated SV P&O control. The performance of both algorithms is compared operating at a fixed DC-bus voltage of  $V_{DC}=140\text{V}$ . Starting from the top in Fig. 9.21, the vectorial MV-P&O variables in

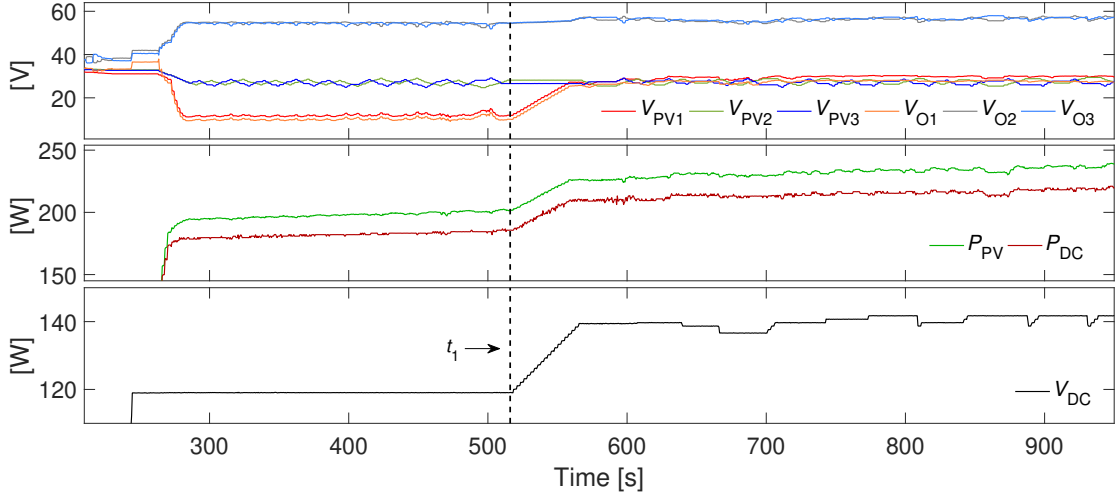


FIGURE 9.20: H-MV experimental results at  $G \simeq 400 \text{ W/m}^2$  and PV1 covered with a static shade of  $Sh=50\%$  with fixed  $V_{DC}$  before, and  $V_{DC}$  control after,  $t_1$ . Top to bottom: PV and output voltages, sum of PV and output powers,  $V_{DC}$ .

the first plot generate the PV voltage references shown in the second plot ( $V_{PV1}^*$ ,  $V_{PV2}^*$ ,  $V_{PV3}^*$ ). Third plot shows the evolution of PV and output voltages for the modules 1 to 3. The next two plots correspond to the SV-P&O control, showing the voltage references ( $V_{PV4}^*$ ,  $V_{PV5}^*$ ,  $V_{PV6}^*$ ) and the resulting PV and output voltages, respectively. Bottom plot compares the PV power of both systems, where  $P_{PV1-3}$  and  $P_{PV4-6}$  are the total PV power for the systems performing H-MV and SV-P&O, respectively. The energy at the PV panel level computed for each system in the time frame  $t=0 \text{ s}$  to  $t=600 \text{ s}$  yields:  $E_{PV1-3}=193.39 \text{ Wh}$  (H-MV) and  $E_{PV4-6}=180.5 \text{ Wh}$  (SV-P&O).

In the event of an irradiance change (at  $t \simeq 100\text{s}$ ), the difference between output voltages caused by the SV control that performs individual and uncoordinated MPPT can be appreciated in the 5th plot starting from the top. This condition highly depends on the tracking direction in each controller at the time of the irradiance variation. The proposed H-MV control detects the irradiance variation, blocks the update of  $\theta_1$ ,  $\theta_2$ , and  $V_{DC}$ , and controls  $|V_{ec}|$ , keeping the PV voltages tracking in the same direction, moving simultaneously and closer to each other, preventing PV and output voltage deviations. Improved MPP recovery is appreciated for H-MV, compared to SV, as in simulations in Fig. 9.18.

Any of the MV-P&O approaches previously presented in literature would cause much larger deviations between output voltages of the modules as shown in simulation results in Fig. 9.18. Staying within the modules' output voltage limits keeps the system stable and in a safe operation mode.

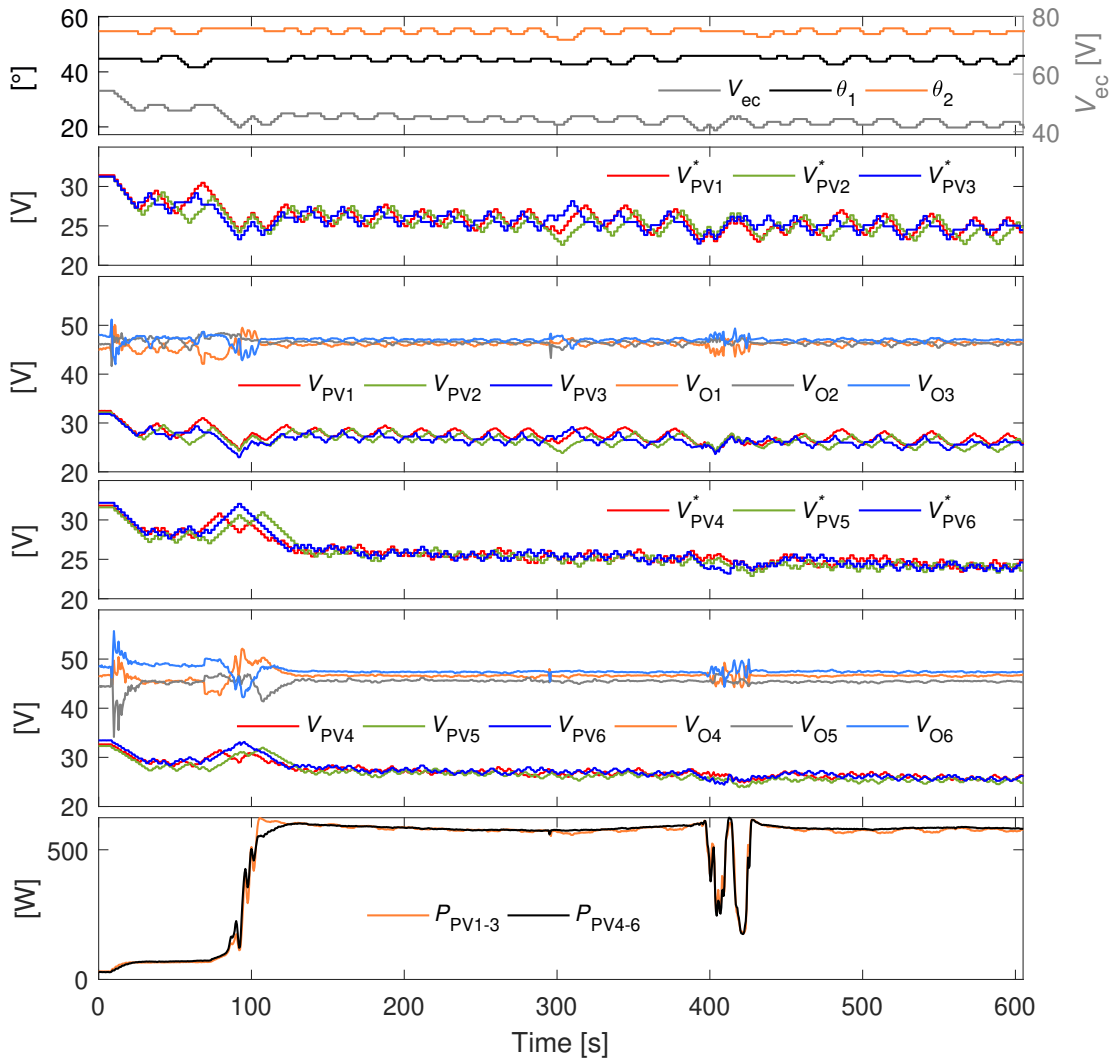


FIGURE 9.21: H-MV dynamic performance: experimental results in a day with scattered clouds. Top to bottom: vectorial variables, H-MV PV voltage references, H-MV PV and output voltages, SV PV voltage references, SV PV and output voltages, H-MV and SV PV powers.

## 9.4 Discussion of results

Multi-variable algorithms have demonstrated to be as effective as individual MPPT control in DMPPT systems. However, the dynamic response of the multi-variable control needs to be treated differently, with a specific functionality that significantly reduces output voltages differences when PV panels operate under changing irradiance conditions. Consequently, the power difference between modules is smaller and the output voltage stress is reduced. System stability is achieved by keeping the output voltages of the modules away from their safe operating limits.

In addition, the inclusion of the DC-bus voltage control in the multi-variable control

sequence has proved to be a straightforward method to coordinate the operation between distributed and central MPPT functions, preventing the simultaneous change of reference for the different variables. The effectiveness of the H-MV algorithm has been demonstrated in DMPPT systems with boost type converters. Besides, H-MV control is suitable for DMPPT systems comprising different converter topologies in their modules.

This new approach provides full control of the PV and DC-bus voltages under static and dynamic operating conditions and opens the door to new strategies such as output voltage balancing of the modules in DMPPT systems.

## Chapter 10

# Improvements in the Multi-Variable P&O control

The H-MV control presented in chapter 9 solves some dynamic performance issues of MV algorithms with a new functionality derived from MVPOV in [92]. Nonetheless, this new functionality is not optimized and the dynamic performance of the H-MV control still presents some undesired PV and output voltage deviations, deteriorating the power generation. Such deviations can be attenuated if the algorithm in charge of controlling the system takes into account the slope of the irradiance variation and adapts the control variables accordingly.

In this chapter a new adaptive control strategy, the centralized MV (CMV) control is introduced, able to correctly track any irradiance variation speed. Moreover, the power is measured at the output terminals of the inverter instead of at the DC bus as in chapter 9, so that the optimization process takes into account the efficiency of the overall power processing system, including both the DC and the AC stages. The proposed CMV control exploits the benefits of the MV approach improving both static and dynamic performances as well as boosting the overall efficiency of the DMPPT system.

Part of this work has been presented at ELECTRIMACS 2019 Salerno (Italy) and published in Springer book in the series *Lecture Note in Electrical Engineering* associated to ELECTRIMACS [98].

### 10.1 Proposed centralized multi-variable control

The proposed CMV approach enhances the H-MV algorithm presented in Chapter 9, (i) improving the dynamic response of the system for any irradiance variation speed,

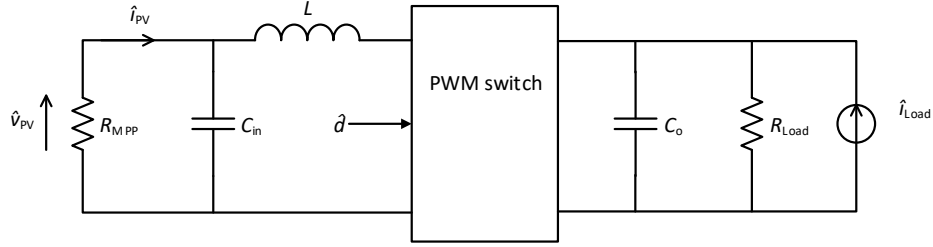


FIGURE 10.1: Small-signal equivalent circuit [99].

(ii) evaluating the power at the AC side of the inverter thus also accounting for the inverter conversion efficiency. Therefore, the irradiance level  $G$  in (9.19) is now considered proportional to the AC power:

$$G = 1\text{kW/m}^2 \cdot \frac{P_{AC}}{P_{AC @ G=1\text{kW/m}^2}} \quad (10.1)$$

According to [91],  $\Delta V_{PV}$  depends on the PV module parameters, on the irradiance level, on  $\Delta t$  and also on the maximum rate of variation of the irradiance ( $\dot{G}_{\max}$ ) the MPPT algorithm is able to track [99].

### 10.1.1 Time interval between two consecutive perturbations

We can determine  $\Delta t$  with the small-signal analysis of the boost converter. The small signal equivalent circuit of the system under study is represented in Fig. 10.1. As first approach, an output voltage of  $V_o=60$  V is considered and operating at a constant load thus the variations of the array voltage caused by load changes is not taken into account. Assuming CCM operation, the small signal PV voltage is [100]:

$$\hat{v}_{PV} = G_{V_p^d} \cdot \hat{d} \quad (10.2)$$

where  $\hat{d}$  is the small-signal variation of the duty cycle ( $d$ ). The control-to-array voltage transfer function  $G_{V_p^d}$  leads:

$$G_{V_p^d} = \frac{V_o}{LC_{in}s^2 + \left( \frac{L}{R_{Load}(1-D)^2} \right) s + 1} \quad (10.3)$$



TABLE 10.1: Characteristic parameters of the BenQ GreenTriplex PM245P00 260Wp.

Electrical characteristics	Value @ STC <sup>1</sup>
Short-circuit current $I_{SC}$	8.83 [A]
Open-circuit voltage $V_{OC}$	37.7 [V]
MPP current $I_{MPP}$	8.34 [A]
MPP voltage $V_{MPP}$	31.2 [V]
Temperature coefficient of $I_{SC}$ ( $\alpha_I$ )	0.065 [%/°C]
Temperature coefficient of $V_{OC}$ ( $\alpha_V$ )	-80 [mV/°C]

TABLE 10.2: Main parameters of the boost DC/DC converter

Symbol	Description	Value
$L$	Inductor	0.45 [mH]
$C_{in}$	Input capacitor	100 [ $\mu$ F]
$V_o$	Converter output voltage	60 [V]

For an ideal boost converter considering no losses,  $R_{in}=R_{Load}(1-D)^2$  [101]. The transfer function  $G_{V_p^d}$  assumes from the classical control theory:

$$G_{V_p^d} = \frac{\mu\omega_n^2}{s^2 + 2\xi\omega_n s + \mu\omega_n^2} \quad (10.4)$$

where  $\mu=-V_o$  is the DC gain,  $\omega_n=1/\sqrt{LC_{in}}$  is the natural resonance pulsation, and  $\xi=\frac{1}{2R_{in}}\sqrt{\frac{L}{C_{in}}}$  is the damping factor. The maximum PV array power is obtained when  $R_{in}=R_{MPP}$ . Using the parameters from Table 10.2,  $\omega_n=4714$  rad/s and  $\xi=0.2835$ . The minimum time interval to ensure that the system reaches steady state, is:

$$T_\zeta \simeq -\frac{1}{\xi\omega_n} \ln(\zeta/2)|_{\zeta=0.1} \quad (10.5)$$

where  $\zeta = 0.1$  is a typical value in control engineering [100]. For the parameters in Tables 10.1 and 10.2,  $\Delta t$  should be equal or higher than  $T_\zeta$ :

$$\Delta t \geq T_\zeta = 3.7\text{ms}. \quad (10.6)$$

### 10.1.2 Design of the voltage step amplitude

Denoting  $\Delta P_{oV}$  as the power variation at the DC-bus due to the voltage step perturbation, and  $\Delta P_{oG}$  as the power variation at the DC-bus due to an irradiance variation, the correct tracking is ensured if:

$$|\Delta P_{oV}| > |\Delta P_{oG}| \quad (10.7)$$

TABLE 10.3: Photovoltaic parameters for the design of  $\Delta V_{PV}$ .

PV parameters	Value
Initial irradiance level $G_{\text{init}}$	600 [W/(m <sup>2</sup> )]
Max irradiance variation $\dot{G}_{\text{max}}$	50 [W/m <sup>2</sup> /s]
Short-circuit coefficient $K$	8.83 [mA · m <sup>2</sup> /W]
$H _{@G=600 \text{ W/m}^2/\text{s}}$	0.0185 [A/V <sup>2</sup> ]
$R_{\text{MPP}} _{@G=600 \text{ W/m}^2/\text{s}}$	6.235 [ $\Omega$ ]
Converter output voltage $V_O$	$\simeq 60$ [V]

With the conventional SV-P&O algorithm, the minimum value of the perturbation amplitude  $\Delta V_{PV}$  for a given maximum irradiance variation  $\dot{G}_{\text{max}}$  is given by [99]:

$$\Delta V_{PV,\text{min}} = \sqrt{\frac{V_{\text{MPP}} \cdot K \cdot \dot{G}_{\text{max}} \cdot \Delta t}{H \cdot V_{\text{MPP}} + \frac{1}{R_{\text{MPP}}}}} \quad (10.8)$$

where  $R_{\text{MPP}}$  is the differential resistance of the PV module evaluated in its MPP,  $V_{\text{MPP}}$  the PV voltage at MPP,  $H$  the second derivative of the PV current with respect to the PV voltage evaluated at the MPP, and  $K$  is a coefficient proportional to the derivative of the PV current with respect to the irradiance [99]. These are characteristic parameters that depend on the chosen PV panel (Table 10.1) and converter (Table 10.2) under a given irradiance level  $G_{\text{init}}$ .

$\Delta V_{PV}$  must fulfil the following condition to ensure a correct tracking for irradiance variations slower than  $G_{\text{max}}$ :

$$\Delta V_{PV} > \Delta V_{PV,\text{min}} \quad (10.9)$$

The electrical characteristics of the BENQ GreenTriplex 260Wp PV panels are gathered in Table 9.1. Following the guidelines in [99], the PV parameters for the MPPT controller are obtained (Table 10.3). With the values in Table 10.3, we obtain that  $\Delta V_{PV,\text{min}} = 0.35$  V. The adopted voltage step is  $\Delta V_{PV} = 0.4$  V.

### 10.1.3 Proposed adaptive control

Unfortunately, for a new irradiance variation  $\dot{G}$  greater than  $\dot{G}_{\text{max}}$ ,  $\Delta V_{PV}$  is no longer sufficient to correctly track the MPP, thus a new value has to be set. An adaptive control that takes into account the irradiance variation speed and the irradiance level is proposed here. If we consider that  $\dot{G} > \dot{G}_{\text{max}}$ , a correction factor is included and the

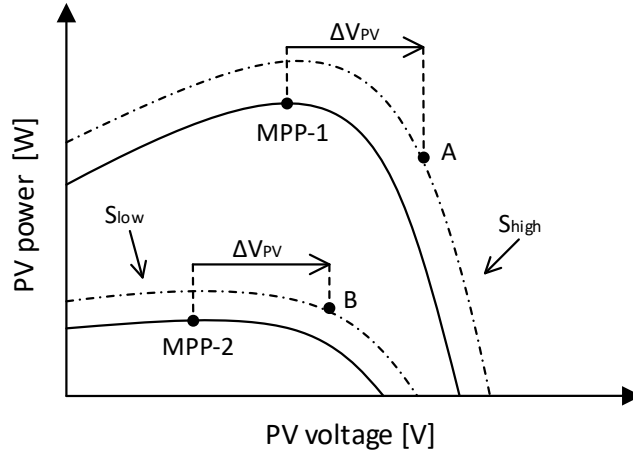


FIGURE 10.2: Zoomed view of the PV panel operating point in presence of an irradiance variation at two different irradiance levels:  $G_{\text{low}}$  and  $G_{\text{high}}$ , solid lines. Increasing variation of the irradiance, dashed lines.

new  $\Delta V_{\text{PV}}$  becomes:

$$\Delta V_{\text{PV},a} = \sqrt{\frac{\dot{G}}{\dot{G}_{\text{max}}}} \cdot \Delta V_{\text{PV}} \quad (10.10)$$

where  $\Delta V_{\text{PV},a}$  is the adapted value of  $\Delta V_{\text{PV}}$ . This condition holds if  $G \geq G_{\text{init}}$ . The CMV algorithm performs a good MPPT if the power variation  $\Delta P_{\text{PV}}$  due to  $\Delta V_{\text{PV}}$  perturbation is bigger than the power variation  $\Delta P_{\dot{G}}$  caused by the irradiance variation  $\dot{G}$ :

$$\Delta P_{\text{PV}} > \Delta P_{\dot{G}} \quad (10.11)$$

The P-V curve of a PV panel based on silicon technology tends to be flatter in the vicinity of the MPP as irradiance  $G$  lowers [62]. Fig. 10.2 shows a zoomed view of the characteristic P-V curve at different  $G$ . The curves change due to a variation of the irradiance between two consecutive sampling instances. The change in power depends on the derivative of the PV power  $\Delta P_{\text{PV}}$  with respect to  $\Delta V_{\text{PV}}$  ( $\Delta P_{\text{PV}}/\Delta V_{\text{PV}}$ ). For the same  $\Delta V_{\text{PV}}$  in Fig. 10.2, if the converter is working at MPP-1, the next operating point will be point A, satisfying the inequality (10.11). On the contrary, if the converter is working at MPP-2, the next operating point will be point B, thus detecting an increase in power and  $V_{\text{PV}}$  will further increase, moving the operating point away from the MPP.

Adding a second correction factor to  $\Delta V_{\text{PV},a}$  in (10.10) improves the MPPT performance of the H-MV at different irradiance levels. As  $\Delta P_{\text{PV}}$  corresponding to a voltage step

TABLE 10.4: Perturbation amplitudes of the variables.

Symbol	Description	Value
$\Delta V_{PV}$	PV Voltage perturbation	0.4 V
$\Delta V_{ec}$	$V_{ec}$ perturbation	0.7 V
$\Delta\theta_1, \Delta\theta_2$	$\theta_1$ & $\theta_2$ perturbation	0.73 °
$\Delta V_{DC}$	DC-bus voltage step perturbation	0.1 V

perturbation is inversely proportional to the irradiance level  $G$ , it follows:

$$\Delta V_{PV,a} = \sqrt{\frac{\dot{G}}{\dot{G}_{\max}}} \cdot \frac{G_{\text{init}}}{G} \cdot \Delta V_{PV} \quad (10.12)$$

Translating (10.12) to the spherical coordinates [92], we obtain the adapted value for the perturbation step of  $|V_{ec}|$  for a system of  $N$  modules:

$$\Delta V_{ec,a} = \sqrt{N} \cdot \Delta V_{PV,a} \quad (10.13)$$

## 10.2 Simulation results

The simulations are carried out in the MATLAB-Simulink environment. The system consists of  $N=3$  modules, each composed of one BENQ-260 W<sub>p</sub> PV panel connected to an interleaved boost-3PC [87] and an inverter. The main electrical characteristics of the PV panel in STC are listed in Table 8.1. The inverter is modeled using the efficiency curves of a scaled-down commercial solar inverter with DC bus voltage control in a range of [70, 240] V and a nominal power of 1.5 kW. The implementation includes a 2-D look-up table of efficiency curves as function of  $P_{DC}$  and  $V_{DC}$ .

Table 10.4 gathers the minimum voltage perturbation steps for the SV and vectorial multi-variable controls, designed to track a maximum irradiance variation of  $\dot{G}_{\max}=50$  W/m<sup>2</sup>/s. According to the guidelines in [99] the minimum time interval that ensures that the system reaches the steady state after a voltage step perturbation is  $\Delta t=3.7$  ms. Simulation results in Fig. 10.3 show the steady state behavior of the system. The vectorial variables (top plot) and  $V_{DC}$  (bottom plot) perform the P&O three-point behaviour in the multi-variable sequence. The resulting PV voltages waveform is observed in middle plot.

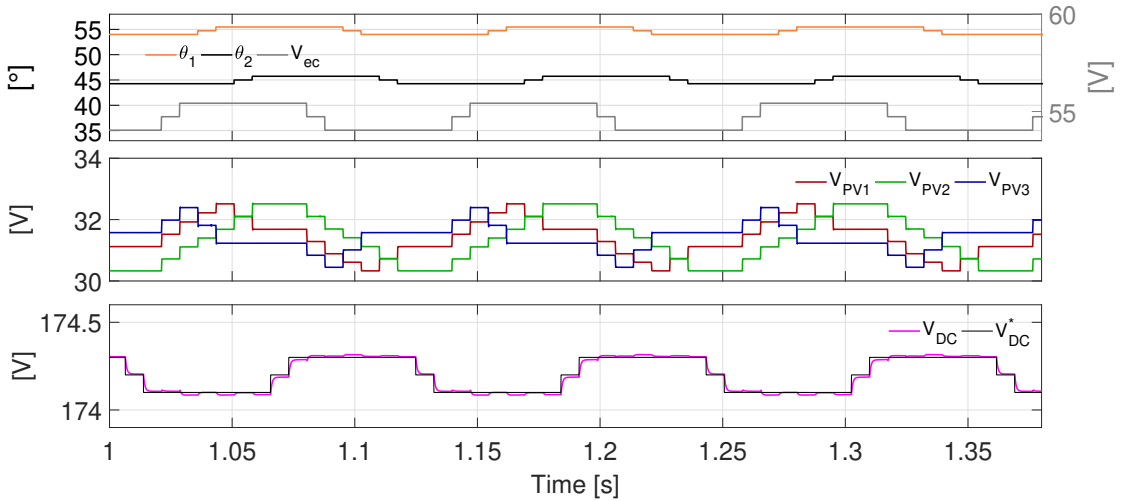


FIGURE 10.3: Simulation results of the steady state operation of the CMV control technique. Top plot: variables in spherical coordinates. Middle plot: PV voltages. Bottom plot:  $V_{DC}$  measurement and reference.

### 10.2.1 $V_{DC}$ control

In Fig. 10.4 the performances of MVPOV and CMV are compared. When the MVPOV performs, the  $V_{DC}$  providing the maximum AC power under homogeneous irradiance condition  $G=700 \text{ W/m}^2$  is fixed to  $V_{DC}=174.2 \text{ V}$ . The simulation starts with the PV panels under non-uniform irradiance levels ( $G_1=700 \text{ W/m}^2$ ,  $G_2=G_3=1000 \text{ W/m}^2$ ). At time  $t=2 \text{ s}$ , the irradiance becomes  $G=700 \text{ W/m}^2$  for all the PV panels. CMV seeks a  $V_{DC}$  value that ensures highest conversion efficiency for the new generation conditions, adapting  $V_{DC}$  stepwise from around  $183.7 \text{ V}$  to the vicinity of  $174.2 \text{ V}$ . At time  $t=4 \text{ s}$  a sudden ambient temperature change from  $T_a=25 \text{ }^\circ\text{C}$  to  $T_a=50 \text{ }^\circ\text{C}$  is imposed on one of the PV panels. Though this condition is not realistic, it shows the ability of the algorithm to adapt  $V_{DC}$  operating point also to different temperature conditions.

The MPPT performance is comparable for both MVPOV and CMV techniques (Fig. 10.4, top plot). When a change in power occurs, MVPOV reaches steady state faster than CMV. This is due to the simultaneity of the power transition event and the variable that is being perturbed. As long as  $V_{DC}$  control is being performed, the PV voltages will remain unchanged. From Fig. 10.4, it can be concluded that CMV ensures the highest overall efficiency of the PV system.

The CMV algorithm is able to correct  $V_{DC}$  operating point as well as the PV voltages under non-homogeneous irradiance conditions. Although the efficiency of the overall system is barely improved, the simulation shown in Fig. 10.4 validates the proposed joint operation of the distributed and centralized control.

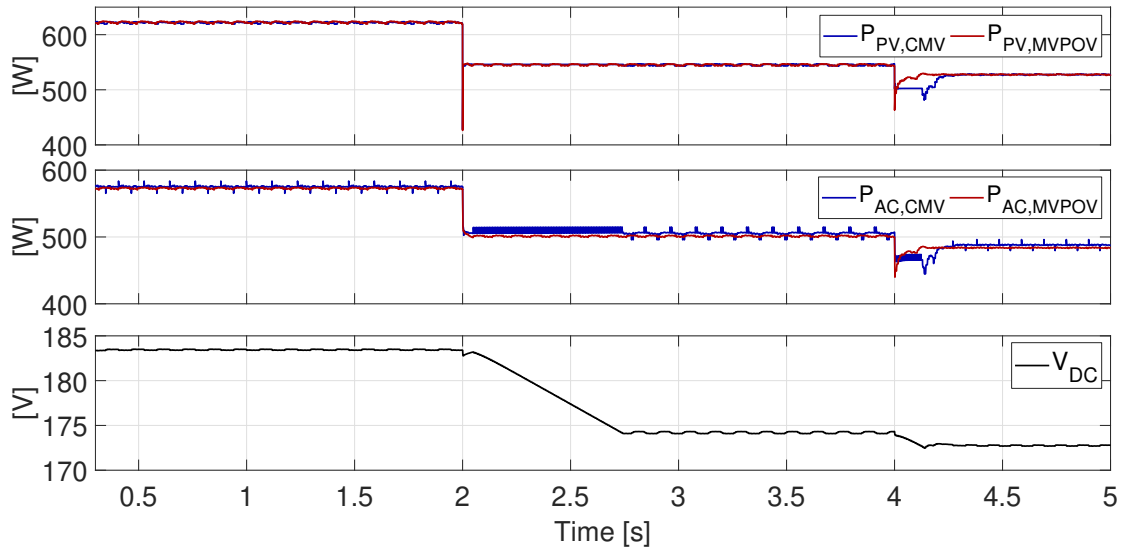


FIGURE 10.4: Simulation results of the system adopting the MVPOV (red line) and the CMV algorithm that includes the  $V_{DC}$  control (blue line). Top to bottom: PV power, AC power and CMV  $V_{DC}$ .

The performance improvement in this kind of PV systems depends on the ratio between the nominal  $P_{DC}$  of the inverter and the PV peak power, the number of PV panels and DC/DC converters, their topology and the efficiency curve of the inverter operating in the system.

### 10.2.2 Dynamic performance of the proposed control algorithm

The CENELEC standard EN 50530 proposes a test procedure to evaluate the dynamic performance of algorithms dedicated to PV system control [102]. Two test sequences with different irradiance levels are proposed (sequence A fluctuates between  $100 \text{ W/m}^2$  and  $500 \text{ W/m}^2$  and sequence B between  $300 \text{ W/m}^2$  and  $1000 \text{ W/m}^2$ ), as well as a range of irradiance variation speeds. The dynamic performance is validated using the fastest irradiance variation of  $\dot{G} = 100 \text{ W/m}^2/\text{s}$  belonging to the sequence B. The simulations are carried out under homogeneous irradiance variation for all the PV panels to prove the validity of the proposed algorithm. The non-homogeneous PV generation can be compensated using batteries at module level and mimic homogeneous irradiance conditions. Fig. 10.5 shows a comparison between the SV and CMV controls. Both SV and CMV algorithms do small perturbation steps in steady state, with  $\dot{G}_{\max} = 50 \text{ W/m}^2/\text{s}$  as the threshold to switch between static and dynamic behavior.

SV  $\Delta V_{PV}$  and CMV  $\Delta V_{ec}$  are calculated using the methodologies described in [91] and [92] (Table 10.4). For the irradiance rise,  $\Delta V_{PV}$  and  $\Delta V_{ec}$  are adapted according to (10.12) and (10.13), respectively.

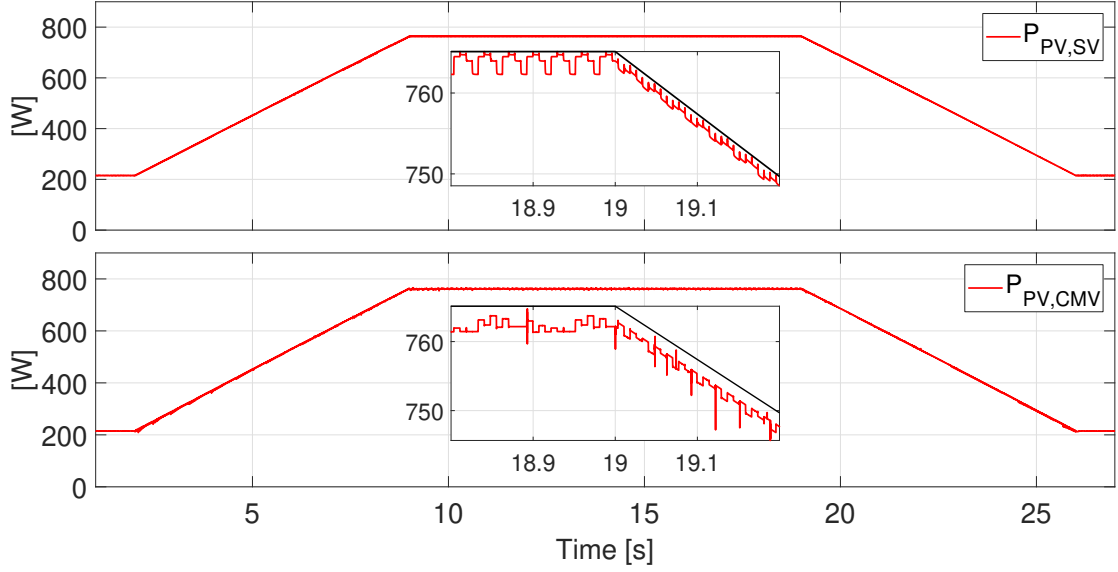


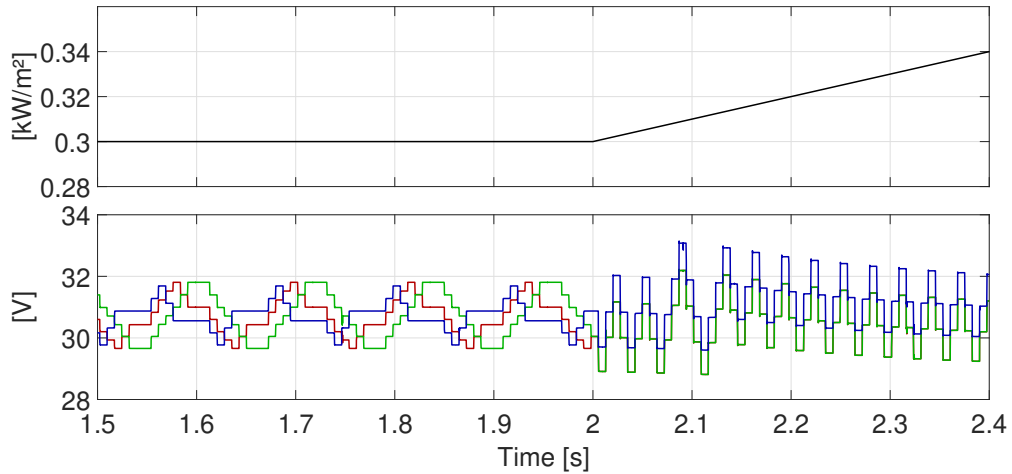
FIGURE 10.5: EN 50530 dynamic performance test adopting either SV (top plot) and H-MV (bottom plot) control algorithms.

TABLE 10.5: MPPT and conversion efficiencies (in %) for the 5 subintervals of the simulations in Fig. 10.5 with either constant irradiance ( $\text{W}/\text{m}^2$ ) or varying irradiance ( $\text{W}/\text{m}^2/\text{s}$ ).

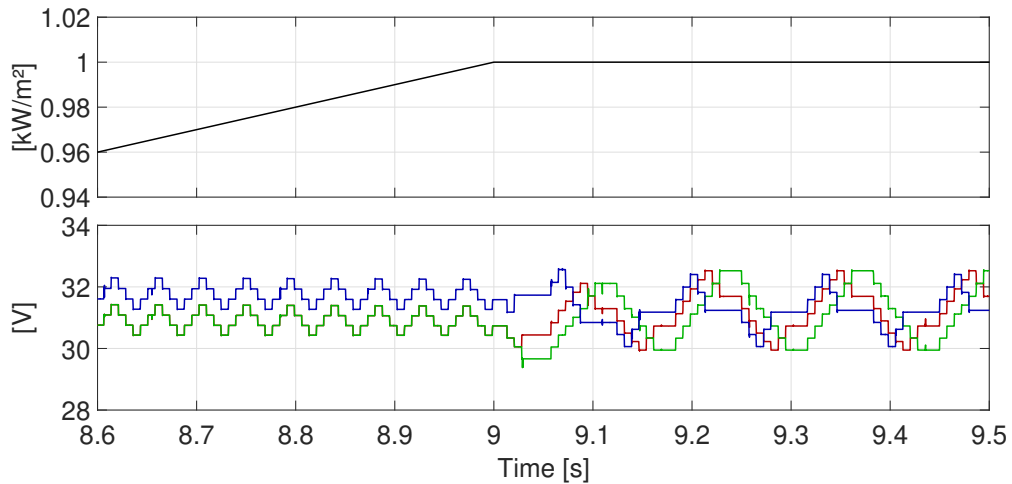
$G$ ( $\text{W}/\text{m}^2$ )	300	$300 \rightarrow 1000$	1000	$1000 \rightarrow 300$	300
$\eta_{\text{MPPT,SV}}$	99.78	99.69	99.87	99.71	99.81
$\eta_{\text{MPPT,CMV}}$	99.58	99.52	99.59	99.62	99.56
$\eta_{\text{conv,SV}}$	92.19	95.74	95.46	95.55	92.19
$\eta_{\text{conv,CMV}}$	96.30	95.67	95.40	95.59	95.80
$\eta_{\text{Inv,SV}}$	91.14	93.37	96.78	96.19	91.64
$\eta_{\text{Inv,CMV}}$	89.75	94.31	96.96	95.57	90.77
$\eta_{\text{Total,SV}}$	83.84	89.12	92.27	91.64	84.32
$\eta_{\text{Total,CMV}}$	86.07	89.79	92.12	91.01	86.58

For the test in Fig. 10.5 the energy yields are  $E_{\text{SV}} = 236.34$  Wh and  $E_{\text{CMV}} = 236.36$  Wh for SV and CMV approaches, respectively. The efficiencies of each conversion stage per subinterval of either constant or varying irradiance gathered in Table 10.5 are computed within the simulation time shown in Fig. 10.5. The total efficiency is obtained by computing the MPPT, converters' and inverter's efficiencies:  $\eta_{\text{Total}} = \eta_{\text{MPPT}} \cdot \eta_{\text{conv}} \cdot \eta_{\text{Inv}}$ .  $\eta_{\text{Total}}$  is considerably higher for CMV compared to SV at lower irradiance levels, thanks to an increase of  $\eta_{\text{conv}}$ .

Figs. 10.6 and 10.7 shows the performance of the proposed CMV algorithm in detail.



(a) Steady state performance at low  $G$  and adaptive  $V_{PV}$  control for  $\dot{G} \neq 0$  starts at  $t = 2$  s for the CMV acting only on  $V_{ec}$ .



(b) CMV implementing the adaptive  $V_{PV}$  control for  $\dot{G} \neq 0$  acting only on  $V_{ec}$  and the steady state performance starts at  $t = 9$  s at high  $G$ .

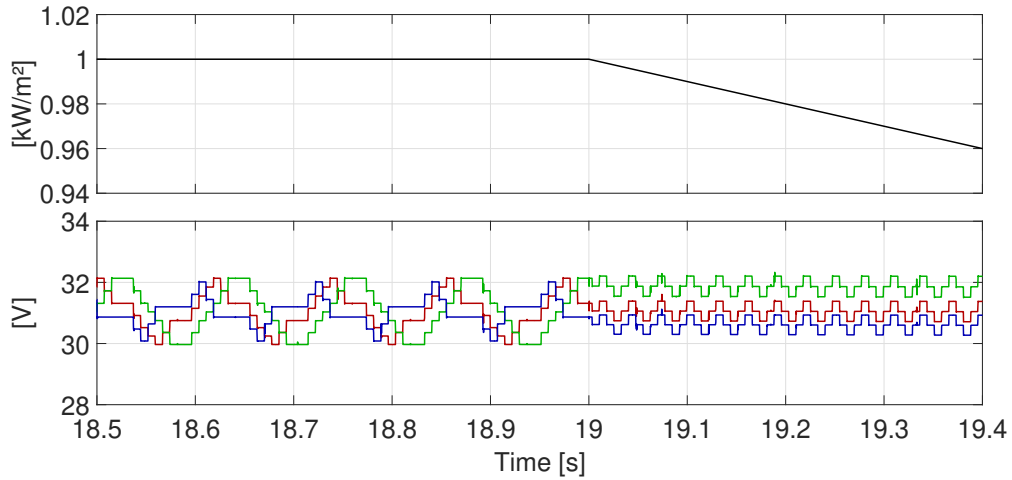
FIGURE 10.6: Details of the CMV control performance. Static and dynamic behaviour of the PV voltages under rising irradiance variation.

At  $\dot{G} = 100 \text{ W/m}^2/\text{s}$  variation, the P&O control acts only on  $|V_{ec}|$ . The amplitude of the PV voltage step is modified according to (10.12), is larger at lower  $G$  (Fig. 10.6(a) and Fig. 10.7(b)) while at high  $G$  it is reduced (Fig. 10.6(b) and Fig. 10.7(a)), showing the characteristic three-point-behaviour in P&O control. This way, CMV is able to track the irradiance variation of any speed without any significant voltage deviation.

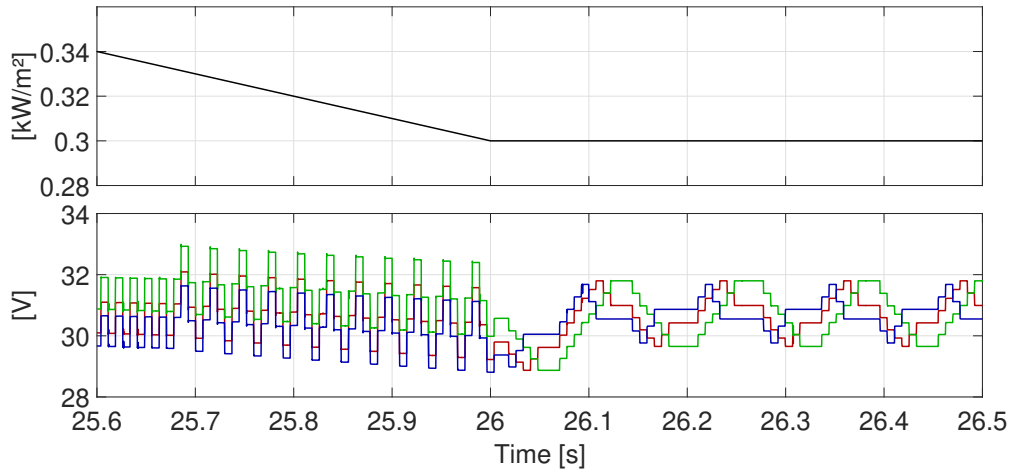
### 10.3 Discussion of results

In DMPPT systems, the dynamic response of the multi-variable control needs to be treated differently from individual MPPT control, with a specific functionality that avoids the divergence of the voltage variables from their respective optimal operating





(a) Steady state performance at high  $G$  and adaptive  $V_{PV}$  control for  $\dot{G} \neq 0$  starts at  $t=19$  s for the CMV acting only on Vec.



(b) CMV implementing the adaptive  $V_{PV}$  control for  $\dot{G} \neq 0$  acting only on Vec and the steady state performance starts at  $t=26$  s at low  $G$ .

FIGURE 10.7: Details of static and dynamic behaviour of the PV voltages under lowering irradiance variation.

points under changing irradiance conditions. The proposed modifications in the CMV control allow the PV voltages to be kept close to their optimal operating point, improving dynamic performance, that is comparable to SV control. Since the design of the perturbation variable does not only depend on the variation speed of the irradiance, but also on its level, a solution that increases the efficiency of the system by improving the MPPT performance of the algorithm is proposed, taking into account the irradiance level.

In addition, the inclusion of the  $V_{DC}$  control in the multi-variable control has proved to be an effective and straightforward method to coordinate the control between distributed and central MPPT. By only evaluating the power at the AC side, the proposed control is able to optimize the overall system's performance and the evaluation of the

performance at each power conversion stage (MPPT, DC/DC and DC-AC conversion) is not necessary.

## Chapter 11

# Control strategies for DMPPT systems including batteries

In this chapter, the DMPPT system uses the interleaved boost-3PC [87] with the PV panel and the battery. Irradiance conditions that are different for some of the PV panels in the string may cause large voltage differences in the output of the converters. In the absence of a suitable  $V_{DC}$  value at least one module has to stop performing its MPPT or force the system to operate at a LMPR. Besides, irradiance variations can affect the PV string partially (e.g. passing clouds cast a shadow only over some of the PV panels in the string), deviating the output voltage of one or more modules.

Batteries at each module are used to compensate the voltage differences storing part of the generated PV energy or discharging previously stored energy. The MPPT operating range is extended with the batteries as support to the PV generation. Two different strategies are presented in this chapter. The first is devoted to keep all modules' output voltages within a certain range, ensuring the MPPT operating range. The second strategy compensates the power difference between modules and performs output voltage equalization.

Part of the work in this chapter has been presented at the *20th European Conference on Power Electronics and Applications (EPE'18 ECCE Europe)* [95].

### 11.1 MPPT operating range extension

The presented system (Fig. 11.1(a)) shows increased performance under large mismatching conditions thanks to the adopted strategies: (i) an adaptive DC-bus voltage extends the MPPT operating range of the converters dedicated to control single photovoltaic

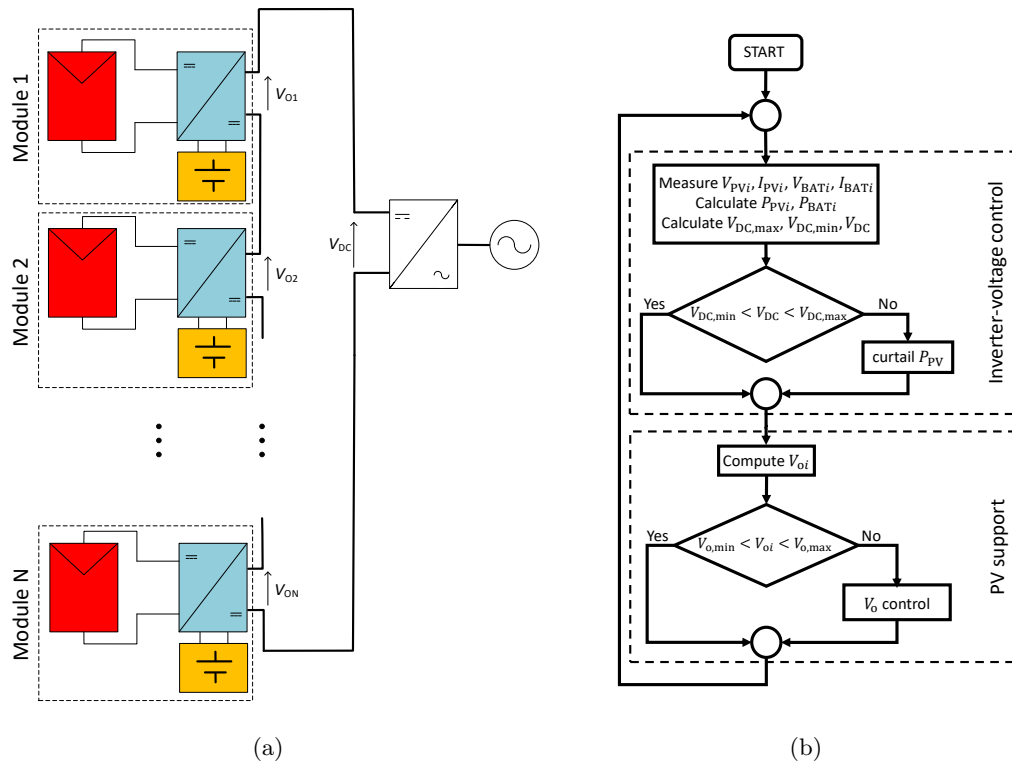


FIGURE 11.1: (a) Battery-integrated DMPPT system consisting of  $N$  DC/DC converters for each PV panel. (b) Control algorithm managing  $V_{DC}$  and output voltages of the converters.

panels and (ii) the integration of batteries at module-level further compensates the output voltage level of the converters. A novel output voltage calculation is presented as well, providing full control of the converters' output voltages along with reduced sensing circuitry.

DMPPT systems are not able to completely suppress mismatching losses. With boost converters in the modules,  $V_{oi}$  must be within  $V_{PV_i}$  and  $V_{o,max}$ , which are the  $i$ -th output and PV voltages of the  $i$ -th module, and the maximum allowed output voltage in the converters, respectively. If the generation conditions between converters are sufficiently different, it may occur that this requirement is not met. Previous chapters analyse the optimal  $V_{DC}$  operating ranges under different mismatching conditions. The implementation of a  $V_{DC}$  control allows each PV panel to operate at its MPP under greater generation differences than in a system with fixed  $V_{DC}$ .

If  $V_{DC}$  is out of the aforementioned range (e.g. if it has to match with the input voltage range of the inverter  $R_{inv}$ ), not all the PV panels can work at their MPP. The integration of batteries in the modules (Fig. 11.1(a)) overcomes this constraint and gives support to the PV generation compensating the unbalance between output voltages ( $V_{os}$ ). The

proposed control algorithm consists of a  $V_{DC}$  control based on [61] and a compensating  $V_o$  control using batteries.

### 11.1.1 Proposed control algorithm

The control algorithm shown in Fig. 11.1(b) consists of two parts. First, the  $V_{DC}$  control part is in charge of setting  $V_{DC}$ . It first calculates the PV and battery powers and determines a suitable  $V_{DC}$  range that allows a proper operation of the modules.  $V_{DC}$  is defined thereafter as the average value within its range. Avoiding the simultaneous setting of the new references for  $V_{DC}$  and any  $V_{PV}$  prevents an incorrect  $P_{DC}$  evaluation.

Second, the  $PV$  support part calculates  $V_{oi}$  and decides if the batteries collaborate to maintaining a proper operation of the system charging or discharging themselves. Since  $V_{oi}$  is proportional to  $P_{oi}$  which is the  $i$ -th output power of the  $i$ -th module, it can be calculated online without the need for additional sensing. The  $V_o$  control block ensures that the output voltages operate within the required voltage range using the batteries as support to the PV generation.

#### 11.1.1.1 $V_{DC}$ control

$V_{DC}$  operating limits are calculated rewriting (8.18) and (8.19) [61] described in section 8.5.1, but also accounting for battery power:

$$V_{DC,max} = V_{o,max} \left( \frac{\sum_{i=1}^N P_{oi}}{\max_{j \in N} P_{oj}} \right) \quad (11.1)$$

$$V_{DC,min} = \frac{k_{min}}{P_{PV,min}/P_{PV,max}} V_{MPP} \left( \frac{\sum_{i=1}^N P_{oi}}{\max_{j \in N} P_{oj}} \right) \quad (11.2)$$

where  $P_{oi}$  is normalized with reference to the maximum output power amongst the converters. The minimum voltage conversion gain  $k_{min}=1$  for boost converters. Considering an ideal system with no losses, the output power of a single converter is the sum of the PV and battery powers ( $P_{oi} = P_{PV_i} + P_{BAT_i}$ ). The maximum output voltage  $V_{o,max}$  is given by the maximum physical constraint of the switching device at the output of the converter. For the converter in Fig. 9.2, this constraint is the maximum allowed voltage across switches  $S_1$  and  $S'_1$ . As the batteries are used as support to the PV generation, there is no minimum battery power to be considered when calculating  $V_{DC,min}$ . Therefore, only the ratio between PV powers is needed ( $P_{oi} = P_{PV_i}$ ). Replacing  $\alpha_{low}$  (section

8.5.1 (8.19), the lowest  $\alpha$  in the PV string) by the normalized minimum PV power ( $P_{PV,\min}/P_{PV,\max}$ ),  $V_{DC,\min}$  can be obtained.  $V_{DC}$  reference is set to an intermediate value within the range  $[V_{DC,\min} < V_{DC}^* < V_{DC,\max}]$ .

### 11.1.1.2 Batteries as support to PV generation

$V_{oi}$  is proportional to the power delivered by the  $i$ -th converter to the DC-bus:

$$V_{oi} = V_{DC} \frac{P_{oi}}{P_{DC}} \quad (11.3)$$

Batteries are used to help the system operate while the ratio between the PV powers is excessively large and the output voltages reach one of the boundaries previously mentioned ( $V_{oi} = V_{BATi}$  or  $V_{oi} = V_{o,\max}$ ). The availability to charge or discharge the battery of each module depends on its state-of-charge ( $SoC$ ), delimited by its maximum and minimum values  $[SoC_{\min} < SoC < SoC_{\max}]$ .  $SoC$  is a value ranging from zero to one, calculated from the battery current ( $I_{BAT}$ ) using the Coulomb counting method:

$$SoC = SoC_{\text{init}} + \frac{1}{C_{\text{BAT}}} \int I_{\text{BAT}} dt \quad (11.4)$$

where  $SoC_{\text{init}}$  is the initial state-of-charge and  $C_{\text{BAT}}$  is the battery capacity. For the  $i$ -th module, when  $V_{oi}$  approaches  $V_{BATi}$  and the state-of-charge of the battery is above  $SoC_{\min}$ , the battery starts discharging ( $I_{BATi} > 0$ ) in order to keep  $V_{oi}$  above  $V_{BATi}$ . If the battery is unable to provide energy, the controller does not act and  $V_{oi}$  can further decrease. Without battery support, the  $V_{PVi} < V_{oi}$  inequality has to be met to avoid that the converter stops the MPPT operation. On the contrary, if  $V_{oi} = V_{o,\max}$  and  $SoC$  is below  $SoC_{\max}$ , the battery is charged ( $I_{BATi} < 0$ ) and  $V_{oi}$  remains under its maximum admissible value.

## 11.1.2 Simulation results

The system consists of 6 series-connected modules connected to a current source in order to model the inverter. The PV model in the Matlab-Simulink uses the parameters of the PV panel in Table 11.1. The battery is modelled as a constant voltage source with a computing  $SoC$  based on (11.4). The averaged model of the interleaved boost-3PC (see chapter 9.1) is used for the converters.

The indices notation of the different variables throughout the discussion of the simulation results is treated as follows:  $G_i$ ,  $V_{PVi}$ ,  $V_{oi}$  and  $SoC_i$  are often grouped according to their

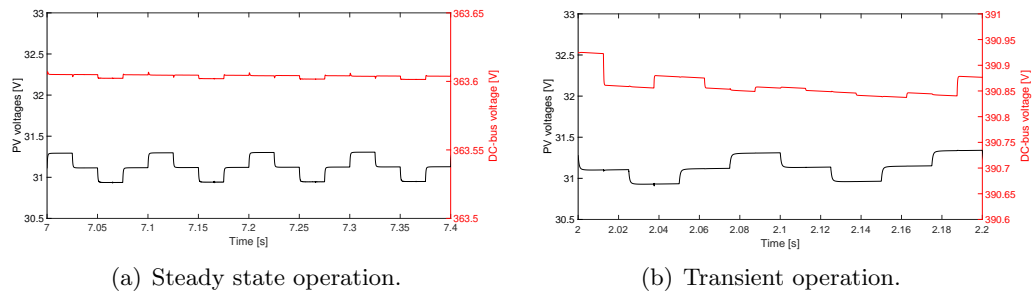


FIGURE 11.2: Coordination of  $V_{DC}$  and PV voltages to prevent an incorrect  $P_{DC}$  evaluation.

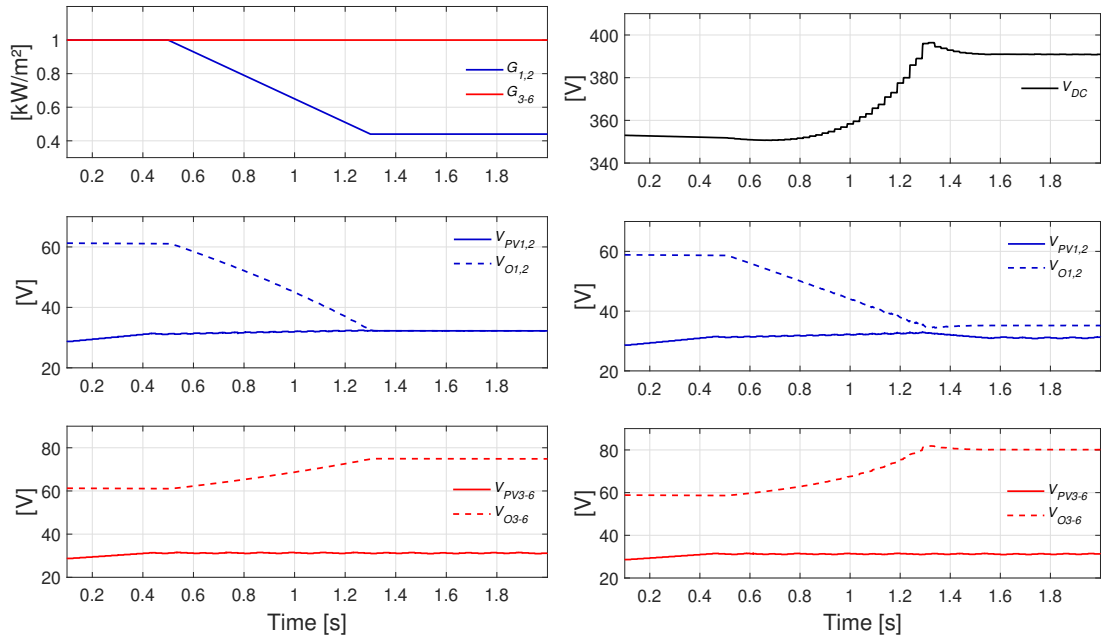
values. If e.g. the  $j$ -th and  $k$ -th  $V_{PV}$  have the same value, these voltages will be referred to as  $V_{PV,j,k}$ . If the  $j$ -th,  $k$ -th and  $h$ -th  $SoC$  have the same value, these  $SoC$  will be referred to as  $SoC_{j-h}$ .

TABLE 11.1: Characteristic parameters at STC of the BenQ GreenTriplex PM245P00 260Wp.

Parameter	Description	Value	Unit
$P_{PV}$	Nominal PV power	260	[W <sub>P</sub> ]
$I_{MPP}$	MPP current	8.34	[A]
$V_{MPP}$	MPP voltage	31.2	[V]
$I_{SC}$	Short-circuit current	8.83	[A]
$V_{OC}$	Open-circuit voltage	37.7	[V]

A coordinated control sets the new voltage references sequentially. Fig. 11.2(a) shows the steady state operation, where the PV voltages are set simultaneously and move in the vicinity of their MPP showing the P&O characteristic three-point-behaviour.  $V_{DC}$  reference is equivalent to the average value of the maximum and minimum values in (11.1) and (11.2) and shifted 180° with respect to the PV voltages. In steady state,  $V_{DC}$  remains unaltered and only changes influenced by the power variation due to the PV MPPT. The time between two consecutive perturbations of the same variable is set to  $T_a=25$  ms, sufficient time to reach the steady state, evaluate  $P_{DC}$  and set a new reference value for the other variable in the coordination sequence. In Fig. 11.2(b) the system is not in steady state condition and  $V_{DC}$  varies according to  $P_{DC}$ .

The simulation in Fig. 11.3 illustrates the benefits of implementing an adaptive  $V_{DC}$  control in DMPPT systems. At this stage, the batteries are not considered. The irradiance conditions (top plot in Fig. 11.3(a)) are the same for both cases: two PV panels out of six operate under varying irradiance  $G_{1,2}$  while the remaining four PV panels receive a constant irradiance of  $G_{3-6}=1$  kW/m<sup>2</sup>.



(a) Top to bottom: irradiance profiles,  $G_{1,2}$   $V_{PV}$  and  $V_o$ ,  $G_{3-6}$   $V_{PV}$  and  $V_o$ . (b) Top to bottom: Adaptive  $V_{DC}$ ,  $G_{1,2}$   $V_{PV}$  and  $V_o$ ,  $G_{3-6}$   $V_{PV}$  and  $V_o$ .

FIGURE 11.3: Comparison of the system performance with (a) fixed and (b) adaptive  $V_{DC}$ .

A voltage level of  $V_{DC}=363.6$  V is set for the system with fixed  $V_{DC}$  operation, allowing a boosting factor close to 2 for each DC/DC converter under homogeneous generation conditions.

Fig. 11.3(a) shows that  $V_{o1,2}$  decrease with  $G_{1,2}$  as long as  $V_{o1,2} > V_{PV1,2}$ , while the output voltages of the rest of the converters rise to compensate the  $V_{DC}$  reduction and meet  $V_{DC}=363.6$  V. According to (8.18) and (8.19), the  $V_{DC}$  range allowing a correct tracking of all the PV panels under  $G_{1,2}=440$  W/m<sup>2</sup> and  $G_{3-6}=1$  kW/m<sup>2</sup> is [ $V_{DC,min}=380.64$  V,  $V_{DC,max}=400.16$  V]. Once  $V_{o1,2}$  equals  $V_{PV1,2}$ , converters 1 and 2 are not able to perform the MPPT. The  $V_{DC}$  control (top plot in Fig. 11.3(b)), sets  $V_{DC}$  to 391 V, and extends the MPPT operation of the converters, as in [61].

Batteries are included in the system for arriving at the simulation results in Fig. 11.4. The irradiance conditions are different from the previous simulation, with varying irradiance for PV panels 1 to 4 and a constant 1 kW/m<sup>2</sup> irradiance for PV panels 5 and 6. The parameters of the batteries are gathered in Table 11.2 and the initial  $SoC$  of the batteries are set to:  $SoC_{1-3}=SoC_{min}$ ,  $SoC_4=20.01$  % almots at  $SoC_{min}$ , and  $SoC_{5-6}=50$  %. Note that the online calculated and the simulated output voltages are nearly the same (Fig. 11.4). Using the online calculated output voltages, the number of sensing circuitry can be reduced and thus the associated costs.



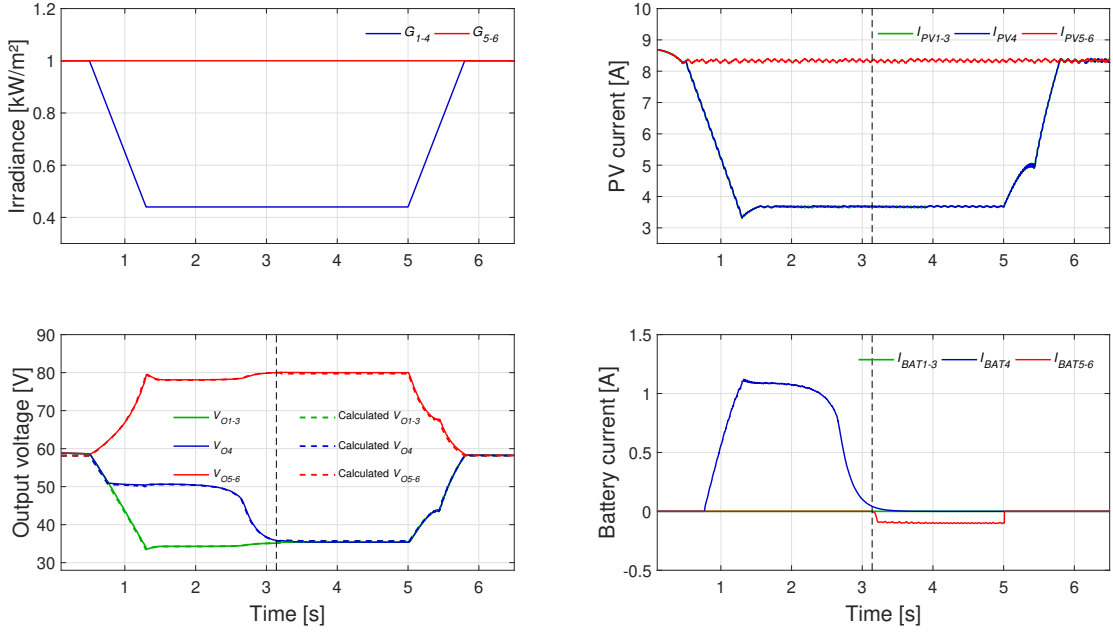


FIGURE 11.4: Performance of the system under mismatch conditions with battery compensating actions at different  $SoC$ . From left to right, top to bottom: irradiance profiles, PV currents, output voltages, battery currents.

At time  $t = 0.5$  s, the irradiance imposed to PV panels 1 to 4 decreases with a negative slope of  $-700$  kW/m<sup>2</sup>/s during 0.8 s. The battery from module 4 discharges to keep  $V_{O4} > V_{BAT4}$ . As batteries 1 to 3 are not able to give support ( $SoC_{1-3} = SoC_{min}$ ),  $V_{O1-3}$  will continue decreasing as long as they meet the condition  $V_o > V_{PV}$ . From (11.1) and (11.2) we can calculate the  $V_{DC}$  range and set an updated  $V_{DC}^*$  (at e.g.  $t = 2$  s. [ $V_{DC,min} = 281.67$  V <  $V_{DC}^* = 303.3$  V <  $V_{DC,max} = 324.91$  V]). At a certain time  $SoC_4$  reaches the minimum  $SoC$  value and  $V_{O4}$  lowers to the same level as for  $V_{O1-3}$ . At time  $t = 3.14$  s,  $V_{O4}$  and  $V_{O5}$  reach  $V_{o,max} = 80$  V. Batteries 5 and 6 charge for these output voltages not to exceed  $V_{o,max}$ . At time  $t = 5$  s, the irradiance for the PV panels 1 to 4 starts increasing until 1 kW/m<sup>2</sup> with a slope of 700 kW/m<sup>2</sup>/s.

TABLE 11.2: Battery parameters

Parameter	Description	Value	Unit
$V_{BAT}$	Rated battery voltage	50	[V]
$C_{BAT}$	Battery capacity	8.34	[Ah]
$SoC_{min}$	Minimum state-of-charge	20	%
$SoC_{max}$	Maximum state-of-charge	80	%

### 11.1.3 Experimental results

For the experimental validation in Fig. 11.5, a reduced version of  $N=3$  modules is used. A static shade of  $Sh = 50\%$  is imposed to PV1 and PV2 to obtain large voltage differences

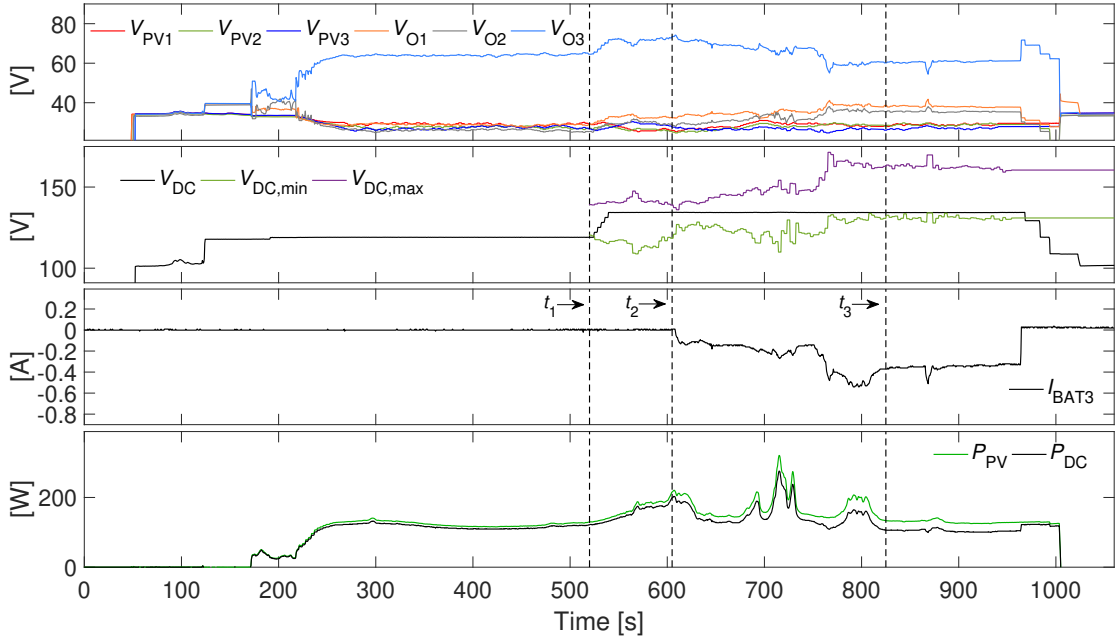


FIGURE 11.5:  $V_{DC}$  control and battery compensation. Top to bottom: PV and output voltages, limits of the  $V_{DC}$  range and  $V_{DC}$  operating point, battery 3 current charging, total PV and DC powers.

between  $V_{oi}$ .  $SoC_{1-6} = 50\%$  with room for charging and discharging the batteries. The maximum  $V_{oi}$  is limited to  $V_{o,max} = 72V$ .

The system starts with an initial  $V_{DC,init} = 120V$ , so  $V_{o1} < V_{PV1}$  and  $V_{o2} < V_{PV2}$ . At time  $t_1$ ,  $V_{DC}$  control is activated.  $V_{DC}^*$  is increased in steps of  $\Delta V_{DC} = 3V$  as long as  $V_{oi} < (V_{PV_i} + 2V)$ , to ensure the converters' boosting operation. If any  $V_{oi} > V_{o,max}$ , the battery of the corresponding module is charged to maintain  $V_{oi} < V_{o,max}$ . An hysteresis of  $V_{hyst} = 10V$  is set to avoid enabling and disabling the battery charge continuously. At time  $t_2$ ,  $V_{o3} \geq V_{o,max}$  and the battery in module 3 ( $I_{BAT3}$ ) is charged with an increment of  $\Delta I_{BAT3} = 0.02A$  starting from  $I_{BAT3} = 0A$ , to keep  $V_{o,max} > V_{o3} > V_{o,max} - V_{hyst}$ . At time  $t_3$   $V_{o3} \leq V_{o,max} - V_{hyst}$  and the absolute value of  $I_{BAT3}$  is not further increased. Meanwhile,  $V_{DC,max}$  and  $V_{DC,min}$  are calculated with (11.1) and (11.2) to verify that  $V_{DC}$  is within an appropriate range. A new  $V_{DC}$  value is set only if  $V_{DC}$  is out of the calculated range, avoiding unnecessary voltage oscillations.

## 11.2 $V_o$ equalization

In this section, the system in Fig. 11.1(a) is used, considering the module-level batteries to equalize  $V_{ok}$ . The  $V_o$  differences are obtained imposing an irradiance variation that affects some of the PV panels in the string. The batteries compensate the uneven PV generation and equalize  $V_{ok}$ .

TABLE 11.3: Simulation parameters

Parameter	Description	Value	Unit
$k_P$	Proportional	5	-
$k_I$	Integral	25	-
$SoC_{\max}$	Maximum $SoC$	0.8	-
$SoC_{\min}$	Minimum $SoC$	0.2	-

The  $V_o$  equalization method basically consists of subtracting the output voltage of two consecutive modules  $i$  and  $j$  ( $\Delta V_{oij} = V_{oj} - V_{oi}$ ), compute the power difference ( $\Delta P_{oij} = P_{oj} - P_{oi}$ ) and calculate the battery current references ( $I_{BATi}^*$  and  $I_{BATj}^*$ ) to compensate  $\Delta P_{oij}$ . For  $i=N$ ,  $j=1$ . A PI controller generates the  $I_{BATk}$  references. A hysteresis with a threshold of  $\Delta P_o = \pm 20W$  activates the PI controller.

Battery charge is considered a priority to discharge. In case of mismatch, high PV power modules with storage capacity charge first to compensate  $\Delta P_{oij}$  and the discharge of low PV power modules is disabled. If the PV power of the  $i$ -th module is higher than of the  $j$ -th module and the  $i$ -th battery ( $BATi$ ) is full ( $SoC_i > SoC_{\max}$ ),  $BATi$  charge is disabled and  $j$ -th battery discharge enabled, as long as  $SoC_j > SoC_{\min}$ . By implementing this method to all the  $N$  possible combinations, the  $I_{BAT}$  references are generated, taking into account each module's battery  $SoC$ .

The system comprises  $N=3$  modules. The modules implement individual P&O control to each PV panel (SV control, see section 9.3) and the inverter has a fixed  $V_{DC}=180V$ . The simulation parameters controlling  $I_{BATk}$  reference and the  $SoC_k$  limits can be found in Table 11.3. A combination of a constant and a varying irradiance profile are imposed to the PV panels. The constant irradiance profile is  $G=300 W/m^2$  and the varying profile follows the predetermined trapezoidal shape determined in *test B* of the European standard EN50530. The initial irradiance level of the trapezoidal profile is  $G=300W/m^2$ , it increases up to  $G=1000W/m^2$  with a slope of  $\dot{G}=100W/m^2/s$  and decreases down to  $G=300W/m^2$  with an slope of  $\dot{G}=-100W/m^2/s$ . It starts at time  $t_1$  for all the cases studied.

### 11.2.1 Simulation results

Four cases are considered: in Fig. 11.6,  $G_1$  trapezoidal profile is imposed to PV1 and  $G_2=G_3=300 W/m^2$  to PV2 and PV3. When the output power difference is detected above the threshold, batteries charge or discharge to equalize the output voltages Battery 1 ( $BAT1$ )  $SoC$  is below the maximum allowed  $SoC$ ,  $SoC_1 < SoC_{\max}$ . Thus, regardless of  $SoC_2$  and  $SoC_3$ ,  $BAT1$  is charged to compensate the power difference with modules 2 and 3. In Fig. 11.7 on the contrary  $SoC_1 > SoC_{\max}$  and battery 2 ( $BAT2$ ) and battery

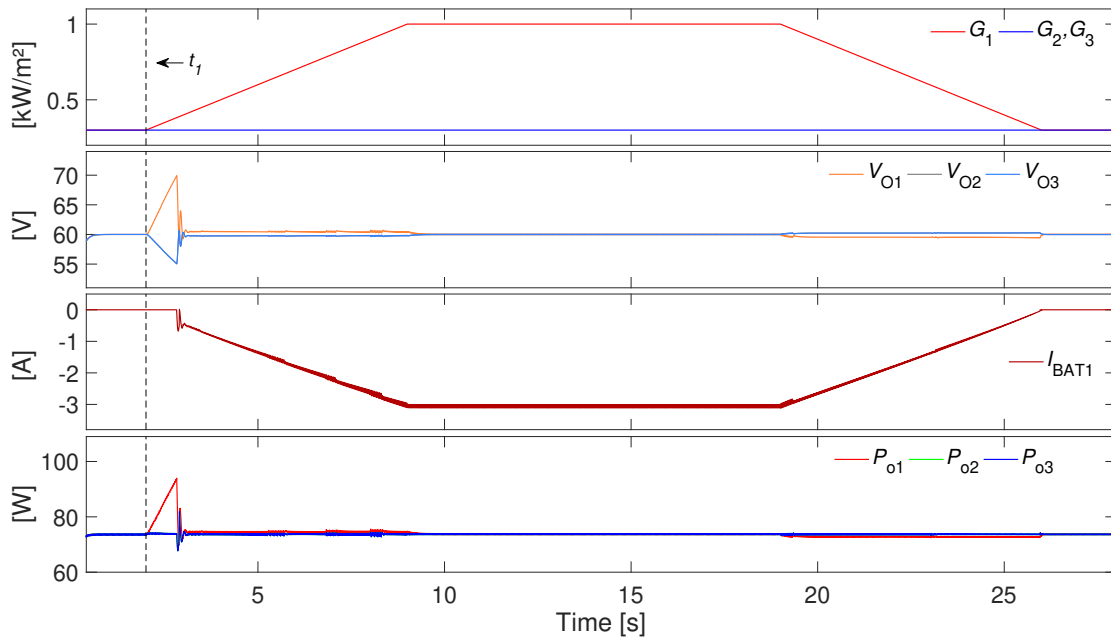


FIGURE 11.6:  $SoC_1 < SoC_{\max}$ . Top to bottom: first plot: PV1 follows a varying  $G_1$  with a trapezoidal profile,  $G_2 = G_3 = 300 \text{ W/m}^2$  for PV2 and PV3. Second plot: output voltages. Third plot: BAT1 charges after  $\Delta P_{o12} \leq -20 \text{ W}$  and  $\Delta P_{o31} \geq +20 \text{ W}$ . Fourth plot: output powers.

3 (BAT3) discharge ( $SoC_2 = SoC_3 > SoC_{\min}$ ). Figs. 11.8 and 11.9 show similar cases but imposing the trapezoidal profile to PV1 and PV2 and the constant  $G_3 = 300 \text{ W/m}^2$  to PV3. In Fig. 11.8 BAT1 and BAT2 have charging capacity  $SoC_1 = SoC_2 < SoC_{\max}$  while in Fig. 11.9  $SoC_1 = SoC_2 > SoC_{\max}$  and BAT3 discharges as  $SoC_3 > SoC_{\min}$ . In all the cases the battery compensation avoids undesired  $V_o$  levels, contributing to system stability.

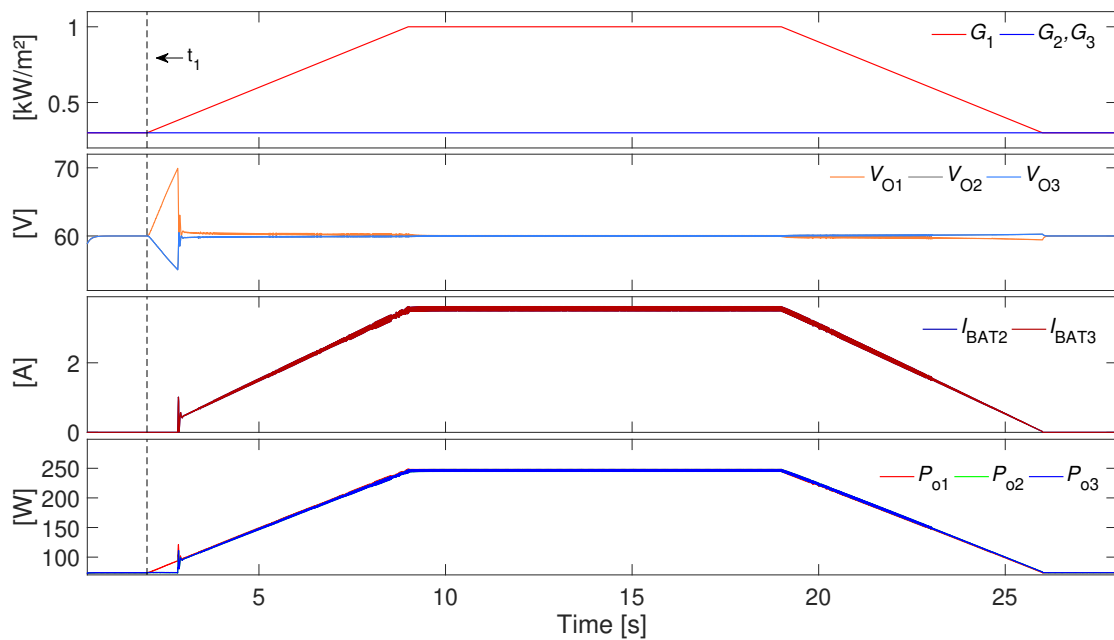


FIGURE 11.7:  $SoC_1 > SoC_{\max}$  (BAT1 charge disabled) and  $SoC_2 = SoC_3 > SoC_{\min}$ . Top to bottom: first plot: PV1 follows a varying  $G_1$  with a trapezoidal profile,  $G_2 = G_3 = 300$  W/m<sup>2</sup> for PV2 and PV3. Second plot: output voltages. Third plot: BAT2 and BAT3 discharge after  $\Delta P_{o12} \leq -20$  W and  $\Delta P_{o31} \geq +20$  W. Fourth plot: output powers.

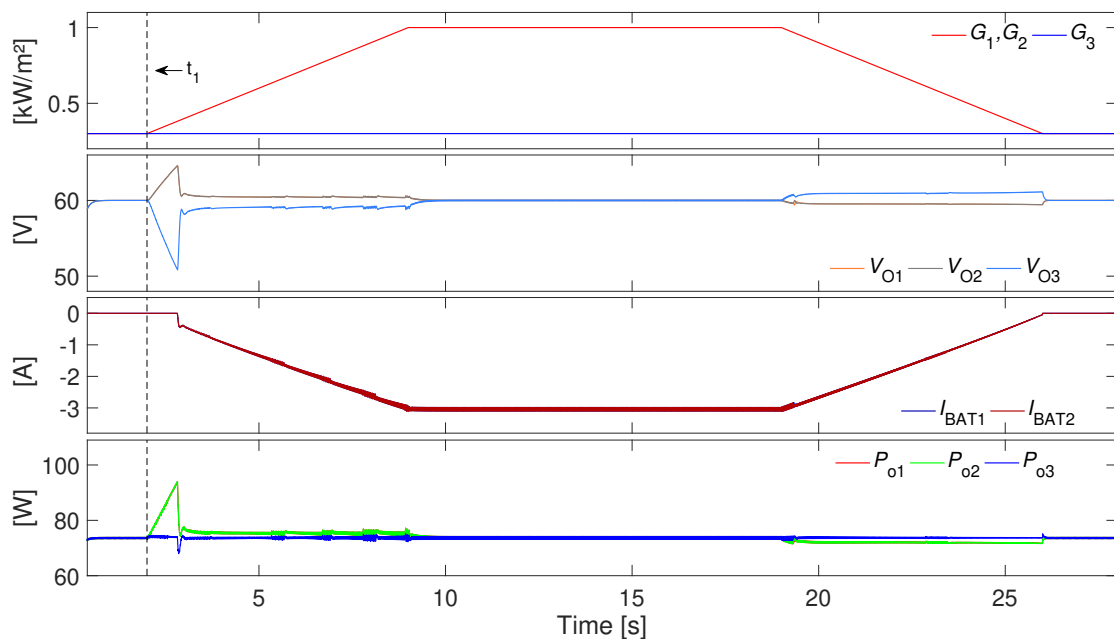


FIGURE 11.8:  $SoC_1 = SoC_2 < SoC_{\max}$ . Top to bottom: first plot: PV1 and PV2 follow varying  $G_1$  and  $G_2$  with a trapezoidal profile,  $G_3 = 300$  W/m<sup>2</sup> for PV3. Second plot: output voltages. Third plot: BAT1 and BAT2 charge after  $\Delta P_{o31} \geq +20$  W and  $\Delta P_{o23} \leq -20$  W. Fourth plot: output powers.

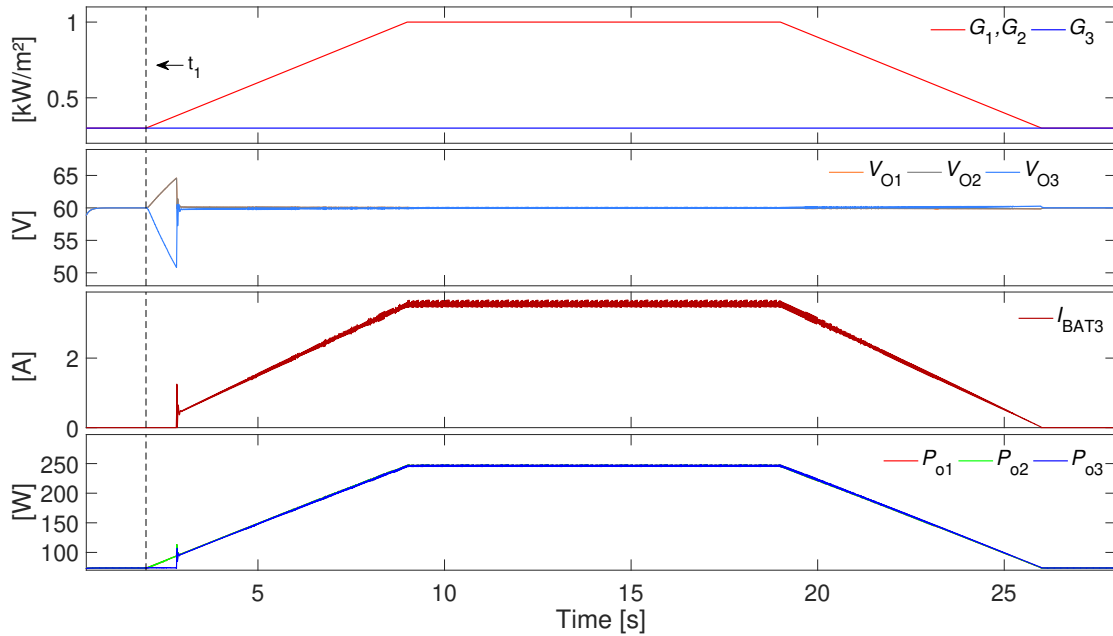


FIGURE 11.9:  $SoC_1=SoC_2>SoC_{max}$  (BAT1 and BAT2 charge disabled) and  $SoC_3>SoC_{min}$ . Top to bottom: first plot: PV1 and PV2 follow varying  $G_1$  and  $G_2$  with a trapezoidal profile,  $G_3=300$  W/m<sup>2</sup> for PV3. Second plot: output voltages. Third plot: BAT3 discharge after  $\Delta P_{o31} \geq +20$  W and  $\Delta P_{o23} \leq -20$  W. Fourth plot: output powers.

### 11.3 Discussion of results

The  $V_{DC}$  control adapted to a battery-integrated DMPPT system has shown to be as effective as the original control presented in [61]. By setting  $V_{DC}$  to a value within the optimal operating range, the variable voltage control allows the PV panels to work at their MPP when there is a certain mismatch between panels. Nonetheless, the algorithm adapting  $V_{DC}$  does not ensure the optimal operation in a DMPPT system without batteries at module-level.

By including batteries, the system is able to operate if the difference in PV generation is even larger. Furthermore, batteries support the PV generation by controlling the output voltage levels of the converters. The use of batteries at module-level in combination with a  $V_{DC}$  control extends the MPPT operation and improves the performance of the system.

If the system operates with a constant  $V_{DC}$ ,  $V_o$  equalization can be implemented to compensate the voltage differences caused by the different power output of the modules. The  $V_o$  equalization method presented in this chapter has shown the ability to keep the system operating at uneven irradiance variation, avoiding  $V_o$  levels that could reach the ratings of some components (e.g. output capacitors) in parallel to the output of the converters.

## Chapter 12

# Conclusions

In the first part of this thesis, the dynamic interaction of PV inverters with grid stability problems has been addressed. The features of the individual PV generation units have been analysed. The capability of commercial PV inverters to compensate voltage issues is strongly influenced by the impedance behaviour of the grid. Grid voltage compensation in residential applications responds better to active power reduction, due to the normally resistive behaviour of LV networks. In general, inverter's reactive power compensation capability is less effective than reducing the active power delivered to the grid. Besides, voltage compensation via reactive power provision can increase power losses in the PV inverters and operational costs of the PV installation [52]. In addition, country grid standards limit the maximum reactive power modulation of each device [13]. Therefore, active power control capabilities must take priority for inverters connected to LV networks.

The voltage increase in the LV network due to the reverse current flow is higher for the most distant PCCs. The local compensating actions of individual PV units may not be sufficient to solve the overvoltage issue in DN with high PV penetration, being detrimental to the most remote PV installations from the distribution transformer. Active distribution systems managing the power flow in the LV networks help ensuring the grid voltage instability. LV networks are generally characterised by PV installations with inverters of different brands and each manufacturer develops its own communication protocol. A control scheme able to interact with each and every PV inverter in the LV network is thus necessary. The universal communication protocol UCP developed in this work makes the specific communication protocols uniform and eases the implementation of active management control schemes in DN.

Active power curtailment of the various PV units of the same LV network in a collaborative framework can attenuate the imbalance in the grid. The grid voltage instability

is ensured, but at the cost of having less profitable PV installations. The integration of batteries in PV systems is suggested as a possible solution to this problem. Instead of reducing the PV generation, part of the PV energy is stored, reducing for a certain period the energy injected to the grid.

In the second part of the thesis, PV DMPPT systems have been addressed. The distributed power electronics individually controlling the MPP of each PV panel allow for an increase in harvested energy in mismatch conditions compared to the traditional CMPPT (e.g. Fig. 8.7). However, if the mismatch is considerable, the DMPPT system considering a constant  $V_{DC}$  may work at a suboptimal power point. Moreover, depending on the  $V_{DC}$  level, large irradiance mismatch between PV panels may lead to dangerous overvoltage in the modules presenting greater output powers, damaging some of the DC/DC converters' components. Atmospheric conditions, number of PV panels in the string, mismatch level between PV panels, number of PV panels and their associated converters under each different irradiance level, conversion gain limitations of the DC/DC stage at the PV panel level, and  $V_{DC}$  level affect the performance of the DMPPT system. In this context, the  $V_{DC}$  range and optimal operating point has been analysed (Figs. 8.8, 8.10). The results obtained suggest the implementation of an adaptive  $V_{DC}$  control to improve DMPPT system's performance.

A central MPPT function that implements the  $V_{DC}$  control has to be coordinated with the DMPPT function. This coordination has been implemented by including the  $V_{DC}$  control into the multi-variable operating sequence. Thanks to the coordination of DMPPT and CMPPT functions, the proposed H-MV control adapts  $V_{DC}$  increasing the performance of the system (Fig. 9.20). In addition, the dynamic response of the multi-variable control is improved with a specific functionality that significantly reduces output voltages differences (Figs. 9.18 and 9.21) contributing to better safety and system stability.

The interleaved boost-3PC [87] including batteries at module level is used in the DMPPT system to implement control strategies that compensate the irradiance mismatch between PV panels. In the absence of a suitable  $V_{DC}$  value allowing the MPP operation of all the PV panels, at least one of the converters in the string stops performing its MPPT or the system is forced to operate a suboptimal operating condition. Besides, if changing atmospheric conditions are not uniformly distributed on all the PV panels (clouds passing by and partially affecting the PV string) the output voltage of one or more modules may be affected and reach some of the component's ratings. Module level batteries are used to compensate the voltage differences, charging part of the generated PV energy or discharging when PV generation of the corresponding module is too low. Two different strategies have been presented to overcome large mismatch conditions.



The first strategy extends the MPPT range in the DMPPT system using batteries as support to the PV generation (Figs. 11.4 and 11.5). A  $V_{DC}$  control calculates the  $V_{DC}$  range to obtain system's maximum performance. If  $V_{DC}$  control is not able to avoid the mismatch situation, the output voltage of the converters are compensated using batteries as support to the PV generation. In the second strategy, the  $V_o$  equalization method has shown the ability to keep the system operating at uneven irradiance variation, prioritizing the battery charge (Figs. 11.6 to 11.9). However, a more intensive use of the batteries is made compared to the first strategy.

A way to improve the performance of the system under mismatch conditions could be the implementation of a strategy that couples the two  $V_{DC}$  controls proposed: the  $V_{DC}$  control implemented in the multi-variable sequence (H-MV, see section 9.3) tracks  $V_{DC}$  to a value corresponding to the  $V_{DC,min}$  (Fig. 9.17), the minimum  $V_{DC}$  value in the GMPR under these operating conditions. The  $V_{DC}$  range calculation (see section 8.5.1) could provide an approximate  $V_{DC}$  operating range and place  $V_{DC}$  at an intermediate point. In addition, with the proposed techniques, the operation at LMPR for some of the mismatch conditions is unavoidable as the algorithm is unable to detect if it is performing at GMPR or LMPR. A method to detect these suboptimal operating regions and the use of the batteries to compensate the mismatch could improve the performance of the system.



# Appendix A

## Universal communication protocol and specific protocols of main PV inverter brands

### A.1 Structure of the communication platform

In the module `inverter_brand.py` the **control module** of an inverter is selected. Each **control module** calls to the corresponding **function module**, and this to the libraries or dictionaries associated to it.

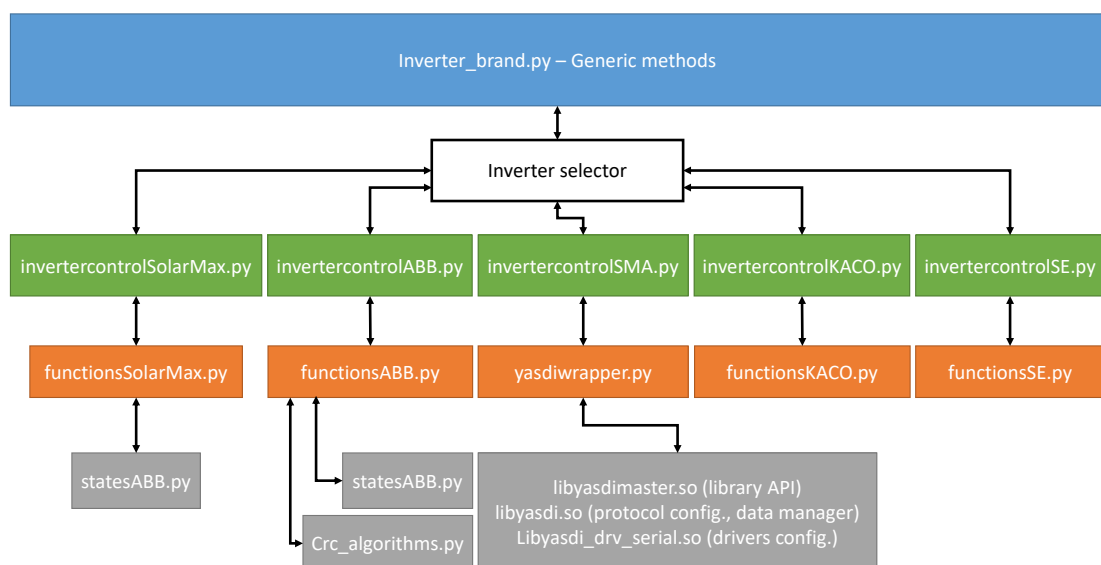


FIGURE A.1: Structure of the communication platform

## A.2 Universal communication protocol

In this section the generic *methods* are described. The corresponding python module `inverter_brand.py` is structured in *methods* or *functions()* belonging to the class `InvBrand`. This class initializes a logger<sup>1</sup> (*.log* text files created automatically in the same folder where the python module is) for post-analysis and error-correction invoking the `_init_()` method:

- In the initialization of `InvBrand` class, the selection of the inverter is done through the if statement. The necessary modules allowing the control of the inverter are imported. The objects declared for each option initialize the corresponding inverter and acquire the functionalities of the *methods* inside the *classes* of the *modules* called (the generic name of the object is *inverter*). Once the call is done, the arguments declared in the `_init_()` *method* of the *classes* are executed.

The generic *methods* are listed hereunder:

1. The reading *methods* return only a value. In case the reading is not well executed, the *methods* return an error code. Reading *methods* available for the inverters tested:
  - `SlimitReading()`: Reads the nominal apparent power of the device. Available only for SMA.
  - `cosPhiMin()`: Reads the minimum cos phi of the device. Available only for SMA.
  - `ActivePowerReading()`: Reads phase active powers injected into the grid. Available only for SMA.
  - `ReactivePowerReading()`: Reads per phase reactive powers. Available only for SMA.
  - `SNReading()`: Reads the serial number of the device. Available for all.
  - `voltageOutReading()`: Reads the output voltage of the device. Per phase for the 3-ph and ph-N for the single-phase. Available for all.
  - `totalActivePowerReading()`: Reads the total active power the device is delivering. Available for all.
  - `totalReactivePowerReading()`: Reads the total reactive power exchanged between the device and the grid. Available for all.
  - `PFReading()`: Reads the operating point of the power factor of the device. Available for all excluding SolarMax.

2. The writing *methods* return the reference value once the order is successfully executed. If that is not the case, the *methods* return an error code. Writing *methods* available:

- `totalActivePowerDisable()`: Disables the active power set point mode and enables back the MPPT mode. Available for SMA and SolarEdge.
- `totalReactivePowerDisable()`: Disables the reactive power mode changing to P.F. = 1.0. Available for SMA and SolarEdge.
- `totalActivePowerLimitation()`: Limits the active power of the device. Available only for SMA.
- `totalApparentPowerLimitation()`: Limits the apparent power of the device. Available only for SMA.
- `totalActivePowerSetPoint()`: Sets the active power operating point reference. Available for all.
- `totalReactivePowerSetPoint()`: Sets the reactive power operating point reference. Available for all excluding SolarMax.
- `PFSetPoint()`: Sets the power factor operating point reference. Available for all excluding SolarMax.

The availability of the methods with respect to the type of inverter is described in Fig. [A.2](#)

Parameter	SMA	ABB	SolarMax	KACO	SolarEdge
<b>Read</b>					
Minimum $\cos\phi$	Y	N	N	N	N
Maximum apparent power	Y	N	N	N	N
Serial number	Y	Y	Y	Y	Y
Output voltage	Y	Y	Y	Y	Y
Active power per phase	Y	N	N	N	Y
Reactive power per phase	Y	N	N	N	Y
Total active power	Y	Y	Y	Y	Y
Total reactive power	Y	N	N	N	Y
Power Factor	Y	Y	N	Y	Y
<b>Write</b>					
Total active power	Y	Y	Y	Y	Y
Total reactive power	Y	Y	N	Y	Y
Power Factor	Y	Y	N	Y	Y
Total Q(P)	Y	Y	N	Y	Y
Total Q(U)	Y	Y	N	Y	Y
Total active power limitation	Y	N	N	N	N
Total apparent power limitation	Y	N	N	N	N
Disable active power setpoint	Y	N	N	N	Y
Disable reactive power setpoint	Y	N	N	N	Y


 Parameter available in the family but not implemented yet or not available for the model

FIGURE A.2: Features of the inverters

# Appendix B

## Simulation models and results

### B.1 Distributed and central MPPT functions

#### B.1.1 Switching model of the boost DC/DC converter

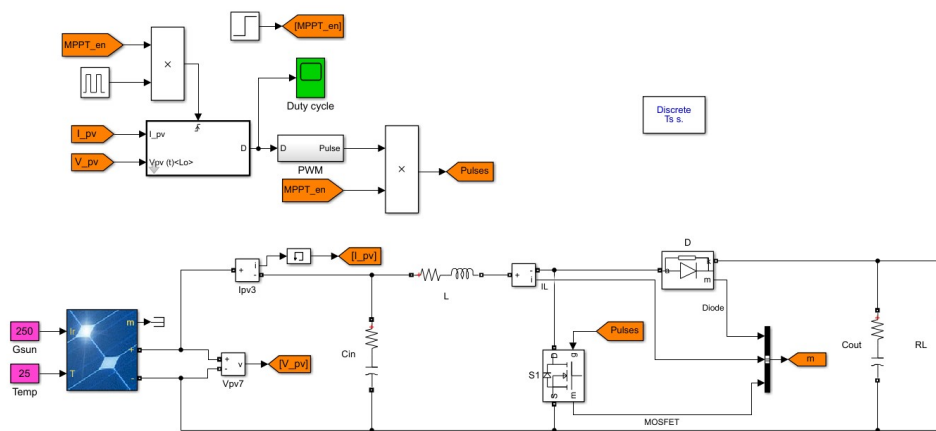


FIGURE B.1: Nonisolated boost converter switching model and its MPPT P&O control

## B.1.2 Averaged model of the central MPPT

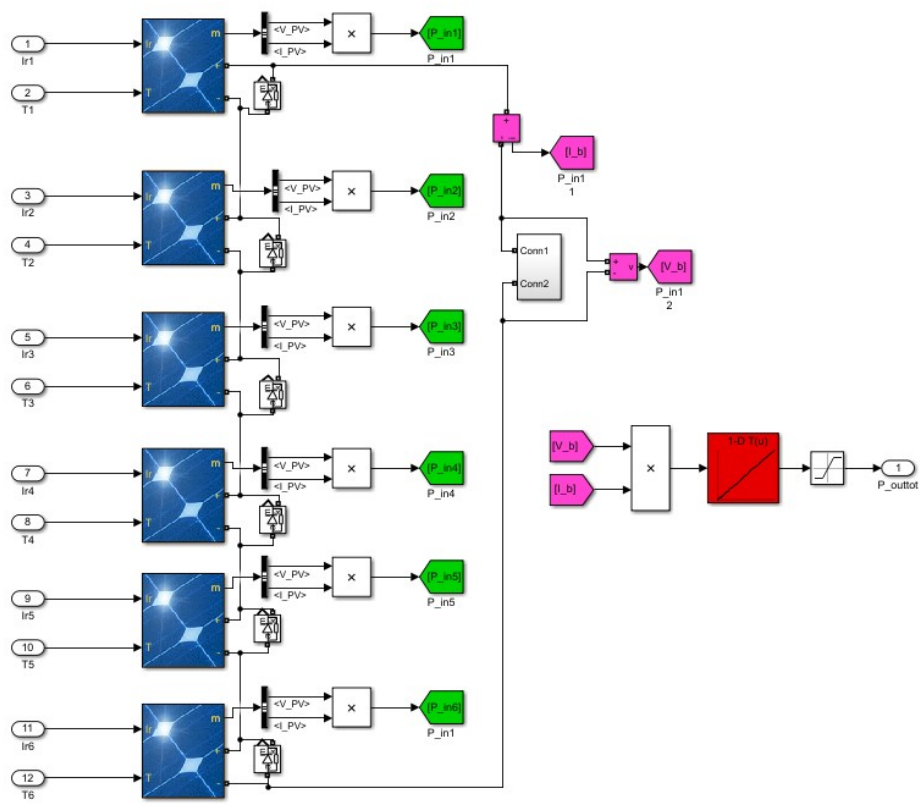


FIGURE B.2: Averaged model of the CMPPT approach



### B.1.3 Averaged model of the distributed MPPT

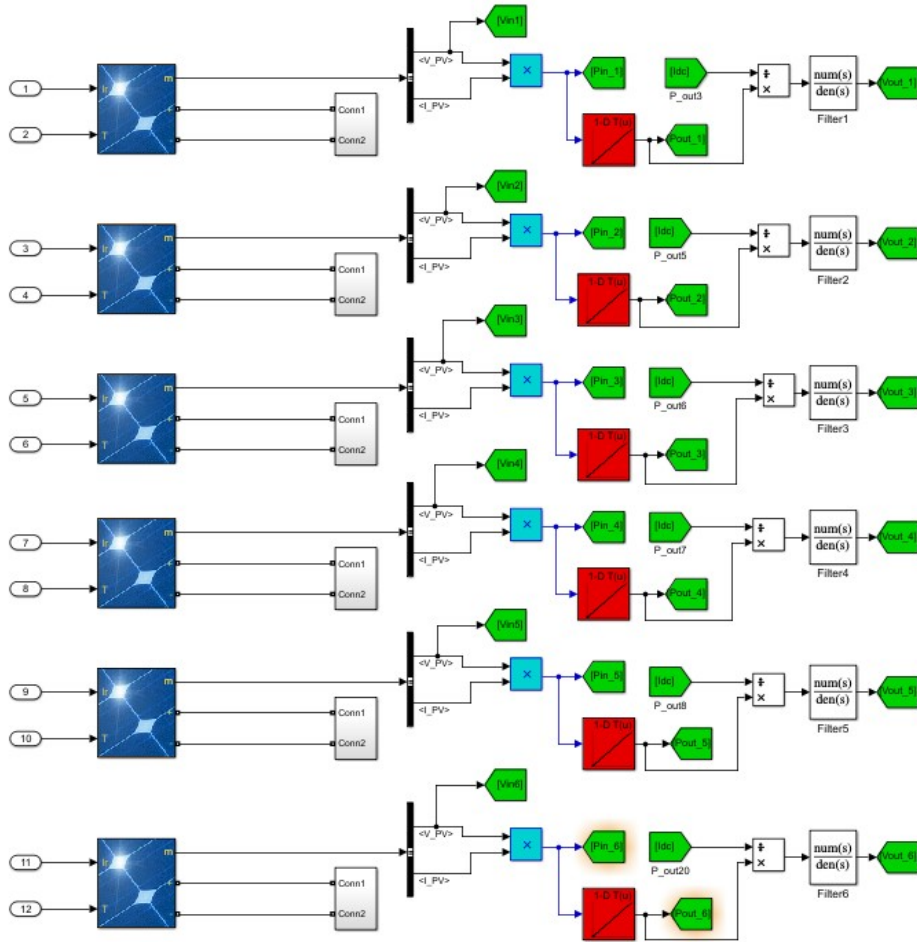


FIGURE B.3: Averaged model of the DMPPT approach

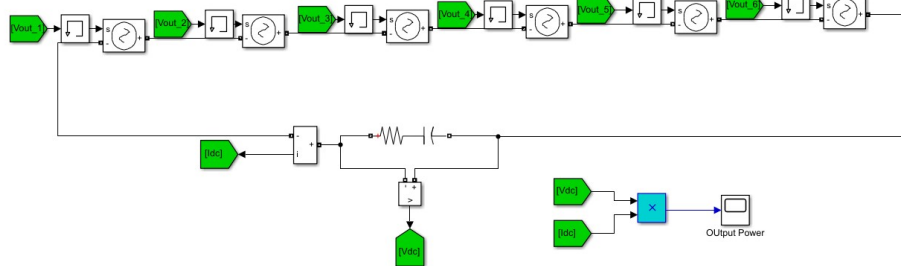
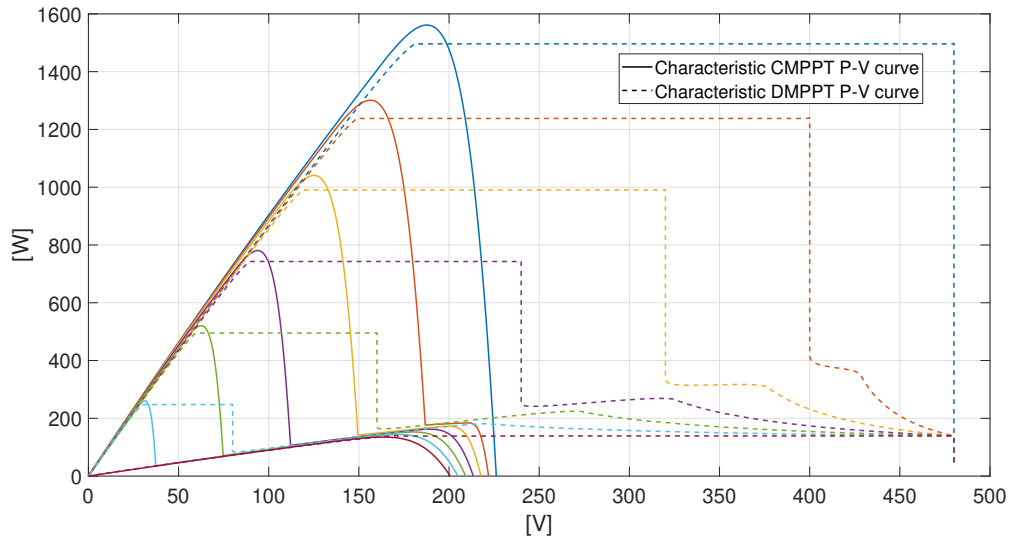


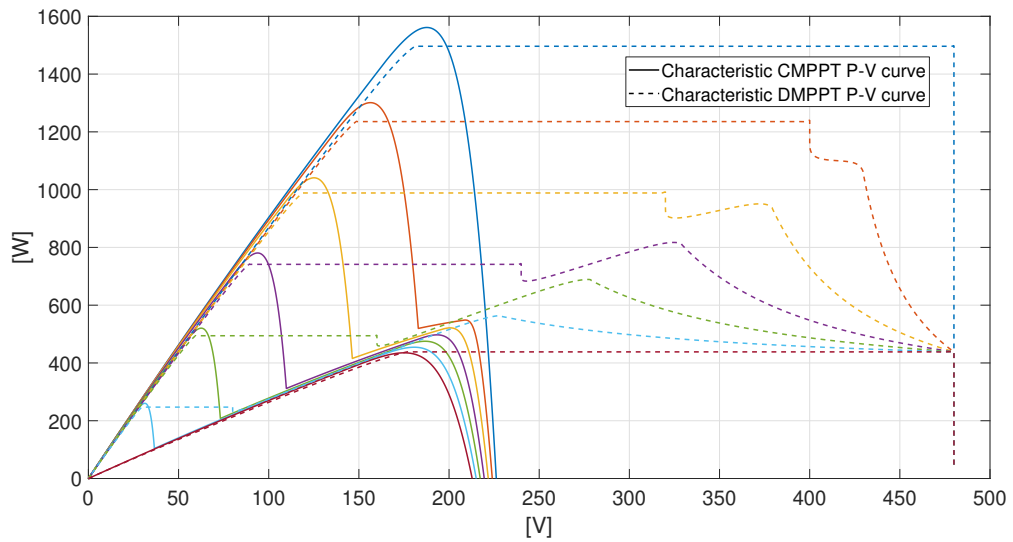
FIGURE B.4: Model of the DC bus for the DMPPT approach

### B.1.4 Additional results

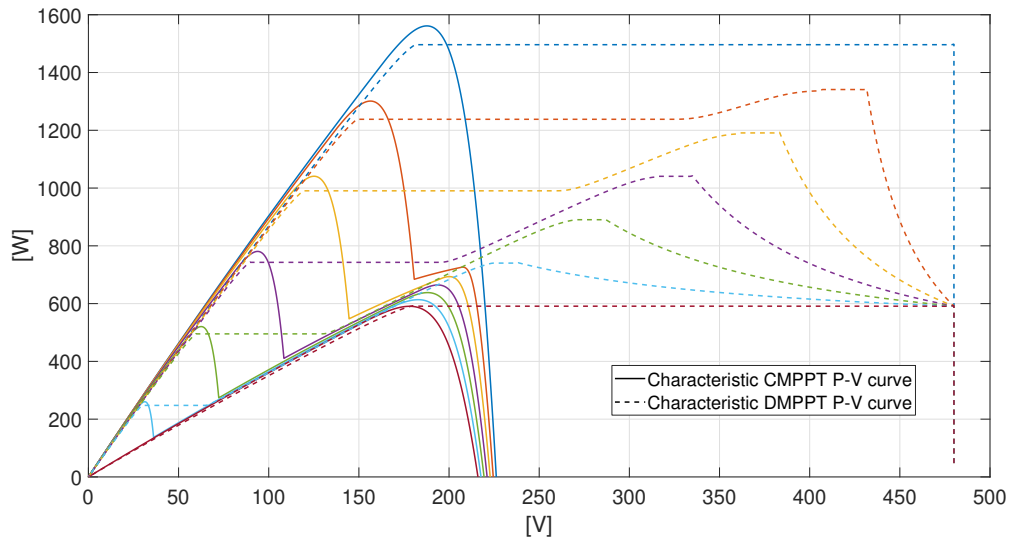
Figs. B.5 and B.6 gather additional CMPPT and DMPPT P-V curves subjected to several different irradiance mismatches.



(a)  $N_H$  panels at  $G_H=1000 \text{ W/m}^2$  and  $N_L$  panels at  $G_L=100 \text{ W/m}^2$ .

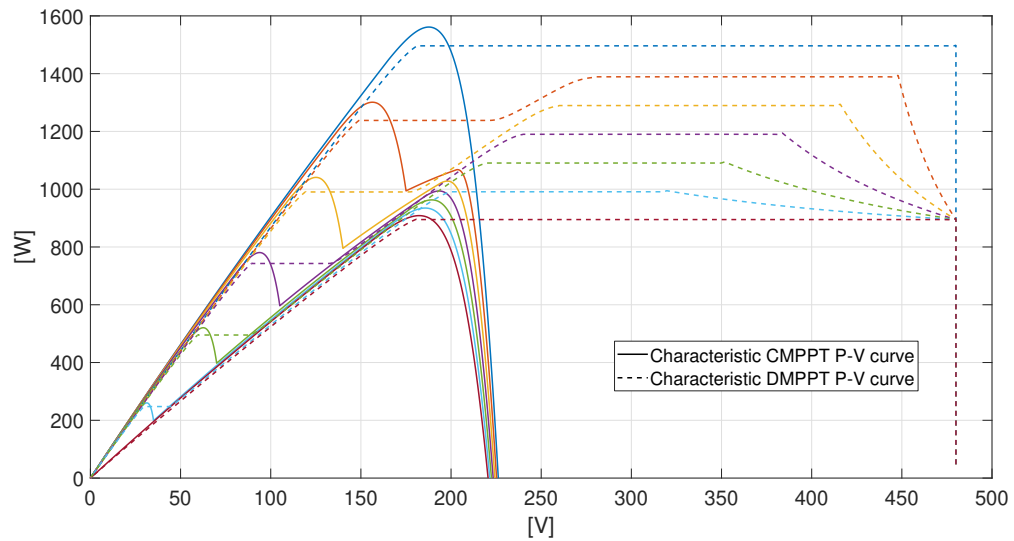


(b)  $N_H$  panels at  $G_H=1000 \text{ W/m}^2$  and  $N_L$  panels at  $G_L=300 \text{ W/m}^2$ .

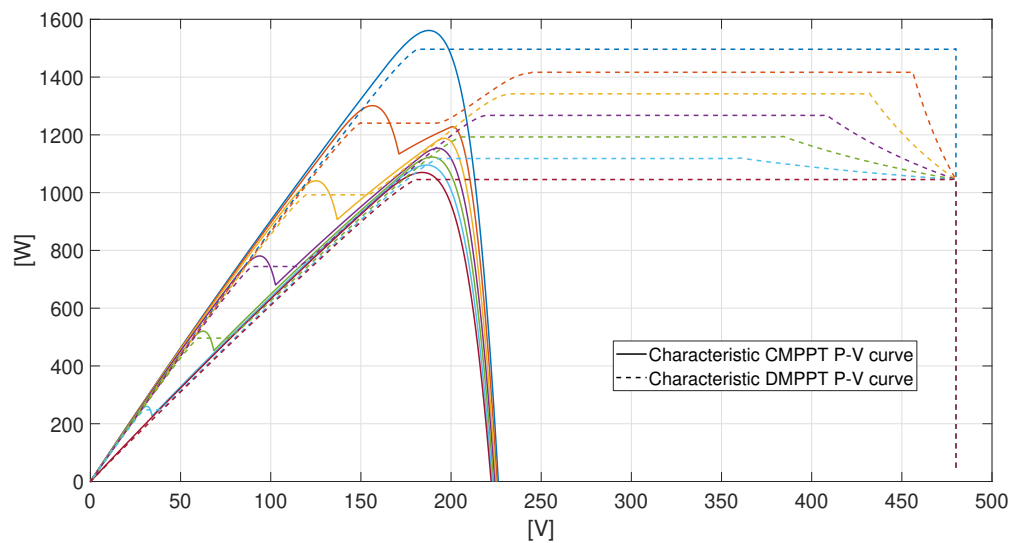


(c)  $N_H$  panels at  $G_H=1000 \text{ W/m}^2$  and  $N_L$  panels at  $G_L=400 \text{ W/m}^2$ .

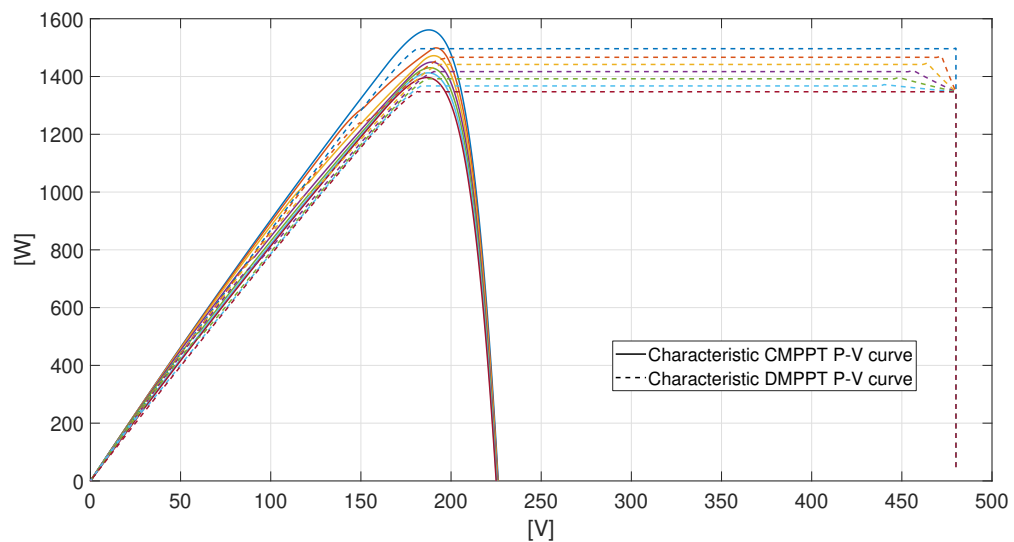
FIGURE B.5: P-V curves of DMPPT and CMPPT systems for an increasing number of shaded PV panels



(a)  $N_H$  panels at  $G_H=1000 \text{ W/m}^2$  and  $N_L$  panels at  $G_L=600 \text{ W/m}^2$ .



(b)  $N_H$  panels at  $G_H=1000 \text{ W/m}^2$  and  $N_L$  panels at  $G_L=700 \text{ W/m}^2$ .



(c)  $N_H$  panels at  $G_H=1000 \text{ W/m}^2$  and  $N_L$  panels at  $G_L=900 \text{ W/m}^2$ .

FIGURE B.6: P-V curves of DMPPT and CMPPT systems for an increasing number of shaded PV panels



# Bibliography

- [1] Tor Håkon Jackson Inderberg, Kerstin Tews, and Britta Turner. Is there a Prosumer Pathway? Exploring household solar energy development in Germany, Norway, and the United Kingdom. *Energy Research and Social Science*, 42(October 2017):258–269, 2018. ISSN 22146296. doi: 10.1016/j.erss.2018.04.006. URL <https://doi.org/10.1016/j.erss.2018.04.006>.
- [2] Jürgen Friedrich Hake, Wolfgang Fischer, Sandra Venghaus, and Christoph Weckenbrock. The German Energiewende - History and status quo. *Energy*, 92: 532–546, 2015. ISSN 03605442. doi: 10.1016/j.energy.2015.04.027. URL <http://dx.doi.org/10.1016/j.energy.2015.04.027>.
- [3] Kerstin Tews. Mapping the Regulatory Features Underpinning Prosumer Activities in Germany: The Case of Residential Photovoltaics. 2016.
- [4] Ministerio para la transición ecológica. Real Decreto 244/2019 (2019/04/05) del Boletín oficial del estado, 2019. URL <https://www.boe.es/eli/es/rd/2019/04/05/244>.
- [5] Elena Ares. Renewable Electricity : Feed-in Tariffs and The Renewables Obligation. Technical report, 2011. URL <https://www.fitariffs.co.uk/library/regulation/110623HOC{ }FITS{ }R0.pdf>.
- [6] Andrew Macintosh and Deb Wilkinson. Searching for public benefits in solar subsidies: A case study on the Australian government’s residential photovoltaic rebate program. *Energy Policy*, 39(6):3199–3209, 2011. ISSN 03014215. doi: 10.1016/j.enpol.2011.03.007. URL <http://dx.doi.org/10.1016/j.enpol.2011.03.007>.
- [7] Andrew J. Chapman, Benjamin McLellan, and Tetsuo Tezuka. Residential solar PV policy: An analysis of impacts, successes and failures in the Australian case. *Renewable Energy*, 86:1265–1279, 2016. ISSN 18790682. doi: 10.1016/j.renene.2015.09.061. URL <http://dx.doi.org/10.1016/j.renene.2015.09.061>.

- [8] Goksin Kavlak, James McNerney, and Jessika E. Trancik. Evaluating the causes of cost reduction in photovoltaic modules. *Energy Policy*, 123(August):700–710, 2018. ISSN 03014215. doi: 10.1016/j.enpol.2018.08.015. URL <https://doi.org/10.1016/j.enpol.2018.08.015>.
- [9] M. Reking, I.T. Theologitis, G. Masson, M. Latour, D. Biancardi, A. Roesch, G. Concas, and P. Basso. Solar Photovoltaics on the Road To Large Scale Grid Integration. Technical Report September, 2012.
- [10] Ran Fu, David Feldman, and Robert Margolis. U. S. Solar Photovoltaic System Cost Benchmark : Q1 2018. Technical Report November, 2018. URL <https://www.nrel.gov/docs/fy19osti/72399.pdf>.
- [11] V. Chadliev, S. Degener, P. Tirtiaux, A. Beauvais, M. Schmela, B. Engel, J. Hauff, and M. Mueller. Unleashing the Full Potential of SMEs : Beyond Financing. Technical Report June, 2018.
- [12] European Commission. Commission regulation (EU) 2016/631 of 14 April 2016 establishing a network code on requirements for grid connection of generators. (April), 2016. URL <https://eur-lex.europa.eu/eli/reg/2016/631/oj>.
- [13] SynerGrid. Specifieke technische voorschriften voor decentrale productie-installaties die in parallel werken met het distributienet. 2012.
- [14] Philip P Barker and Robert W De Mello. Determining the impact of distributed generation on power systems. I. Radial distribution systems. *Power Engineering Society Summer Meeting*, 03(c):1645–1656, 2000.
- [15] Remus Teodorescu, Marco Liserre, and Pedro Rodríguez. *Grid Converters for Photovoltaic and Wind Power Systems*. 2011. ISBN 9780470057513. doi: 10.1002/9780470667057.
- [16] Wenxin Peng, Salim Haddad, and Yahia Baghzouz. Improving power quality in distribution feeders with high PV penetration through inverter controls. In *CIREN Workshop: Integration of Renewables into the Distribution Grid*, number 97, pages 1–4, 2012. doi: 10.1049/cp.2012.0749.
- [17] Silvestros Vlachopoulos and Charis Demoulias. Voltage regulation in low-voltage rural feeders with distributed PV systems. *EUROCON 2011 - International Conference on Computer as a Tool - Joint with Conftele 2011*, 3(1), 2011. doi: 10.1109/EUROCON.2011.5929198.
- [18] Georgios Tsengenes and Athanasios D Karlis. Improving the voltage profile of a medium voltage grid using distributed generation units Keywords Grid connected inverter control scheme analysis. 2013.

- [19] Majid Taghizadeh, Javad Sadeh, and Ebadollah Kamyab. Protection of grid connected photovoltaic system during voltage sag. *2011 International Conference on Advanced Power System Automation and Protection*, pages 2030–2035, oct 2011. doi: 10.1109/APAP.2011.6180769.
- [20] Xiaogao Chen, Qing Fu, Shijie Yu, and Longhua Zhou. Unified Control of Photovoltaic Grid-connection and Power Quality managements. pages 360–365, 2008. doi: 10.1109/PEITS.2008.66.
- [21] Frédéric Olivier, Petros Aristidou, Damien Ernst, and Thierry Van Cutsem. Active management of low-voltage networks for mitigating overvoltages due to photovoltaic units. *IEEE Transactions on Smart Grid*, 7(2):926–936, 2016. URL <http://ieeexplore.ieee.org/abstract/document/7063267/>.
- [22] Ramón López-Erauskin, Thomas Geury, Johan Gyselinck, María Emilia Hervás, and Alexis Fabre. Testing the Enhanced Functionalities of Commercial PV Inverters Under Realistic Atmospheric and Abnormal Grid Conditions. *5th Solar Integration Workshop*, 2015.
- [23] R A Mastromauro, M Liserre, and A Dell Aquila. Single-Phase Grid-Connected Photovoltaic Systems With Power Quality Conditioner Functionality. In *European Conference on Power Electronics and Applications*, pages 1–11, Aalborg, 2007.
- [24] R. Kabiri, D. G. Holmes, and B. P. McGrath. The influence of pv inverter reactive power injection on grid voltage regulation. *2014 IEEE 5th International Symposium on Power Electronics for Distributed Generation Systems (PEDG)*, pages 1–8, jun 2014. doi: 10.1109/PEDG.2014.6878640. URL <http://ieeexplore.ieee.org/lpdocs/epic03/wrapper.htm?arnumber=6878640>.
- [25] Hannu Laaksonen, Pekka Saari, and Risto Komulainen. Voltage and Frequency Control of Inverter. In *2005 International Conference on Future Power Systems*, pages 6 pp.–6, 2005. doi: 10.1109/FPS.2005.204293.
- [26] Radu Dan Lazar and Adrian Constantin. Voltage balancing in LV residential networks by means of three phase PV inverters. In *EUPVSEC conference*, pages 1–4, 2012.
- [27] Eurelectric. Power distribution in Europe, Facts and figures. Technical report, 2013.
- [28] Ahmed K Allehyani and Mohammed J Beshir. Overhead and Underground Distribution Systems Impact on Electric Vehicles Charging. *Journal of Clean Energy Technologies*, 4(2):125–128, 2016. doi: 10.7763/JOCET.2016.V4.265.

- [29] SynerGrid. Prescriptions techniques spécifiques de raccordement d'installations de production décentralisée fonctionnant en parallèle sur le réseau de distribution. pages 1–84, 2019. URL <http://www.synergrid.be/index.cfm?PageID=16824>.
- [30] IEEE Standard Definitions for the Measurement of Electric Power Quantities Under Sinusoidal, Nonsinusoidal, Balanced, or Unbalanced Conditions. *IEEE Std 1459-2010 (Revision of IEEE Std 1459-2000)*, pages 1–50, 2010. doi: 10.1109/IEEESTD.2010.5439063. URL <https://ieeexplore.ieee.org/document/5439063>.
- [31] Eckehard Troester. New German Grid Codes for Connecting PV Systems to the Medium Voltage Power Grid. *2nd International Workshop on Concentrating Photovoltaic Power Plants: Optical Design, Production, Grid Connection*, pages 1–4, 2009.
- [32] Connection and Operation of Power Generating Plants to Low-Voltage Grid, (VDE-AR-N 4105), 2018.
- [33] Erhan Demirok, Pablo Casado Gonz, Kenn H B Frederiksen, Dezso Sera, Pedro Rodriguez, and Remus Teodorescu. Local Reactive Power Control Methods for Overvoltage Prevention of Distributed Solar Inverters in Low-Voltage Grids. *IEEE Journal of Photovoltaics*, 1(2):174–182, 2011. doi: 10.1109/JPHOTOV.2011.2174821.
- [34] Thomas Geury, Johan Gyselinck, and Libre D E Bruxelles. Emulation of Photovoltaic Arrays with Shading Effect for Testing of Grid-Connected Inverters. In *2013 EPE European Conference on Power Electronics and Applications*, pages 1–9, 2013. ISBN 9789075815177.
- [35] M.G. Villalva, J.R. Gazoli, and E.R. Filho. Comprehensive Approach to Modeling and Simulation of Photovoltaic Arrays. *IEEE Transactions on Power Electronics*, 24(5):1198–1208, may 2009. ISSN 0885-8993. doi: 10.1109/TPEL.2009.2013862.
- [36] Indu Rani Balasubramanian, Saravana Ilango Ganesan, and Nagamani Chilakapati. Impact of partial shading on the output power of PV systems under partial shading conditions. *IET Power Electronics*, 7(3):657–666, 2014. ISSN 1755-4535. doi: 10.1049/iet-pel.2013.0143.
- [37] B de Metz-Noblat, F Dumas, and C Poulain. Calculation of short-circuit currents. Technical Report 158, 2005.
- [38] D Das and H S Nagi. Novel method for solving radial distribution networks. *IEE Proceedings - Generation, Transmission and Distribution*, 141(4):291–298, 1994. doi: 10.1049/ip-gtd:19949966.



- [39] Yu-Jen Liu, Pei-Hsiu Lan, and Hong-Hsun Lin. Grid-connected PV inverter test system for solar photovoltaic power system certification. *2014 IEEE PES General Meeting — Conference & Exposition*, pages 1–5, jul 2014. doi: 10.1109/PESGM.2014.6939471. URL <http://ieeexplore.ieee.org/lpdocs/epic03/wrapper.htm?arnumber=6939471>.
- [40] R J Bravo, R Yinger, S Robles, and W Tamae. Solar PV Inverter Testing for Model Validation. pages 1–7, 2011.
- [41] Eung-Sang Kim and Dae-Won Kim. Performance testing of grid connected photovoltaic inverter based on an integrated electronic protection device. *IEEE Transmission and Distribution Asia*, 2009.
- [42] Massimo Valentini, Alin Raducu, Dezso Sera, and Remus Teodorescu. PV inverter test setup for European efficiency, static and dynamic MPPT efficiency evaluation. *2008 11th International Conference on Optimization of Electrical and Electronic Equipment*, pages 433–438, may 2008. doi: 10.1109/OPTIM.2008.4602445. URL <http://ieeexplore.ieee.org/lpdocs/epic03/wrapper.htm?arnumber=4602445>.
- [43] Ramón López-Erauskin, Johan Gyselinck, Frédéric Olivier, Damien Ernst, María Emilia Hervás, and Alexis Fabre. Modelling and Emulation of an Unbalanced LV Feeder with Photovoltaic Inverters. *Proc. of 8th IEEE Benelux Young researchers Symposium in Electrical Power Engineering*, 2016.
- [44] International Energy Agency. Energy policies of IEA countries. Technical report, 2009.
- [45] Hermann J. Abts. *Verteil-Transformatoren, Distribution-Transformers*. 2017. ISBN 978-3-8007-4019-2.
- [46] James H. Harlow. *Electric Power Transformer Engineering*. Taylor & Francis Group, 3 edition, 2012. doi: <https://doi.org/10.1201/b12110>.
- [47] Sudheer Mokkapaty, Jens Weiss, Frank Schalow, and Jan Declercq. New generation voltage regulation distribution transformer with an on load tap changer for power quality improvement in the electrical distribution systems. *CIREN - Open Access Proceedings Journal*, 2017(June):784–787, 2017. doi: 10.1049/oap-cired.2017.0881.
- [48] Jawad Faiz and Behzad Siahkolah. *Electronic tap-changer for distribution transformers*. 2011. ISBN 9783642199103. doi: 10.1007/978-3-642-19911-0.
- [49] José María Canales, Daniel Serrano, Manex Barrenetxea, Jon Andoni Barrena, Ander Goikoetxea, and Jon Anzola. Electronic On Load Tap Changer Transformer

- for DC Electrical Railway Power Supply Systems. In *2019 IEEE Vehicle Power and Propulsion Conference (IEEE-VPPC 2019)*, pages 1–4, 2019.
- [50] SMA Solar Technology AG. Sunny Mini Central 6000T1 / 7000T1 / 8000T1. Technical report. URL <http://files.sma.de/d1/5695/SMC8000TL-DEN102330.pdf>.
- [51] KACO new Energy. blueplanet 3.0 5.0 TL1. Technical report.
- [52] Kyriaki-nefeli D Malamaki and Charis S Demoulias. Estimation of additional PV Converter Losses operating under PF = 1 based on Manufacturer ' s Data at PF = 1. *IEEE Transactions on Energy Conversion*, 34(January):540–553, 2019. doi: 10.1109/TEC.2019.2893065.
- [53] Enrique Romero-Cadaval, Giovanni Spagnuolo, Leopoldo Garcia Franquelo, Carlos Andres Ramos-Paja, Teuvo Suntio, and Weidong Michael Xiao. Grid-Connected Photovoltaic Generation Plants : Components and Operation. *IEEE Industrial Electronics Magazine*, 3(September):6–20, 2013. doi: 10.1109/MIE.2013.2264540.
- [54] Eftichios Koutroulis and Frede Blaabjerg. A New Technique for Tracking the Global Maximum Power Point of PV Arrays Operating Under. *IEEE Journal of Photovoltaics*, 2(2):184–190, 2012.
- [55] Stefan Daraban, Dorin Petreus, and Cristina Morel. A novel global MPPT based on genetic algorithms for photovoltaic systems under the influence of partial shading. *IECON 2013 - 39th Annual Conference of the IEEE Industrial Electronics Society*, pages 1490–1495, nov 2013. doi: 10.1109/IECON.2013.6699353. URL <http://ieeexplore.ieee.org/lpdocs/epic03/wrapper.htm?arnumber=6699353>.
- [56] Robert W Erickson and Aaron P Rogers. A Microinverter for Building-Integrated Photovoltaics. pages 911–917, 2009. doi: 10.1109/APEC.2009.4802771.
- [57] Chien-yao Liao, Student Member, Wen-Shiun Lin, Yaow-ming Chen, and Senior Member. A PV Micro-inverter with PV Current Decoupling Strategy. *Transactions on Power Electronics*, 32(8):6544 – 6557, 2016. doi: 10.1109/TPEL.2016.2616371.
- [58] Geoffrey R. Walker and Paul C. Sernia. Cascaded DCDC Converter Connection of Photovoltaic Modules. *IEEE Transactions on Power Electronics*, 19(4):1130–1139, jul 2004. ISSN 0885-8993. doi: 10.1109/TPEL.2004.830090. URL <http://ieeexplore.ieee.org/lpdocs/epic03/wrapper.htm?arnumber=1310401>.
- [59] N. Femia, G. Lisi, G. Petrone, G. Spagnuolo, and M. Vitelli. Distributed Maximum Power Point Tracking of Photovoltaic Arrays: Novel Approach and System Analysis. *IEEE Transactions on Industrial Electronics*, 55(7):2610–2621, jul 2008.

- ISSN 0278-0046. doi: 10.1109/TIE.2008.924035. URL <http://ieeexplore.ieee.org/lpdocs/epic03/wrapper.htm?arnumber=4497229>.
- [60] Leonor Linares, Robert W. Erickson, Sara MacAlpine, and Michael Brandemuehl. Improved energy capture in series string photovoltaics via smart distributed power electronics. In *24th IEEE Applied Power Electronics Conference and Exposition*, pages 904–910, 2009. ISBN 9781424428120. doi: 10.1109/APEC.2009.4802770.
- [61] Ricardo Alonso, Eduardo Román, Asier Sanz, Víctor E Martínez Santos, and Pedro Ibáñez. Analysis of Inverter-Voltage Influence on Distributed MPPT Architecture Performance. *IEEE Transactions on Industrial Electronics*, 59(10):3900–3907, 2012.
- [62] Massimo Vitelli. On the necessity of joint adoption of both Distributed Maximum Power Point Tracking and Central Maximum Power Point Tracking in PV systems. *Progress in Photovoltaics: Research and Application*, 2012. doi: 10.1002/pip.
- [63] Xiaoqiang Lin, Jinhao Wang, and Peng Wang. Partly-isolated four-port converter based on bidirectional full-bridge DC / DC converter. *2018 13th IEEE Conference on Industrial Electronics and Applications (ICIEA)*, pages 287–292, 2018. doi: 10.1109/ICIEA.2018.8397730.
- [64] SolarEdge Technologies Inc. SolarEdge Power Optimizers P300-P505. Technical report. URL <http://www.solaredge.com/products/power-optimizer>.
- [65] Tigo Energy Inc. Tigo TS4 Integrated Modular Platform. Technical report. URL <https://www.tigoenergy.com/products/>.
- [66] Jinko Solar Inc. JKMS280PP-60-MX. Technical report, 2008. URL [www.jinkosolar.com](http://www.jinkosolar.com).
- [67] Huawei Technologies Co. LTD. SUN2000P-375W Smart PV Optimizer. Technical report, 2018.
- [68] Bailu Xiao, Lijun Hang, Jun Mei, Cameron Riley, Leon M Tolbert, and Burak Ozpineci. Modular Cascaded H-Bridge Multilevel PV Inverter with Distributed MPPT for Grid-Connected Applications. *IEEE Transactions on Industry Applications*, 51(2):1722–1731, 2015. doi: 10.1109/TIA.2014.2354396.
- [69] Chris Deline, Bill Marion, Jennifer Granata, Sigifredo Gonzalez, Chris Deline, and Bill Marion. A Performance and Economic Analysis of Distributed Power Electronics in Photovoltaic Systems. Technical Report January, 2011.

- [70] G. Adinolfi, N. Femia, G. Petrone, G. Spagnuolo, and M. Vitelli. Energy efficiency effective design of DC/DC converters for DMPPT PV applications. In *2009 35th Annual Conference of IEEE Industrial Electronics*, pages 4566–4570. Ieee, nov 2009. ISBN 978-1-4244-4648-3. doi: 10.1109/IECON.2009.5414868. URL <http://ieeexplore.ieee.org/document/5414868/>.
- [71] Eduardo Román, Ricardo Alonso, Pedro Ibañez, Sabino Elorduizapatarietxe, and Damián Goitia. Intelligent PV Module for Grid-Connected PV Systems. *IEEE Transactions on Industrial Electronics*, 53(4):1066–1073, 2006.
- [72] Alex J Hanson, Christopher A Deline, Sara M Macalpine, Jason T Stauth, and Charles R Sullivan. Partial-Shading Assessment of Photovoltaic Installations via Module-Level Monitoring. *IEEE Journal of Photovoltaics*, 4(6):1618–1624, 2014. doi: 10.1109/JPHOTOV.2014.2351623.
- [73] Geoffrey R Walker and Jordan C Pierce. PhotoVoltaic DC-DC Module Integrated Converter for Novel Cascaded and Bypass Grid Connection Topologies: Design and Optimization. In *IEEE Annual Power Electronics Specialists Conference*, pages 3094–3100, 2006.
- [74] Robert C N Pilawa-podgurski, David J Perreault, and Senior Member. Submodule Integrated Distributed Maximum Power Point Tracking for Solar Photovoltaic Applications. *Power Electronics, IEEE Transactions on*, 28(6):2957–2967, 2013.
- [75] G. Adinolfi, N. Femia, G. Petrone, G. Spagnuolo, and M. Vitelli. Design of dc/dc Converters for DMPPT PV Applications Based on the Concept of Energetic Efficiency. *Journal of Solar Energy Engineering*, 132(2):1–10, 2010. ISSN 01996231. doi: 10.1115/1.4001465. URL <http://solarenergyengineering.asmedigitalcollection.asme.org/article.aspx?articleid=1473767>.
- [76] Victor Andrean, Pei Cheng Chang, and Kuo Lung Lian. A Review and New Problems Discovery of Four Simple Decentralized Maximum Power Point Tracking Algorithms Perturb and Observe, Incremental Conductance, Golden Section Search, and Newton’s Quadratic Interpolation. *Energies*, 11(11):1–25, 2018. doi: 10.3390/en11112966.
- [77] Moacyr A G De Brito, Leonardo P Sampaio, Luigi G. Jr., Guilherme A e Melo, and Carlos A Canesin. Comparative Analysis of MPPT Techniques for PV Applications. In *International Conference on Clean Electrical Power, ICCEP*, pages 99–104, 2011. ISBN 9781424489305.

- [78] Ahmed Saidi. Comparison of IC and P & O algorithm algorithms ms in MPPT for grid connected PV module. In *8th International Conference on Modelling, Identification and Control, ICMIC*, pages 213–218, 2016. ISBN 9780956715760.
- [79] K H Hussein, I Muta, T Hoshino, and M Osakada. Maximum photovoltaic power tracking : an algorithm for rapidly changing atmospheric conditions. *IEE Proceedings on Generation, Transmission and Distribution*, 142:59–64, 1995.
- [80] Jae Ho Lee, Hyunsu Bae, and Bo Hyung Cho. Advanced Incremental Conductance MPPT Algorithm with a Variable Step Size. In *12th International Power Electronics and Motion Control Conference, EPE-PEMC*, number 1, pages 603–607, 2006. ISBN 1424401216.
- [81] Roberto Faranda and Sonia Leva. Energy Comparison of MPPT Techniques for PV Systems. *WSEAS TRANSACTIONS on POWER SYSTEMS*, 03(06):446–455, 2008. ISSN 1942-0730. doi: 10.4236/jemaa.2009.13024.
- [82] C Liu, B Wu, and R Cheung. Advanced Algorithm for MPPT control of Photovoltaic Systems. In *Canadian Solar Buildings Conference*, pages 20–24, 2004.
- [83] Yeong Chau Kuo, Tsorng Juu Liang, and Jiann Fuh Chen. Novel maximum-power-point-tracking controller for photovoltaic energy conversion system. *IEEE Transactions on Industrial Electronics*, 48(3):594–601, 2001. ISSN 02780046. doi: 10.1109/41.925586.
- [84] Canras Batunlu, Mohamad Alrweq, and Alhussein Albarbar. Effects of Power Tracking Algorithms on Lifetime of Power Electronic Devices Used in Solar Systems. *Energies*, 9:1–23, 2016. doi: 10.3390/en9110884.
- [85] SMA Solar Technology AG. Sunny Tripower 5000TL-12000TL. Technical report, 2017. URL <https://files.sma.de/dl/17781/STP12000TL-DAU1723-V10web.pdf>.
- [86] Ramón López-Erauskin, Ander González, Giovanni Petrone, Giovanni Spagnuolo, and Johan Gyselinck. Multi-Variable Perturb & Observe Algorithm for Grid-tied PV Systems with Joint Central and Distributed MPPT Configuration. *IEEE Transactions on Sustainable Energy*, pages 1–8.
- [87] Ander Gonzalez, Ramon Lopez-Erauskin, and Johan Gyselinck. Interleaved Three-Port Boost Converter for Photovoltaic Systems Including Storage. In *19th European Conference on Power Electronics and Applications*, pages 1–9, 2017. doi: 10.23919/EPE17ECCEurope.2017.8099225.

- [88] Kosuke Kurokawa, D H Uchida, K Sakamoto, T H Oshiro, K Otani, and K Fukasawa. Sophisticated verification of simple monitored data for Japanese Field Test Program. In *2nd World Conference and Exhibition on Photovoltaic Solar Energy Conversion*, volume 4, pages 1941–1946, 1998.
- [89] Ulrike Jahn and Wolfgang Nasse. Operational performance of grid-connected PV systems on buildings in Germany. *Progress in Photovoltaics: Research and Applications*, 12(6):441–448, sep 2004. ISSN 1062-7995. doi: 10.1002/pip.550. URL <http://doi.wiley.com/10.1002/pip.550>.
- [90] Sara M Macalpine, Robert W Erickson, and Michael J Brandemuehl. Characterization of power optimizer potential to increase energy capture in photovoltaic systems operating under non-uniform conditions. *IEEE Transactions on Power Electronics*, 28(June):2936–2945, 2013.
- [91] Giovanni Petrone, Carlos Andrés Ramos-Paja, Giovanni Spagnuolo, and Massimo Vitelli. Granular control of photovoltaic arrays by means of a multi-output Maximum Power Point Tracking algorithm. *Progress in Photovoltaics: Research and Applications*, pages n/a–n/a, mar 2012. ISSN 10627995. doi: 10.1002/pip.2179. URL <http://doi.wiley.com/10.1002/pip.2179>.
- [92] C. a. Ramos-Paja, G. Spagnuolo, G. Petrone, S. Serna, and a. Trejos. A vectorial MPPT algorithm for distributed photovoltaic applications. *2013 International Conference on Clean Electrical Power (ICCEP)*, pages 48–51, jun 2013. doi: 10.1109/ICCEP.2013.6586964. URL <http://ieeexplore.ieee.org/lpdocs/epic03/wrapper.htm?arnumber=6586964>.
- [93] Ander González, Ramón López-Erauskin, and Johan Gyselinck. Grid-tied Modular and Scalable Photovoltaic Distributed Maximum Power Point Tracking System with Storage at Module Level Using Non-Isolated Three-Port Converters. In *20th European Conference on Power Electronics and Applications (EPE'18 ECCE Europe)*, 2018.
- [94] M. Balato, M. Vitelli, N. Femia, G. Petrone, and G. Spagnuolo. Factors limiting the efficiency of DMPPT in PV applications. In *2011 International Conference on Clean Electrical Power (ICCEP)*, pages 604–608. Ieee, jun 2011. ISBN 978-1-4244-8929-9. doi: 10.1109/ICCEP.2011.6036319. URL <http://ieeexplore.ieee.org/lpdocs/epic03/wrapper.htm?arnumber=6036319>.
- [95] Ramón López-Erauskin, Ander González, and Johan Gyselinck. Control Strategies for Modular Grid-tied DMPPT Systems Integrating Photovoltaic Generation and Battery Storage at Module Level. In *20th European Conference on Power Electronics and Applications (EPE'18 ECCE Europe)*, 2018.

- [96] Dezso Sera, Remus Teodorescu, Jochen Hantschel, and Michael Knoll. Optimized Maximum Power Point Tracker for Fast Changing Environmental Conditions. In *IEEE Transactions on Industrial Electronics*, pages 2401–2407, 2008. ISBN 9781424416660. doi: 10.1109/ISIE.2008.4677275.
- [97] Ander González, Ramón López-Erauskin, and Johan Gyselinck. Analysis, modeling, control and operation of an interleaved three-port boost converter for DMPPT systems including PV and storage at module level. *Heliyon*, 5(3):e01402, 2019. doi: 10.1016/j.heliyon.2019.e01402.
- [98] Ramón López-Erauskin, Ander González, Johan Gyselinck, Giovanni Petrone, and Giovanni Spagnuolo. Centralized control in photovoltaic distributed maximum power point tracking systems. In Springer Books, editor, *Lecture Notes in Electrical Engineering (LNEE)*, number May, 2019.
- [99] N. Femia, G. Petrone, G. Spagnuolo, and M. Vitelli. Optimization of Perturb and Observe Maximum Power Point Tracking Method. *IEEE Transactions on Power Electronics*, 20(4):963–973, jul 2005. ISSN 0885-8993. doi: 10.1109/TPEL.2005.850975. URL <http://ieeexplore.ieee.org/lpdocs/epic03/wrapper.htm?arnumber=1461481>.
- [100] Nicola Femia, Giovanni Petrone, Giovanni Spagnuolo, and Massimo Vitelli. *Power Electronics and Control Techniques for Maximum Energy Harvesting in Photovoltaic Systems*. Taylor & Francis Group, 2013. ISBN 9781466506916.
- [101] Robert W. Erickson and Dragan Maksimović. *Fundamentals of Power Electronics*. Springer Science+Business Media, LLC, 2001. ISBN 9781475705591. doi: 10.1007/978-0-306-48048-5.
- [102] Patrizio Manganiello, Mattia Ricco, Giovanni Petrone, Eric Monmasson, and Giovanni Spagnuolo. Optimization of perturbative PV MPPT methods through online system identification. *IEEE Transactions on Industrial Electronics*, 61(12):6812–6821, 2014. ISSN 02780046. doi: 10.1109/TIE.2014.2317143.